

UNCLASSIFIED

---

AD 284 282

*Reproduced  
by the*

ARMED SERVICES TECHNICAL INFORMATION AGENCY  
ARLINGTON HALL STATION  
ARLINGTON 12, VIRGINIA

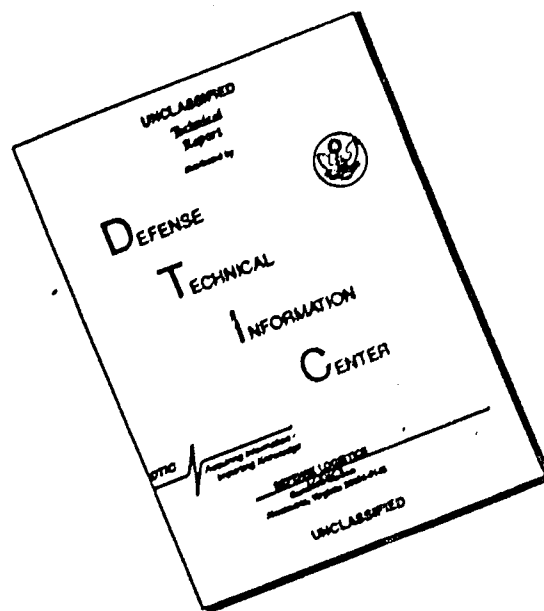


---

UNCLASSIFIED

NOTICE: When government or other drawings, specifications or other data are used for any purpose other than in connection with a definitely related government procurement operation, the U. S. Government thereby incurs no responsibility, nor any obligation whatsoever; and the fact that the Government may have formulated, furnished, or in any way supplied the said drawings, specifications, or other data is not to be regarded by implication or otherwise as in any manner licensing the holder or any other person or corporation, or conveying any rights or permission to manufacture, use or sell any patented invention that may in any way be related thereto.

# DISCLAIMER NOTICE



THIS DOCUMENT IS BEST QUALITY AVAILABLE. THE COPY FURNISHED TO DTIC CONTAINED A SIGNIFICANT NUMBER OF PAGES WHICH DO NOT REPRODUCE LEGIBLY.

Proceedings

of the



Fifth  
Symposium  
on

Hypervelocity

IMPACT

VOLUME I - PART I  
APRIL, 1962

284 282

Denver  
October 30, 31,  
November 1, 1961

Volume 1 of the Fifth Symposium on Hypervelocity Impact appears in two parts. Part 1 contains pages 1 through 330 - Sessions I through III. Part 2 contains pages 331 through 663 - Sessions IV through VI.

Proceedings of the  
Fifth Symposium  
on  
Hypervelocity  
IMPACT

***Sponsored by:***

**U.S. Navy  
U.S. Army  
U.S. Air Force**

***Contract No.***

**Nonr-(G)-0020-62(X)**

***Tri-Service Committee:***

**W. W. Atkins, Navy, Chairman  
R. J. Zichelberger, Army, BRL  
H. L. Davis, Air Force**

***Colorado School of Mines (Conference Host)***

**John S. Rinehart**

NOTE: Not included in the published Proceedings of the Fifth Hypervelocity Impact Symposium are:

"Welcoming Remarks" by Dr. John W Vanderwilt, President, Colorado School of Mines.

Luncheon address, "The Challenge of Hypervelocity to Education," by Dr. John S. Rinehart, host to the Symposium and Director, Mining Research Laboratory, Colorado School of Mines.

Banquet address, "Academic Standards for the Aerospace Age," by Dr. William L. Whitson, Vice President, The Martin Company, Denver.

Discussions taking place during the Symposium were not transcribed.

Some informal opening remarks by session chairmen have been omitted.

The views, conclusions and recommendations expressed herein do not necessarily reflect the official views or policies of either the United States Army, United States Navy or the United States Air Force.

# TABLE OF CONTENTS

	Page
SESSION I - TECHNIQUES	
INTRODUCTORY PAPER H. F. Swift	I
INTRODUCTORY PAPER (C) H. F. Swift	Vol. II
SUMMARY OF NAVAL RESEARCH LABORATORY ACCELERATOR DEVELOPMENT C. D. Porter, H. F. Swift and R. H. Fuller	23
INTERIOR BALLISTICS OF HYPERVELOCITY PROJECTORS INSTRUMENTED LIGHT GAS GUN AND TRAVELING CHARGE GUN P. G. Baer and H. C. Smith	53
THE APPLICATION OF THE "q" METHOD OF HYPERVELOCITY GUN PROBLEMS (C) D. Piacitelli and H. M. Sternberg	Vol. II
EXPLOSIVE DEVICES FOR PROJECTING HYPERVELOCITY PELLETS UP TO 2100 KM/SEC (C) S. K. Manian and J. H. Kineke, Jr.	Vol. II
EXPERIMENTS WITH A TWO MILLION VOLT ELECTROSTATIC ACCELERATOR J. F. Friichtenicht	79
SUMMARY OF SESSION H. F. Swift	95
SESSION II - THEORY	
INTRODUCTORY PAPER F. E. Alton	99
STUDIES OF HYPERVELOCITY IMPACT OF METALS H. G. Hopkins	105
SOME THEORETICAL MODELS OF HYPERVELOCITY N. Davidson, Y. K. Huang and W. Jaunzemis	111
SESSION III - THEORY	
CHAIRMAN'S REMARKS H. G. Hopkins	134

# CONTENTS

	Page
INERTIAL, VISCOUS AND PLASTIC EFFECTS IN HIGH SPEED IMPACT T. D. Riney and P. R. Chernoff	135
A THEORETICAL STUDY OF DYNAMIC PLASTIC DEFORMATION UNDER IMPACT LOADS L. E. Fugelso	163
HYDRODYNAMICS APPLIED TO HYPERVELOCITY IMPACT	
I. Scaling Laws for Dissimilar Materials	185
II. Role of Melting and Vaporization	225
III. Impacts on Thin Targets (not submitted for publication) A. E. Olshaker and R. L. Bjork	
IV. Analysis of the Formation of Meteor Crater, Arizona: A Pre- liminary Report, published in Journal of Geophysical Research, October, 1961.	
V. Cratering from a Megaton Surface Burst R. L. Bjork (Not submitted for publication)	
PENETRATION BY HYPERVELOCITY PARTICLES M. Zaid	241
A MODEL OF NON-EXPLOSIVE IMPACT J. F. Schipper	267
APPLICATION OF 'HYDRODYNAMIC' THEORY TO THE LOW STRESS RANGE OF HYPERVELOCITY IMPACT PROBLEMS I. M. Fyfe	299
VISCO-PLASTIC FLOW THEORY IN HYPERVELOCITY PERFORATION OF PLATES Pei Chi Chou	307
SUMMARY OF SESSION F. E. Allison	329
SESSION IV -- EXPERIMENTS	
CHAIRMAN'S REMARKS F. E. Howard	332
INTRODUCTORY PAPER R. J. Eichelberger	333
OBSERVATIONS OF CRATER FORMATION IN DUCTILE MATERIALS J. H. Kineke, Jr.	339
IMPACT EXPERIMENTS ON WAX J. T. Frasier and B. G. Karpov	371
CORRELATION OF HYPERVELOCITY IMPACT DATA W. Herrmann and A. H. Jones	389

# CONTENTS

	Page
REVIEW AND ANALYSIS OF HIGH VELOCITY IMPACT DATA E. P. Bruce	439
HYPERVELOCITY LAUNCHERS AND HYPERVELOCITY IMPACT EXPERIMENTS AT <u>ARDE</u> , FORT HALSTEAD F. Smith, W. A. Clayden, C. R. Wall and D. T. F. Winter	475
EXPERIMENTAL OBSERVATIONS OF IMPACT S. M. Halperson and W. W. Atkins	497
OBLIQUE IMPACT OF HIGH VELOCITY STEEL PELLETS ON LEAD TARGETS George M. Bryan	511
HYPERVELOCITY IMPACT OF HEATED COPPER M. Rockowitz, C. Carey and J. Dignam	535
CRATER CHARACTERISTICS DUE TO IMPACTS BETWEEN 4 AND 15 KM/SEC E. Cannon, W. A. Clark and T. W. Lee	549
SESSION V -- EXPERIMENTS	
CHAIRMAN'S REMARKS Maurice Dubin	565
AN EXPERIMENTAL INVESTIGATION OF SINGLE ALUMINUM METEOR BUMPERS D. Humes, R. N. Hopko and W. H. Kinard	567
THE PERFORATION OF THIN PLATES BY HIGH VELOCITY FRAGMENTS R. W. Watson	581
PERFORATION OF FINITE TARGETS BY HIGH VELOCITY PROJECTILES R. Vitali, K. R. Becker, and R. W. Watson	593
PENETRATION OF THIN PLATES K. N. Kreyenhagen and L. Zernow	611
HIGH VELOCITY IMPACT PHENOMENA WITH HYPERSTRENGTH PARTICLES (C) R. L. Hill and Fred E. Howard	• Vol. II
ON THE EFFECT OF PROJECTILE MASS DISTRIBUTION IN HYPER VELOCITY IMPACT (C) Donald R. Dudas	Vol. II
THE GEOLOGY OF HYPERVELOCITY IMPACT CRATERS H. J. Moore II and R. V. Jahn	625

# CONTENTS

	Page
HIGH VELOCITY IMPACT INTO PLASTIC FIBREGLASS LAMINATES (S) P. L. Cowan and P. L. Roney	Vol. II
MICRO-PARTICLE HYPERVELOCITY IMPACTS FROM RANGER I W. M. Alexander and O. E. Berg	645
SUMMARY OF SESSION R. J. Eichelberger	653
SESSION VI -- APPLICATIONS	
CHAIRMAN'S REMARKS (C) R. C. Weidler	Vol. II
INTRODUCTORY PAPER (S) W. W. Atkins (S)	Vol. II
CRATER FORMATION IN MISSILE SURFACE MATERIALS (S) J. G. Dante	Vol. II
HIGH VELOCITY PARTICLE IMPACT EFFECTS ON ICBM RE-ENTRY VEHICLE STRUCTURES (S) R. E. Soloski, E. P. Bruce and A. M. Smith	Vol. II
HYPERVELOCITY IMPACT -- EFFECTS ON SOME ABLATIVE RE- ENTRY HEAT SHIELD STRUCTURES (S) J. A. Hull, R. Rockowitz and W. L. McKay	Vol. II
AEROTHERMAL EFFECTS OF HYPERVELOCITY PARTICLE IMPACT ON RE-ENTRY VEHICLES (S) D. E. Nestler, E. E. VandenEykel, D. A. Clunies and R. J. Berman	Vol. II
THERMAL EFFECTS IN HYPERVELOCITY KILL MECHANISMS (S) H. Hoercher	Vol. II
VULNERABILITY OF RE-ENTRY VEHICLES (S) H. S. Kostiak	Vol. II
A PROTOTYPE FRAGMENTATION WARHEAD FOR NIKE ZEUS (S) T. W. Stevens and S. D. Stein	Vol. II
IMPACT EFFECTS AGAINST PROPULSION SYSTEMS (S) K. N. Kreyenhagen, R. B. Mortenson and L. Zernow	Vol. II
SUMMARY AND DISCUSSION W. W. Atkins	Vol. II
ATTENDANCE ROSTER	659

SESSION I  
TECHNIQUES  
CHAIRMAN  
VICE ADMIRAL CHARLES B. MARTELL  
OFFICE OF THE SECRETARY  
OF DEFENSE

## HYPERVELOCITY BALLISTIC ACCELERATORS

H. F. Swift

U. S. Naval Research Laboratory  
Washington, D. C.

### INTRODUCTION

During the past seven years, there has developed an increasing need for laboratory facilities capable of accelerating a variety of model configurations to hypervelocities. In response to this need, a wide range of model-acceleration techniques has been developed to the point where many hypervelocity phenomena now can be studied directly in the laboratory. The results of the papers presented in this section will show that the capabilities of hypervelocity ballistic facilities are advancing at an ever-increasing rate, widening the range of phenomena directly reproducible under laboratory conditions, and reducing the range of extrapolation needed to study presently unattainable ones.

There are at present four fields of research using data obtained with hypervelocity accelerators. Aerodynamic ballistic facilities that study problems concerned with drag and stability of high-speed vehicles, such as missiles and space ships, under conditions encountered during re-entry into the earth's atmosphere are in operation. Ideally they require accurate scale models of vehicles fitted with instrumentation and telemetry equipment that can be launched at full vehicle re-entry velocities. In terms of acceleration performance, large-bore guns (2 inches or greater) are needed that can fire models to velocities of 7.75 km/sec with peak accelerations below 250,000 g's. At present, large instrumented models can be successfully launched to 4.6 km/sec, and similar inert ones to 6.7 km/sec.

Aerophysics studies are being carried out to evaluate the ablation rate of high-speed objects re-entering the atmosphere and to determine the characteristics of their wakes. For these studies relatively small homogeneous models of simple geometric form will suffice for the present investigations. The immediate interest is in satellite and missile re-entry velocities, but preparations are being made to study re-entry of deep-space probes and meteoroids that can enter the atmosphere at speeds up to 72 km/sec. At present combinations of gas gun, explosive, and special accelerator techniques are capable of firing a variety of models at velocities up to 7.5 km/sec and a limited number of model shapes and materials to 21 km/sec.

The results of impact experiments at hypervelocities are being applied to three areas of study. Most interest at present is in the evaluation of techniques to destroy ballistic missiles by fragment attack. Present requirements for these

## BALLISTIC ACCELERATORS

pressure immediately behind it below the value within the chamber at the same instant of time. A velocity is finally reached at which the pressure at the rear of the projectile drops to zero, ending its acceleration. Thus, a limit of maximum projectile velocity exists for a powder gun.

To understand the nature of this reduction of pressure with increased projectile velocity, a simple gas-dynamic argument can be used. As the gas in the high-pressure reservoir of a gun flows down the launch tube after a moving projectile, it must expend a fraction of the energy stored in it in the form of pressure and temperature to accelerate its own mass up to the projectile's instantaneous velocity. Since the stored energy per unit volume in the gas is proportional to its mass per unit volume, the percentage loss is stored energy during its acceleration to a particular velocity is independent of its original density. The removal of this stored energy reduces its pressure, so that the pressure immediately behind the projectile falls below that in the reservoir. A projectile maximum velocity is eventually reached at which the gas must expend all of its energy accelerating itself, and its pressure drops to zero. This velocity represents the maximum expansion velocity of the driver gas, or its "efflux" velocity. For the ideal-gas case:

$$a = \sqrt{\frac{2}{\gamma - 1}} a_0$$

or

$$a = \sqrt{\frac{2}{\gamma - 1}} \sqrt{\frac{R}{M} T}$$

$a$  = efflux velocity  
 $a_0$  = reservoir sound speed  
 $\gamma$  = ratio of specific heats  
 $R$  = universal gas constant  
 $T$  = gas temperature  
 $M$  = gas molecular-wt

Table 1

Gas	Temp. (°K)	$a_0$ (km/sec)	Experimental Gun	Gun Type
			Max. Vel. (km/sec)	
powd.	3,000 <sup>o</sup>	3.46	3.1	Mann
He	5,000	7.20	6.7	Small piston
He	12,000	11.2		
H <sub>2</sub>	3,000	9.3	8.8	Small piston
H <sub>2</sub>	12,000	19.6		

Efflux Velocity for Various Gas-Gun Reservoir Conditions are Shown in Table 1.

It must be emphasized that the efflux velocity limitation on peak gun performance can be approached only when sufficient gas pressure and launch-tube length are available to accelerate the projectile to such velocities that efflux effect is dominant.

The only way to increase gas efflux velocity over a wide range, and hence maximum gun performance, is to increase  $T/m$ . This can be accomplished either by increasing the driver-gas temperature or decreasing the molecular weight.

## BALLISTIC ACCELERATORS

studies are for models of simple geometric forms made from materials with a wide range of densities, weighing from 2 to 500 grams. Peak velocities of 9 km/sec are satisfactory for the present, but projected future requirements will be for similar models at considerably higher velocities. Presently available techniques cover the entire velocity region of interest, but the higher velocity areas are limited to low-mass models made from low-density materials. Gas-gun facilities are presently under construction that are designed to provide full coverage of present antimissile-system evaluation requirements.

Another impact-study program concerns the effect of both large and micro-meteoroid impacts into space-probing vehicles. For these studies, projectiles of fairly low densities, with masses between  $10^{-12}$  grams and 10 grams are required, with peak speeds up to 85 km/sec. At present no techniques exist that can reach the upper regions of the velocity requirements, but gas guns, explosives, and special techniques are capable of covering the mass spectrum up to one gram at velocities up to 20 km/sec.

A field that has benefited from all phases of impact experimentation is solid-state physics. Hypervelocity impacts are capable of producing higher pressures within a target than those attainable by any other techniques.

Generally, the accelerator development efforts of the past several years have developed capability for studying at least a limited range of all hypervelocity phenomena under realistic conditions, but significant benefits will be achieved in each area of interest as capability is increased in the future. Hypervelocity ballistic accelerator development has generally progressed along two main lines of approach: light-gas-gun development and explosive-charge development. A series of techniques has also been developed for specialized acceleration tasks that are of importance to the general technology.

### LIGHT-GAS GUNS

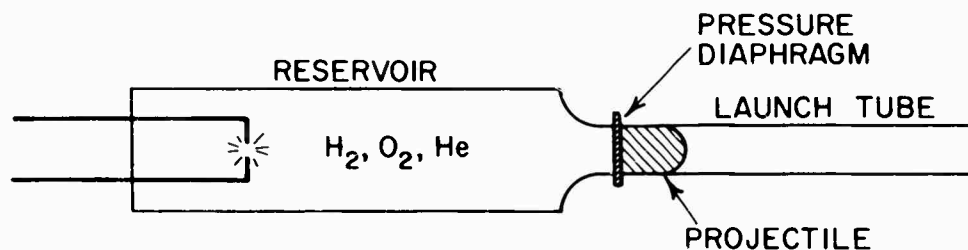
Gun systems powered by reservoirs of low-molecular-weight gas at high temperature and high pressure have found wide use as model projectors in hypervelocity range facilities throughout the country. Presently existing units are capable of firing projectiles weighing 0.1 gram to 10 km/sec and 900 grams to 3.6 km/sec. The basic limitations on the performance of gas-powered ballistic accelerators have been the subject of intense study in recent years. Results of these studies have provided the information required for the design of present high-performance guns.

The nature of gun-velocity limitations can best be understood for the case of the simple powder gun. The firing sequence of a powder gun begins with ignition of the solid propellant in a sealed chamber at one end of a launch tube. The propellant is rapidly consumed, liberating a volume of high-temperature and high-pressure gas that exerts an even pressure on the walls of the chamber, one of which is the rear surface of the projectile. Since the projectile is relatively free to move, it accelerates, and as long as the projectile velocity remains low, the pressure on its rear surface remains the same as that on the rest of the chamber. As the projectile velocity increases, however, a pressure gradient is observed to develop between the stationary chamber and the projectile that reduces the

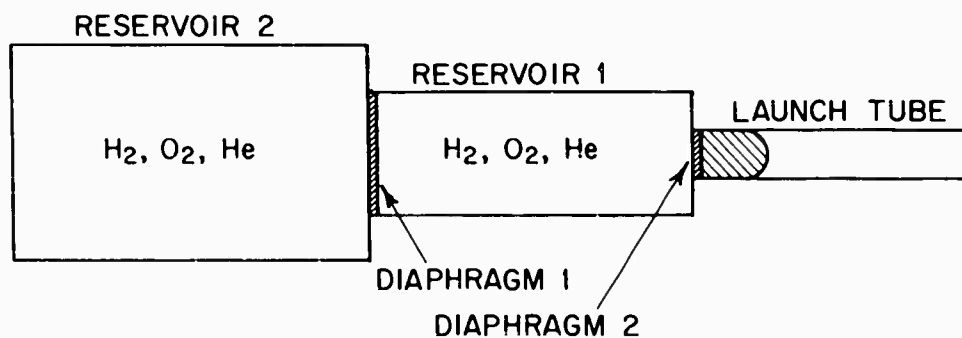
## BALLISTIC ACCELERATORS

### Helium and Steam Gun

The most direct approach to increasing the efflux velocity of the driver-gas in a gun is to devise a propellant that will yield as low-molecular-weight gas as possible at as high a temperature as possible when burned. A widely used high-efflux-velocity propellant is a gaseous mixture of helium with a stoichiometric mixture ratio of hydrogen and oxygen. Upon ignition, the hydrogen and oxygen react, yielding steam with a molecular weight of 18 and a large amount of heat. Thermal equilibrium is rapidly established between the steam and helium, thus generating a high-temperature gas mixture with a mean molecular weight between that of helium and steam. Such a gun is shown in Figure 1. After gas reaction, the reservoir pressure is sufficient to rupture the diaphragm, and the helium-steam mixture accelerates the projectile down the launch tube. The helium added to the hydrogen and oxygen serves the double purpose of preventing detonation during the steam formation and reducing the mean molecular weight of the heated gas mixture. There is an optimum ratio of helium to steam at approximately 20 percent steam by molecular concentration for maximum efflux velocity. An optimum ratio occurs, because addition of steam increases gas temperature and molecular weight at different rates.



(a) SINGLE STAGE



(b) DOUBLE STAGE

### PISTONLESS LIGHT GAS GUNS

Figure 1

## BALLISTIC ACCELERATORS

Since the energy released from steam formation must be used to heat more gas than it generates, energy densities are restricted to values below those common for powder propellants. This limitation on energy density limits peak pressures in turn, so that single-stage helium-steam guns must operate at relatively low peak acceleration. For this reason, they have found their principle application in the acceleration of large, relatively delicate models to the low hypervelocity region.

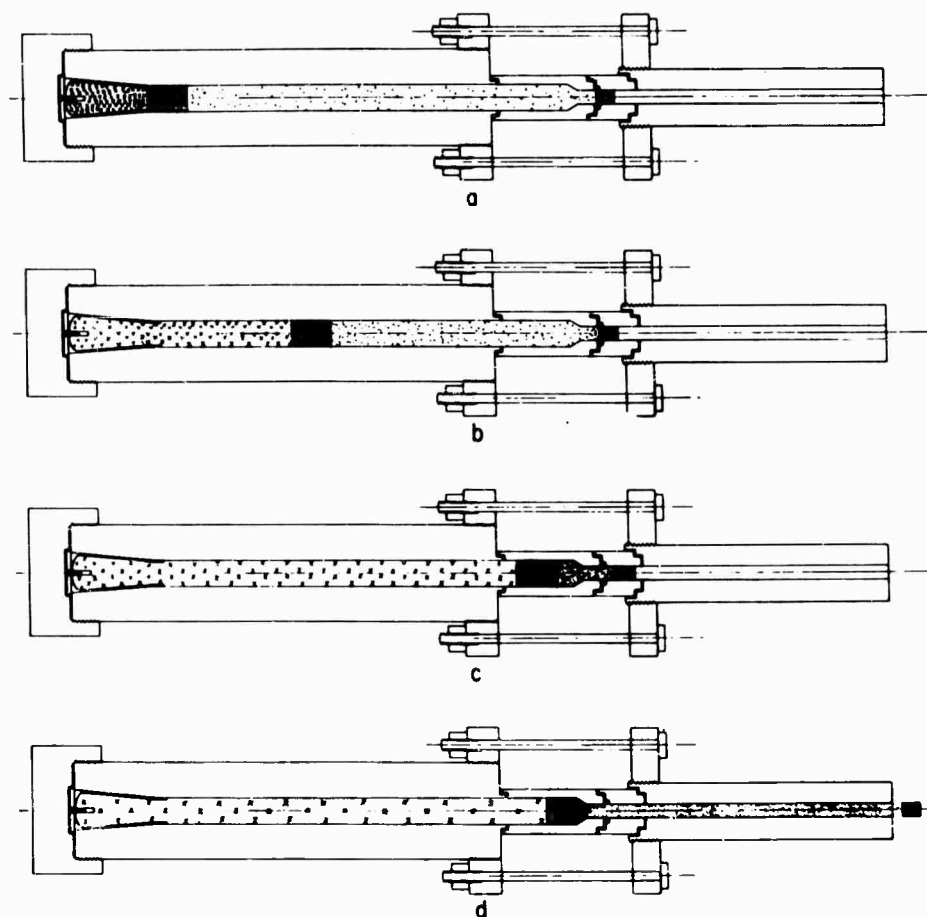
Somewhat higher velocities have been achieved with  $H_2$ ,  $O_2$ , He guns by increasing the energy density of the driver-gas mixture through shock compression. A typical gun design of this type is shown in Figure 1. Here, two reservoirs charged with hydrogen, oxygen, and helium are connected end to end. The front reservoir is ignited, thereby increasing its temperature and pressure to near the rupture level of diaphragm 2. The rear reservoir (at higher initial density) is then ignited, rupturing diaphragm 1 and driving a strong shock wave through the front reservoir. This shock wave heats the gas in the front reservoir and ruptures diaphragm 2, allowing projectile acceleration to begin. The high-density gas from the rear reservoir flows rapidly into the front one during the early stages of projectile acceleration, thereby compressing the driver-gas and further increasing the temperature and pressure of the driver-gas mixture. Double-stage helium, steam guns are generally smaller than single-stage ones, since they are more complicated, and peak gas pressures can be made higher. They have been used to accelerate smaller, less delicate models to somewhat higher velocities at higher acceleration levels than is possible with single-stage guns. Double-stage helium, steam guns are no longer in general use, because another technique for generating reservoirs of very high efflux-velocity gas has proved itself considerably more effective.

### Piston-Compression Light-Gas Guns

Piston-powered light-gas guns utilize the rapid compression of a volume of low-molecular-weight gas to produce a reservoir of high efflux-velocity gas at high pressure for projectile acceleration. An initial volume of gas at relatively low density is held in a heavy-walled smooth tube sealed at one end by a movable piston and at the other by a quick-opening valve arrangement. Beyond the valve is a projectile mounted in a launch tube. Figure 2 shows the operation of one type of piston-powered gas gun (expendable-central-breech model). Firing is initiated by igniting the propellant, which accelerates the piston violently down the tube, compressing the light gas and increasing its temperature and pressure. As a critical value of pressure is reached, the quick-opening valve mechanism opens, and projectile acceleration begins. Depending on the mode of operation being utilized, the piston will either be stopped by the high gas pressure ahead of it at the time of projectile release or continue compression until it is later stopped either by higher gas pressure or impact into the transition section (each of these possibilities will be discussed in detail).

In all types of piston-compression gas guns, there need be no tradeoff between temperature and molecular weight, as was the case in the helium-steam guns, so that the driver-gas molecular weights can be kept to a minimum. Also the maximum energy density in the gas is limited only by the structural strength of the containing hardware, so that very high reservoir pressures and temperatures

## BALLISTIC ACCELERATORS



SCHEMATIC DIAGRAM OF LIGHT-GAS GUN OPERATION

Figure 2

can be achieved. These two effects combine to permit very high driver-gas efflux velocities to be developed. Since pressures can become very large, relatively short launch tubes are required to accelerate projectiles to near driver-gas efflux velocity. Guns utilizing compression pistons presently are capable of achieving higher projectile velocities than any other type of gun for projectiles weighing less than 500 grams. Pistonless guns are used most effectively at present for large size low-density projectiles. Relatively high driver-gas pressures are used in the piston type guns and as a consequence projectile acceleration levels are generally higher than pistonless guns; the smaller and more compact projectiles are more capable of withstanding the high acceleration forces of the piston type guns.

## BALLISTIC ACCELERATORS

### Modes of Operation

Let us now consider in some detail the operations of gas guns. Since the piston rapidly compresses the driver-gas, the process can be considered, to a first approximation, adiabatic, so that the temperatures and pressures are governed by the following relationship for the ideal gas case:

$$P = P_0 \left( \frac{V_0}{V} \right)^\gamma$$
$$T = T_0 \left( \frac{V_0}{V} \right)^{\gamma-1}$$

$P$	= instantaneous gas pressure
$P_0$	= initial gas pressure
$T$	= instantaneous gas temperature
$T_0$	= initial gas temperature
$V$	= instantaneous gas volume
$V_0$	= initial gas volume
$\gamma$	= ratio of specific heats

Thus, halving the volume of a perfect monatomic driver-gas during a piston compression stroke increases its pressure by a factor of 3.17 and its temperature by a factor of 1.59. Since the temperature increases more slowly than the pressure, extreme compression ratios are required to develop the high gas temperatures needed for high efflux velocities. For this reason, many high-performance piston-compressed-gas guns have very long compression tubes.

The requirement for large gas-compression ratios can be greatly reduced through the use of supplementary gas-heating techniques. The most widely used method to date consists of firing the piston into the driver-gas at speeds exceeding the local speed of sound in the gas, thereby generating a shock wave near the face of the piston that leaves it as its velocity becomes subsonic (due both to its deceleration and the increased sound speed in the driver-gas with compression). The shock wave will propagate in the compression tube, reflecting several times between the transition section and the piston during compression, heating the gas with each transit. Thus, by use of piston-shock heating, high driver-gas temperature can be achieved with relatively short guns.

Several alternative means of increasing driver-gas temperature exist. Various chemically active gas mixtures like the  $H_2O_2$ -He mixture used in pistonless guns have been considered in detail for use in piston guns, but none have provided spectacular results thus far. Another group of techniques which seem quite promising rely on preheating the driver-gas before firing to increase peak gas temperatures. The adiabatic temperature relationship  $T = T_0(V_0/V)^{\gamma-1}$  shows that doubling the initial temperature will double all subsequent ones. Thus, heating a reservoir of a gas gun to 327°C prior to firing will double its peak gas temperatures and increase its driver-gas efflux velocity by a factor of 1.4\*.

The operation of piston-compression gas guns is also affected by the motion of the piston after projectile release. In the original light-gas gun developed at the New Mexico Institute of Mining and Technology, efforts were made to impart enough kinetic energy to the piston so that it can compress the driver-gas to the exact projectile release pressure. The piston was then accelerated back down the compression

\* See paper on "Summary of NRL Hypervelocity Accelerator Development for Comprehensive Review of Such Techniques."

## BALLISTIC ACCELERATORS

tube as the projectile was launched. It was later found possible to increase the driver-gas peak temperature and pressure substantially by providing the piston with sufficient energy to continue compression after projectile release and be stopped by the increased gas pressure later in the cycle. Still higher driver-gas temperatures and pressures are available if the compression piston has enough energy to empty the gas reservoir completely at high speed and impact into the transition section. All present high-performance light-gas guns are operated in one of the latter two modes.

### Piston-Gas-Gun Classification

During the past several years, such a large number of piston gas guns have been built and successfully operated that it is virtually impossible to catalog them in a report of this scope. Upon examination, however, all are found to be made up of combinations of a relatively small number of piston driver devices and transition sections between the compression and launch tubes. Each of these will be discussed in turn. Examples of most combinations are feasible and have been constructed.

The simplest piston driver is shown in Figure 3A. A case of solid propellant is ignited, and the resultant gas drives the piston down the compression tube just as in a standard gun. This type of driver has found particularly wide use, since it can be simply modified from standard guns. Piston velocities up to 2.3 km/sec can be attained with powder guns, so that both subsonic and low supersonic piston firings into helium or hydrogen are possible.

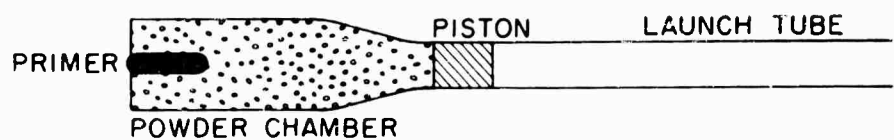
The second driver (Figure 3B) is a one-stage pistonless gun of the type described above. Such drivers can readily achieve 3.6 km piston velocities and have the advantages of clean operation (steam and helium are the only reaction products).

A modification of the helium-steam driver is shown in Figure 3C. Here pure helium is heated by a shock wave generated by the fast-burning powder, and is compressed by the advancing powder gas front. This driver has performance comparable with powder-gun drivers, but peak pressures are considerably lower, so that lighter construction is possible. Powder-helium drivers are mainly used with larger gas guns at present.

Figure 3D shows the basic scheme of a three-stage piston-compression gas gun. Here the projectile from the first gun serves as a piston for the second. Piston velocities up to 5 km/sec have been reached, so that extreme driver-gas shock heating can be accomplished. Guns of this form were among the first to develop projectile velocities as high as typical ICBM and satellite velocities, but their complicated nature has prevented their large-scale use.

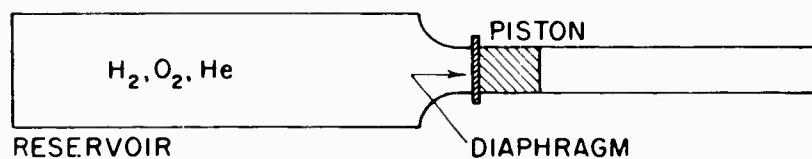
Three basic transition sections in general use today are shown in Figure 4. Figure 4A shows the expendable central-breech assembly, consisting of an independent section containing the transition that connects the compression tube to the launch tubes. This section is used with a gun in which the piston receives sufficient kinetic energy to complete the compression stroke at high speed and deform itself into the conical taper. In this way pressures above  $10^6$  psi have been achieved and used to accelerate projectiles to above 8.2 km/sec. The expendable section is

# BALLISTIC ACCELERATORS



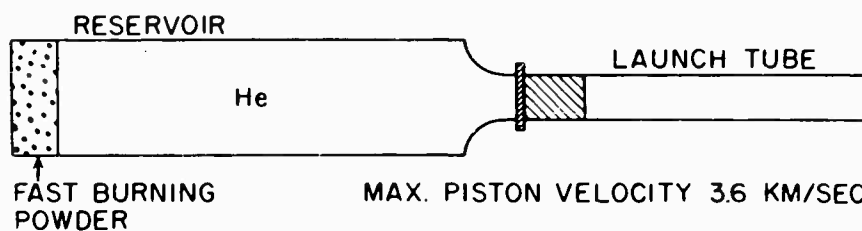
MAX. PISTON VELOCITY 2.3 KM/SEC

(a) POWDER GAS DRIVER



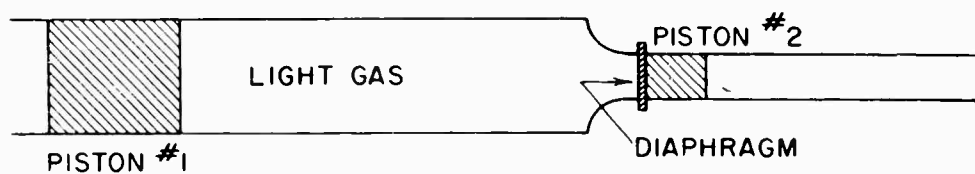
MAX. PISTON VELOCITY 3.6 KM/SEC

(b) STEAM HEATED HELIUM DRIVER



MAX. PISTON VELOCITY 3.6 KM/SEC

(c) POWDER HEATED HELIUM DRIVER

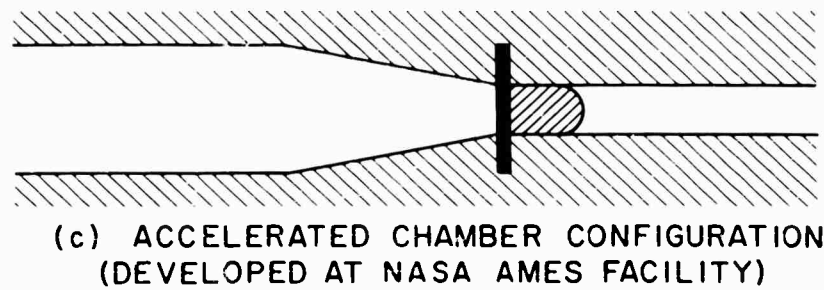
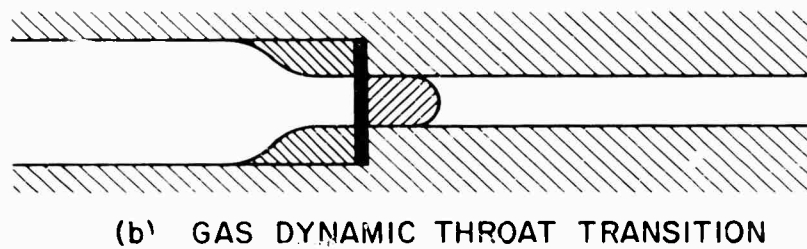
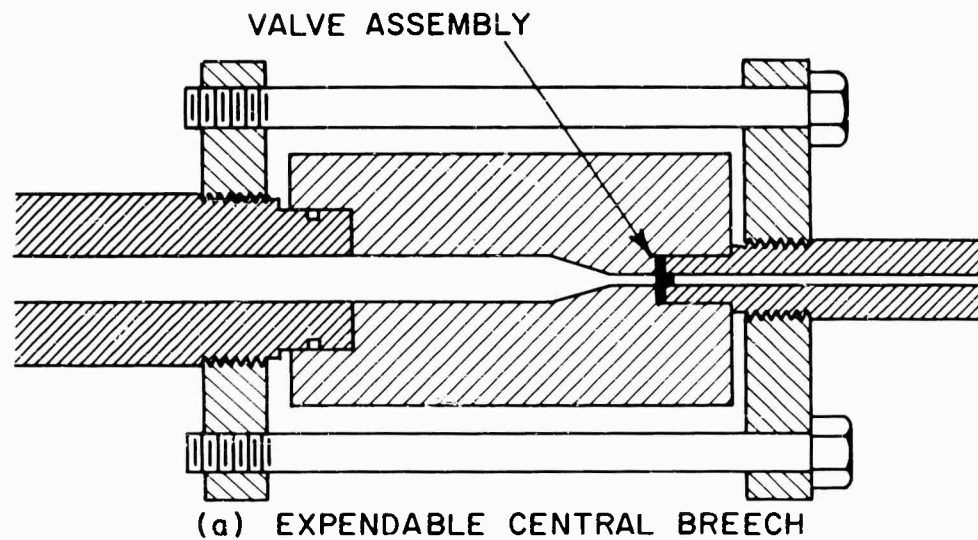


(d) GAS GUN DRIVER

## PRESENT GAS GUN PISTON DRIVERS

Figure 3

BALLISTIC ACCELERATORS



PRESENT GAS GUN TRANSITION SECTIONS

Figure 4

## BALLISTIC ACCELERATORS

deformed with each shot because of high driver-gas pressure and piston impact, so it must be discarded.

Figure 4B shows a similar section with an aerodynamic throat transition that provides a minimum resistance to gas passage. It is more efficient than the simple conical section of the expendable central-breech configuration, but it is limited in peak gas pressure (and hence temperature) by the requirement that no large deformation occurs, since the unit is not expendable. Successful gun operation using minimum-resistance throats at pressures up to 350 k psi has been carried out, however; guns using this type of transition are among those with the best performance of those presently in operation.

Figure 4C shows the accelerated-breech-transition concept that was first utilized at the Ames Research Center during the fall of 1960. This transition is used with a piston of low mechanical strength that completes the compression stroke by extruding itself into the very low-angle conical transition. In this way all of the chamber volume is displaced at high speed, and peak pressure is maintained on the base of the projectile for a relatively long time. When peak gas pressures are limited to 350 k psi, and if the piston is made from a very soft material (polyethylene), nonexpendable transition section designs become feasible. Guns utilizing this design have successfully launched 0.22-inch-diameter, 0.1-gram plastic pellets at 10 km/sec and 1/8-inch-diameter sabot glass balls at 7.6 km/sec.

### Present Gas Guns

Table 2 is a representative list of the high performance gas guns presently in operation. They have been classified according to their piston drivers and transition sections, as described above. Each gun has a spectrum of maximum velocities for the various projectile weights it fires. In almost all cases the maximum velocity achieved, regardless of projectile mass, was reported. This list generally represents the maximum present capability of light gas-gun accelerators, although some particular mass-velocity records may not be represented. All of the guns listed are in a developed state and are available as research tools.

## EXPLOSIVE ACCELERATORS

Present explosive-accelerator techniques are capable of firing pellets at velocities higher than any other projector techniques. Other characteristics that are responsible for their widespread use are their relatively low cost, and the small amount of assembly effort required for many firing configurations.

Since peak accelerations imparted to pellets by explosive accelerators generally are several orders of magnitude higher than those encountered during gas-gun launches, the selection of pellet shapes that can be fired at hypervelocities is severely limited, and in-flight pellet mass must be determined after firing, since considerable pellet mass is generally lost during launch. The blast effects generated by detonating explosive charges require the use of special firing facilities, and often semi-expendable range facilities must be used if controlled atmospheric firings are to be made.

## BALLISTIC ACCELERATORS

### Explosive Accelerator Operation

Before discussing the operation of particular accelerator configurations in detail, let us consider some basic characteristics of explosive detonations. Detonation is set apart from rapid burning or deflagration by the fact that the chemical reaction propagates through the fuel material along a shock front instead of a thermal one. If a long rod of explosive is detonated at one end, the reaction or detonation front will propagate down the rod at a velocity that is controlled by the dilatational wave velocity in the explosive rod and the pressure differential across the reaction front, just as in the case of a shock tube. As the front progresses, the pressure differential will increase (and hence the detonation front's velocity) until a maximum pressure is developed. The front will then continue its advance through the unconsumed explosive at a constant velocity known as the "detonation velocity." The detonation velocity and the peak pressure at the detonation front are determined by the chemical composition of the explosive. Present explosives have detonation velocities ranging from 5 to 8 km/sec and peak pressures as high as two million atmospheres.

The simplest technique for accelerating pellets to hypervelocities using explosives is shown in Figure 5A. The flat end charge consists of a cylinder of explosive with a detonator assembly mounted at one end and a pellet at the other. The detonator assembly is designed to initiate a detonation front in the explosive which accelerates to the explosive's detonation velocity before reaching the front surface. At the front surface, the detonation pressure reacts on the pellet, causing it to accelerate (peak accelerations above  $10^9$  g have been developed). The final pellet velocity is dependent upon the explosive detonation velocity and the ratio of explosive mass per unit area behind the pellet to the mass per unit area of the pellet (the C/M ratio). Pellet velocity raises approximately linearly with the C/M ratio at low velocities and asymptotes to a peak value as the C/M ratio becomes large. Depending upon the explosive properties, peak projectile velocities achievable with this technique range up to 4.5 km/sec. Thus far only a few pellet shapes have been accelerated intact to these velocities, because the high pressures experienced during maximum velocity launch deform or shatter most configurations. Considerable effort has been expended in developing techniques for mounting pellets on the face of charges to prevent them from shattering during launch. At present, pellets that can withstand high-velocity launches are limited to thin disks, often spaced away from the charge by a thin layer of buffering material, and specially shaped fragments that are thicker in the center than at the edges. Since the C/M ratio of these pellets is greater near their edges than at their center, a velocity differential is generated across the pellet surface during launch that results in it being fuzed into a nearly spherical form. At lower velocities a variety of geometric shapes have been successfully accelerated by flat end charges. The pellets have been either partially imbedded into the end of the charge, placed directly on its surface, or spaced away from its surface by a buffer layer.

Higher peak pellet velocities have been achieved by a fundamental modification of a flat-end-charge configuration called the cavity charge (Fig. 5B). The detonation wave propagates through the explosive as in the previous case, until it reaches the base of the cavity. Here, a strong shock wave is produced that propagates forward through the cavity. The detonation front continues forward through the walls of the now tubular charge at a velocity considerably higher than that of the shock wave and continuously generates another shock wave from the

## BALLISTIC ACCELERATORS

inner side wall of the cavity that interacts with the original shock wave and progressively compresses it. As compression continues, the peak pressure of the original shock wave increases, thus increasing the impulse it can transfer to a pellet during acceleration. Thus a conical volume is swept out by the shock wave generated at the rear surface as it progresses up the cavity (referred to as the Mach stem).

In a practical cavity charge, the depth-to-diameter ratio of the cavity behind the pellet is adjusted to form a sufficient reduction in the original shock-wave area to increase the maximum pellet velocity considerably without generating pressures high enough to shatter it. Since the area of the pellet beyond the stem (near its outer edge) receives relatively little acceleration during launch, there is a tendency for this type of charge to punch out the center of the pellet when a high velocity launch is attempted. This effect has been experimentally observed. Within the past 18 months, several techniques have been developed to place the entire pellet within the Mach stem and thereby eliminate the central-punchout tendency.

Other hypervelocity explosive accelerators have been developed that differ from the two described above in that the accelerated pellet is generated during launch. These are the liner charges. Since the pellets accelerated by these charges are not at hand before firing, the charge designer has only indirect control over their in-flight mass and shape. For many ballistic applications this disadvantage is more than compensated by the fact that these charge configurations are capable of accelerating pellets to maximum velocities above 20 km/sec.

When the conical liner charge (Fig. 5C) is initiated, a detonation wave propagates forward through the explosive. As it progresses, it collapses the liner material onto the charge axis. A visualization of the progressive collapse of the liner will show that the point of total liner collapse (the point where the material from the inside surface of the liner has just reached the charge axis) will initially move forward at the velocity of the detonation wave in the explosive, but will rapidly decelerate as liner collapse continues because of the progressively longer distances individual liner segment must travel before reaching the charge axis.

If the forward velocity of the liner collapse point is less than the dilatational wave velocity in the liner material, the hydrodynamic theory of metal forming predicts that the liner material divides along a surface contained within the original liner shell. The metal within this surface forms a jet that moves forward at twice the liner collapse point velocity, while the remainder of the liner material forms a rod (slug) which follows the jet at low velocity. The jet continues to be formed until the charge and liner are consumed at which point it severs itself from the slug and travels down its trajectory.

Since the liner collapse point velocity and hence the instantaneous jet velocity steadily reduces during the jet launch, a velocity gradient is generated along the jet. This gradient will cause the jet to first stretch and then progressively break up until the velocity gradient across the individual fragments is reduced to the point where the internal strength of the material can hold them together. The resulting train of pellets is highly advantageous from a weaponry standpoint but makes this type of charge difficult to use for exterior and terminal ballistic studies.

# BALLISTIC ACCELERATORS

Table 2; Present High Performance Light-Gas Guns

Type Gun	Piston Driver	Transition Section	Dimensions		Projectile		Installation	Remarks
			Comp Tube	Launch Tube	Mass (grams)	Max Velocity (km/sec)		
Adiabatic Compression	Powder	Accelerated chamber design	40 mm dia 168 cal (22 ft)	.22 cal 218 cal (4 ft)	0.1	10	NASA (Ames Aero. Lab)	Subsonic piston. (High Proj. Acceleration).
Const. Vol. Electric	25 cc arc heated chamber	Aerodynamic throat		.22 cal 136 cal 2.5 ft	0.1	5.8	AVCO Res. Lab.	
Piston Gas	Powder	Expendable tapered throat	40 mm 80 cal (10.5 ft)	.22 cal 109 cal (2 ft)	0.2	8.24	USNRL	Either supersonic or subsonic piston. (Very high proj. acceleration.
Piston Shock	Steam heated He 2-3/4" dia.	Aerodynamic throat	40 mm dia 77 cal (10.5 ft)	.50 cal 200 cal (8.33 ft)	1	8.85	AEBC (Tullahoma)	Supersonic piston. High proj. acceleration.
Piston Gas	Powder	Expendable tapered throat	40 mm 77 cal (10.5 ft)	.60 cal 100 cal (5 ft)	4	6.1	USNRL	Either supersonic or subsonic piston. Very high acceleration
Piston Shock	Powder heated He-4.25" dia.	Aerodynamic throat	2.25" dia. 64 cal (12 ft)	20 mm 250 cal (16 ft)	4.2	7.8	NASA (Ames Aero. Lab)	Supersonic piston (high proj. accel.)
Shock Compression	Powder heated He 10" dia.	Aerodynamic throat	5 in. 72 cal (30 ft)	2 in. 197 cal (33 ft)	60	6.7	USNOL	Supersonic piston. Med. proj. accel.
Double Stage Steam	4" dia 75 cal (30")	Aerodynamic throat	2 in. 78 cal (13 ft)	20 mm 200 cal (13 ft)	3.5	4.6	USNOL	This gun is no longer in use. Low Proj. acceleration.
Single stage Steam		Aerodynamic throat	10 in. dia. 8.4 cal (7 ft)	4 in. 180 cal (60 ft)	500 900	4.0 3.35	USNOL	Low Proj. acceleration

## BALLISTIC ACCELERATORS

A technique presently in use at the Aerojet General Corporation, Downey, California, largely eliminates this difficulty by detonating the conical liner charge off center. The resulting nonsymmetrical detonation front causes a skewed collapse of the liner resulting in the various jet segments traveling in slightly different directions. In this way, the craters from the various jet fragments can be separated on a target for individual study.

A different phenomenon occurs when the liner collapse point velocity exceeds the dilatational wave velocity in the liner material. It is experimentally observed that no jet is formed, but that a cloud of hypervelocity particles varying in size up to several metallic grain volumes is fired along the charge axis. The mechanism responsible for the production of this particle cloud is not yet fully understood, but charges of this form are being used extensively for studies of micrometeoroid impacts. (See BRL paper presented in this session.)

A more complete discussion of liner explosive charges is presented in a classified addendum to this paper.

Another group of accelerators are essentially explosively powered gas guns. One configuration developed at BRL consists of a thin-walled chamber containing hydrogen gas that is surrounded by an explosive charge. The chamber is connected to a launch tube with a projectile mounted at its base. Upon detonation of the explosive, the chamber walls are collapsed, thereby compressing the hydrogen gas and shock heating it. The high temperature and pressure driver-gas then expands down the launch tube accelerating the projectile. Such guns have accelerated gram mass low density projectiles to peak velocities of 6.0 km/sec, but appear to be limited in maximum performance by high acceleration levels, and limited launch tube lengths. If the launch tube is made too long, a strong compression wave that is generated in the barrel during the explosive detonation will overtake the projectile and shatter it.

A similar gun has been developed at the General Electric Company (MSVD). In this gun, the explosive charge is used to supply both the motivating power and the driver-gas. A thick-walled lead cap is partially filled with explosive, and sealed at the open end with a launch tube and projectile. Upon detonation, the explosive charge shock heats and compresses the air in the remainder of the cavity which initiates projectile motion. The advancing explosive gas front continues compression during the remainder of the projectile acceleration. Such guns have achieved similar projectile velocities to the hydrogen-explosive guns, and have similar limitations.

Both of these configurations are totally expendable due to the blast effects of their explosive charges, but they are inherently very inexpensive. Therefore, they have found wide use for gathering ballistic data.

### Present High-Performance Explosive Accelerators

Table 3 shows a representative list of the explosive accelerators that together represent the maximum performance that has been achieved to date with explosive techniques. All the macroparticle explosive accelerators described in this presentation can be enlarged to accelerate higher mass pellets with a minimum of engineering difficulty. Therefore, the maximum masses of macropellets

# BALLISTIC ACCELERATORS

Table 3: Current Explosive Accelerators

Charge Type	PELLET PARAMETERS				Installation
	Shape	Mass (grams)	Material	Max. Velocity (km/sec)	
Flat end	Disc and simple Forms	0.1 - 10	Ductile metal	3.5	Several
Flat end	Self-forging pellet	0.5 - 5	Ductile metal	4.0	Carnegie Inst. of Tech.
Cavity	Disc	0.2 - 10	Ductile metal	7.5	BRL, Picatinny
Conical Liner	Particle jet	-	Metal	15	BRL, Carnegie Inst. of Tech.
Cylindrical Liner	Thin rod	0.2 - 1	Beryllium Iron Nickel Aluminum	21 10	BRL
Cylindrical Liner	Micro particle	-12 -5 10 -10	Iron	12	BRL
Explosive Gas Gun	Cylinders	0.1 - 5	Low density metal	6	BRL General Electric MSVD

## BALLISTIC ACCELERATORS

presented in Table 3 represent the peak values that have been accelerated to date, but they do not represent maximum capability.

### SPECIAL ACCELERATOR TECHNIQUES

The majority of ballistic research is being carried out at this time with the various gas-gun and explosive ballistic accelerators described above. However, there are a number of other accelerator techniques that have been developed which are especially useful for a series of specialized ballistic applications.

#### Electrostatic Accelerator

A technique shown schematically in Figure 6 has been developed at STL where individual or small numbers of very lightweight particles are charged to a high positive potential and injected into an electrostatic field (with potential differences up to  $2 \times 10^6$  volts). They are accelerated by the field and allowed to impact into a target. For reasons to be discussed in the STL paper presented in this session, the technique is limited to very light particles, but velocities above 20 km/sec are possible. Since single particles whose composition, mass, and velocity are measured can be identified, this technique is highly useful for precise studies of micrometeoroid impact effects.

#### Drag Accelerator

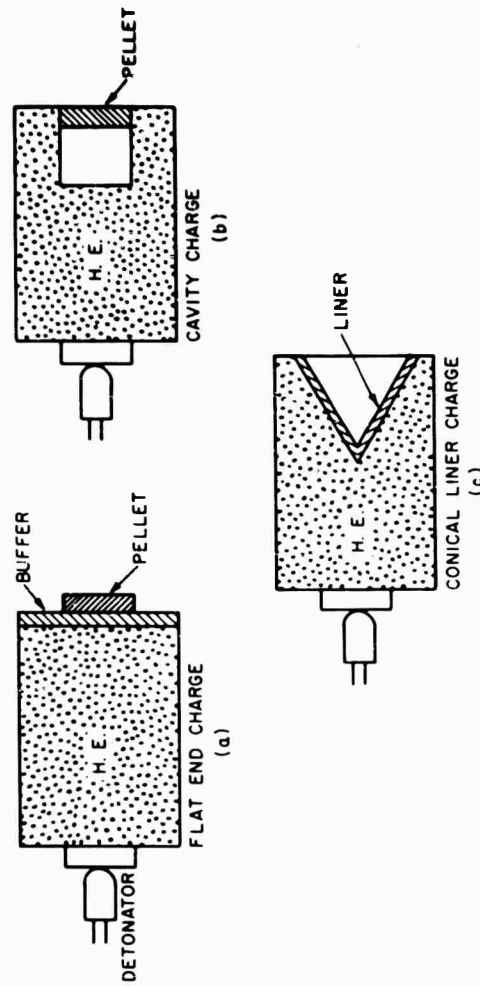
Another electrically powered ballistic accelerator useful for micrometeoroid studies has been designed by North American Aviation, Inc. (Fig. 6). In this case, a thick wire of low-molecular-weight metal (lithium) is vaporized by the discharge of a capacitor bank through it. The rapidly generated vapor is electrically pulse-heated to temperatures above  $12,000^\circ\text{K}$  and allowed to expand into an aerodynamic throat, where it encounters several suspended particles. If the density of the particle material is near that of the expanding gas, the particles can be accelerated to near the gas-flow velocity in very short distances. Using this technique, NAA personnel have accelerated single 0.1-mm diameter glass spheres to peak velocities of 9.5 km/sec.

#### Constant-Chamber-Volume Electric Gun

The constant-chamber-volume electric gun system (Fig. 7) consists of a chamber filled with low-molecular-weight gas that is pulse heated to peak temperatures above  $12,000^\circ\text{K}$  by a capacitor-bank-powered arc discharge. The high-temperature and high-pressure gas then accelerates a projectile down a launch tube, as in the case of a gas gun. Although the potential velocity capability of such guns is very high, peak velocities with 0.1-gram and 0.2-gram 0.22-inch-diameter pellets have been limited to 5.8 km/sec. The practical problems associated with this type of gun will be discussed in the NRL paper presented in this session.

#### Secondary Particle Accelerator

It has been noticed that a spray of fine particles is ejected parallel to a target when it is struck by a projectile (Fig. 7). Partial theories of their formation have indicated that peak velocities of the smallest of these could achieve two times



PRESENT HYPERVELOCITY EXPLOSIVE ACCELERATORS

Figure 5



PARTICLE SIZE:  $0.1-10\mu$   
 MATERIAL: ANY  
 MAX. VELOCITY: 20 KM/SEC

ELECTROSTATIC ACCELERATOR  
 SPACE TECHNOLOGY LABORATORIES

(a)

PARTICLE SIZE:  $10-100\mu$   
 MATERIAL: CERAMIC  
 MAX. VELOCITY: 10 KM/SEC

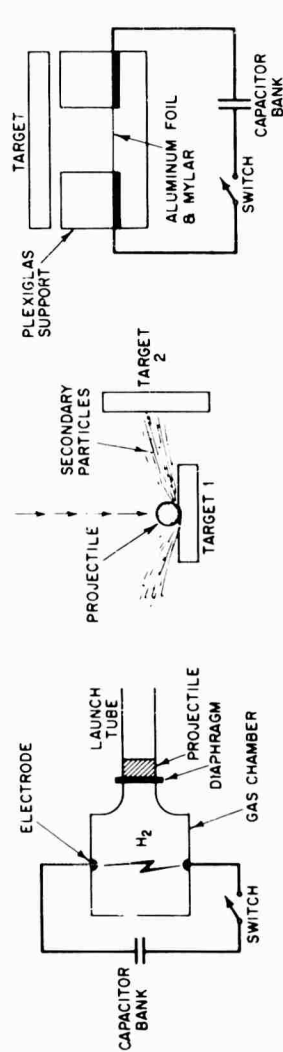
DRAG ACCELERATOR  
 NORTH AMERICAN AVIATION

(b)

# SPECIAL TYPES OF MICROPARTICLE ACCELERATORS

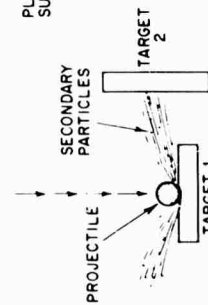
Figure 6

# BALLISTIC ACCELERATORS



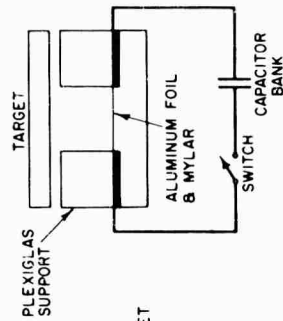
CONSTANT CHAMBER VOLUME ELECTRIC GUN  
AVCO RESEARCH LAB  
USNRL

(a)



PARTICLE SIZE: 0.1-100 $\mu$   
MATERIAL: ANY  
MAX. VELOCITY: 20 KM/SEC  
SECONDARY PARTICLES ACCELERATOR  
UNIVERSITY OF UTAH  
UTAH RESEARCH & DEVELOPMENT CO.

(b)



PROJECTILE SIZE: 0.007" x 2" x 1"  
MATERIAL: PLASTIC FILM  
MAX. VELOCITY: 5.18 KM/SEC  
PLASMA POWERED ACCELERATOR  
PULSE POWER LAB, AF SWC  
USNRL  
BOEING AIRCRAFT CORP.

(c)

## SPECIAL ACCELERATORS

Figure 7

## BALLISTIC ACCELERATORS

the primary projectile velocity. Thus, if a 20-km/sec jet pellet is used for the primary projectile, 40-km/sec secondary particles might result. Thus far, work has progressed on this technique only to the point at which the existence of such particles has been verified. The experimental difficulties associated with using them will be great, however, because their number per primary impact is large, and their velocity distribution is great. Should 40-km/sec velocities be realized, however, they will be of great utility for micrometeoroidal studies.

### Plasma Plate Accelerator

A technique (Fig. 7) has been developed at the Pulse Power Laboratory (AFSWC) for electrically accelerating thin plastic sheets to peak velocities of 5.5 km/sec using the heated vapor of a piece of electrically exploded aluminum foil. The acceleration is sufficiently even to prevent significant tipping of the plastic sheet over short distances of its travel. Also, total energy transfer efficiencies between the electrical energy stored in a capacitor bank and the kinetic energy of the plastic can approach 50 percent. Thus the possibility exists of using such techniques for accelerating large distributed mass fragments.

## CONCLUSIONS

In the course of this presentation, each of the major types of acceleration has been discussed. In general, present gas guns can fire large instrumented models to 4.6 km/sec, homogeneous models with a variety of shapes to 7.5 km/sec, and small plastic cylinders to 10 km/sec. Gas guns are most useful when accurate control of model flight parameters such as dimensions, weight, velocity, etc., is required and relatively slow firing rates can be tolerated.

Explosive accelerators are of limited usefulness where precise model parameter control and measurement are needed, but they are comparatively inexpensive to purchase and require relatively low-cost firing facilities. They can be used to acquire large amounts of data at a rapid rate, thereby making statistical treatment of ballistic data feasible. Since explosive-accelerator sizes can be scaled, projectile mass and size can be conveniently varied over a wide range. At present, explosives provide the only techniques for acceleration of macroprojectiles above 10 km/sec.

Several other ballistic accelerator techniques have been developed for specialized research tasks. They have been particularly successful in launching simulated micrometeoroids for individual impact studies.

## ACKNOWLEDGMENTS

The very wide range of information presented in this paper would have been almost impossible to gather without the close cooperation of personnel from the following organizations.

Ballistics Research Laboratory,  
Aberdeen, Maryland

## BALLISTIC ACCELERATORS

U. S. Naval Ordnance Laboratory,  
White Oak, Maryland

National Aeronautics and Space Administration  
Ames Research Center,  
Moffett Field, California

Air Force Special Weapons Center  
Pulse Power Laboratory,  
Kirtland Air Force Base, New Mexico

North American Aviation, Inc.  
Aero-Space Laboratories,  
Downey, California

General Motors Corporation  
Defense Systems Laboratories,  
Santa Barbara, California

Utah Research and Development Company,  
Salt Lake City, Utah

It should be emphasized that information from many other organizations was used in compiling this paper, and that the cooperation of their personnel has been most appreciated.

## SUMMARY OF NRL HYPERVELOCITY ACCELERATOR DEVELOPMENT

C. D. Porter, H. F. Swift, and R. H. Fuller

Naval Research Laboratory  
Washington, D. C.

### INTRODUCTION

The U. S. Naval Research Laboratory is engaged in a continuing effort to develop high-performance gas-powered accelerators for ballistic research studies. Present NRL light-gas guns are capable of accelerating sabotaged projectiles with an in-gun weight of 4 to 5 grams to 6 km/sec (shear-type projectiles having a mass of 0.2 gram have been accelerated to 8.5 km/sec). Continued research is necessary in order to produce velocities in excess of 6 km/sec with sufficiently low pressure and acceleration to avoid breakup of fragile sabotaged packages. Hypervelocity sabotaging has required a complementary program in the development of small quick-opening valves.

Larger guns with improved designs are currently under development for substantially increasing the mass and velocity capabilities over that of previous guns. One of the most serious limitations on gun performance has been low driver-gas temperature. Substantial progress has been made toward developing techniques for raising this temperature by adding electrical energy to the driver-gas. To speed this progress, a program utilizing the NRL-Narec high-speed digital computer has been formulated, and computations have been carried out to predict results for a wide variety of gun parameters with about 95-percent accuracy.

### COMPUTER STUDY

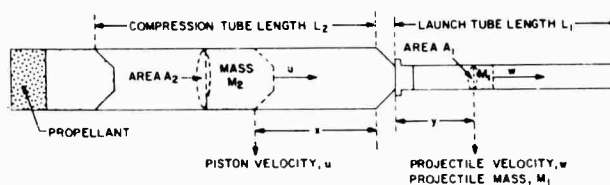
Figure 1 is a drawing of the NRL light-gas gun, with symbols and definitions used in the theoretical analysis of the gun. The theoretical treatment of gun operation is conducted by numerical solution of the basic equations of motion of the piston and projectile under assumed equilibrium conditions of the driver-gas (Fig. 2). Real gas is simulated with the use of Van Der Waals' equations of state and of adiabatic volume change. Terms are included to account for the blackbody radiation from the driver-gas to the bore enclosure, the reduced pressure at the projectile base caused by Mach-number effects of the fast-moving projectile, and the reduced acceleration caused by bore friction. This form contains  $M_1$ ,  $M_2$ ,  $A_1$ , and  $A_2$ , all of which apply only to one specific size of gun. If in the basic equation substitution is made of the generalized parameters shown in Figure 3, a general dimensionless form will be obtained. The results will depend only on the parameters used and will be valid for any size gun.

# ACCELERATOR DEVELOPMENT

Figure 1  
Specific Gun Parameters and Conditions

## Symbols

$M_1$	Projectile mass
$D_1$	Diameter of launch tube
$A_1$	Launch tube area (cross section)
$L_1$	Launch tube length
$w$	Velocity of projectile
$y$	Projectile distance from start
$M_2$	Piston mass
$D_2$	Diameter of Compression Tube
$A_2$	Compression tube area (cross section)
$L_2$	Compression tube length (effective piston travel)
$U_f$	Velocity of piston fired in vacuum (from open ended compression tube, free flight)
$P$	Driver gas pressure (function of $\tau$ )



$g$	(acceleration of gravity)
$T$	Driver Gas Temperature (function of $\tau$ )
$T_b$	Driver gas Temperature Characteristics at Projectile Base Established at maximum temperature (subject to radiation losses)
$u$	Piston velocity
$x$	Effective piston distance from boundary of travel
$t$	Time from projectile start

## Driver Gas Constants

$R$	Universal Gas constant/molecular wt.
$\gamma$	$C_p/C_v$ ; ratio of specific heats
$C_v$	Specific heat at constant volume
$a_1$	Van der Waals constant of interaction (dimensionless form)
$b_1$	Van der Waals constant of molecular volume (dimensionless form)

## Initial Conditions

$i$	Initial temperature of compression and launch tube
$T_o$	Initial average temperature of driver gas at start of compression
$d$	Initial loading pressure of driver gas

# ACCELERATOR DEVELOPMENT

Figure 2  
Basic Equations to be Solved

(Iterative Form  $\begin{cases} k \text{ refers to k'th step} \\ j \text{ refers to preceding step} \end{cases}$ )

$$\frac{M_2}{\pi} \left( \frac{u_j - u_k}{\Delta t} \right) + F_2 = A_2 \left[ \frac{(P_k + P_j) - (P_{gh} + P_{gl})}{2} \right]$$

(1)  $\begin{cases} \text{Equation relating piston Newtonian} \\ \text{dynamic forces to pressure on the faces} \\ P_g = \text{Propellant gas pressure} \end{cases}$

$F_1, F_2 =$  Respective average friction force  
in launch and compression tubes  
 $\Delta t = \Delta t_k = \Delta t_j$

$$\frac{M_1}{\pi} \left( \frac{w_k - w_j}{\Delta t} \right) + F_1 = A_1 \left( \frac{P_k - P_j}{2} \right) \left[ 1 - \frac{\gamma-1}{2} \left( \frac{w_k + w_j}{2} \right)^2 \frac{1}{\gamma R T_b} \right]^{(\gamma/\gamma-1)}$$

(2)  $\begin{cases} \text{Equation relating projectile Newtonian} \\ \text{dynamic forces to driver gas pressure} \\ \text{with a Mach Number, } M, \text{ correction} \end{cases}$

$$T'_k = T_j \left[ \frac{(A_2 x_j + A_1 y_j) - b_1 V_o}{(A_2 x_k + A_1 y_k) - b_1 V_o} \right]^{\gamma-1}$$

(3)  $\begin{cases} \text{Equation relating temperature to} \\ \text{adiabatic volume change} \end{cases}$

$$\Delta T_k = \frac{\sigma \left( \frac{S_k + S_j}{2} \right)}{M_D C_v} \left[ \left( \frac{T'_k + T'_j}{2} \right)^4 + j^4 \right] \Delta t$$

(4)  $\begin{cases} \text{Equation relating temperature loss in} \\ \text{driver gas to black-body heat loss to walls} \\ M_D = \text{Mass of driver gas} \\ S = \text{Surface enclosing the driver gas} \\ \sigma = \text{Body radiation per unit of surface} \end{cases}$

$$T_k = T'_k - \Delta T_k$$

(5)  $\begin{cases} \text{Driver gas temperature correction} \end{cases}$

$$P_k = \frac{R T_k M_D}{(A_2 x_k + A_1 y_k) - b_1 V_o} - a_1 \left( \frac{V_o}{A_2 x_k + A_1 y_k} \right)^2 P_a$$

(6)  $\begin{cases} \text{Van der Waals Equation of State for} \\ \text{Driver Gas (dimensionless coefficient form)} \\ T_v = \text{Std. Van der Waal temperature -} \\ \text{0}^\circ \text{centigrade} \\ P_a = \text{Std. Atmospheric pressure} \\ V_o = A_2 L_2 \frac{i P_a}{T_v d} \end{cases}$

$$P_{gh} \cong P_a \left( \frac{L_2}{L_2 - x_k} \right)^{1.23}$$

(7)  $\begin{cases} \text{Equation relating propellant gas pressure,} \\ P_{gh}, \text{ to free-firing muzzle pressure, } P_a \end{cases}$

Figure 4 is a typical generalized output of one of these runs, showing respectively the line number, the dimensionless piston position (X), the piston velocity (u), the light-gas pressure (P), the scaled time (tau), the light-gas temperature (T), the dimensionless projectile position (Y), and the projectile velocity (W). These outputs are all in decimal floating-point format. Figure 5 shows the independent variable, tau, and the time-dependent curves of the other program outputs for helium driver-gas under the list of conditions shown in the figure. On the left side is shown the projectile velocity W, which reaches almost 17,000 ft/sec, or 5.1 km/sec, the driver-gas pressure, and the driver-gas temperature. At the right of the figure the piston velocity (u), the dimensionless piston position (X), and the dimensionless projectile position (Y) are shown. This may be compared with Figure 6, which shows the same set of conditions of piston energy and piston weight for hydrogen at an initial temperature of 300° K. It is noted that the hydrogen reaches a considerably higher maximum driver-gas pressure, but for a shorter time. The projectile velocity is about 10 percent higher. Figure 7 is presented to show how an elevated initial temperature (1200° K) with helium gas raises the maximum projectile velocity to 24,200 ft/sec (7.4 km/sec), compared with 5.1 km/sec attained at 300° K. This value

## ACCELERATOR DEVELOPMENT

**Figure 3**  
**GENERALIZED GUN PARAMETERS (Definitions)**

E	$M_2 U_2^2 / 2g(D_2)^3$	Piston energy per cube of compression tube diameter
b	$M_2 / (D_2)^3$	Piston mass per cube of compression tube diameter
c		Shot start pressure
e	$L_2 / A_2^{1/2}$	Dimensionless compression tube length
f	$A_2 / A_1$	Chamberage Area ratio
h	$L_1 / A_1^{1/2}$	Dimensionless launch tube length
j	$M_1 / (D_1)^3$	Projectile mass per cube of launch tube diameter
f <sub>1</sub>	$F_1 / A_1$	Average launch tube friction per cross sectional area
f <sub>2</sub>	$F_2 / A_2$	Average compression tube friction per cross sectional area

### GENERALIZED OUTPUTS

X	$x / L_2$	Dimensionless piston position
Y	$y / L_2$	Dimensionless projectile position
$\tau$	$t / L_2$	Scaled time

is only slightly below the velocity of 7.5 km/sec attained with hydrogen initially at 1200°K. At higher initial driver-gas temperatures, helium outperformed hydrogen, at a much lower maximum pressure. For this reason much of the latter theoretical work was carried on with helium as the driver gas.

### ISOMETRIC PARAMETER STUDY

Over 400 Narec runs were made, and the envelopes of maximum velocity are presented in isometric form. Values for Figure 8 were computed with an E value of 7,202 joules per cubic centimeter (1E<sub>0</sub>), a piston weight parameter b of 7.5 grams per cubic centimeter, a shot-start pressure of 9,500 atmospheres, and a loading pressure of 18.9 atmospheres. The surface is generated by a series of characteristic velocity-temperature curves, each representing a successively lighter projectile where the j value decreases from j<sub>0</sub> to one-eighth of j<sub>0</sub>. All the generating curves plunge steeply to zero at absolute 0° because of an infinite Mach number at this temperature. It is very difficult to read values where the top of the surface is obscured as the curves start their steep descent.

### TEMPERATURE-MASS STUDY

In Figure 9 the axial direction of the temperature variation was reversed to give a more readable picture of the surface in a left-hand-axis presentation. All lines under the velocity surface are dotted. The upper tip of the surface, as outlined by thin-line projections of the grid lines on the velocity surface, shows velocities above 12.19 km/sec (heavy contour line) between the temperatures of 2,778° and 2,222°K and between the j values of a quarter and one-eighth of j<sub>0</sub>.

## ACCELERATOR DEVELOPMENT

Figure 4  
NAREC OUTPUT

LINE NUMBER	$x/L_2$		$u_1$ (ps)		$P$ (psf)		$t/L_2$		$T$ (°g)		$y/L_2$		$w$ (ps)	
0000	+92034	+00	+88344	+03	+95728	+03	+91851	-04	+37120	+03	+0	-01	+0	-01
0001	+45866	+00	+28907	+04	+31801	+06	+30281	-03	+92081	+03	+0	-01	+0	-01
0002	+23472	+00	+31164	+04	+10565	+07	+37662	-03	+14844	+04	+0	-01	+0	-01
0003	+15311	+00	+36188	+04	+23795	+07	+40282	-03	+20501	+04	+0	-01	+0	-01
0004	+10181	+00	+29848	+04	+55053	+07	+41873	-03	+28813	+04	+0	-01	+0	-01
0005	+77981	-01	+28757	+04	+10084	+08	+42788	-03	+38396	+04	+75185	-05	+21884	+03
0006	+77884	-01	+26738	+04	+10176	+08	+42798	-03	+39328	+04	+75186	-05	+21884	+03
0007	+70829	-01	+28286	+04	+12377	+08	+43048	-03	+39738	+04	+45845	-02	+36708	+04
0008	+43698	-01	+27736	+04	+15235	+08	+43293	-03	+42882	+04	+17874	-01	+70806	+04
0009	+58921	-01	+27630	+04	+16004	+08	+43540	-03	+43823	+04	+38806	-01	+96575	+04
0010	+50328	-01	+26233	+04	+20754	+08	+43788	-03	+48485	+04	+83135	-01	+11530	+05
0011	+43954	-01	+23283	+04	+23345	+08	+44033	-03	+50803	+04	+85414	-01	+12886	+03
0012	+37827	-01	+24240	+04	+25610	+08	+44282	-03	+32709	+04	+12859	+00	+13893	+03
0013	+31872	-01	+23091	+04	+27373	+08	+44530	-03	+54122	+04	+16393	+03	+14654	+05
0014	+26411	-01	+21872	+04	+28486	+08	+44777	-03	+54887	+04	+20091	+00	+15228	+03
0015	+21157	-01	+20817	+04	+28881	+08	+45024	-03	+55286	+04	+23913	+00	+15633	+03
0016	+16214	-01	+18358	+04	+28364	+06	+45272	-03	+35044	+04	+27924	+00	+15958	+03
0017	+11580	-01	+18127	+04	+27632	+08	+43319	-03	+34323	+04	+31799	+00	+16778	+03
0018	+72436	-02	+16848	+04	+26227	+08	+43786	-03	+33207	+04	+33820	+00	+16333	+03
0019	+31903	-02	+15843	+04	+24509	+08	+46013	-03	+31794	+04	+38874	+00	+16446	+05
0020	-13864	-03	+14944	+04	+25667	+08	+48221	-03	+30387	+04	+43441	+00	+16518	+03
0021	+0	+1	+0	-01	+22504	+08	+48229	-03	+30067	+04	+43579	+00	+16520	+05
0022	+0	+1	+0	-01	+17942	+08	+46434	-03	+45757	+04	+47299	+00	+16563	+03
0023	+0	+0	+0	-01	+14305	+08	+46711	-03	+41818	+04	+51562	+00	+16380	+05
0024	+0	-01	+0	-01	+11406	+08	+47006	-03	+38219	+04	+56448	+00	+16374	+05
0025	+0	-01	+0	-01	+90940	+07	+47344	-03	+34928	+04	+62048	+00	+16546	+05
0026	+0	-01	+0	-01	+72310	+07	+47732	-03	+31922	+04	+68467	+00	+16496	+03
0027	+0	-01	+0	-01	+37817	+07	+48179	-03	+29174	+04	+75823	+00	+16424	+05
0028	+0	-01	+0	-01	+46102	+07	+48694	-03	+26863	+04	+84254	+00	+16329	+03
0029	-21916	+07	+0	-01	+0	-01	+0	-01	+0	-01	+0	-01	+0	+26

# ACCELERATOR DEVELOPMENT

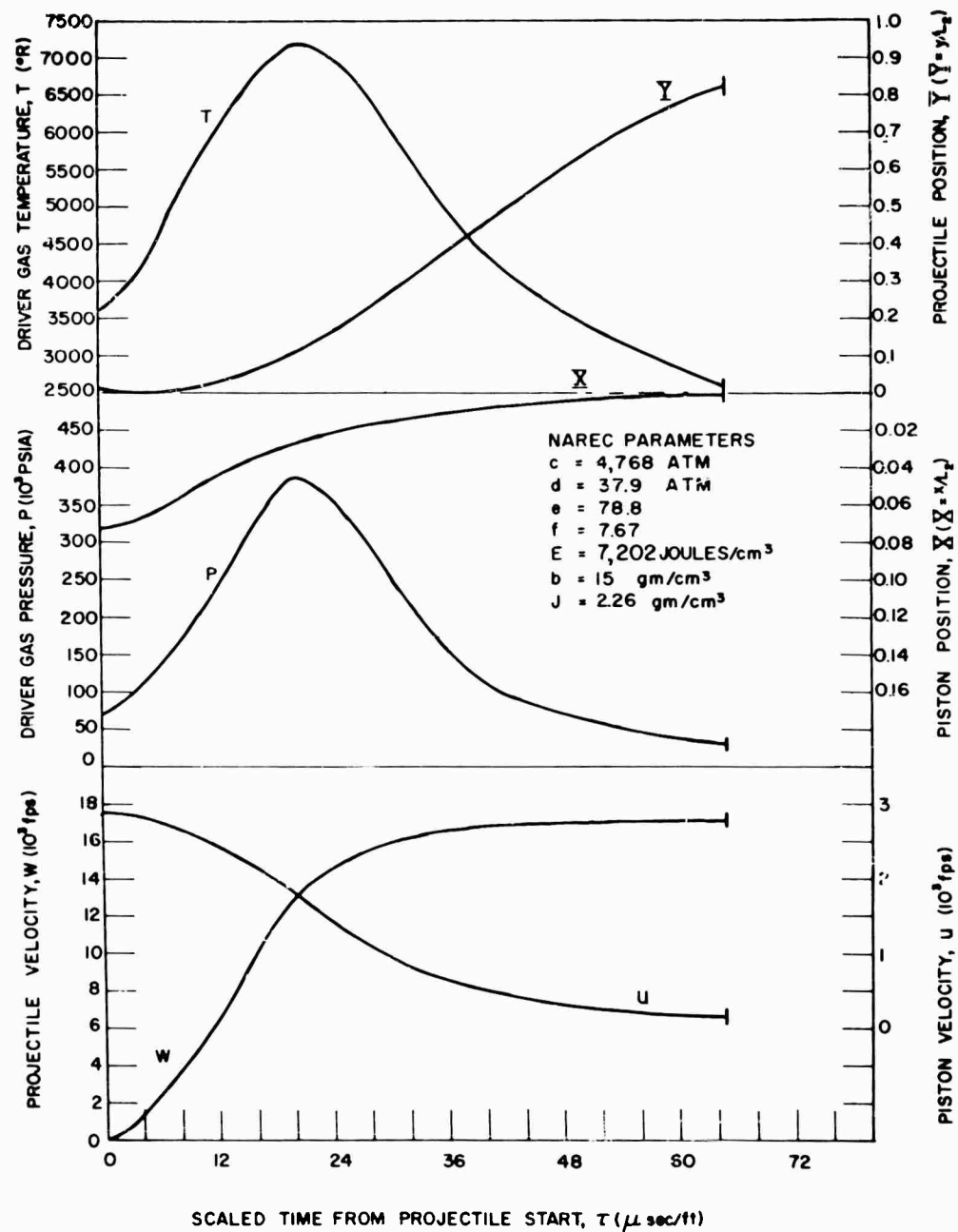


Fig. 5 - Gun action with helium driver gas at 300°K

# ACCELERATOR DEVELOPMENT

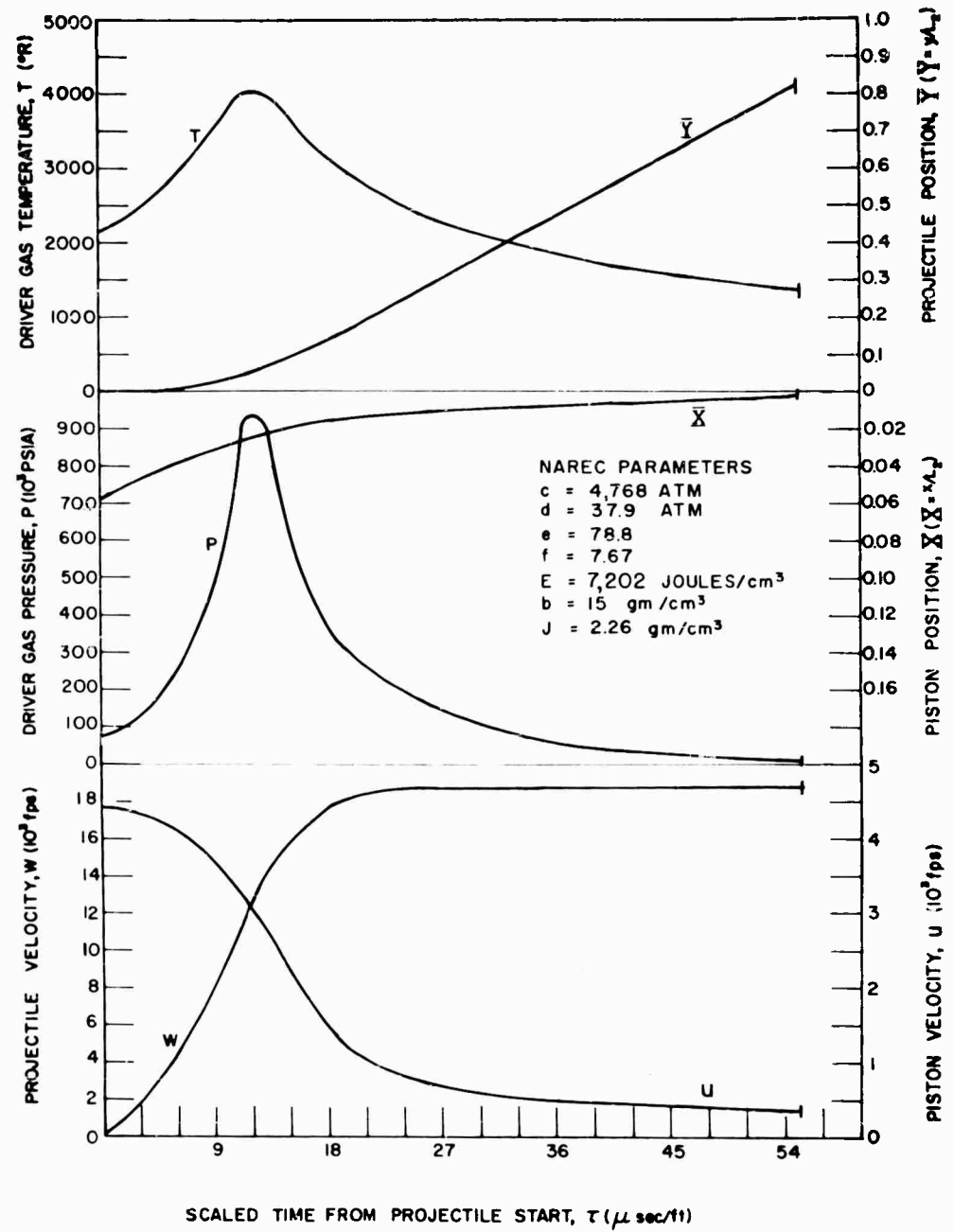


Fig. 6 - Gun action with hydrogen driver gas at 300°K

# ACCELERATOR DEVELOPMENT

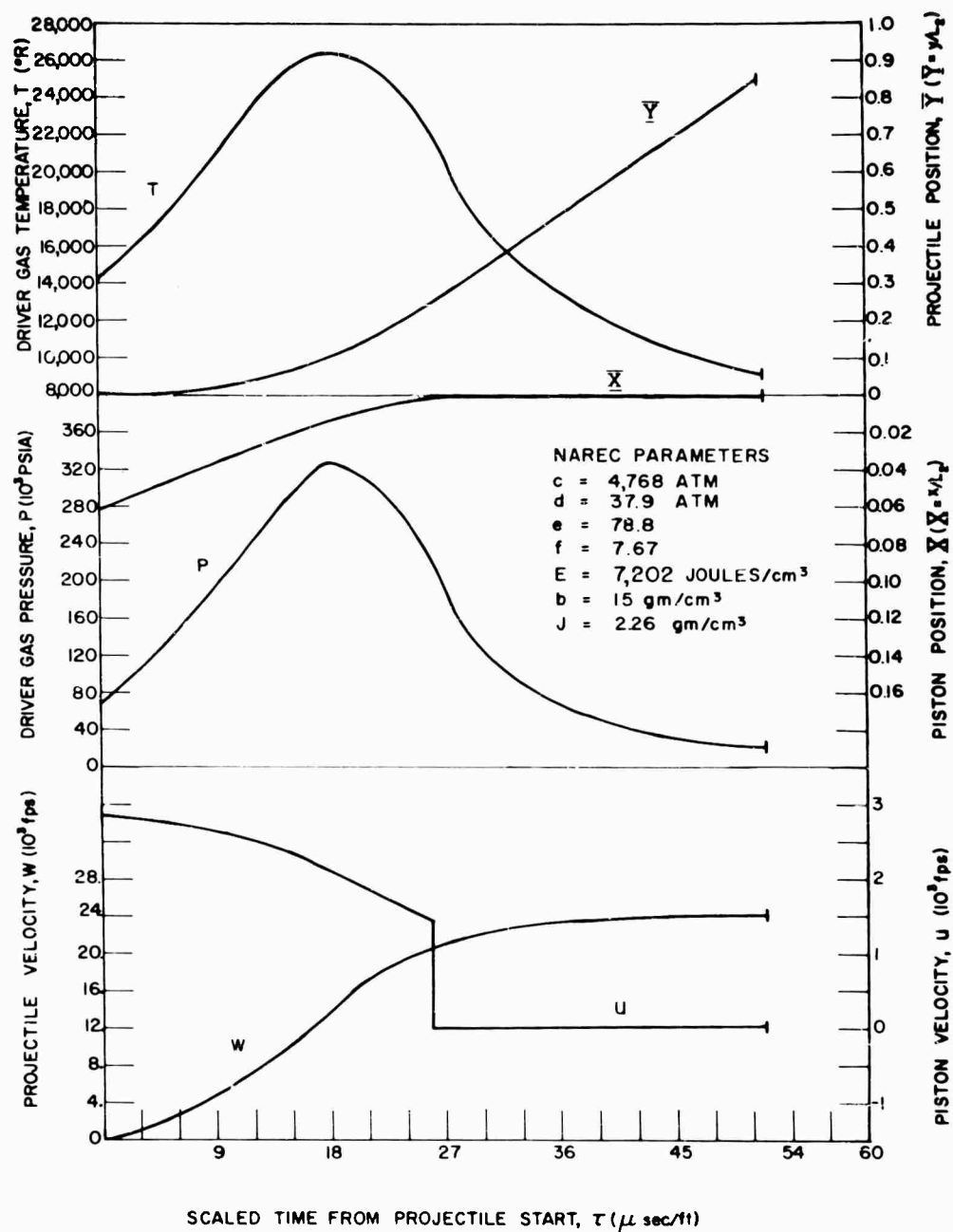


Fig. 7 - Gun action with helium driver gas at 1200°K

## ACCELERATOR DEVELOPMENT

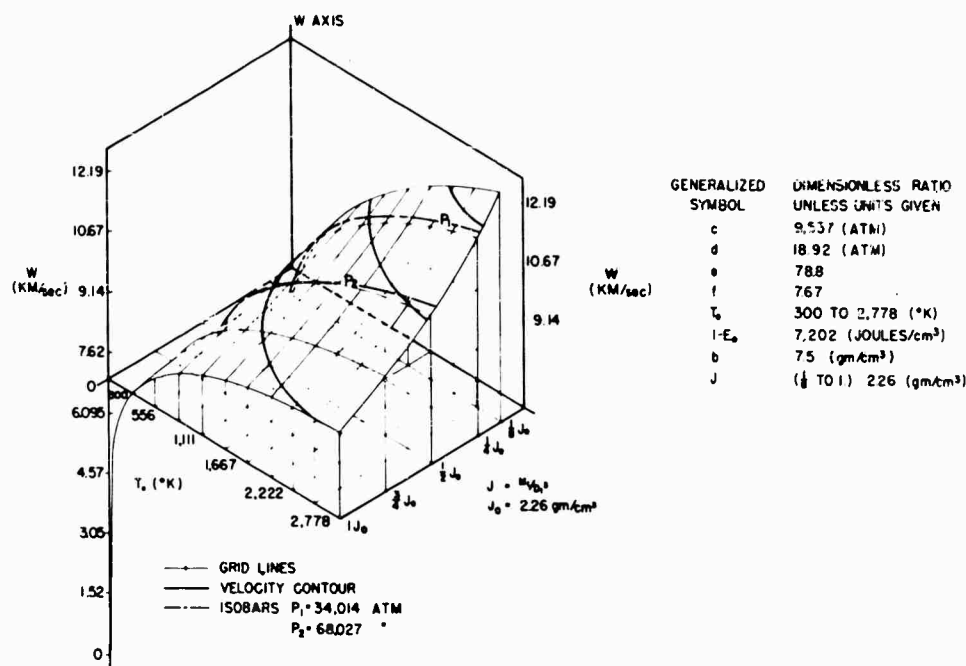


Fig. 8 - Variation of velocity  $W$  with driver gas temperature  $T_g$  and projectile mass  $J$  (rt hand axis)

which represent very light projectiles. Successive curved lines extended to the velocity scale show the other heavy-line velocity contours of 10.67, 9.14, and 7.92 km/sec. Isobar  $P_1$  (broken heavy lines) shows that between the quarter and one-eighth  $J_0$  value the pressure is about 34,000 atmospheres. Along the one-half  $J_0$  value is a line showing the isobar  $P_2$  representing conditions with 68,000 atmospheres maximum pressure. It can be seen that the increases in velocity with temperature are not nearly as pronounced with the heavier projectiles (larger  $J$  values). In agreement with experimental observations, the curve at 300°K shows an optimum velocity at a  $J$  value between the one-half and three-quarters  $J_0$ . With increasing temperatures the projections of the grid curves parallel to the  $J$  axis change gradually from convex up to concave up. This means that with increasing temperatures lightening of the projectile will result in a higher rate of velocity increase.

### EFFECT OF LOADING PRESSURE

In Figure 10 the only parameter changed was the loading pressure, which was raised to 28.6 atmospheres. In this case, above the 12.19-km/sec contour the projectile velocity surface is slightly smaller than that shown in Figure 9. There is a significantly wider region to the right of the  $P_1$  isobar, ranging between one-half  $J_0$  to one-quarter  $J_0$ , where maximum pressures are below 34,000 atmospheres. For almost all of the velocity surface, the pressure is less than 68,000 atmospheres. At 300°K the velocity is considerably less than in Figure 9.

## ACCELERATOR DEVELOPMENT

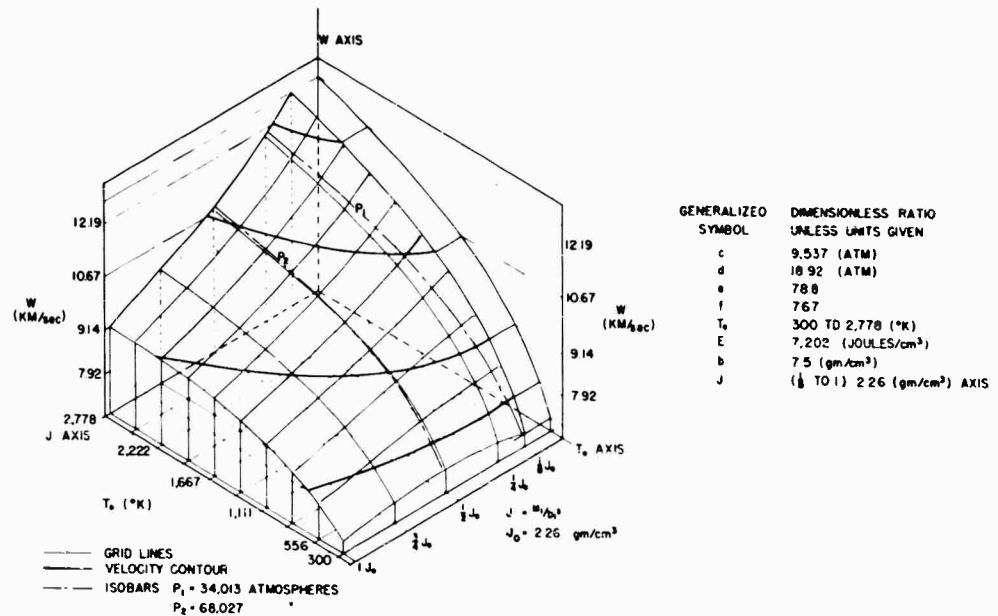


Fig. 9 - Variation of velocity  $W$  with driver gas temperature,  $T_0$  and projectile mass,  $J$  (left hand axis)

Before passing on to the next figure, it is instructive to review some of the conditions under which the isometric curves were generated. First, leakage past the piston or projectile was assumed to be zero. Experiments with a Bridgman seal and electrical instrumentation showed that gas leakage actually has considerable influence on projectile velocity. The standard steel piston had up to 16.7-percent loss in velocity over that obtainable with a piston with negligible leakage. Another physical reality is projectile friction, which seems to vary directly with pressure. In research with Teflon and other plastics, it was found that friction resistance (figured in terms of force per cross-sectional area) can with light projectiles be held to about 121 atmospheres. Since interest is in exploring the higher velocity ranges, this low value was chosen as a constant average value and used in all studies in this series. Comparative runs exist in which it is necessary to correct by subtracting about 3 percent in Narec projectile velocity for the heavy ( $j = 2.26$ ) Teflon-coated cylindrical projectiles and about 8 percent for the plain uncoated ones. Also, maximum proof-loading piston energy ( $E_0$ ) for the 20-mm piston has been selected to get an idea of optimum performances. Small variations in piston energy may also be treated as corrections to the optimum program. In each of the experimental-versus-Narec comparisons appropriate adjustments have been made to obtain the Narec curve fitting experimental conditions as closely as possible.

Experimental and theoretical studies have been made showing the effect of loading pressure on projectile velocity, as shown in Figure 11. At high

## ACCELERATOR DEVELOPMENT

pressures the curves agree quite well, but they depart at low loading pressures, where peak driver-gas pressure rises to above 66,680 atmospheres. Visible gas leakage occurs around the two-piece catcher at pressures slightly over 34,000 atmospheres. This is the most likely cause of the substantial variance between theory and observation. The theoretical curve will also fall sharply as initial gas pressures are reduced further.

No experimental data exist on the effect of loading pressure with gas at high initial temperature; and since experimental high-temperature work is planned, a theoretical study was made as shown in Figure 12. With heavier projectiles ( $j = 2.26$ ), optimum loading pressure is about 35 atmospheres, while with very light projectiles the optimum loading pressure falls to about 19 atmospheres. The peak driver-gas pressure over most of the surface as indicated by the Isobars  $P_1$ ,  $P_2$  is under 34,000 atmospheres.

### PISTON ENERGY TEMPERATURE STUDY

Figure 13 shows how velocity varies with  $E_0$  values and temperature. There is considerable velocity surface above 24 km/sec. This study was extended to consider ten times the standard proof-loading energy. These energies are attainable experimentally by utilizing three-stage hypervelocity guns; however, when one looks at the isobar contours the pressures are too high for practical considerations. There is only a narrow region above one  $E_0$  value (7202.2 joules/

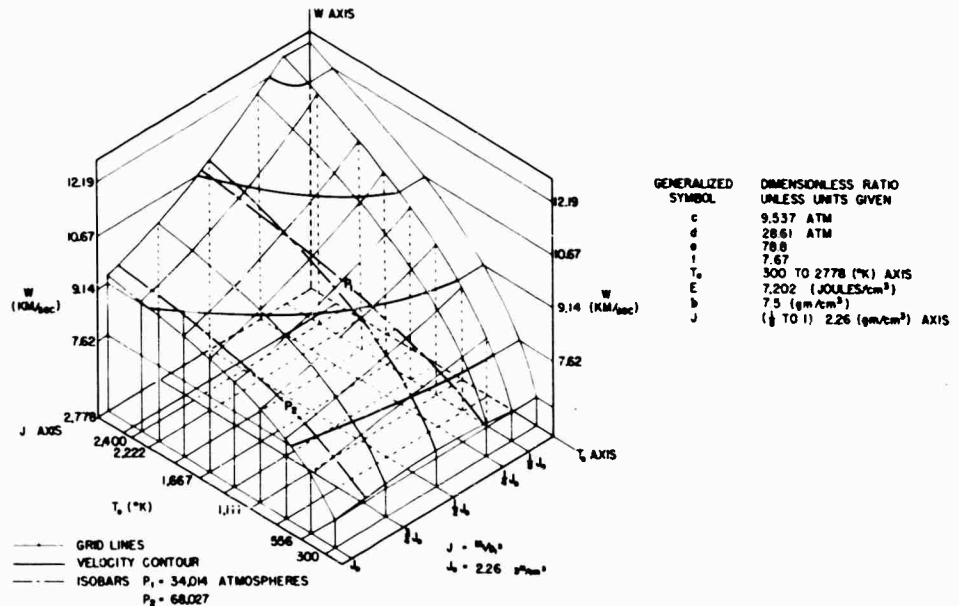


Fig. 10 - Variation of velocity  $w$  with driver gas temperature  $T_g$  and projectile mass,  $J$  (higher loading pressure  $d$ )

## ACCELERATOR DEVELOPMENT

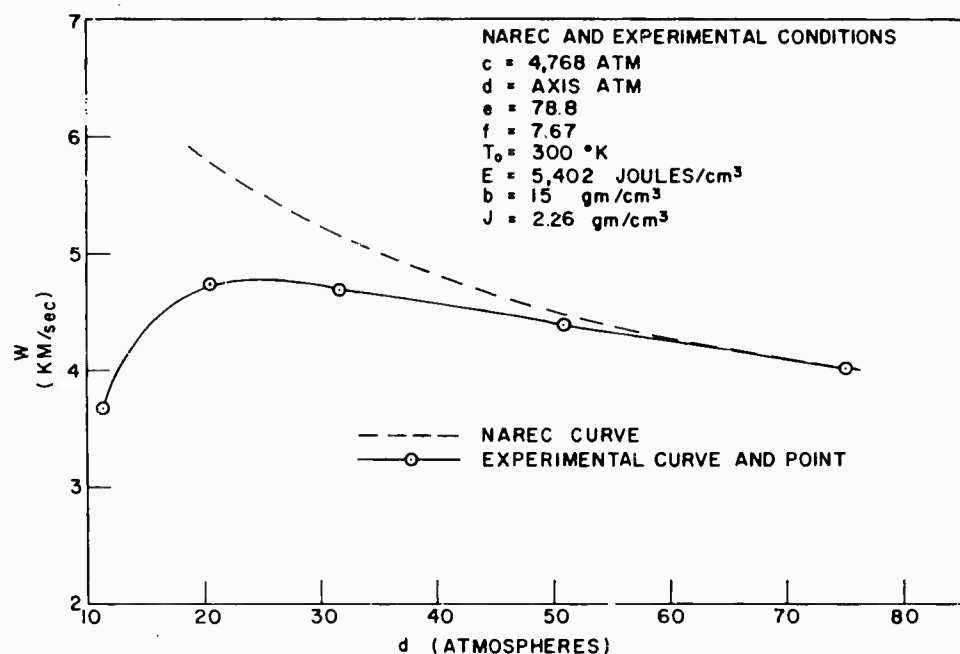


Fig. 11 - The variation of projectile velocity,  $W$ , with initial driver gas pressure,  $d$

$\text{cm}^3$ ) where peak driver-gas pressures are below 33,340 atmospheres. There is a small region between 2 and  $1\frac{1}{2} E_0$  where pressure is 66,680 atmospheres, and between 3 and  $2.5 E_0$  there is a region where pressure is below 132,360 atmospheres. Most of the experimental work has taken place at  $E$  values of three-quarters  $E_0$ . At this energy the projectile velocities are about 4 percent below those with an  $E_0$  value of one at an initial driver-gas temperature of  $2,770^\circ \text{K}$  and about 5 percent below at  $300^\circ \text{K}$ . In general there is considerable projectile-velocity gain with increasing piston energy, but the pressures rise to values where gas-container surfaces distort and leakage is certain to occur.

### HEATED DRIVER-GAS STUDY

In Figure 14 the Narec curves were extrapolated using the method for generating Figure 13 to give temperature-velocity correlations for experimental piston energies and other conditions. In the first experiment using steel pistons (lower experimental data points), the higher initial driver-gas temperature  $T_0$  was attained by heating about 75 percent of the compression tube electrically. Experimental points are 2 percent higher than predicted where an experimentally determined value of 16 percent velocity reduction was allowed for steel piston leakage. The elevation in driver-gas temperature in the upper experimental data points was accomplished by raising the volume ratio by a factor of 2.09. In the two experiments, the data points lie close to the theoretical curves, and the gains in velocity from driver-gas heating were as predicted.

## ACCELERATOR DEVELOPMENTS

### CHAMBERAGE-AREA STUDY

At NRL a projectile velocity of about 8.1 km/sec has been reached with a gun where the chamberage-area ratio  $f$  was about 52. Narec solutions with the same experimental conditions gave about 10.7 km/sec and peak pressures of about 181,000 atmospheres.

Figure 15 shows how velocity varies as a function of the log of this chamberage-area ratio  $f$ . It is noted that velocities in excess of 24 km/sec are obtained in the upper parts of the surface. At high chamberage-area ratios (above 20) the pressure exceeds 133,000 atmospheres over much of the velocity surface. These high pressures always cause considerable distortion at the entrance section of the launch tube, forming a very small venturi which lowers the velocities considerably below those predicted. The natural log of the  $f$  value, 2.03, represents a chamberage-area ratio of 7.67, which corresponds to a 20-mm compression tube and a 30-cal launch tube. The curves illustrate that a slight increase in chamberage-area ratio results in a considerable gain in projectile velocity and that gains as a result of high initial driver-gas temperature are independent of  $f$ .

### PISTON ENERGY STUDY

The study of the effect of piston energy  $E$  and chamberage ratio  $f$  aids in

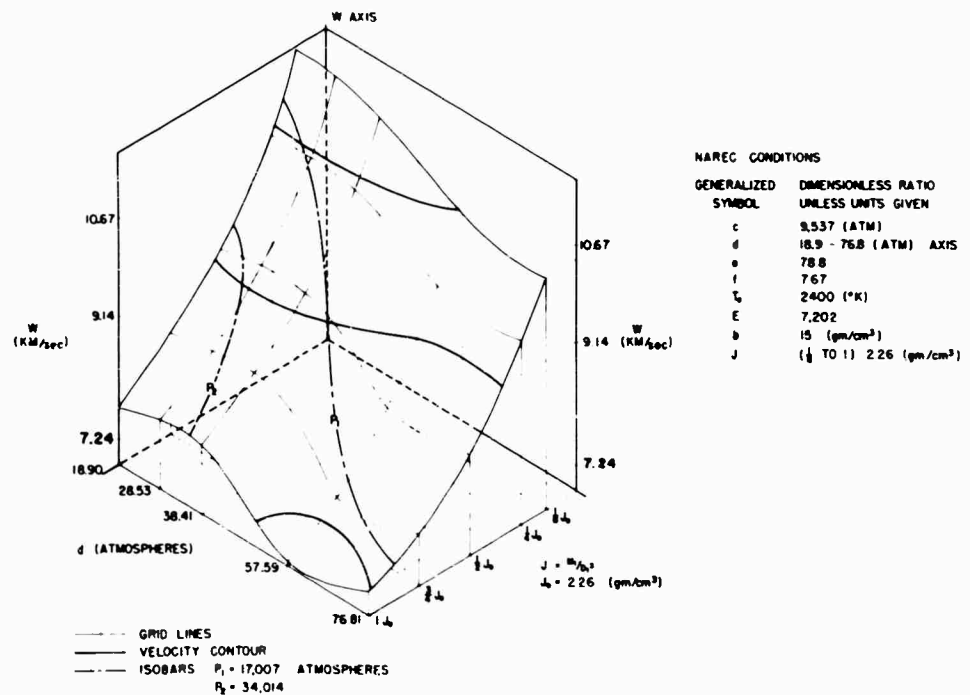


Fig. 12 - Variation of projectile velocity,  $w$ , with gas loading pressure,  $d$ , and projectile mass,  $J$

## ACCELERATOR DEVELOPMENTS

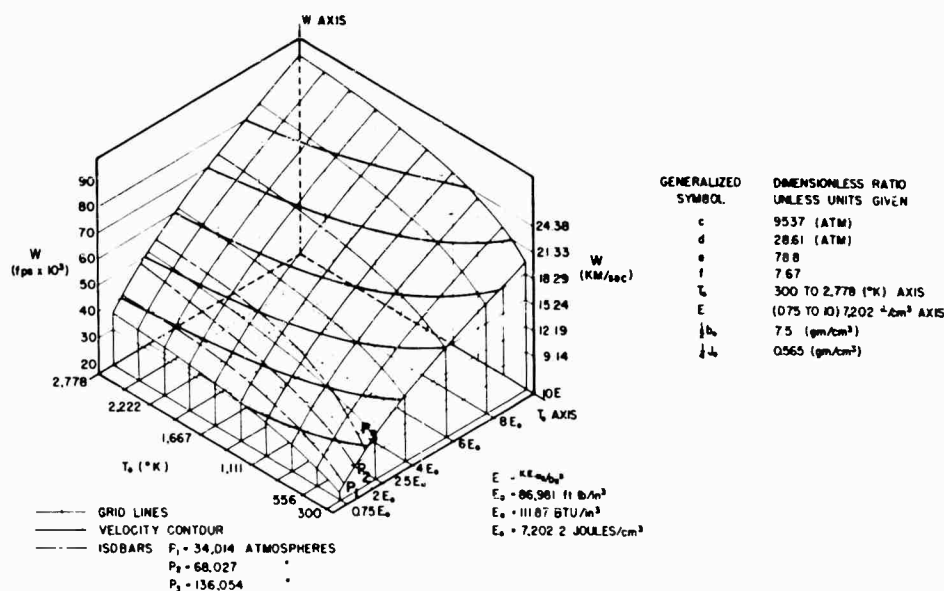


Fig. 13 - Variation of velocity  $W$  with driver gas temperature,  $T_0$ , and piston energy,  $E$

extrapolation of the Narec study. The theoretical curves of Figure 16 were developed for the experimental parameters where piston energy  $E$  was varied from  $3/4 E_0$  to  $1 E_0$  with a chamberage-area ratio of 7.67. The copper-piston data points fall on the curve, while the steel-piston datum point is low, indicating the effect of leakage. A piston energy of  $2E_0$  was reached in a three-stage gun at a chamberage-area ratio of 5.62 in the upper datum point. This represents a 20-mm, 35-cal combination in the final stages, which is the most successful combination. Pressures were too high to be contained when the 20-mm, 30-cal combination was used; consequently projectile velocities were lower. The generality of the program is shown by the experimental datum point obtained with 1.1-inch, 50-cal combination, which is the closest low-piston-energy experimental point available at NRL.

## PISTON AND PROJECTILE WEIGHT STUDY

Figure 17 is a plot showing velocity variation versus piston and projectile weight parameters,  $b$  and  $j$ . Parameter  $b$  varies from 15 grams per cubic centimeter ( $b_0$ ) to  $1/8$  of that value, and  $j$  varies from 2.26 grams per cubic centimeter ( $j_0$ ) to  $1/8$  of that value. Velocity contours vary from 8.38 to 6.1 km/sec. The pressure isobars ( $P_1$ ,  $P_2$ ,  $P_3$ ) show that if the  $b$  value is greater than  $1/2$  of  $b_0$  and the  $j$  value is less than  $1/2$  of  $j_0$  peak pressures will be about 33,000 atmospheres.

# ACCELERATOR DEVELOPMENT

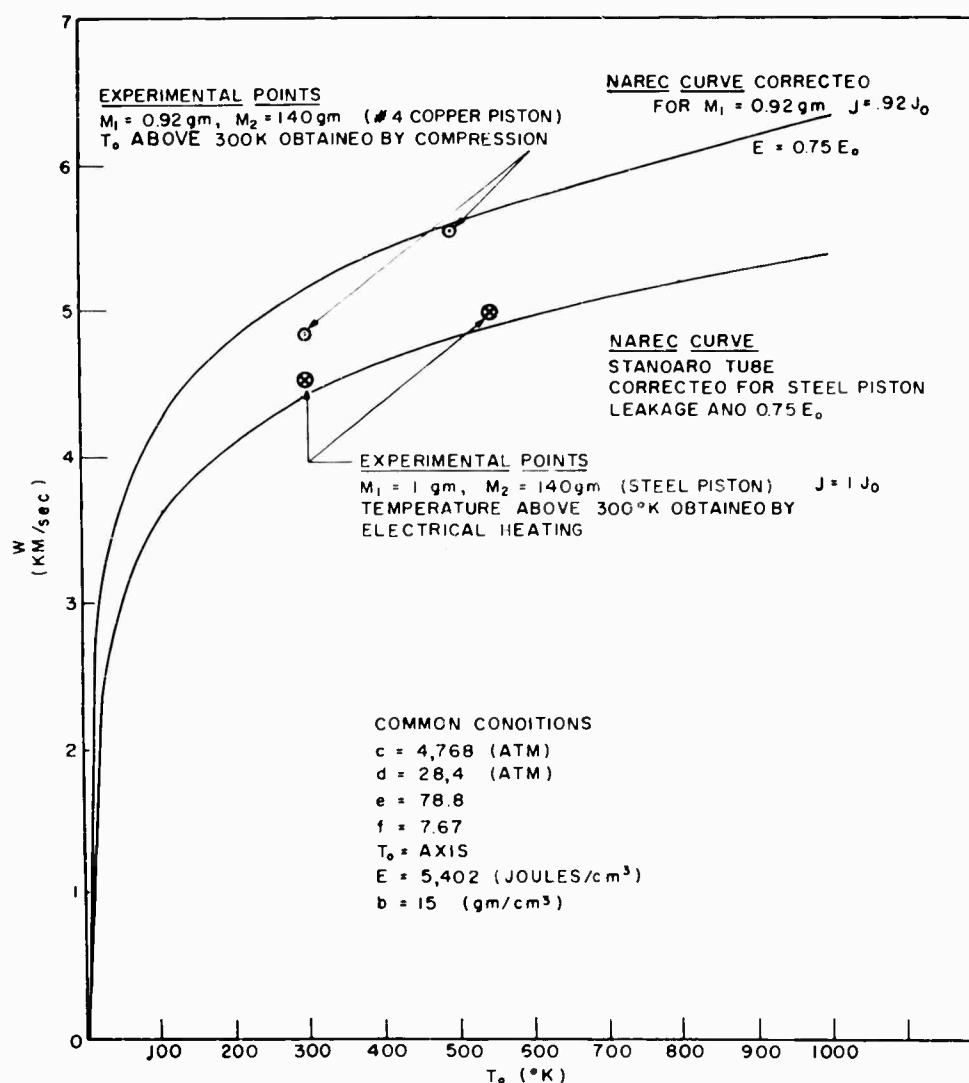


**FIG.14 THE VARIATION OF PROJECTILE VELOCITY, W, WITH DRIVER GAS TEMPERATURE  $T_o$ .**

The two experimental points showing the effect of reducing piston weight by 10 percent (1-gram projectile fired from a 20-mm, 30-cal gun) are within 5 percent of the theoretical values when proper allowances are made for experimentally determined friction and low piston energy to match the experimental firing parameters. The same is true for the interior datum point on the velocity surface using the magnesium 0.63-gram projectile ( $j=0.63j_o$ ) and the 40-gram piston ( $b=2/7b_o$ ).

## ACCELERATOR DEVELOPMENT

Figure 18 is a similar plot, with the initial driver-gas temperature at  $2400^{\circ}\text{K}$ , where an appreciable part of the velocity surface is above 12,2 kilometers per second. The velocities presented in these curves are much greater than those presented in previous curves for equivalent pressures.

In both Figures 17 and 18, as the weight of the projectile is reduced the piston weight must be reduced while holding the kinetic energy constant, in order to achieve maximum velocity gains from a lightweight projectile. In both figures the 68,000-atmosphere isobar almost bisects the surfaces diagonally.

## EFFECTS OF RADIATION ON PROJECTILE VELOCITY

The Naree program offers an easy means of examining the theoretical gain from the elimination of hot-gas-radiation effects. It is only necessary to zero the Stefan-Boltzman radiation coefficient and rerun the program. Comparison is then made between two identical runs with zero and finite radiation constants. This has been computed for several configurations using helium as the driver gas under the conditions shown in Figure 19. Figure 20 shows four-run

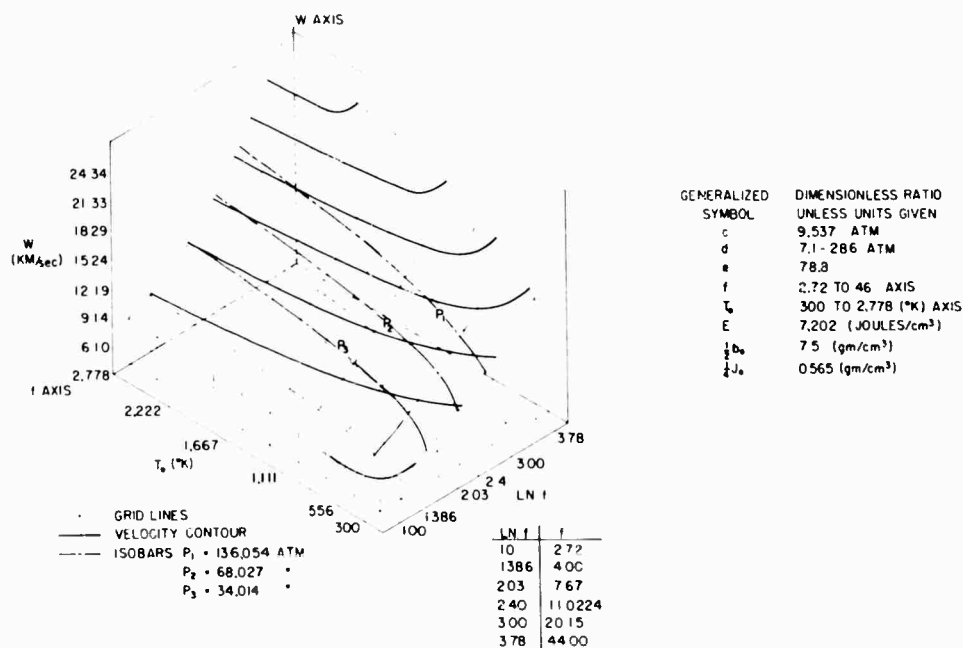


Fig. 15 - Variation of projectile velocity  $W$  with initial temperature,  $T_0$ , and Chamberage ratio,  $f$

# ACCELERATOR DEVELOPMENT

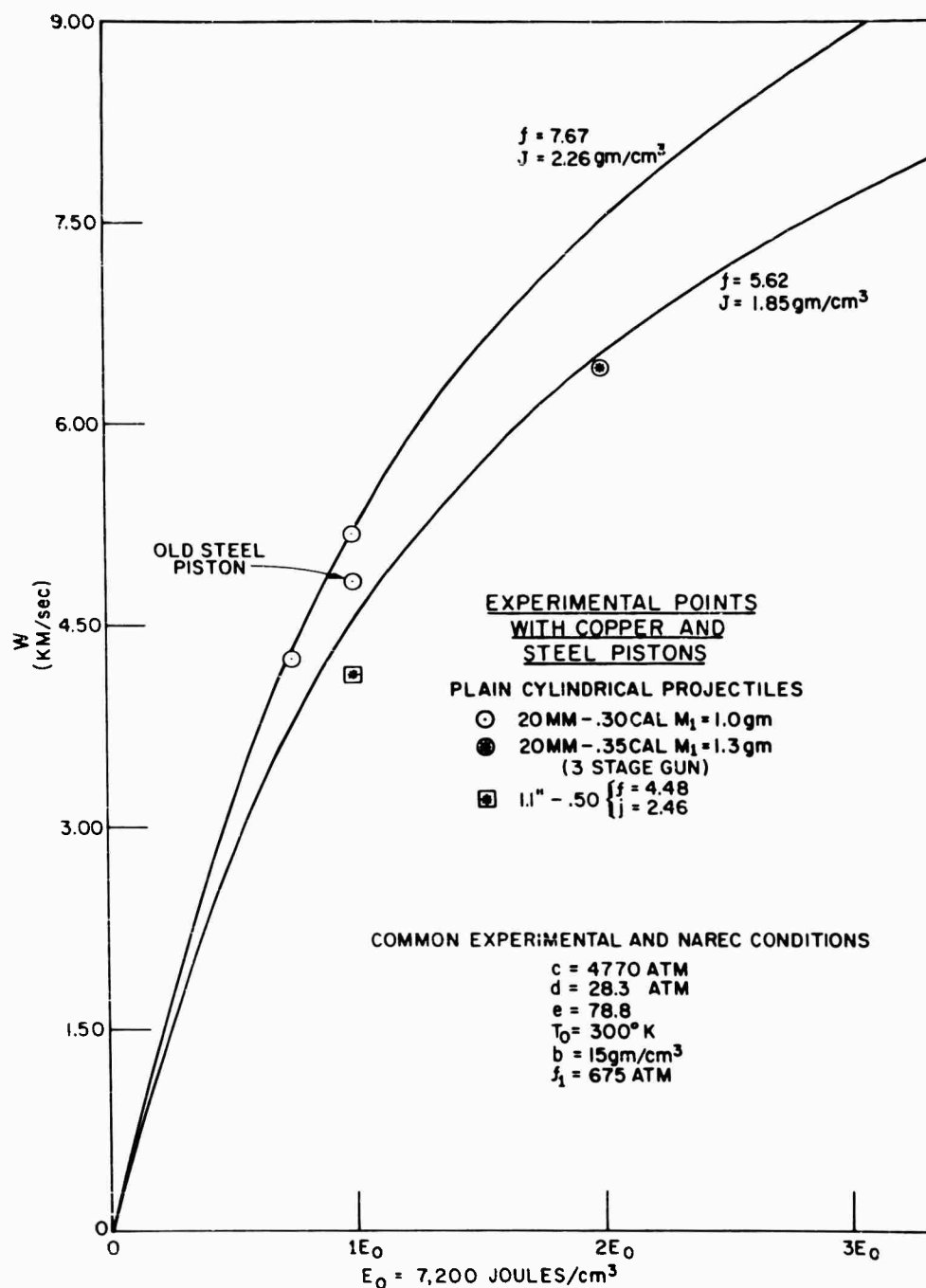


Fig. 16 - Variation of projectile velocity, W, with piston energy, E

# ACCELERATOR DEVELOPMENT

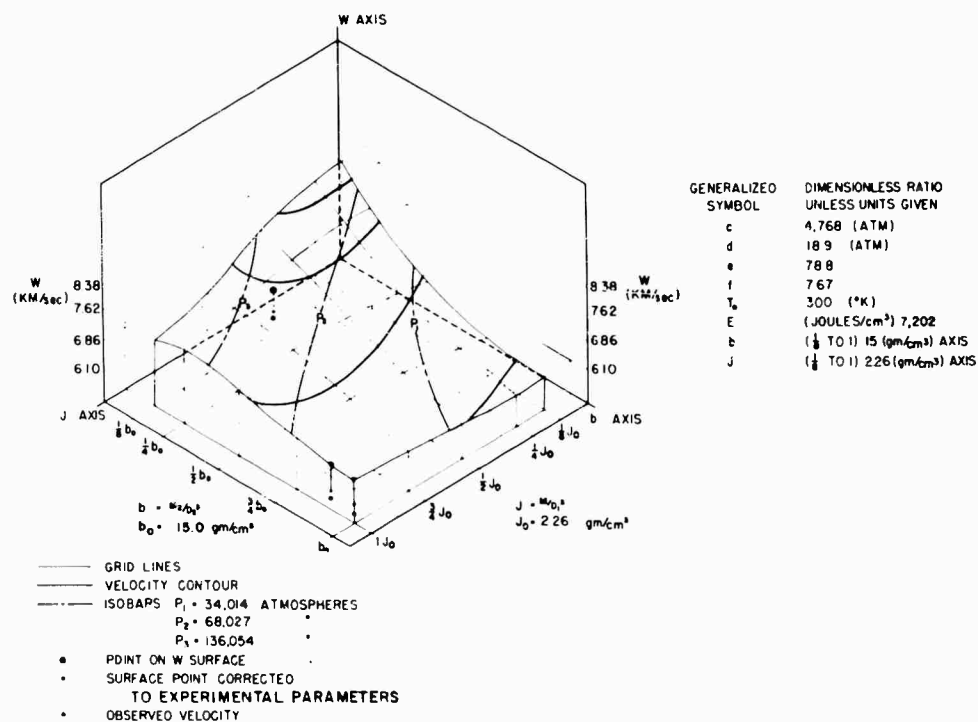


Fig. 17 - Variation of velocity  $W$  with projectile, and piston mass parameters  $J$  and  $b$

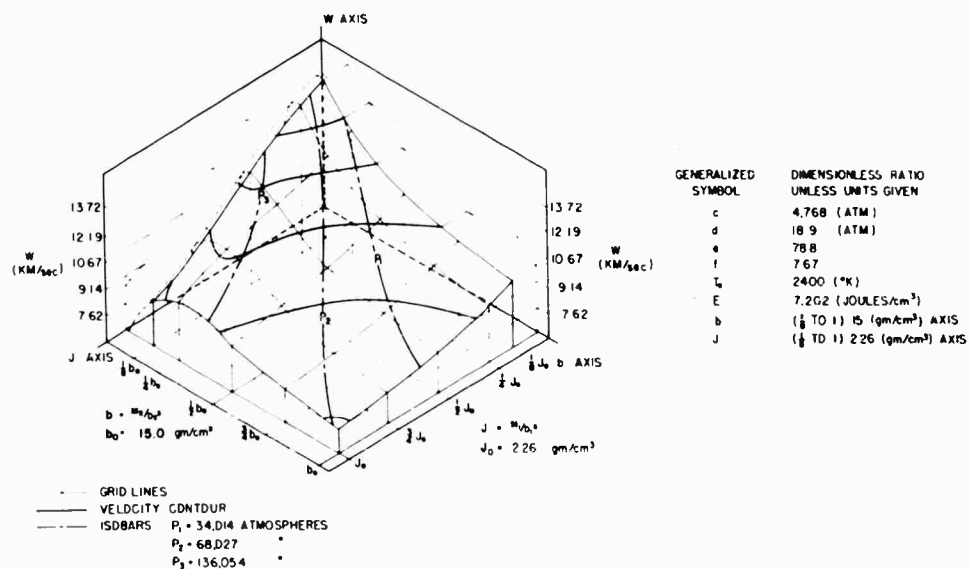


Fig. 18 - Variation of velocity  $W$  with projectile, and piston mass parameters  $J$  and  $b$  (heated driver gas)

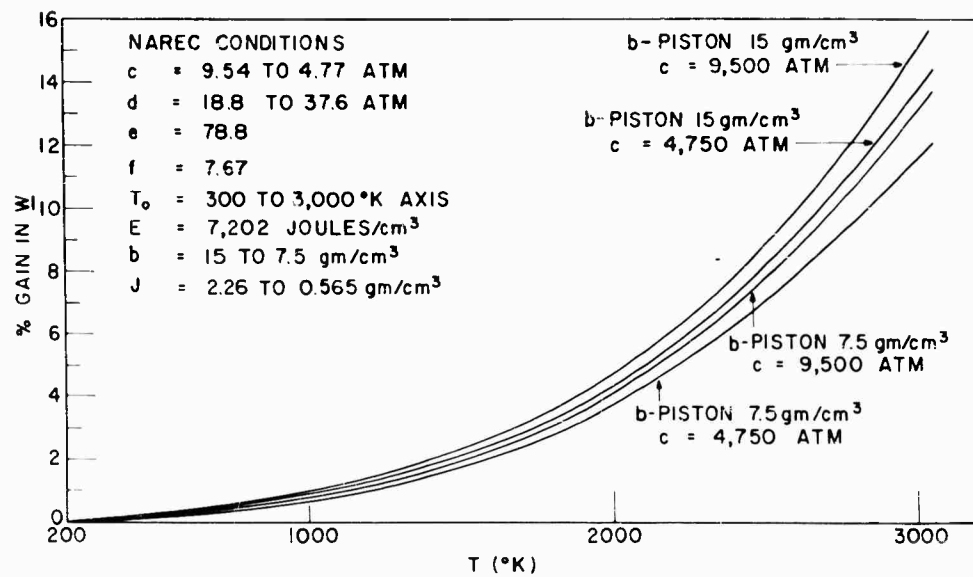


Fig. 19 - Projectile velocity percentage gain from zero radiation

Figure 20  
Gain in NAREC Projectile Velocity for Elimination of  
Radiation Loss ( $T_0 = 1200$  K)

Common Parameter	Condition	Av. Gain in Velocity (4 Runs)	
		$\Delta v$ fps (for $H_e$ )	$\Delta v$ fps (for $H_2$ )
j	0.565 gm/cm <sup>3</sup> (light projectile)	263	22
	2.26 gm/cm <sup>3</sup> (heavy projectile)	241	5
c	4,750 Atm. (shot-start press)	233	11
	9,500 Atm. (shot-start press)	270	16
b	7.5 gm/cm <sup>3</sup> (light piston)	232	8
	15 gm/cm <sup>3</sup> (heavy piston)	272	19

averages of projectile-velocity gain listed with the common parameter. Velocity gain from a zeroed radiation constant can also be interpreted in terms of percentage of departure or velocity loss from a basic logarithmic curve of velocity-gain percentage versus initial driver-gas temperature  $T_0$ . This loss increases approximately as the third power of the initial absolute temperature of the driver gas.

## ACCELERATOR DEVELOPMENT

Since the basic percentage increase in projectile velocity increases only in a logarithmic fashion, it is easy to conjecture that at some temperature the percentage of velocity gain in the basic curve will be counterbalanced by percentage of velocity losses from radiation effects. At this optimum initial-temperature point, projectile-velocity losses may occur from further increase in initial gas temperature. An experiment in which  $6,000^{\circ}\text{K}$  initial temperature could be reached by a combination of electrical and compressive heating may yield some information on this optimum temperature.

### HEAT ADDITION DURING COMPRESSION

Since the light-gas-gun piston starts slowly, it appears that electrical heat added during the latter portion of the compressive cycle may have considerably less heat loss and thereby be more effective in raising the projectile velocity than other types of preliminary heating. In this type of operation electrical energy may be added at low driver-gas density, and the additional pressures required for effective acceleration can be achieved later in the cycle by piston compression of the gas. Experimental investigation of these techniques will be carried out by using 20,000- and 100,000-joule capacitors, and the newly developed 250,000-joule capacitor banks presently under construction (Fig. 21). Also shown is the gas gun which will be used for the initial electrocompression studies. The gun consists of a 90-inch long, 37-mm compression tube fitted for 22-cal and 30-cal launch tubes. Projectile velocities of about 7.8 km/sec have been achieved with this gun without the addition of electrical energy.

Recent advances in switching techniques, shown schematically in Figure 22, enable the 20,000-, 100,000-, and 250,000-joule capacitor banks to be used in any desirable combination. A total of 370,000 joules can be delivered in about six microseconds. Maximum current is about 15 million amperes. To handle this large current load, extensive engineering was necessary to develop the light-weight energy collector (Fig. 23) which is designed for withstanding the enormous peak magnetic repulsive pressures generated by the peak current. A cylindrical design was chosen in order to utilize the hoop strength of the cylindrical elements.

Results of initial computations from the Narce program show that velocity increases ranging from 3 to 6 km/sec should be possible above maximum performance of the gun with increased driver-gas temperatures from electrical-energy input. As the computer program is further developed to handle the effects of heat input to the driver-gas during compression, it will be used to help establish design and firing criteria for the electro-compression gun.

### CONSTANT-VOLUME ELECTRIC GUN

The simplest type of electric gun is the constant-chamber-volume model, which is a chamber filled with low-molecular-weight gas. Research is continuing, and Figure 24 shows a newly designed constant-volume gun. This gun will be used in further research to optimize the firing parameters and to obtain minimum contamination of the light gas from metallic vaporization. Shown in this figure are the launch tube, the projectile, the ground electrode, the gas-filling port, electrical insulation, and the high-voltage electrode. During arc-discharge in this gun the

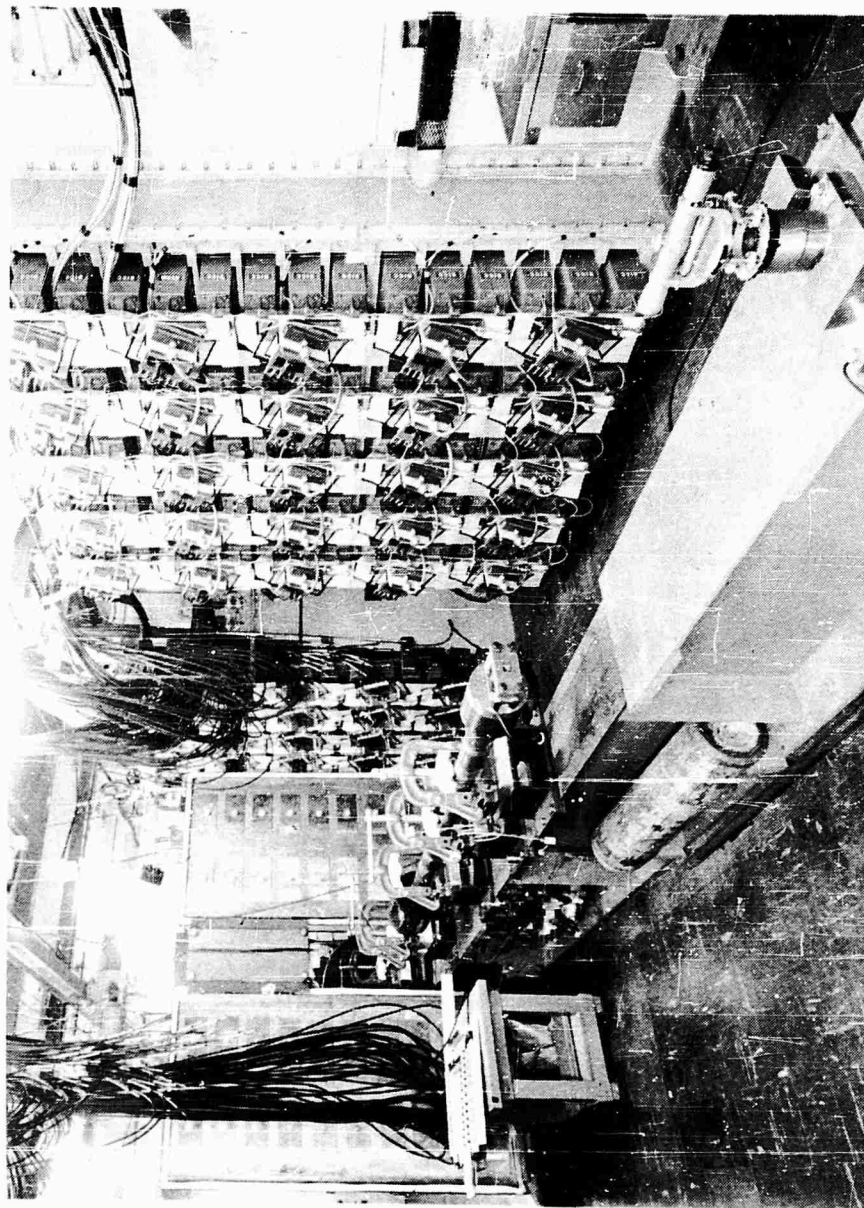
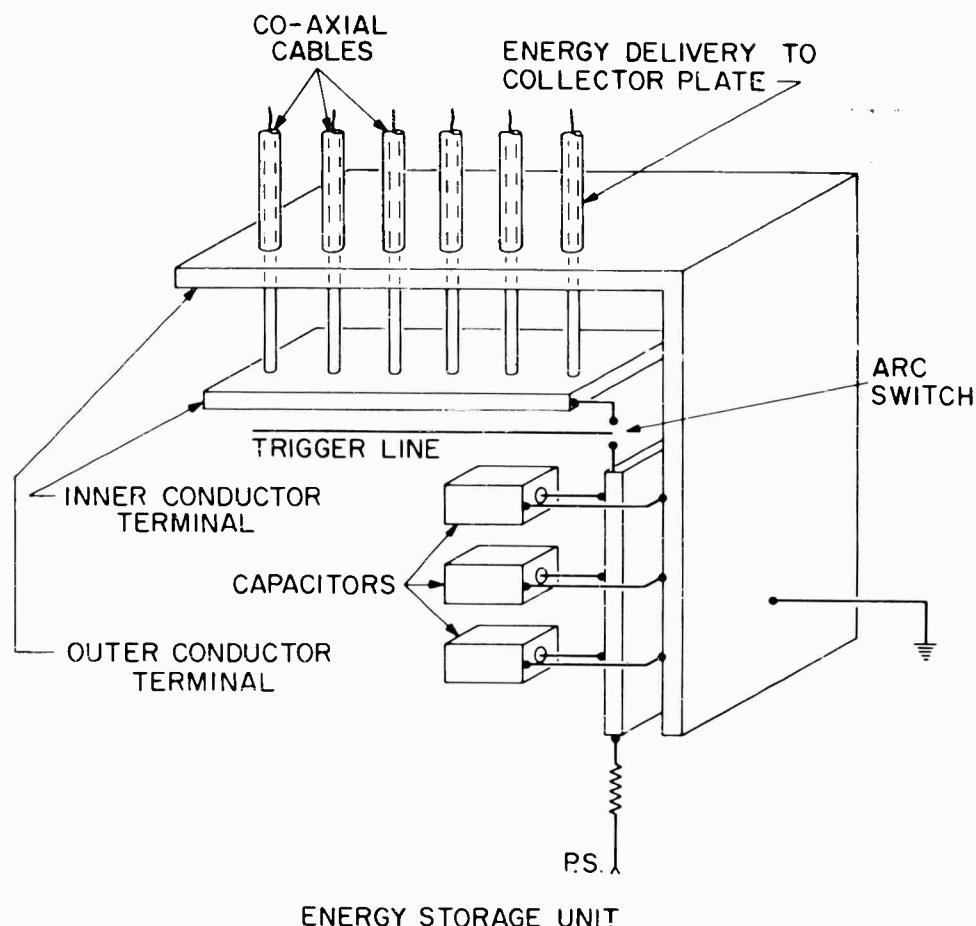


Fig. 21 - Capacitor banks (100 and 250 kilojoule)

## ACCELERATOR DEVELOPMENT



## ENERGY STORAGE UNIT

Fig. 22 - Switching and distribution arrangement

gas temperature is raised to about  $18,000^{\circ}\text{K}$ . After a thin diaphragm is ruptured, the heated gas accelerates a projectile down the launch tube. Although this has proven possible with present equipment, which is capable of generating gas temperatures in excess of  $15,000^{\circ}\text{K}$ , the extreme electrical current required for this heating vaporizes enough metal from the electrode surfaces to contaminate the gas and seriously restrict gun performance to velocities below 4.6 km/sec. Some of the limitations may be reduced in future studies.

## CONSIDERATION OF LARGE LIGHT GAS GUNS

At this time it is well to consider the effect of the analysis. It is clearly shown that velocities in excess of 12 km/sec can be achieved with reasonable pressures, provided there is sufficient driver-gas temperature and the projectile

## ACCELERATOR DEVELOPMENT

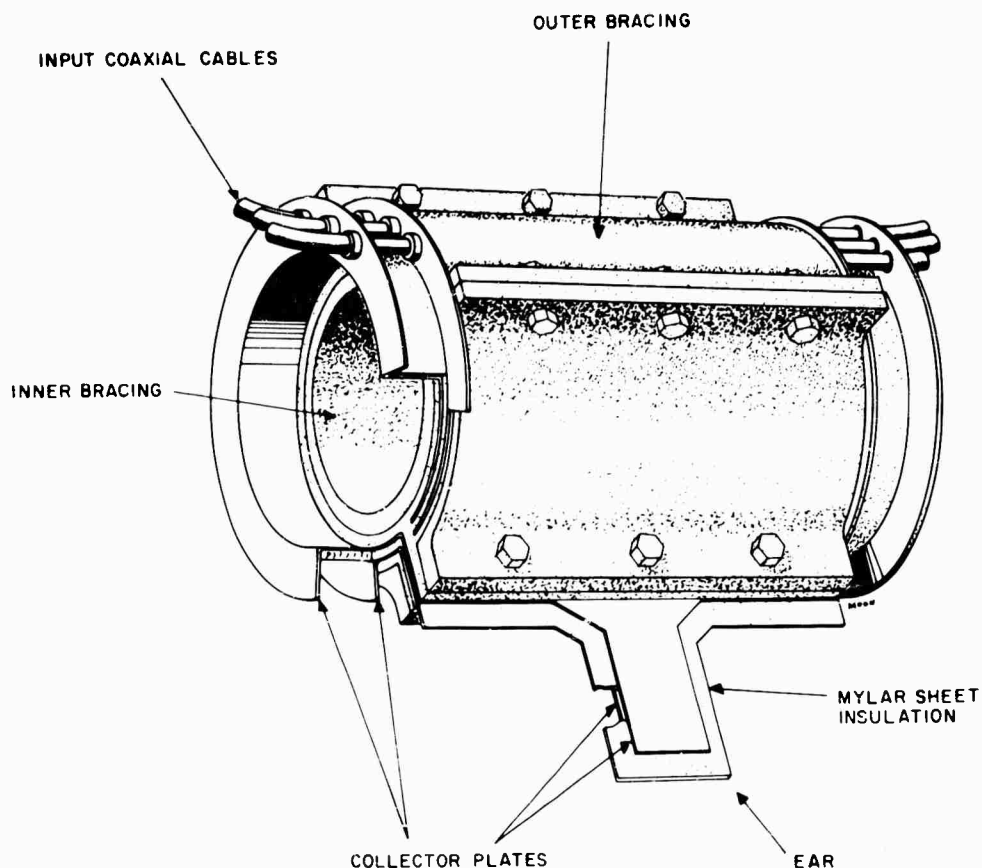


Fig. 23 - Main collector plate

weight parameter is lowered to  $1 \text{ g/cm}^3$  or below. This can be achieved with lightweight sabot material, provided peak accelerative pressures are kept below 34,000 atmospheres. To achieve low acceleration and a reasonable value of sabot projectile mass, large guns become necessary.

A much larger gun than the 40-mm and 3-inch tubes in current use at NRL is approaching the assembly phase. The gun (Figure 25) consists of standard 8-inch guns smooth bored and mounted muzzle to muzzle on rail trucks to form a compression tube 57.5 feet long. A pair of 3-inch smooth-bored guns are used for the 34-foot launch tube. This gun has been designed to launch a 225-gram projectile to speeds up to 9.0 km/sec and 900 grams to 6.0 km/sec.

Since the central breech is so massive (35 tons) it is infeasible to make it entirely expendable. Therefore, a partially expendable catcher has been designed that consists of a relatively thin steel inner liner surrounded by a lead sheath which is held within a massive steel outer ring, fabricated from the breech of a 16-inch naval gun. During operation the inner core will be partially destroyed

## ACCELERATOR DEVELOPMENT

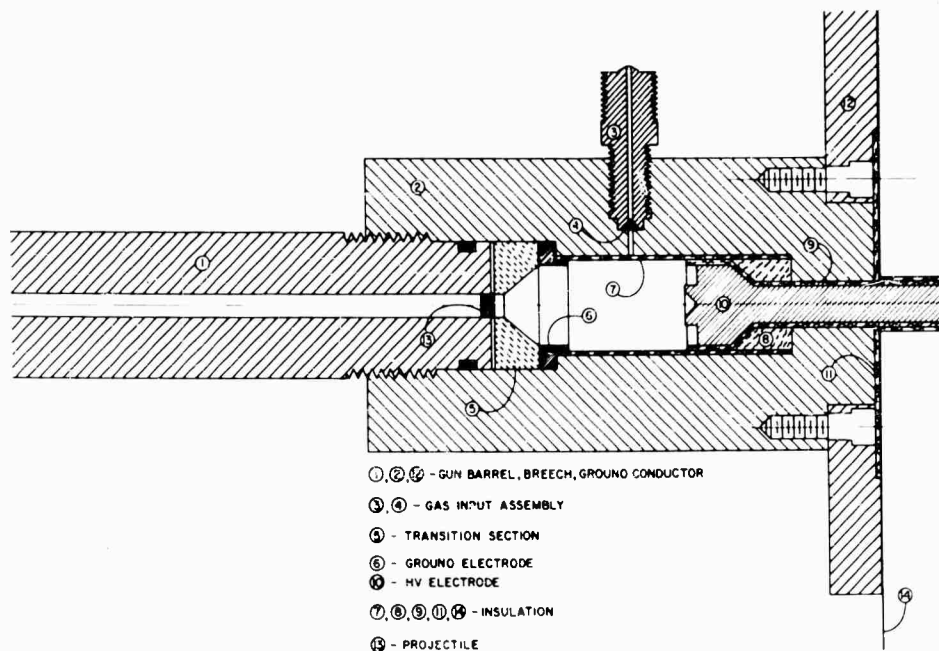


Fig. 24 - Constant-volume electric gun M-5



Fig. 25 - Rail mounted 8 - 2.5 in. hypervelocity gun

but the lead will prevent damage to the outer ring, and the liner can be replaced for another shot.

Because of the large diameter of the pump and launch tubes, maximum gas pressure must be kept considerably below values normally used in similar small guns to prevent permanent deformation from occurring. An extremely important task for the Narec program is to determine initial firing parameters that will yield high-performance results with lower operating pressures.

### PISTON CONSIDERATIONS

One source of large deformations in the high-pressure section is an unyielding piston. Current research is aimed at finding the best piston in certain

# ACCELERATOR DEVELOPMENT

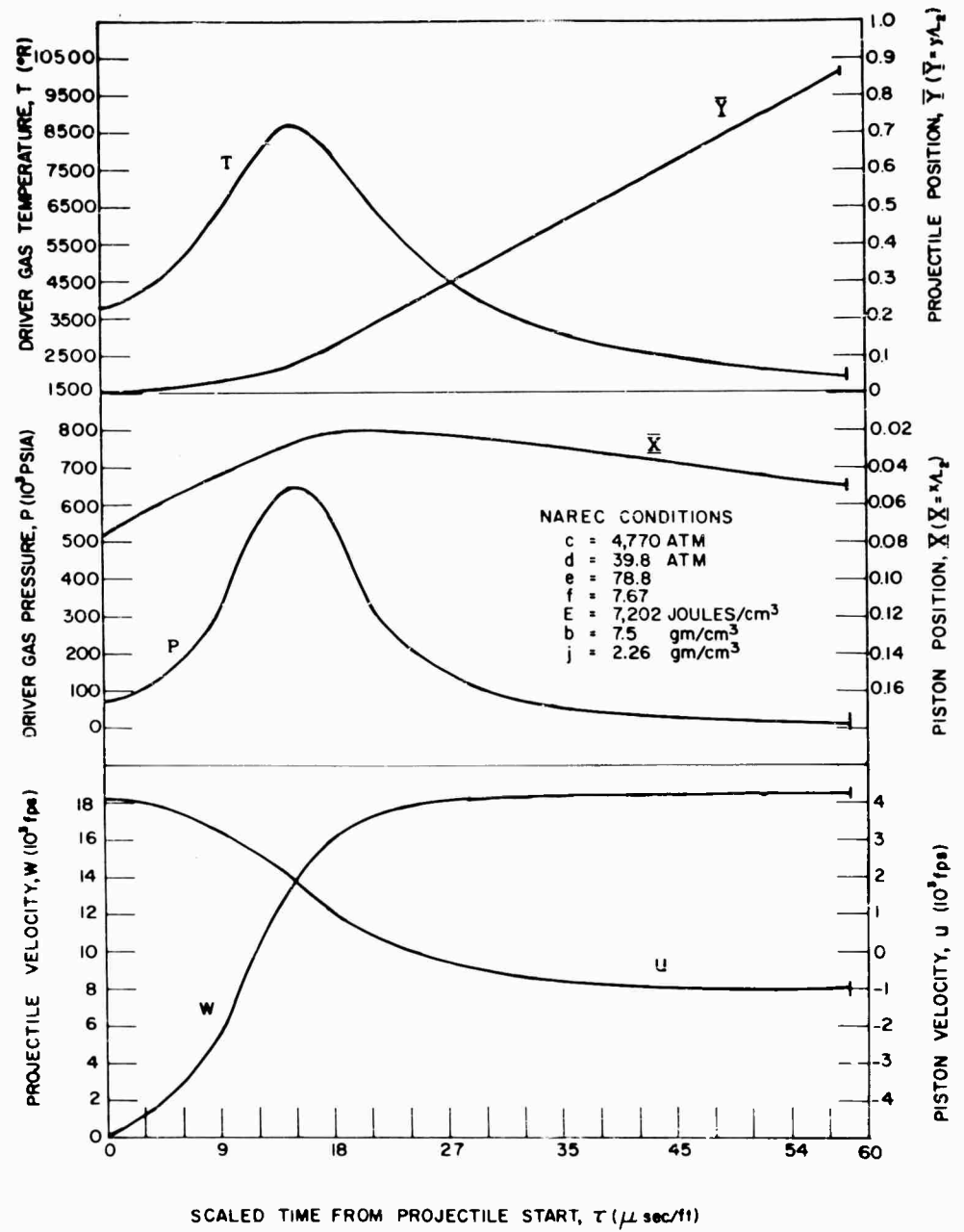


Fig. 26 - NAREC output with piston bounce

## ACCELERATOR DEVELOPMENT

weight classes. In the heavy- and medium-weight class, copper and lead have performed well with low distortions in the high-pressure sections. In the light-weight class plastics and soft aluminum appear to be quite good.

In several experiments, in which piston weight was varied, piston bounce occurred under the combination of parameters predicted in the Narec curves of Figure 26. Parameter X, representing piston position, approaches a minimum value and then increases as the piston velocity  $u$  goes negative. Figure 27 shows a copper piston with a Bridgman seal which has entered the conical portion of the high-pressure section, as indicated by the white dotted line, and then has backed up to the indicated final position, with the Bridgman seal intact. The edges of

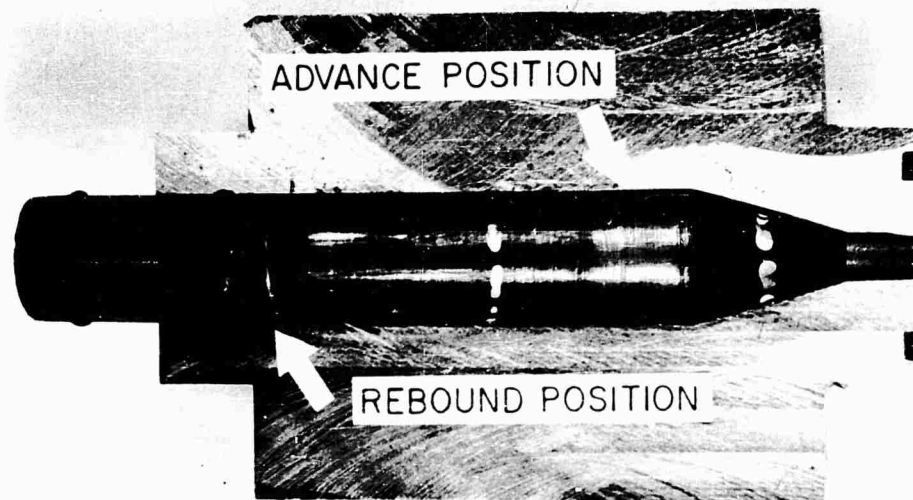


Figure 27. Photograph of Piston-Bounce with Seal Intact

the piston, which are used to form the seal, were expanded back to the full bore diameter in the final position. Computer studies show that the time from the first conical-surface contact to its final contact with the Bridgman surface edge is about 150  $\mu$  sec. The O-rings were not gummy and were in perfect condition, which indicates a very effective Bridgman seal throughout this piston motion.

Data points with the new piston agree closely with predicted Narec values, and velocity increases were achieved up to 20 percent above identical shots where standard steel pistons were used. A Bridgman seal only on the powder side of the piston yielded a 6-percent increase in projectile velocity; the seal on the driver-gas side only yielded a 16-percent increase over that of a standard steel piston.

## ACCELERATOR DEVELOPMENT

### PROJECTILE FRICTION

A qualitative theory of bore friction has been developed that depends on the movement of dilatational waves in the launch tube. It has been used to explain many of the observed bore-friction phenomena, such as:

1. Moderate friction in the first few inches of projectile travel
2. Steeply rising forces proportional to incident pressures and the dry coefficient of friction between the projectile material and the bore
3. A rapid fall-off to almost fixed moderate values.

Recently very successful high-velocity shots have been made with solid cylindrical projectiles where proper clearances were established behind the seal surfaces, to avoid postulated interference between the bore and projectile body.

### CONSIDERATION OF TERMINAL NEEDS

In order to obtain meaningful terminal ballistic data utilizing the light-gas gun, it is imperative that only the projectile impacts the target and that the mass of the projectile be accurately known. Techniques have recently been developed utilizing the quick-opening valve to eliminate the shear disk required in the standard gas-gun accelerator and to sabot projectiles to insure that no mass loss occurs during acceleration.

In previous models of the light-gas gun it was necessary to use a disk between the propellant gas and the projectile assembly. This disk prevented expansion of the light gas into the launch tube until a desired pressure was reached. When the low-molecular-weight gas was compressed to a predetermined value, the disk would shear from its support, and the disk and projectile assembly would then be accelerated down the launch tube. Impact damage could and generally was caused not only by the projectile but also by at least two fragments of sabot, dependent upon design of the sabot and the shear disk. Also, because of the shear disk, the total mass accelerated was unnecessarily high.

### QUICK-OPENING VALVE

Original work to eliminate the shear disk was done at NOL and resulted in the development of a high-pressure petal valve. Independently, Ames Aeronautical Laboratory, NASA, developed a break-type valve. The NRL gun utilizes the basic idea of this Ames device. Quick-opening valves have been developed for the 22-, 30-, and 60-cal launch tubes. Figures 28 and 29 are diagrams of the same basic valve. The opening action occurs when the lateral component of pressure acting on the notch or milled slot exceeds the tensile strength of the valve material. The break, or shot-start pressure, is controlled by the shape and depth of the notch or slot. Upon breaking, the two sections of the valve are driven apart, strike the valve-holder surfaces located perpendicular to the direction of travel of the two valve sections, and rebound into the closed position. Because of the time required for closure of the steel valve in the 60-cal gun, there is no detrimental effect of closure on projectile velocity. However, the valves developed

## ACCELERATOR DEVELOPMENT

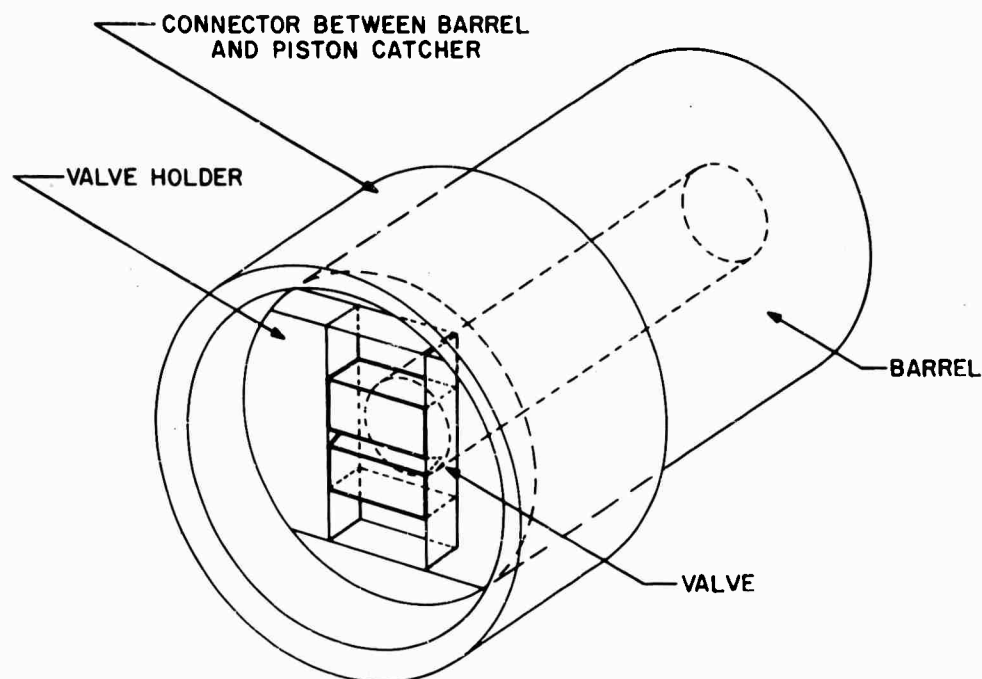


Fig. 28 - Quick Opening Valve  
49 mm-60 Caliber Light-Gas Gun

for the 22- and 30-cal launch tubes are made of aluminum and travel a shorter distance before rebound occurs. Hence, closure occurs prior to the time that the projectile reaches the muzzle. The resultant effect is a reduction in projectile velocity. To prevent closure of the aluminum valve, a small metal cone has been inserted into each end of the valve. These expander-cones wedge into the valve sections upon striking the end of the valve holder. This wedging action expands the valve end into slots in the walls of the holder and prevents rebound. Trapped air, which could have a cushioning effect and defeat the purpose of the device, is removed by a simple venting arrangement. Smaller vent holes may be used to control valve opening rate should this be necessary to limit accelerative forces in delicate projectiles.

## SABOT DESIGN

The design of a sabot which is strong enough to withstand the extremely high acceleration forces of the launch phase and light enough so that the resultant projectile velocity is not drastically decreased is a problem which has plagued the terminal ballistician for years. Various sabot configurations and materials have been tried, with only minimum success. Sabots previously used at NRL were made of cloth-impregnated bakelite and aluminum. These were found to be unsatisfactory for tests involving high projectile density and high velocity. Currently sabots made of lithium-magnesium alloy (approximate density  $1.46 \text{ g/cm}^3$ )

# ACCELERATOR DEVELOPMENT

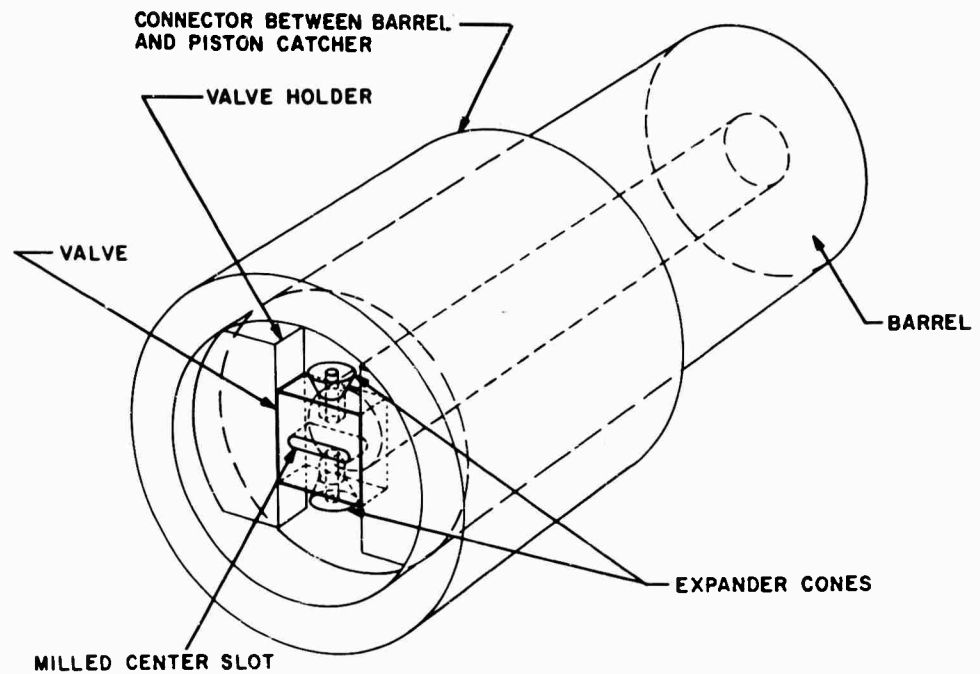


Fig. 29 - Quick Opening Valve  
20 mm Compression Section; 22 Caliber or  
30 Caliber Launch Section

are being used with 3/8-inch-diameter aluminum spheres, mass of 1.25 grams. A diagram of a sabot now being tested is shown in Figure 30. The sabot is split for easier egress of the sphere, and the four holes are included for the same

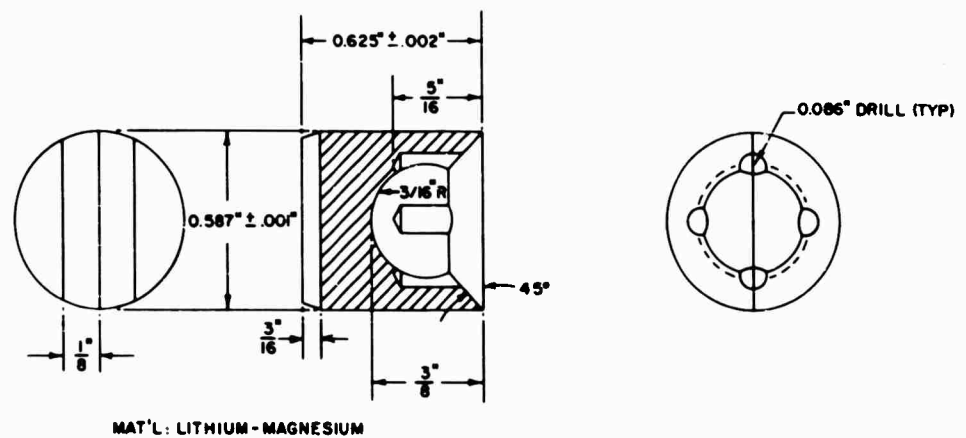


Fig. 30 - Sabot design for projecting 3/8 in. d. spherical metallic projectiles

## ACCELERATOR DEVELOPMENT

reason. With this sabot and a quick-opening valve assembly, a maximum terminal velocity of 6.0 km/sec was attained in a test environment of 10 mm mercury. There was no extraneous damage to the target face after firing. The results from these tests are quite encouraging, not only from the aspect of acquisition of accurate terminal ballistic data but also from the viewpoint that accelerator techniques have developed to the point at which a relatively large mass, 4.10 grams (1.27-gram projectile and 2.83-grain sabot), has attained a velocity of 6 km/sec.

## SUMMATION

Experimental work is continuing to increase mass, size, and velocity capabilities using sabot projectiles for impact research. Use of isometric charts to interpolate Narec results to a new set of design parameters representing a specific gun has resulted in about 95-percent agreement with experimental results. Increased energy storage and distribution capabilities and development of electroballistic techniques will considerably extend the scope of electroballistics work.

## REFERENCES

1. Halperson, S. M., and Fuller, R. H., "Small Particle Impact Studies," NRL Memo. Report 1130, Dec. 1960.
2. Halperson, S. M., and Fuller, R. H., "Sabot Techniques at the NRL Hypervelocity Facility," NRL Memo. Report 1143, Feb. 1961.
3. Swift, H. F., and Porter, C. D., "Hypervelocity Capability and Impact Research," NRL Memo. Report 1135, (1 July-31 Dec. 1960).

INTERIOR BALLISTICS OF HYPERVELOCITY PROJECTORS  
INSTRUMENTED LIGHT GAS GUN AND TRAVELING CHARGE GUN

P. G. Baer and H. C. Smith

Ballistic Research Laboratories  
Aberdeen Proving Ground, Maryland

INTRODUCTION

For the last two years the Interior Ballistics Laboratory has undertaken an investigation into the design of hypervelocity projectors. This paper reports the progress of the Laboratory on two types of hypervelocity projectors; namely, the two stage light gas gun and the traveling charge gun. The investigation has been funded under two Ordnance Projects - (1) Project: TB-3-0116; Task: Supercapacity Launchers, and (2) Project: TB5-22; Task: Supercapacity Ammunition.

Light gas gun design has been investigated under two parallel subtasks:

(1) The development of a mathematical model or models which, when programmed on a digital computer, will predict the performance of any two stage light gas gun regardless of its dimensions.

(2) Experimental verification of the above theoretical computer model. A similar approach has been adopted for the traveling charge gun studies.

The first report on the interior ballistics of light gas guns was presented at the 4th Symposium on Hypervelocity Impact<sup>(1)</sup>. This report presented a background to the interior ballistics of light gas guns. In addition to the background, theoretical computations were presented for single and two stage light gas guns in order that the limitations of these guns might be fully understood. The desirability of confirming theoretical predictions with experimental results was stressed.

The portion of this paper which applies to light gas guns, continues the investigation presented in the first report. However, investigation in this case is limited to the interior ballistics of two stage light gas guns, emphasis being laid on agreement between predicted and experimental results.

A report on the applicability of the traveling charge gun to hypervelocity projection was also presented at the 4th Symposium on Hypervelocity Impact<sup>(2)</sup>. Both experimental and theoretical work was discussed; however, the major emphasis in the traveling charge gun task was in the development of a propellant

## INTERIOR BALLISTICS OF GAS AND CHARGE GUN

which would burn at a certain prescribed rate.

Since the initial traveling charge paper, two BRL Technical Notes have been published on traveling charge gun design <sup>(3)</sup>, <sup>(4)</sup> in which a simple theoretical model of a traveling charge gun has been amplified into a system which can be used to examine the potentialities of any type of traveling gun device.

The portion of this paper, which applies to the traveling charge gun, continues the investigation presented in the first traveling charge gun report. A more complex theoretical model will be discussed and experimental data presented.

### THEORY

A complete discussion of the mathematical models used in simulating the two stage light gas gun and the traveling charge gun on digital computers is outside the scope of this paper. Models for both guns will be briefly described without using mathematical notation; in addition, some of the assumptions used in deriving the equation will be presented. A more complete discussion of the mathematical models used to simulate the two stage light gas gun and the traveling charge gun together with computer flow diagrams will be reserved for subsequent BRL reports.

Four mathematical models simulating the two stage light gas gun have been derived and programmed for the digital computer. These theories are listed according to increasing complexity.

- (1) Charters' method
- (2) Simple Isentropic Compression method
- (3) Richtmyer-Von Neumann "q" method
- (4) Method of Characteristics

The four mathematical models used to simulate the two stage light gas gun have numerous assumptions. In Table I the major assumptions used in these models are listed and compared.

The simplest model which can be used to simulate the two stage light gas gun is the one developed by Dr. Charters of Ames Laboratories. The mathematical equations used in this model have been presented in the first report <sup>(1)</sup>. The method consists of a set of simultaneous equations (not differential equations) which can be solved numerically for any particular light gas gun case.

In the simple isentropic compression method the mathematical equations used to simulate the two stage light gas gun are a set of simultaneous ordinary non-linear differential equations with time as the independent variable. The equations are similar to those described in the first report <sup>(1)</sup> (eq. 9 - 27); however, some revisions have been made in order to more accurately simulate the gun. In order to obtain a solution to a particular two-stage light gas gun problem, these equations have to be integrated numerically from a time corresponding to ignition of the solid-propellant behind the piston to a time corresponding to ejection of the projectile from the barrel of the launcher tube. The results from these

## INTERIOR BALLISTICS OF GAS AND CHARGE GUN

numerical integrations consist of a table in which the variables of interest (pressure, displacement, velocity, etc.) are given for even increments of time.

The equations used in the Richtmyer-VonNeumann "q" method are a set of simultaneous non-linear ordinary differential equations and partial differential equations of the hyperbolic type. The partial differential equations used in this method have been described by Richtmyer<sup>(9)</sup>; these equations have been adapted by the authors so as to simulate the two stage light gas gun. In this method, time and a particle coordinate (or Lagrangian variable) are the independent variables. Numerical integration of these equations gives the variables of interest as a function of time and a mass segment number.

The equations used in the method of characteristics are of the same type as in the Richtmyer-VonNeumann "q" method. However, the independent variables are a pair of "characteristic variables". Numerical integration of these equations gives the variables of interest as a function of the two characteristic variables.

Two mathematical models simulating the traveling charge gun have been developed. In the simpler model it is assumed that:

1. The thrust developed by the burning traveling charge propellant is a constant.
2. The propellant burning rate (and thus the mass loss) is a constant.
3. The frictional forces between the barrel and the projectile are negligible.
4. The barrel ahead of the projectile is evacuated.

The resulting differential equations can be integrated giving three simple simultaneous equations. Numerical solutions are obtained by substitution in the equations.

A more complex model simulating the traveling charge gun has been developed. Originally, this model was based on equations developed by Armour<sup>(5)</sup> for predicting the interior ballistics of gun-fired rockets. It was found, however, that these equations did not completely describe the interior ballistic behavior of a traveling charge gun, so they were revised so as to more nearly correspond to the actual gun.

The events which are simulated by this model are the following:

1. Initially the propelling charge consists of a base charge, composed of granulated solid propellant and an end burning traveling charge, composed of a porous propellant, which is attached to the projectile.
2. Upon ignition, the base propellant starts burning, raising the pressure in the chamber. Hot gases from the burning base propellant flow into porous grain, these gases eventually igniting the grain.
3. As the porous grain burns, gases flow from a region near the end of the grain toward the head of the grain, thus opening up new grain surface area which in turn burns.

## INTERIOR BALLISTICS OF GAS AND CHARGE GUN

4. An inflow-outflow balance is set up across the end of the grain. Inflow occurs as long as the pressure outside the grain is greater than pressure inside the grain. Outflow occurs when pressure inside the grain is greater than the pressure outside the grain.

5. The projectile and the traveling charge grain begin to move when the pressure in the chamber of the gun exceeds the shot start pressure.

6. The above process continues until the grain burns out; then the projectile is driven by the residual gas in the gun.

Some of the assumptions used in the above model are (Fig. 1):

1. The pressure from the breech of the gun to the base of the traveling charge grain is a variable depending upon time only. That is, no pressure gradient exists in the gun.

2. The pores at the rear end of the traveling charge grain can be simulated by an ideal nozzle. The throat area of this nozzle is the cross sectional area of the pores.

3. Gas flow into or out of the traveling charge grain cannot have a velocity greater than sonic.

4. At any instant of time the gas pressure inside the grain is a constant from the rear end of the grain to a moving boundary inside the grain. On one side of this moving boundary the gases are hot and at a high pressure. On the other side of this moving boundary the gases are cool and at atmospheric pressure.

5. The velocity of this moving boundary is given by the pressure difference across the boundary.

6. The traveling charge propellant is assumed to consist of fibers of a known diameter oriented so that the axis of the fibers are parallel to the axis of the traveling charge grain. As the moving gas boundary moves into the grain the surface area of the fibers exposed is the surface area of the propellant burning in the grain. When the moving boundary reaches the end of the grain all of the fiber surface area is exposed. The fibers continue to burn until all the traveling charge propellant is burned out.

Mathematically, these assumptions consist of a series of ordinary differential equations which are integrated numerically using the method of Runge-Kutta-Gill. The results of this numerical integration, consisting of a table in the values of the variables of interest (gun chamber pressure, traveling charge grain pressure, velocity, etc.) are listed for even increments of time.

## EXPERIMENTAL - LIGHT GAS GUN

In the initial phase of this project, since the Interior Ballistics Laboratory did not have a two stage light gas gun, it was decided to verify theoretical predictions with experimental results from two stage light gas guns possessed by other

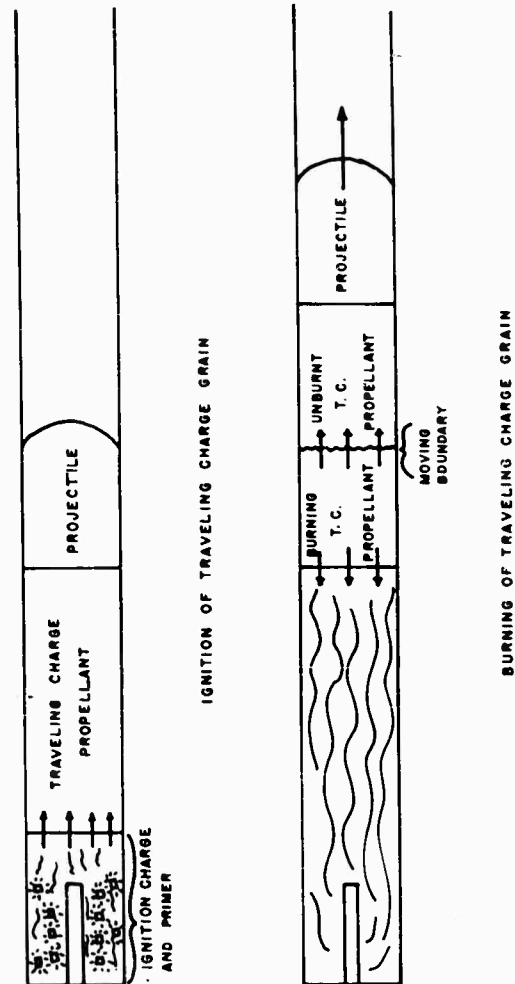


Figure 1  
Theoretical Model of Traveling Charge Gun

## INTERIOR BALLISTICS OF GAS AND CHARGE GUN

laboratories in BRL and other defense agencies. The data obtained this way was extremely varied, generally consisting of projectile muzzle velocity and initial conditions in the gun. For one two stage light gas gun possessed by Weapon Systems Laboratory we were fortunate to obtain helium pressure-time records and muzzle velocity. This gas gun has a 57mm pump tube 15 feet long and a .59 cal launch tube 6 feet long. The gun used an 18 lb piston and normally fired a 240 grain projectile. Helium pressures were measured at the head end of the pump tube. The transducer used to measure the helium pressures consisted of a column whose deformation by the gas pressure was measured by resistance strain patches. Projectile velocities were measured in air outside the launcher tube by paper break screens.

In none of the light gas installations inspected by the author was any attempt made to measure simultaneously the piston position, projectile position, propellant gas pressure, and helium gas pressure. Since this data was needed for the complete verification of the light gas gun theories, it was decided to build a small light gas gun in which all of the above variables could be measured simultaneously.

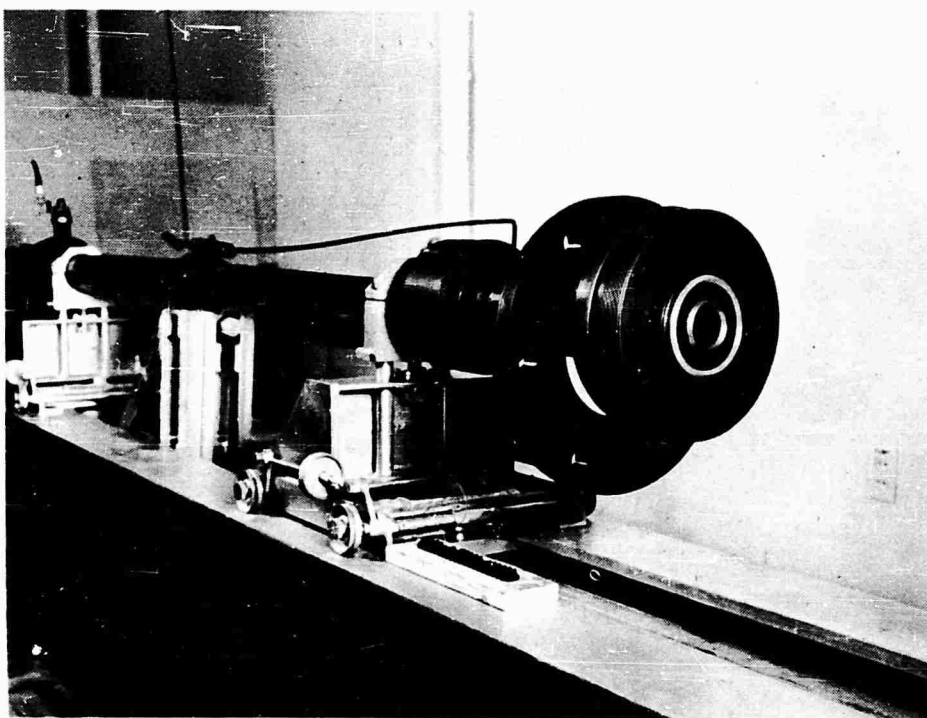


Figure 2  
IBL Light Gas Gun  
Pump Tube With Attached High Pressure Section

## INTERIOR BALLISTICS OF GAS AND CHARGE GUN

Initially, the instrumented two stage light gas gun was to be built as cheaply as possible from existing hardware, the objective for the initial experiments being to check out the instrumentation. No attempt was made in the design of this gun to attain velocities in excess of 20,000 f/s, it being felt that design data obtained from the lower velocity gun could be used to design a gun which would launch projectiles at velocities in excess of 20,000 ft/sec.

The gun as finally designed is expected to launch a 5 gram projectile at velocities ranging from 10,000 ft/sec to 15,000 ft/sec. The pump tube for this gun consists of a 1.5 inch I.D. smooth bored 37mm gun and a high pressure section attached to the muzzle end of the gun giving an overall pump tube length of 6 feet 5 inches. Pump tube with attached high pressure section is shown in Figure 2.

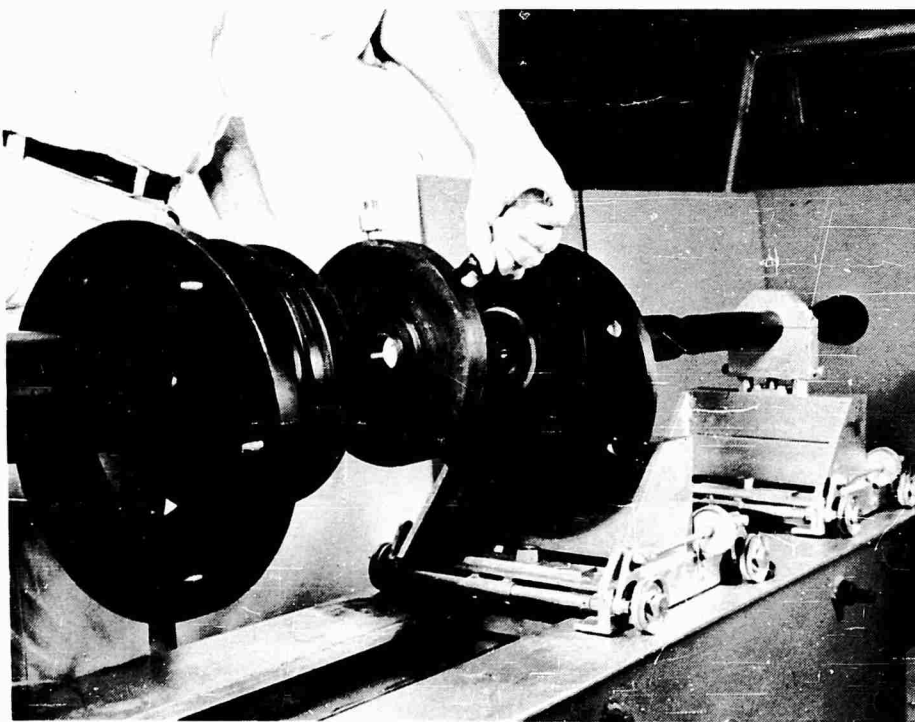


Figure 3  
IBL Light Gas Gun  
Inserting Gauge Ring in High Pressure Section

The launch tube is a .50 cal smooth bore Mann barrel 47 inches long. The muzzle end has a vacuum adapter so that the tube may be evacuated. A thin nylon plastic disc is used in the vacuum adapter to seal off the bore. Between the high pressure section and the launch tube is placed a gauge ring containing the tourmaline piezo gauge used to measure helium pressures at the chamber end. Figure 3 shows the gauge ring, with an inserted tourmaline piezo gauge in place between the

## INTERIOR BALLISTICS OF GAS AND CHARGE GUN

launcher tube and the high pressure section of the pump tube. In Figure 4 is shown the assembled high pressure sections. The high pressure section is held together by two flanges connected by 6 special bolts. Since only about two inches of the high pressure section need withstand pressures over 50,000 psi, the section was made in two diameters. The maximum diameter portion (9-1/2" O.D.) was designed to withstand a pressure up to 200,000 psi, and the minimum diameter portion (4" O.D.), a pressure of about 50,000 psi. There were two reasons for this design: (1) the high pressure section was made lighter and (2) it was necessary to have a minimum thickness of steel between the radioactive source held on the base of the piston and the scintillation counters used to detect the position of the source. The entire light gas gun is mounted on 4-wheeled carriages. These carriages can be clamped to the double I-beam track when it is desired to fire the gun or they can be unclamped and moved when it is desired to take the gun apart.

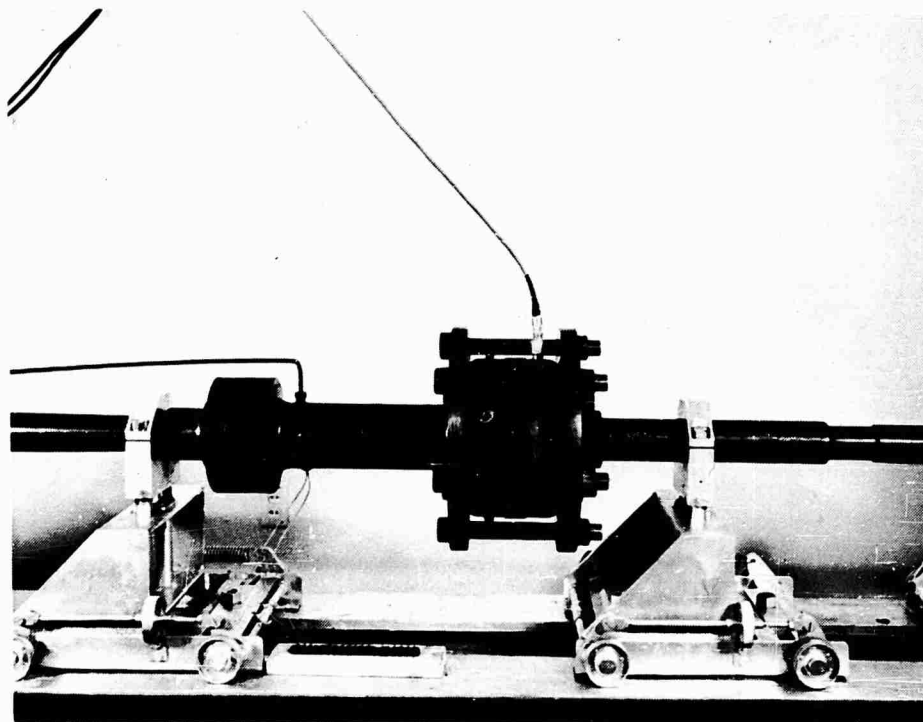


Figure 4  
IBL Light Gas Gun  
Assembled High Pressure Section

It is important in locating the position of the piston by means of the scintillation counters that recoil of the gun be held to a minimum. To prevent this recoil an angle iron support was clamped to the middle portion of the pump tube and to the ends of the I-beam supports. In firings, using a recoil meter to measure displacement, gun recoil was held to less than 1/4 inch displacement. This supporting brace is shown under the pump tube in Figure 2.

## INTERIOR BALLISTICS OF GAS AND CHARGE GUN



Figure 5  
IBL Light Gas Gun  
Piston Assembly and Projectiles

The piston used in the pump tube is a right circular cylinder  $4\frac{3}{4}$  inches long and weighs about 2 pounds. In Figure 5 is shown an assembled piston. The piston consists of a steel cylinder with O-Ring grooves, a copper cup at the base of the piston to prevent propellant gases from leaking around the piston, a nylon disc at its head end to take the shock of impact of the piston with the nozzle on the launcher tube, and a hollow nut threaded into the base of the piston, acting as a holder for the radioactive source.

To obtain interior ballistic information from the light gas gun the following instruments are used:

- (1) Quartz crystal piezo pressure gauge - used to measure the propellant gas pressure in the pump tube.
- (2) Tourmaline crystal piezo pressure gauge - used to measure helium pressure at the head end of the pump tube.
- (3) Eight scintillation counters - used to detect the radioactive source in the base of the piston during the last two feet of travel.

## INTERIOR BALLISTICS OF GAS AND CHARGE GUN

(4) Microwave interferometer - used to measure projectile displacement in the launcher tube.

The quartz crystal piezo gauge is of a type used at the Ballistic Research Laboratories for the measurement of transient gun chamber pressure for a period of about 20 years. When properly used the gauge has given quite reliable results.

The tourmaline crystal gauge is a special type developed by Atlantic Research Corporation to measure transient pressures up to about 100,000 psi. In operation the tourmaline crystal is suspended in a chamber surrounded by a plastic material. Gas pressure upon the plastic material is transmitted hydrostatically to the crystal which produces an electrical signal upon being compressed. In previous light gas gun investigations this gauge was found capable of responding to high pressure shocks with very little ringing. The signal from both piezo gauges is sent to a multi-channel recorder thus recording propellant gas pressure and helium pressure as a function of time.

The scintillation counters used to track a radioactive source held in the base of the piston have been described previously (6), as they were used in a program to track solid propellant grains in a 37mm gun. Briefly, the tracking system consists of a 90 millicurie Cobalt 60 source held in the base of the moving piston and eight scintillation counters placed along a two-foot length of the high pressure section. A scintillation counter consists of a container of plastiflour resin. The gamma particles from the radioactive source strike the resin, flashes of light are emitted. These flashes are detected by two RCA Photo-multiplier tubes, which generate an electrical pulse for each flash. The pulses are electrically integrated within the counter, giving a voltage signal which is proportional to the count rate. Thus the voltage is highest when the source is directly opposite to the counter. These voltage signals are sent to a multi-channel recorder and recorded as a function of time. Figure 6 shows the scintillation counters placed along the high pressure section of the pump tube. The counters and lead blocks separating them (the blocks being used as radiation slits) are supported by a portable A-frame, which may be placed at any position along the gun tube.

It is important, in using the scintillation counters, that the gun system does not recoil to any appreciable extent, since the piston position will be in error by the amount of recoil. To measure this recoil, a linear differential transformer (Shavitz Corporation) was used to measure displacement of the pump tube barrel. This unit is capable of measuring displacements as small as .001 inch. The voltage signal from the displacement meter is fed to a multi-channel recorder, giving tube displacement as a function of time.

A microwave interferometer is used to measure position of the projectile in the launcher tube as a function of time. This system has been described in detail elsewhere (7) and only a brief description will be given here. The principle on which it works is the same as that for an optical interferometer. A radar signal from a klystron is propagated through a hybrid junction into two branches of a wave guide. The signal along one branch is directed to the muzzle by means of a horn and reflector, propagates along the bore of the barrel to the projectile face. The signal propagated along the other branch is directed to a fixed wave guide short. The reflected signals from both branches return to a junction and thence to a crystal detector. The output of the crystal is a constant D. C. voltage if the projectile is

## INTERIOR BALLISTICS OF GAS AND CHARGE GUN

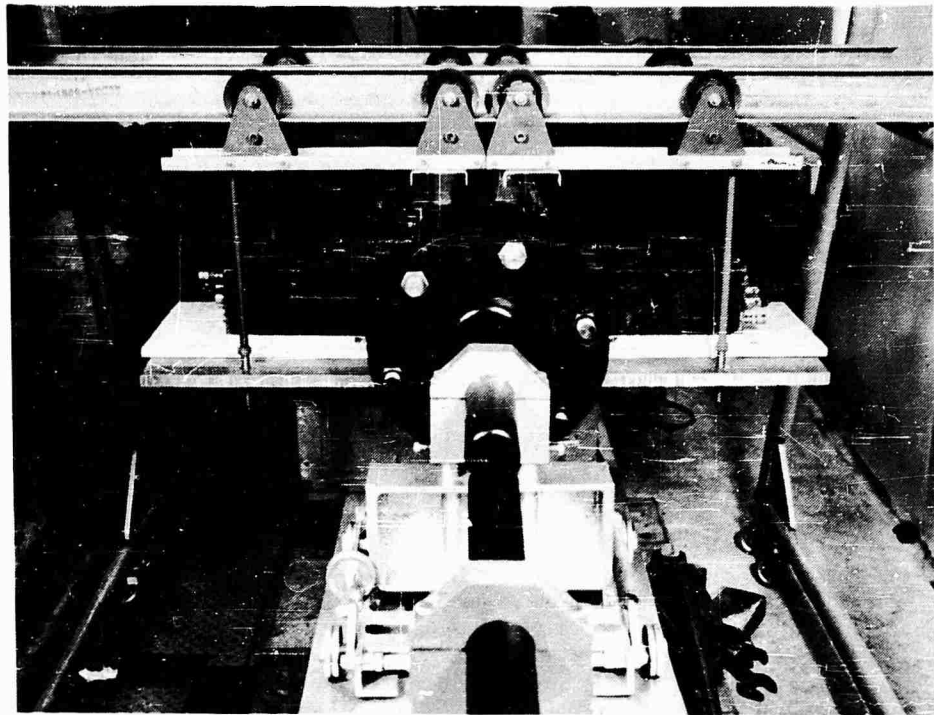


Figure 6  
IBL Light Gas Gun  
Scintillation Counters Along Pump Tube

motionless; however, if the piston moves, the crystal voltage changes in amplitude as a nearly sinusoidal wave, which goes from maximum to minimum for each quarter wave length change in projectile position. After being amplified, this wave is sent to an oscilloscope and is recorded either on a General Radio Camera or a rotating mirror camera.

Initial firings of the light gas gun have been, and will be, made without the launcher tube attached, using the interferometer to track the piston in the pump tube. The purpose of these firings is two-fold: namely, to compare the predicted initial motion of the piston with experimental results (the influence of helium pressure in piston position being small for initial motion of the piston) and to compare the position of the radioactive source from scintillation counter readings and interferometer readings. For these piston firings only three measurements are taken: propellant gas pressure-time, piston position as measured by the microwave interferometer, and piston position as measured by the scintillation counters.

Subsequent firings are made with the assembled light gas gun using all of the instrumentation.

## INTERIOR BALLISTICS OF GAS AND CHARGE GUN

### EXPERIMENTAL - TRAVELING CHARGE GUN

The initial experimental work on the traveling charge gun project was with a small (.625 cal) thrust stand used to evaluate possible propellants. This thrust stand has been adequately described in the 4th Symposium Report<sup>(2)</sup> and will not be described here.

Experimental work using this stand was terminated when it was discovered that opening of the rupture disc set up a shock wave in the gas column. This shock wave fractured the propellant causing erratic burning rates. Significant results from thrust stand firings are given in the results section of this report.

Subsequent firings on the traveling charge project have been made with the .625 cal traveling charge gun. The gun was initially designed by Vest for the traveling charge gun program in 1950 and is described in a report issued in 1951<sup>(8)</sup>. This gun has been somewhat modified for the purpose of the present program. The gun has a chamber with an internal diameter of .625 inches and a length of 7 inches. Ignition of the igniter propellant is accomplished by using an electric squib, the leads of which are brought into the chamber by means of an insulated firing pin. The projectile with the attached traveling charge is held in the forward end of the chamber by means of a brass rupture disc (.015 inch thick). The propellant arrangement used in the chamber of the gun is shown in Figure 7. Placing of the traveling charge propellant in the breech is shown in Figure 8. The length of the barrel is 9 feet (173 calibers). Attached to the muzzle of the gun is an adapter by which the barrel may be evacuated for high velocity firings. In this adapter a thin disc of nylon is used to seal out the atmosphere. In Figure 9 is shown an overall view of the gun.

The present objective in the traveling charge gun program is to operate the gun at high velocities (8,000 - 12,000 ft/sec) and determine if the porous propellant used as a traveling charge will burn in a reproducible manner. Consequently the instrumentation is quite simple and consists of a quartz piezo gauge to measure chamber pressure-time, and three printed circuit break screens. The chamber with the attached quartz gauge is shown in Figure 8 and the three screens are shown in Figure 10. A plywood shield with a hole cut in it is used in front of the first screen to prevent propellant fragments from rupturing the screen prematurely. The screens are connected to a 1 MC Potter Chronograph which measures the elapsed time between the breaking of the screens. Muzzle velocities are obtained by extrapolating the screen velocities back to the muzzle of the gun.

The traveling charge projectile for this gun consists of a duraluminum right circular cylinder to which is cemented a cylinder of felted nitrocellulose. The grain of nitrocellulose is inhibited on the outside by a layer of spray enamel and two layers of Teflon tape. The Teflon tape, besides acting as an inhibitor, fills the gap between the sub caliber felted nitrocellulose grain and the bore of the gun. An assembled traveling charge projectile is shown in Figure 7.

### RESULTS - LIGHT GAS GUN

In this section of the paper we will attempt to compare theoretical predictions with each other and with experimental results, where such results are

INTERIOR BALLISTICS OF GAS AND CHARGE GUN



Figure 7  
Traveling Charge Gun  
Scintillation Counters Along Pump Tube

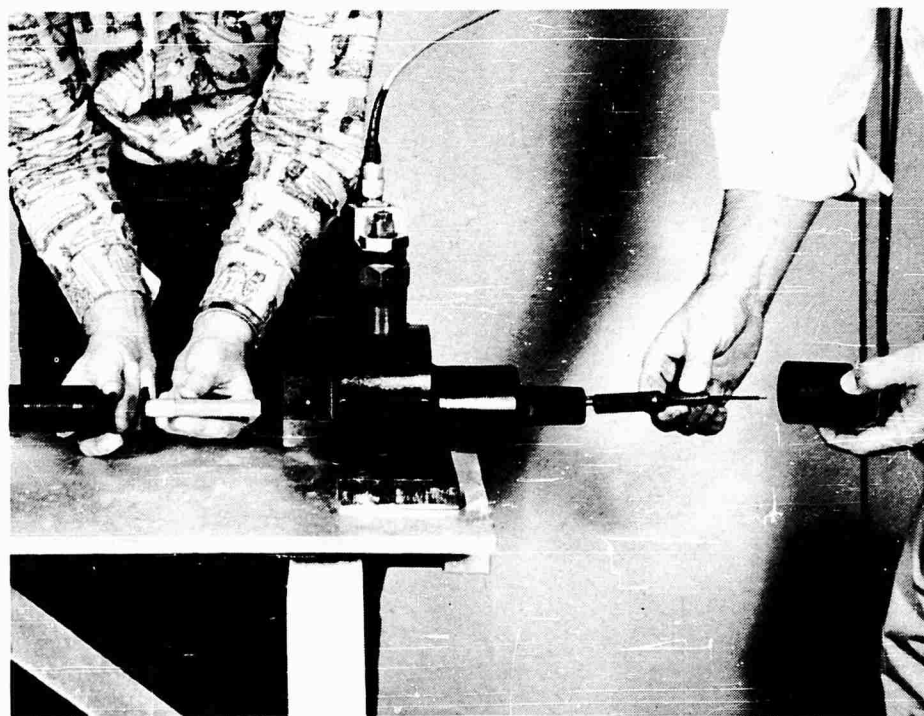


Figure 8  
Traveling Charge Gun  
Placing of Propellant in Gun Breech

## INTERIOR BALLISTICS OF GAS AND CHARGE GUN

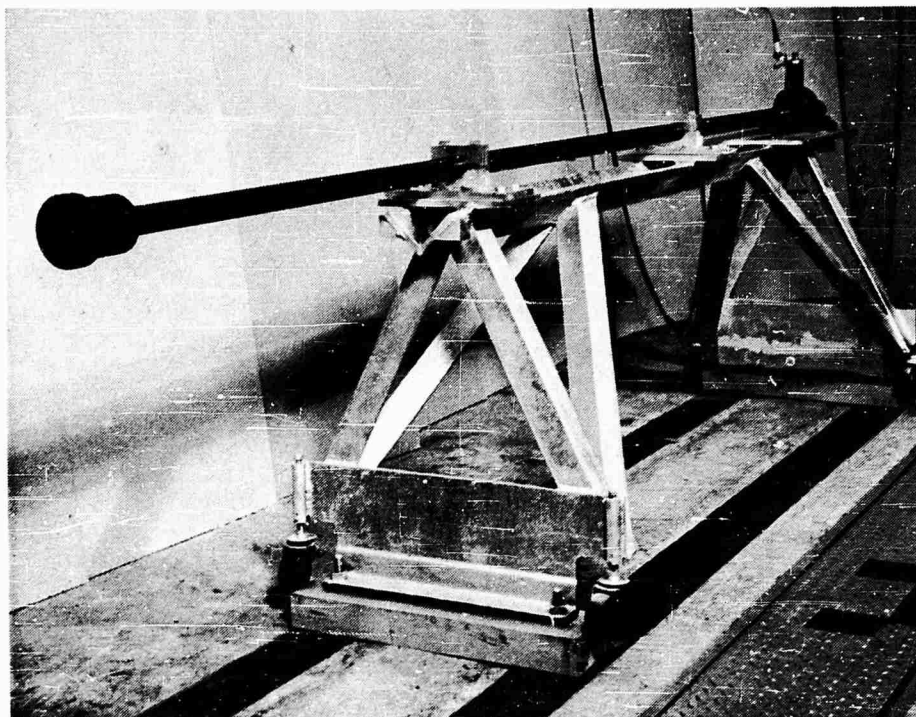


Figure 9  
Traveling Charge Gun  
Overall View

available. These comparisons are not complete, but merely serve to illustrate the methods used.

The first prediction method and the easiest to use is Charters' Method for a two-stage light gas gun.

Because of the assumptions used in the method, predictions are limited to guns with heavy pistons, that is, the velocity of the piston is always subsonic with respect to the sound velocity of the light gas being compressed ahead of it. In addition, there must be sufficient light gas left in the chamber of the gun so that the chamber appears to be of infinite size to the projectile (e. g. , a rarefaction wave does not catch up with the projectile).

The Charters' method is useful in the initial design of a light gas gun and it was so used in the case of the 37mm - .50 cal light gas gun. While the method is easy enough to do by hand on the desk calculator, it was felt that it would be easier to survey a large number of cases by setting up the equations on the high speed digital computer, so the method was programmed on the ORDVAC. Input data to the problem consisted of:

## INTERIOR BALLISTICS OF GAS AND CHARGE GUN

1. Length and caliber of launcher tube
2. Weight of projectile
3. Thermodynamic constants of light gas
4. Caliber of pump tube
5. Maximum pressure and pressure increment
6. Maximum temperature and temperature increment
7. Minimum distance between piston face and end of pump tube (buffer zone)

The question was asked of the program that, given launcher tube characteristics, pump tube caliber, projectile weight, and a range of light gas temperatures and pressures, what would be projectile velocities obtained, and what would be the initial light gas pressure, piston weight, and pump tube length necessary to attain these velocities.

The chart shown in Figure 11 is a summary of the results of these computations for the 37mm-.50 cal light gas gun. Maximum helium pressure is shown in the range from 100,000 psi to 400,000 psi, maximum helium temperature, in the range from 2000 to 2500°K. The results are given in terms of pump tube lengths ranging from 5.5 to 7.0 feet; piston weights from 1.9 to 2.5 pounds; and muzzle velocities from 14,000 to 15,500 ft/sec. A compromise had to be made between muzzle velocity and pump tube length, so a muzzle velocity of 15,000 ft/sec and a pump tube length of 7.0 feet was chosen. This gives a maximum helium pressure of 120,000 psi and a piston weight of about 2.0 pounds. These values were reasonable for a first design of the 37mm-.50 cal light gas gun.

A study has been made on the agreement between experimental firings of a heavy free-piston light gas gun (57mm-.50 cal) fired by Weapons System Laboratory and Charter's Method predictions. Figure 12 shows the agreement between predictions and experimental results. This study indicates that, for this gun, predictions using Charter's equation give optimistic muzzle velocities for helium chamber pressures less than 95,000 psi and pessimistic muzzle velocities for helium chamber pressures in excess of 95,000 psi. However, further study will have to be made of the agreement between prediction using Charter's Method and experimental results with closer control of the experimental conditions so that they conform in part to the assumptions used in the theory.

A prediction method possessing greater design usefulness is that of the simple isentropic compression method to determine the performance of the light gas gun. In the design of the 37mm-.50 cal gun this method was used to predict piston displacement-time data, which in turn were used to determine the position of the scintillation counters for tracking the piston. The data was also used for the design of the high pressure section of the pump tube, since it was desired that portions of the high pressure section be as thin as possible in order that the maximum amount of radiation from the source reach the scintillation counters.

Results from this prediction method have been compared with experimental firings using Weapons System Laboratory's 57mm-.50 cal light gas gun. In Figure 13 this comparison is illustrated. As can be seen, agreement between measured and predicted helium pressures is very good. Slight oscillation in the measured pressure-time trace is believed to be due to weak shocks moving in the gas column between the face of the piston and the rear of the projectile. It will be noticed that

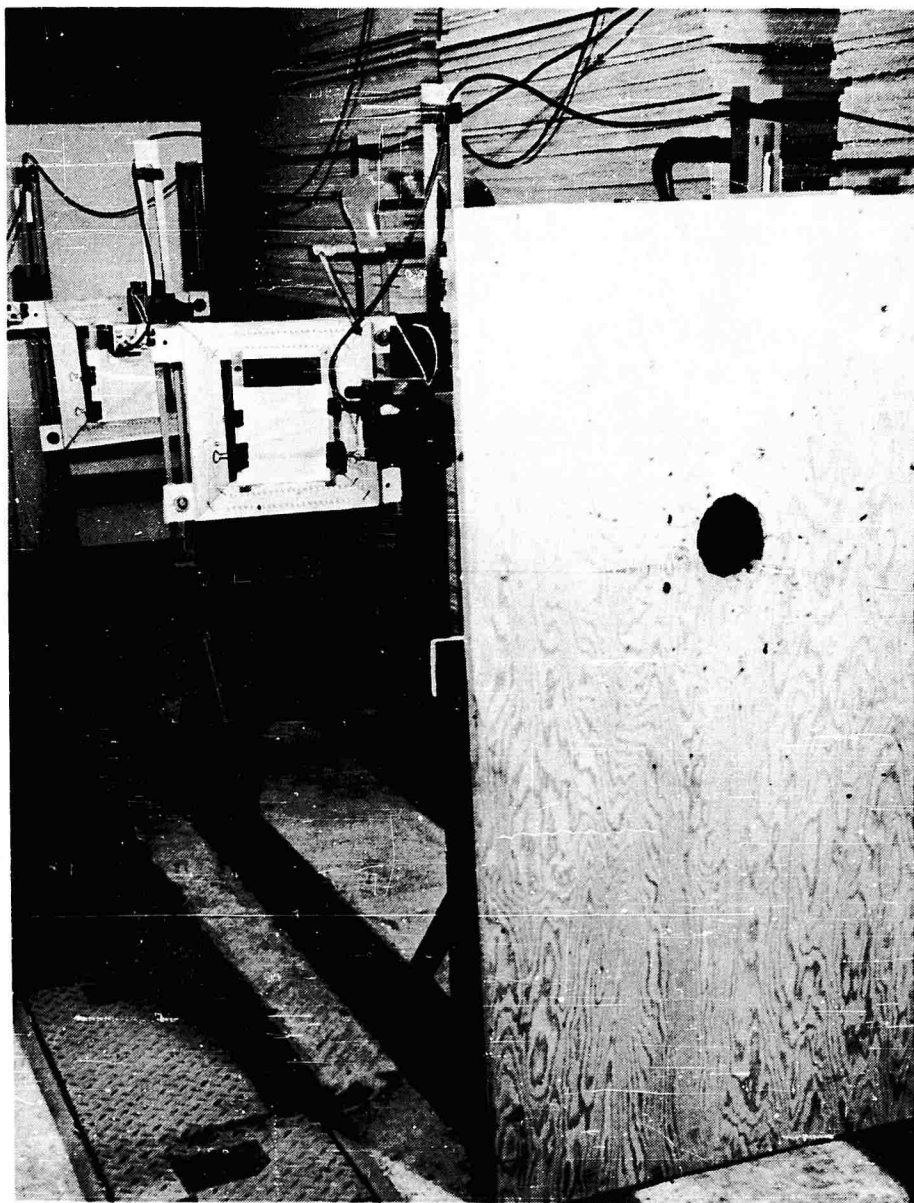


Figure 10  
Printed Circuit Break Velocity Screens

# INTERIOR BALLISTICS OF GAS AND CHARGE GUN

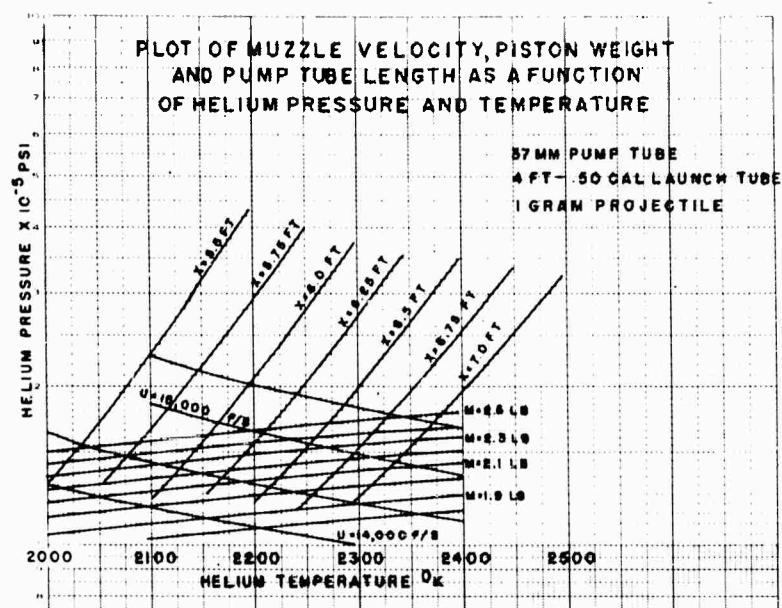


Figure 11  
Plot of Muzzle Velocity

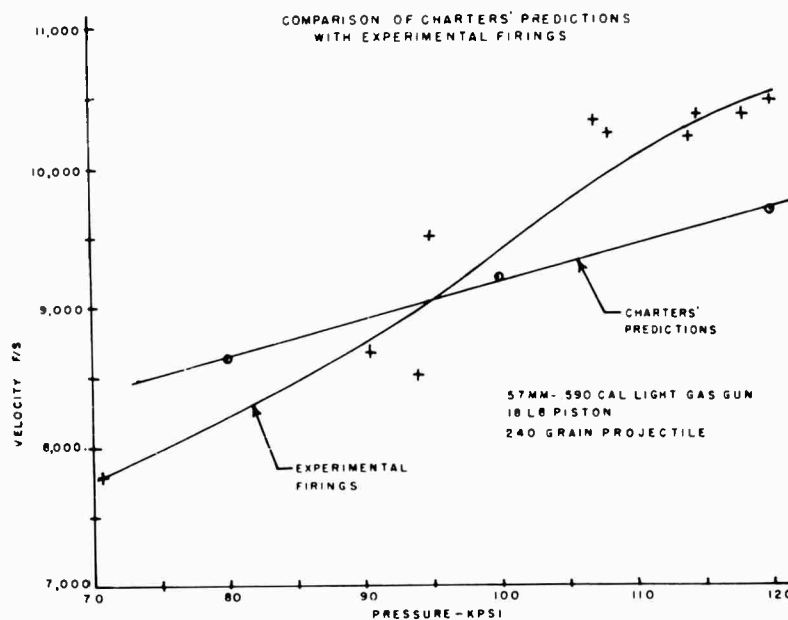


Figure 12

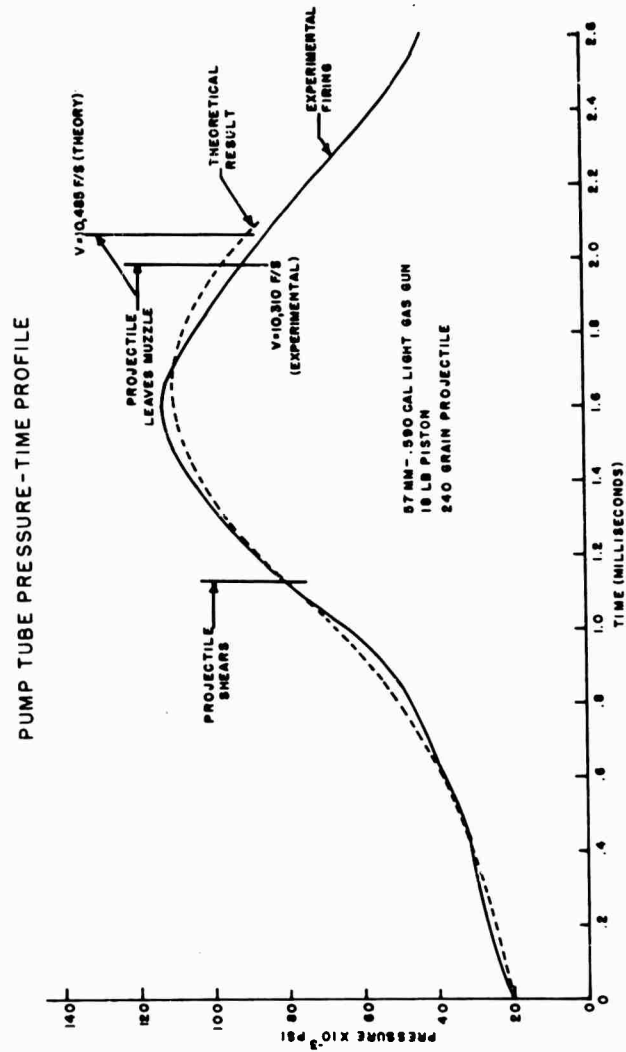


Figure 13

# INTERIOR BALLISTICS OF GAS AND CHARGE GUN

TABLE I  
ASSUMPTIONS USED IN LIGHT GAS GUN PREDICTION METHODS

	CLAUDET'S METHOD	SIMPLE ISENTROPIC COMPRESSION METHOD	REYNOLDS-VON KERNAN "q" METHOD	METHOD OF CHARACTERISTICS
Light Gas Thermodynamics	Ideal gas Constant specific heat	Ideal gas Constant specific heat (Can use real gas equation of state)	Ideal gas Constant specific heat (Can use real gas equation of state)	Ideal gas Constant specific heat (Can use real gas equation of state)
Frictional Loss Projectile and Launcher Bore	Assumed negligible	Considered as a function varying with projectile travel	Considered as a function varying with projectile travel	(Unable to consider launcher conditions)
Frictional Loss Piston and Pump Tube	Assumed negligible	Considered as a function varying with piston travel	Considered as a function varying with piston travel	Considered as a function varying with piston velocity
Frictional Loss Gas and Pump Tube Gas and Launcher Tube	Assumed negligible	Assumed negligible	Assumed negligible	Assumed negligible
Gas Ahead of Projectile?	No Evacuated bore	No Evacuated bore	No Evacuated bore	(Unable to consider launcher conditions)
Gas Flow in Bore	Subsonic and sonic flow in bore	Subsonic and sonic flow in bore	Subsonic to supersonic flow in bore	(Unable to consider launcher conditions)
Gas Flow in Pump Tube	No flow Isentropic compression of gas	Some arbitrary fraction of piston velocity	Sonic or supersonic flow with shock waves	Sonic or supersonic flow with shock waves
Gas Flow in Launcher Tube	Reflection caused by initial motion of projectile and reflected off piston face does not catch up with projectile	Some arbitrary fraction of projectile velocity (used also as empirical function)	Sonic or supersonic flow with shock waves	(Unable to consider launcher conditions)
Heat Losses from Gas to Pump Tube or Launcher Tube Walls	Assumed negligible	Assumed negligible	Assumed negligible (Can be considered in equations)	Assumed negligible (Can be considered in equations, but with difficulty)
Propellant Driver Gas for Piston	Propellant burnout occurs before piston starts to move. Isentropic expansion of propellant gas as piston moves	Propellant burnout occurs before piston starts to move. Gas Interior to Ballistic Equations used.	Propellant burnout occurs before piston starts to move. Gas Interior to Ballistic Equations used.	Propellant burnout occurs after piston starts to move. Gas Interior Ballistic Equations used.

## INTERIOR BALLISTICS OF GAS AND CHARGE GUN

agreement between measured and predicted muzzle velocity is also quite good. The nearly smooth rise in helium pressure indicates that the piston in the 57mm pump tube is moving at a velocity which is either subsonic with respect to the helium ahead of it, or slightly supersonic, such that any shock waves generated are quite weak. Since the prediction method assumed no shock wave formation or pressure gradients in the gas column up to start of motion of the projectile, and the gun acts in a similar manner, it would be expected that there would be fair agreement between prediction and experiment. This agreement has been observed not only in the case illustrated but in others of the same type. This type of gun is called the heavy piston gun, which can be defined as a gun in which the piston always moves at a velocity which is subsonic to the gas being compressed ahead of it. The opposite type of gun is the light piston gun in which the piston for an appreciable portion of its travel moves at a velocity which is supersonic to the gas ahead of it. Shock waves of greater or less intensity are formed in the light gas. Attempts to obtain agreement between data from the prediction method utilizing ordinary differential equations and experimental data from the light piston type of light gas gun have been difficult if not impossible. Thus this prediction method should not be used for guns of this type.

The method of characteristics as applied to light gas gun problems has been programmed for the ORDVAC digital computer. Programming this method on to a digital computer proved to be a very complex process, which ultimately was completed only for the compression cycle of the two-stage light gas gun. Memory limitations in the ORDVAC (maximum word capacity-4096 words) prevented the programming of the launch cycle on to the machine. Another limitation of the program was discovered in that the shock wave had to form in the light gas before a sound wave from initial motion of the piston reflected off the base of the projectile, which meant that cases for which the initial piston velocity was appreciably subsonic could not be solved using this method. Changes in the programming logic to take care of such cases would have exceeded the memory capacity of the machine.

In Figure 14 a theoretical prediction is illustrated using the method of characteristics. The gun used as an example is a 20mm-.50 cal light gas gun, dimensions of which correspond to a gun fired by the personnel at the Naval Research Laboratory. Because of the initiation of shock limitations in the characteristics program, the release pressure of the piston had to be increased to 130,000 psi. The solid lines in the figure are the piston, incident, and reflected shock paths as computed by the characteristics program. Experimental confirmation of these theoretical results would require the installation of pressure transducers at intervals along the length of the pump tube. As yet this has not been done, nor is this data available from other sources.

Because of the digital computer memory limitations, work on this programming approach had to be abandoned. This program is now being used to compare its predictions with predictions from the Richtmyer-Von Neumann "q" method.

The most promising approach used by this laboratory to date is that of the Richtmyer-Von Neumann "q" method. In this method the light gas region between the face of the piston and the base of the projectile is divided into 50 mass elements. In the computer calculations, the position, pressure, velocity,

## INTERIOR BALLISTICS OF GAS AND CHARGE GUNS

energy, and volume of these mass segments are computed for each time step as the piston is pushed by the propellant gas into the light gas. When the pressure of the mass segment next to the base of the projectile increases above a predetermined level, the projectile starts to move. The problem is terminated when the projectile leaves the bore of the gun. This method has been programmed in a code which can be used interchangeably on both the ORDVAC and BRLESC digital computers; however, all of the completed light gas gun prediction runs have been made on the BRLESC computer. The program as coded on to the BRLESC is quite small (1220 words) but because of numerical stability considerations a problem requires a very large number of computations in order to run to completion. A problem which takes about 5 minutes on BRLESC would run for 30 hours on ORDVAC.

At the present time, very few computer runs have been made using this problem. It is of interest to compare the results from this program with that of the characteristics program mentioned previously. In Figure 14 is shown such a comparison. The solid lines represent piston and shock paths as determined by the characteristics method for the compressor portion of the 20mm-.30 cal light gas gun. The dotted lines represent piston and shock paths as computed for the same conditions using the Richtmyer-Von Neumann "q" method. It can be noticed that while there are differences in position of the shock path, both paths are nearly parallel, indicating that shock velocities are nearly the same. Differences in piston paths are attributed to different methods used in computing the coefficient of frictional resistance between the piston and the bore of the compressor tube.

The few results obtained from the computer to date have not allowed us to make any comparison between predicted and experimental results.

### RESULTS - TRAVELING CHARGE GUN

Theoretical results for the constant pressure traveling charge gun have been presented in two BRL technical notes<sup>(3), (4)</sup> and these results will not be repeated here. The results obtained, however, indicate that traveling charge guns used to obtain hypervelocities will be quite long; lengths ranging from 50 to 1000 feet would not be uncommon.

The more complex mathematical model of the traveling charge gun has been programmed on to the ORDVAC computer. Figure 15 portrays the results obtained for a typical computer run. Presented are the pressures in the chamber of the gun and the pressure in the traveling charge grain. An initial pressure rise is given to the traveling charge projectile by the burning of an igniter charge in the chamber of the gun. This igniter gas pressurizes the traveling charge grain, ultimately causing the pressure inside the grain to rise. For a period of time the pressure in the gun chamber is greater than the pressure inside the traveling charge grain. This is called the inflow period. Ultimately, the pressure inside the traveling charge grain exceeds the chamber pressure and gases flow out of the traveling charge grain. This is called the outflow period. This outflow period continues until the traveling charge burns out. For the theoretical case presented here 99.8 grains of traveling charge propellant accelerated a 5-grain projectile to a velocity of 17,150 ft/sec in 60 feet of travel. Unlike comparable light gas guns, the maximum pressure experienced was about 60,000 psi.

# INTERIOR BALLISTICS OF GAS AND CHARGE GUN

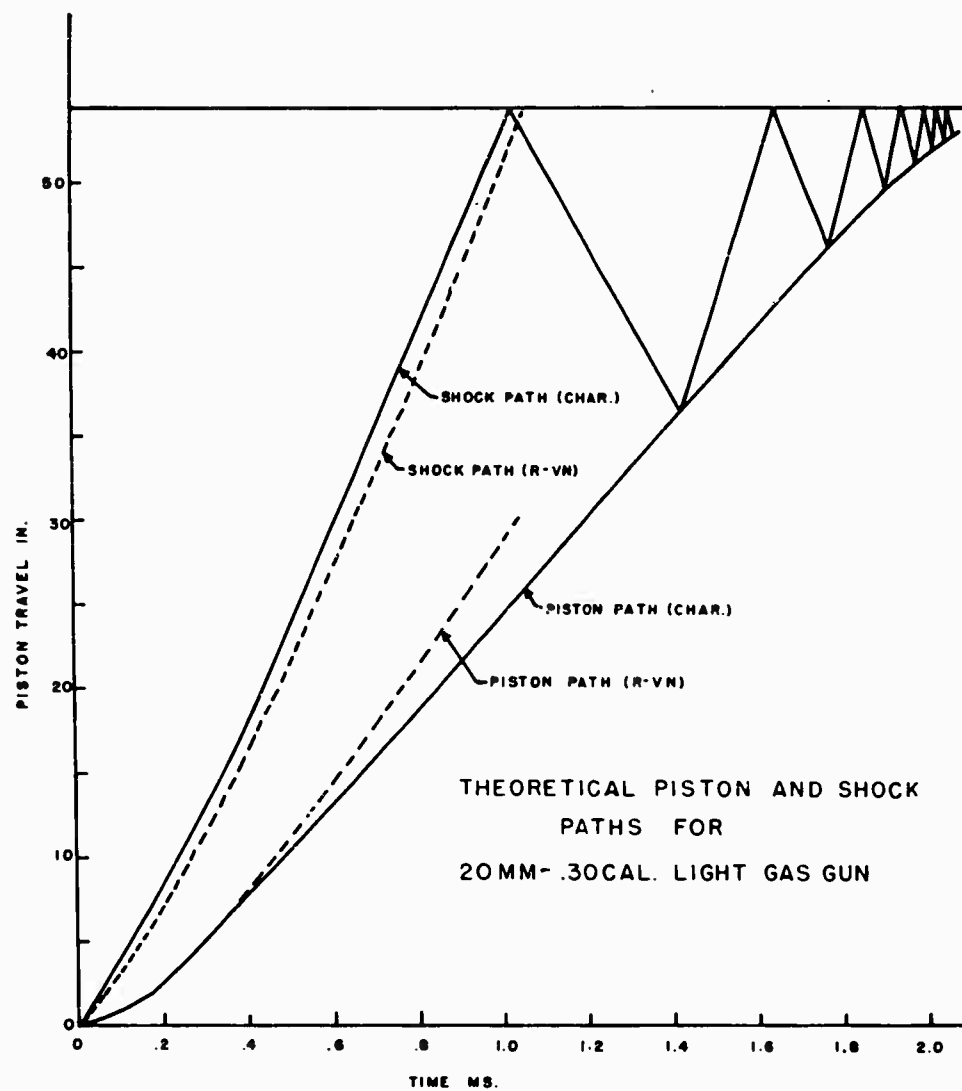


Figure 14

INTERIOR BALLISTICS OF GAS AND CHARGE GUN

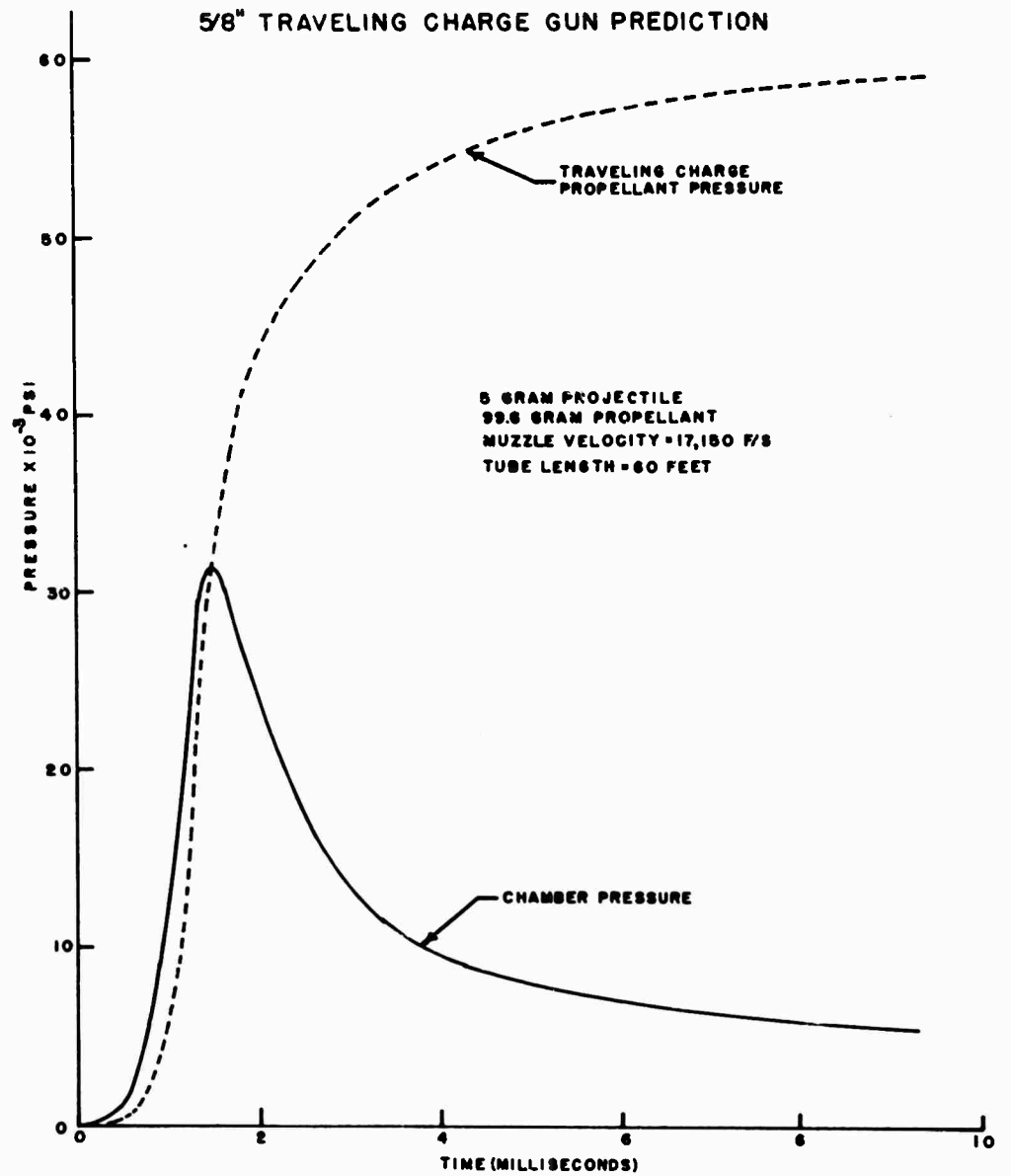


Figure 15

## INTERIOR BALLISTICS OF GAS AND CHARGE GUN

At the present time only a very limited number of firings have been made in the .625 cal traveling charge gun, so it is too early in the program to make any comparison between traveling charge gun theory and experimental results.

As mentioned previously, the thrust stand firings were made as part of an effort to evaluate possible propellants for the traveling charge gun. Among the propellants tested in the thrust stand were:

1. Armour combustible cartridge case material containing cotton liners and ammonium perchlorate
2. Cast rocket propellant
3. Cast propellant with voids provided by microballoons
4. Cemented ball powder propellant
5. Felted nitrocellulose propellant

Of the five propellants tested, the felted nitrocellulose propellant showed the most promise in firing tests on the thrust stand. In a series of tests, grains of felted nitrocellulose with densities ranging from 0.86 to 1.09 gm/cc were fired in the thrust stand. Grains whose densities were less than 0.93 gm/cc exhibited uncontrolled burning rates of 10,000 in/sec or greater at a pressure range of 30,000 to 50,000 psi. Table II gives specific impulse and overall burning rates for grains where densities range from 0.93 to 1.09 gm/cc. It will be noticed that the burning rate of the propellant decreases as the density increases and that in general the specific impulse of the propellant increases as the density increases.

TABLE II

Density gm/cc	Length in	Isp sec	Burning Rate in/sec
0.93	2.94	80	8400
0.94	3.375	110	8440
1.03	2.5	73	4200
1.06	3.25	135	4330
1.09	1.75	171	4375

### DISCUSSION

As was mentioned previously in both papers presented at the 4th Symposium in Hypervelocity Impact, we are limited in the advancement of both programs by the lack of adequate experimental data. Work with the heavily instrumented 37mm - .50 cal light gas gun is expected to provide some data which can be used to verify the highly developed theories concerning the light gas gun. In addition, other investigators are beginning to instrument their guns, so we can expect in the future to see greater effort being expended in developing a sounder design for these guns.

## INTERIOR BALLISTICS OF GAS AND CHARGE GUN

Currently, light gas gun work in the Interior Ballistics Laboratory will consist of using the predictions supplied by the Richtmyer-Von Neumann "q" method to guide experimental work on the instrumented light gas gun. Concurrently the theoretical method will be used to design a 37mm - .50 cal light gas gun which will be capable of accelerating projectiles to velocities in excess of 20,000 ft/sec.

It is also planned that the Richtmyer-Von Neumann "q" method will be revised so as to account for real gas effects and heat losses from the light gas to the wall of the bore. Attempts will also be made to use this program for a 3-stage gun such as the shock-heating light gas gun devised by Bioletti.

Theoretical work on the traveling charge gun is considerably more difficult than theoretical work on the light gas gun; so at the moment traveling charge gun theory is not as well advanced as that for the light gas gun. Some effort will be made to apply the principles developed for the light gas gun to traveling charge gun theory.

Meanwhile development of a hypervelocity traveling charge gun will rely heavily on experimental work.

### REFERENCES

1. Baer, P. G., "The Application of Interior Ballistic Theory in Predicting the Performance of Light Gas Hypervelocity Launchers," 4th Symposium on Hypervelocity Impact, AGP-TR-60-39 (II), September 1960.
2. Baer, P. G., "The Traveling Charge Gun as a Hypervelocity Launching Device," 4th Symposium on Hypervelocity Impact, APG-TR-60-39 (II), September 1960.
3. Baer, P. G., and Bryson, K. R., "Tube Configuration for a 120mm Constant Pressure Traveling Charge Gun," BRL Technical Note No. 1332, August 1960.
4. Baer, P. G., and Bryson, K. R., "Design Data for the Constant Pressure Traveling Charge Gun," BRL Technical Note No. 1360, November 1960.
5. "Research and Development Work on Rocket-Assist Projectile," Final Report OCO Project TMI-5004, Armour Research Foundation, October 1953.
6. Epstein, R., et al., "Propellant Motion in a 37 mm Gun Using Gamma Ray Tracer Techniques," BRL Report No. 940, May, 1955.
7. Vest, D. C., et al., "Ballistic Studies with a Microwave Interferometer-- Part II," BRL Report No. 1006, February 1957.
8. Vest, D. C., "An Experimental Traveling Charge Gun," BRL Report No. 773, October 1951.
9. Richtmyer, R. D., "Difference Methods for Initial Value Problems," Chapter X, p. 215-222, Interscience Publishers, Inc., New York (1957).

## EXPERIMENTS WITH A TWO MILLION VOLT

### ELECTROSTATIC ACCELERATOR

J. F. Friichtenicht

Space Technology Laboratories, Inc.  
Canoga Park, California

#### I. INTRODUCTION

Previous papers<sup>1,2</sup> discussed the pertinent aspects of accelerating charged particles by electric fields for hypervelocity studies and described the operation of a 120 kilovolt accelerator. This work demonstrated the feasibility of the electrostatic method and indicated that an electric accelerator would be a valuable supplement to the more conventional light gas gun and explosive techniques. A two million volt particle accelerator designed to increase the particle size and velocity ranges previously available from the 120 kilovolt accelerator has been constructed and tested at the Research Laboratory of Space Technology Laboratories. A description of the accelerator and a discussion of experiments performed using it are included in the following sections.

The velocity attained by a charged particle in an electric accelerator is limited only by the charge to mass ratio of the particle and the total accelerating voltage to which it is subjected and is given by  $v = \sqrt{\frac{2q}{m} V}$ . Let us first consider the problem of charging the particles. The presence of charge results in an electric field at the surface of the particle. The maximum positive charge which can be placed on a particle is that which produces an electric field sufficient to evaporate ions from the surface. A method of depositing charge on particles by contact has been described elsewhere<sup>1,2</sup> and results in charge to mass ratios for iron spheres ranging from about 85 coulombs/kilogram for 0.1 micron radius particles to about 0.85 coulombs/kilogram for particles of 10 microns radii. Larger values are obtained for particles of less dense materials. These values are lower than might be attainable by other techniques but the simplicity and ease of operation of the contact charging method appear to fit best the needs of this particular application.

Using the experimental values of charge to mass ratios as a basis, the accelerating voltage required to obtain given velocity and size ranges is easily calculated. These considerations as well as questions of cost and versatility led to our choice of a commercially available voltage generator as the main component of the electrostatic accelerator. A two million volt Van de Graaff accelerator was obtained from High Voltage Engineering Corporation and subsequently modified. The solid line in Figure 1 indicates the predicted performance of this device using a nominal accelerating voltage of 1.75 million volts and iron particles with

## TWO MILLION VOLT ELECTROSTATIC ACCELERATOR

charge to mass ratios as indicated above. The points on Figure 1 are the results of a typical set of experimental measurements made upon completion of the particle accelerator and show generally good agreement with the predicted performance.

### II. MODIFICATION OF THE ACCELERATOR

The modification of the Van de Graaff was accomplished by removing most of the components of the positive ion source and associated circuitry from within the high voltage terminal and replacing them by the particle charging and injection mechanism. Among the components retained for integration into the new system were two 300 watt, 400 cps belt-driver alternators to supply primary power, a low voltage D. C. power supply, and the focus power supply. The remote control system which consists of selsyn and solenoid driven lucite rods extending from ground to the high voltage terminal was also retained.

A drawing of the mechanical portion of the charged particle injector is shown in Figure 2 and its operation is as follows: The source of particles, in the form of a powder, is placed in a rectangular cavity. During operation, the assembly supporting the charging electrode and that containing the powder are initially at a high positive potential. The particle reservoir is pulsed to a lower potential which produces an electric field between the elements. The field induces a net charge on the particles on the surface of the bed of material and thus produces an electrical force on those particles. When this force exceeds those of gravity and cohesion, the particle is lifted from the bed and accelerated across the gap. Actually, a number of particles are lifted almost simultaneously and form a cloud which has properties similar to those of a gas. Some of the particles within the cloud diffuse from within the reservoir through the horizontal holes in the electrode assembly into the region of the charging electrode. Since the mating flange is at ground potential, an electric field always exists between the flange and the electrode assembly. The particles are accelerated by the electric field back and forth across the gap, exchanging charge each time they touch a surface. The fields are shaped so as to direct the particles toward the charging electrode. Once a particle comes in contact with the electrode it develops a much larger net charge and is forced away from the electrode. Some of the highly charged particles pass through the small entrance hole into the accelerating region to the left, where they are subsequently accelerated through the entire accelerating voltage.

A block diagram of the circuit wiring within the high voltage terminal of the accelerator is shown in Figure 3. Control of the circuits is accomplished by means of plastic rods which extend the length of the accelerator column and are driven by selsyns or solenoids as indicated. The charging and injection mechanism requires an electrode power supply and a high voltage pulser to pulse the reservoir. High voltage is supplied by a half-wave voltage doubler circuit variable from 0 to 28 KV D. C. The output of the pulser is a flat topped pulse about 10 milliseconds long whose amplitude is variable from 0 volts to almost the full voltage of the power supply.

The existing focusing system was found to be adequate and was retained for incorporation in the completed particle accelerator. Calibration curves

# TWO MILLION VOLT ELECTROSTATIC ACCELERATOR

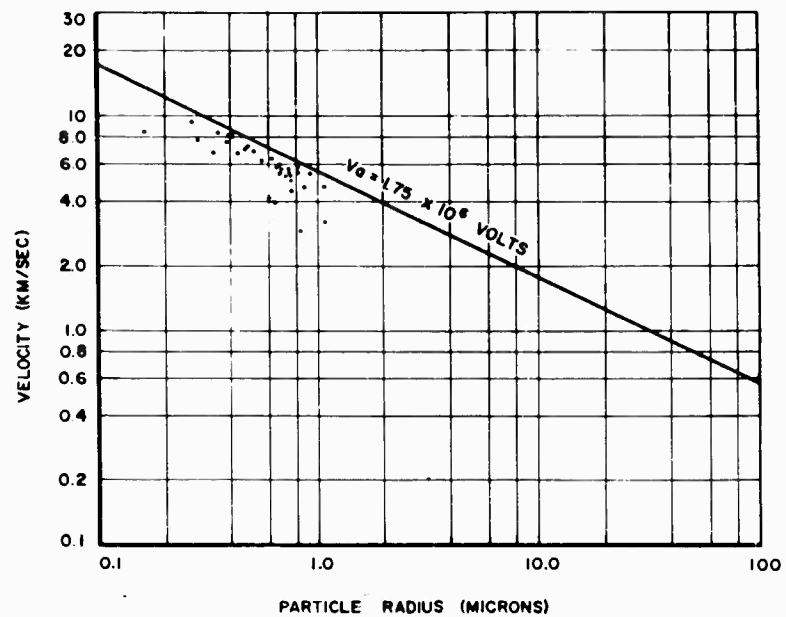


Figure 1 - Performance Curve for an Electrostatic Accelerator

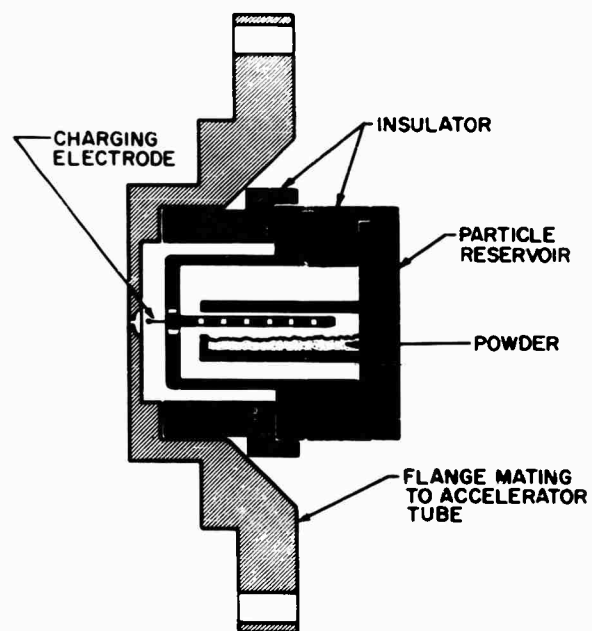


Figure 2 - Drawing of the Charged Particle Injector for the Two Million Volt Accelerator

# TWO MILLION VOLT ELECTROSTATIC ACCELERATOR

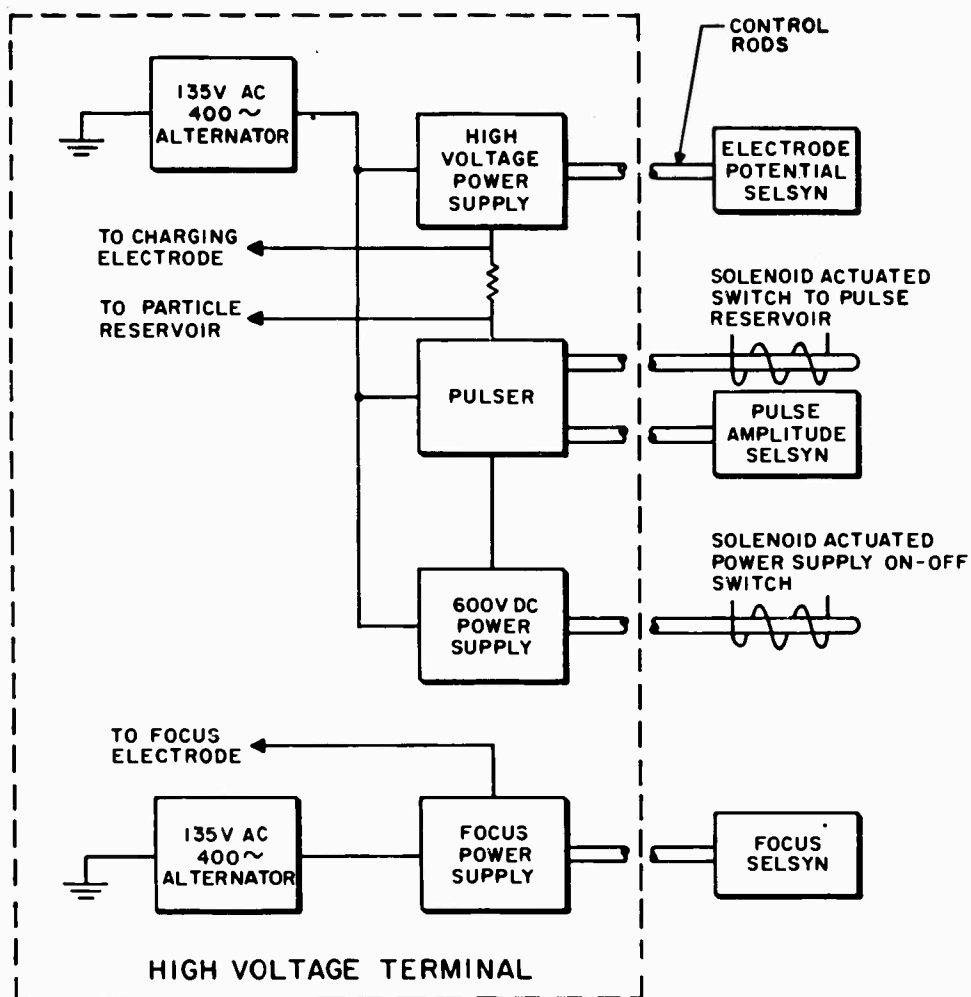


Figure 3 - Circuit Wiring Diagram Within the High Voltage Terminal of the Two Million Volt Accelerator

## TWO MILLION VOLT ELECTROSTATIC ACCELERATOR

giving the best focus conditions for wide ranges of electrode voltage and accelerator voltage were obtained. It was found that about 90 percent of the particles injected into the accelerator tube could be focused into a 3/16 inch diameter spot.

Figures 4 and 5 are photographs of the completed accelerator. Figure 4 is a rear view of the accelerator showing the pressure vessel and the concrete radiation shielding. The high voltage terminal and accelerating column are contained within the pressure vessel. The experimental area of the accelerator is shown in Figure 5. The control console is located at the left while the accelerator tube extension can be seen extending from within the concrete enclosure.

### III. EXPERIMENTAL TECHNIQUES

An active experimental program using the accelerator is in progress. Most of the work so far has been done under the terms of NASA Contract NAS5-763, Subcontract No. C135A-1043 and has been concerned with those properties of high speed impact which might prove useful in micro-meteor detection systems. Effort has been concentrated on studies of impact ionization and impact light emission and tests involving acoustical detectors. The results of experiments on the light flash and ionization effects will be described in another paper while tests of the acoustical detectors will be described below to illustrate the operation of the accelerator.

In all of the experiments on transient phenomena the projectiles were iron spheres ranging from about 0.2 micron radius to about 1.5 microns radius. The smaller particles achieved velocities up to about 12 km/sec and the larger ones as low as 2 km/sec. The average particle was about 1.5 microns in diameter and had a velocity of about 5 km/sec. In all cases, however, the velocity and mass of each particle was measured prior to impact and correlated with the observed phenomena.

The charge on each accelerated particle is determined by measuring the amplitude of the voltage signal induced on a cylindrical drift tube of known capacitance as the particle passes through it. The duration of the observed signal is simply the transit time through the tube. From this the velocity can be determined. The mass of the particle can then be computed from  $m = 2qV/v^2$  where  $V$  is the total accelerating voltage. Since the particles are spherical, the radius can readily be determined. Techniques for measuring the trajectory of the particle through the detector have also been developed<sup>1</sup> and these allow the correlation of particle parameters to observed impact sites.

For the most of the dynamic measurements the detector signal was amplified and displayed on one trace of a Tektronix 551 dual-beam oscilloscope. The information from the experiment in question was displayed on the other trace. Generally, the oscilloscope was set to trigger on a signal from the detector. Photographs of the observed traces were made for data reduction purposes. The length of the detector was tailored to fit specific experiments and many different detectors were used during the course of this work. This arrangement provides a time base for time-of-flight measurements to insure an exact correlation between observed particles and observed impact effects.

TWO MILLION VOLT ELECTROSTATIC ACCELERATOR

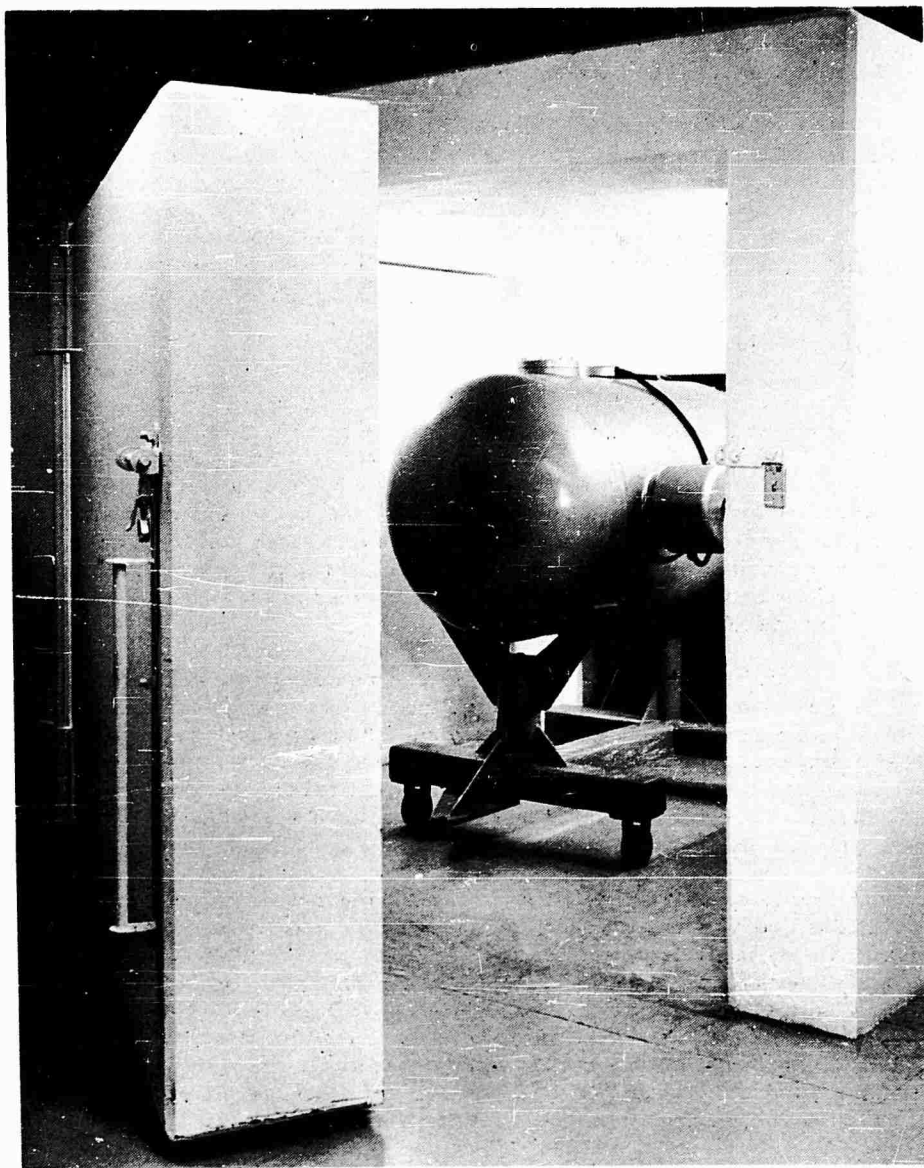


Figure 4. Rear View of the Two Million Volt Accelerator.

# TWO MILLION VOLT ELECTROSTATIC ACCELERATOR

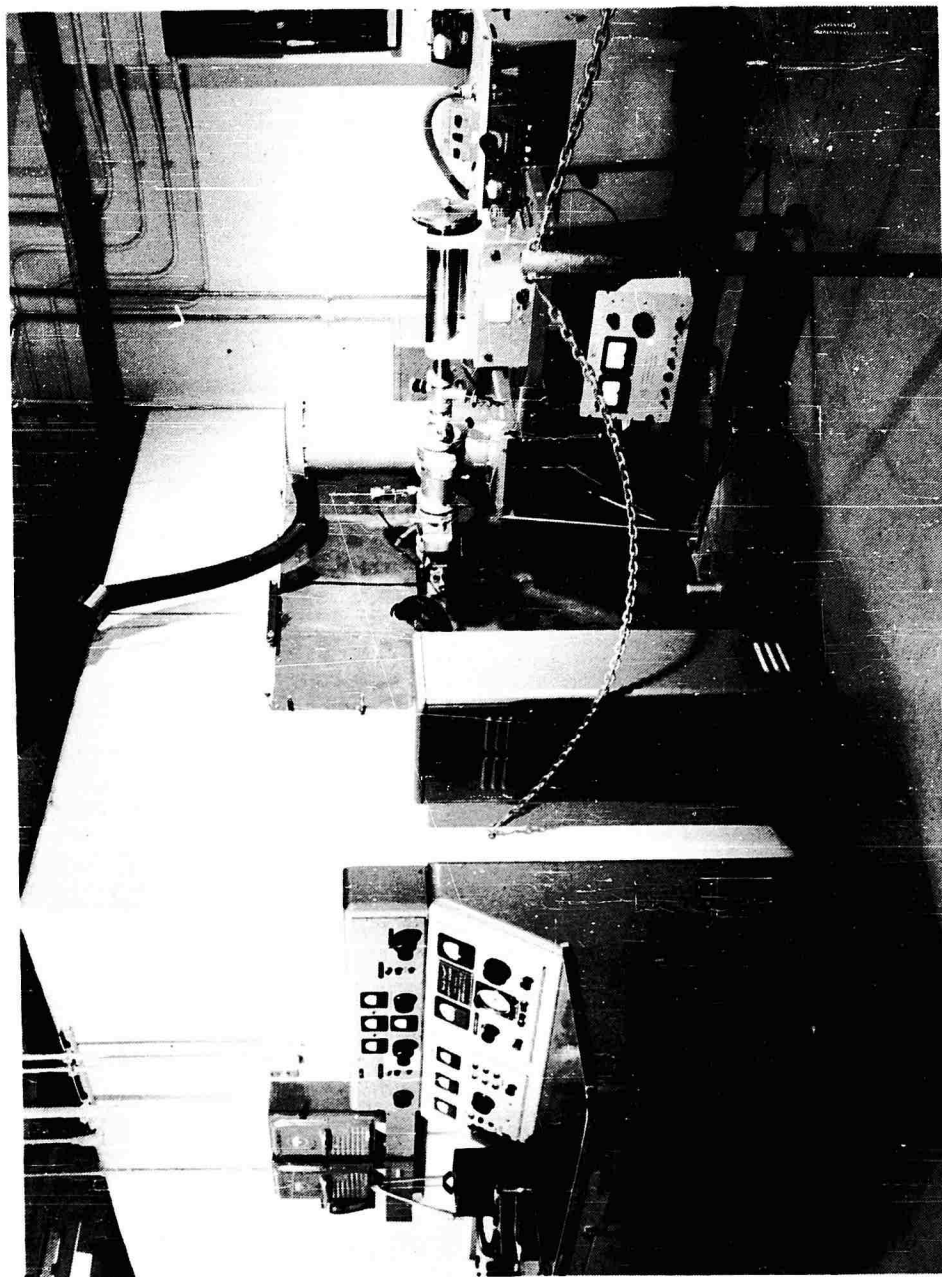


Figure 5. View of the Experimental Area of the Accelerator.

## TWO MILLION VOLT ELECTROSTATIC ACCELERATOR

It might be instructive to include a brief qualitative discussion of errors in measurement at this point. Perhaps the largest single source of error is that of the measurement of pulse height and length from the photographs. There is usually quite a large variation in these quantities due to the size variation of the particles used. The gains are usually adjusted so that the larger signals remain visible on the oscilloscope screen. Consequently, some of the smaller signals may have deflections of only a centimeter or so and it is difficult to measure these signals to within ten percent. The same reasoning applies to pulse duration and to signals observed from the phenomena under study. In some cases, precision is further sacrificed to preserve a certain time relationship between detector signals and specific impact effects. In general, the relative errors are greater for smaller signals. Most of the experimental information is probably dependent upon surface conditions of localized areas. It is possible that there might be significant differences in these conditions during the course of any one experiment. All of these things contribute to the spread in data which is evident for most of the results shown in the following section. Most of the error can be reduced by improved techniques but at the sacrifice of quantity of data obtained. Future measurements will probably be refined to eliminate most of the errors discussed in this section.

The accelerator itself is manually controlled by the operator. Particles are injected and subsequently accelerated at the discretion of the operator. The number of particles injected at one time can be coarsely adjusted from the control console. For most of the work to be described, only a few particles (and frequently one or none) were accelerated at any one time. This simplified correlation of observed results.

### IV. TESTS OF THE ACOUSTICAL DETECTOR

The acoustical detector<sup>3</sup> has enjoyed the most widespread use in direct measurements of micrometeorites from satellite vehicles. Such a detector consists of a crystal transducer which is mechanically coupled to a metallic plate of large area. The crystal is sensitive to mechanical vibrations of the plate caused by the impact of a meteorite. An electrical signal is produced by the crystal which is amplified and subsequently transmitted in an appropriate fashion.

It has been shown that the electrical impulse is proportional to the momentum of the impinging particle. This has been verified by experimental measurements of both elastic and inelastic impacts. The measurements described in the following paragraphs were made to extend both the size and velocity of the calibration particles. The use of particles from the electrostatic accelerator reduces the momentum by about four orders of magnitude compared to the momenta of particles previously used for calibration purposes. This reduction caused experimental difficulties, however, because the detectors provided for use by the NASA were not sufficiently sensitive to be used directly and modification was required in order to make measurements. The results of the measurements are quite general in nature, though, and are adequate for describing the phenomena involved.

A sample crystal transducer was given to us by the NASA for study. It consisted of a cylindrically shaped lead zirconate crystal encapsulated in an

## TWO MILLION VOLT ELECTROSTATIC ACCELERATOR

aluminum can. Its natural frequency of vibration was about 100 KC. Early experiments showed that impacts on an aluminum plate which was coupled mechanically to the can failed to produce measurable signals. The aluminum plate was removed and particles were allowed to impinge on the face of the can. In this case signals were observed but it was apparent that shock waves reflected from support members impaired the validity of the measurements. As a consequence of this, the crystal was removed from the can and suspended in a rubber grommet with its axis parallel to the beam of particles from the accelerator. The face of the crystal exposed to the impinging particles was coated with conducting silver paint and electrically grounded. The signal from the crystal was picked up by means of loops around the ends of the crystal.

The observed signal was fed through a wide band amplifier and displayed on an oscilloscope in the usual manner. This results in an exponentially decreasing signal as illustrated in Figure 6-a. (The signal illustrated resulted from a glass bead dropped from a height of a few centimeters.) The presence of low frequency noise restricted the use of this technique to simply measuring frequency. To reduce some of the noise problems the amplified signal was fed through a relatively low  $Q$  resonant circuit which was tuned to the resonant frequency of the crystal. This circuit is shown in Figure 6-b and a typical observed signal is illustrated in Figure 6-c. The amplitude of the transducer signal was measured at the point of maximum excursion from the base line. It can be shown that the signal at the output terminals of the tuned circuit is given by

$$V = V_0 \left[ e^{-\frac{\omega t}{2Q_c}} A \sin(\omega t + \phi) + e^{-\frac{\omega t}{2Q}} B \sin(\omega t + \delta) \right]$$

where  $V_0$  is the amplitude of the first half-cycle of the crystal output,  $Q_c$  is the  $Q$  of the crystal,  $Q$  is the  $Q$  of the tuned circuit,  $\omega$  is the angular frequency of vibration, and  $A$  and  $B$  are constants. Thus, the measured signal is proportional to the electrical impulse produced in the crystal by a high speed impact.

It is reasonable to assume that for particles of constant mass the amplitude of the observed signal can be written as  $V = F(v) v$  where  $V$  is the amplitude defined above and  $F(v)$  is a function which depends upon the nature of the impact. There are essentially three kinds of impact which should be considered. These are elastic impacts, completely inelastic impacts, and inelastic impacts enhanced by the expulsion of material from the crater which increases the amount of momentum imparted to the crystal. According to Reference 3, the additional momentum imparted by the expelled material is about two and one-half times the initial particle momentum at 70 km/sec and less than that for lower velocities. It is likely that all of the impacts observed in this work were of the latter type. For this reason, the microphone signal was normalized to the mass of the particle and plotted as a function of particle velocity in Figure 7.

There has been some conjecture that the impulse delivered to the crystal is proportional to the square of the velocity. It is evident from Figure 7 that the data are not of sufficient precision to justify a choice between a velocity or velocity squared dependence. However, solid curves for each possibility are

## TWO MILLION VOLT ELECTROSTATIC ACCELERATOR

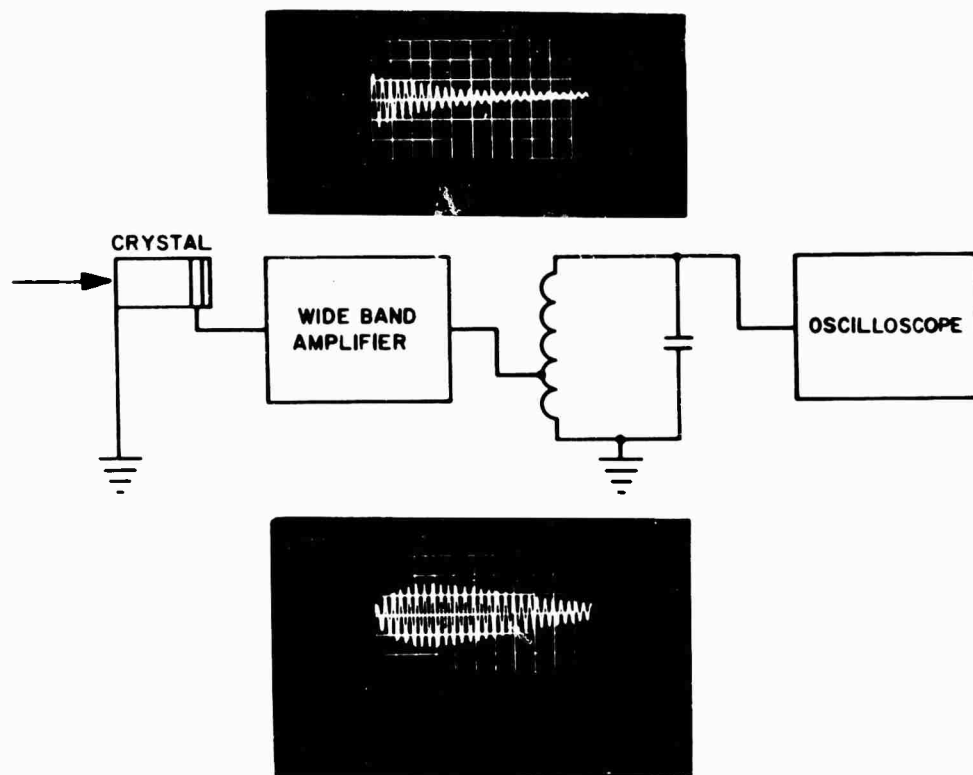


Figure 6. Circuit Diagram for Measuring the Output of an Acoustical Detector and Observed Waveforms.

## TWO MILLION VOLT ELECTROSTATIC ACCELERATOR

shown on the figure. Each curve was arbitrarily normalized at the open circle. Except for three points it appears that the velocity dependence is a slightly better fit.

If one makes the assumption that  $F(v)$  is a slowly varying function over the velocity range of interest, it can be replaced by a constant. This implies that the microphone signal is proportional to the momentum of the impacting particle. The data of Figure 7 are replotted to test this hypothesis in Figure 8. Again it is clear that the large spread in the data points prohibits the establishment of a precise relationship. Also, the range of momentum available is quite small. To obtain an independent calibration point with a different value of momentum, plastic beads weighing approximately 100 micrograms were dropped on the face of the crystal from a known height. This was done in air but no drag corrections were made nor was the observed departure from an elastic impact taken into account. However, the computed value of momentum was probably accurate to better than ten percent which is at least as good as our other measurements. Using this point and the origin as the other, the elastic impact line shown in Figure 8 was obtained. Our hypothesis that  $F(v)$  is a constant is undoubtedly violated but the experiment illustrates one significant point. Nearly all of the data points obtained with the high speed particles lie above the elastic impact line. This tends to indicate that the ejected material imparts at least as much (and in most cases more) momentum than does the impacting particle over the velocity range studied.

Surface irregularities of the impacted area might account for some of the scatter in the data. Therefore, measurements were made using a plate of chemically polished aluminum which was glued to the crystal face. Optical examination indicated that the surface was quite smooth and little evidence of surface imperfections could be observed. The results of measurements using this arrangement are shown in Figure 9. The spread is still quite large and it is not at all evident that the situation was improved by this means. It is apparent, though, that the data is in quite good agreement with the data obtained with the silver coated surface.

In future work, efforts should be made to improve the precision of the measurements so that a better determination of velocity dependence can be made. A more sensitive crystal would facilitate the measurements as well.

### V. SUMMARY

A two million volt electrostatic hypervelocity projector has been constructed and tested and is presently being used in a program of hypervelocity research. The device has been found to be particularly well suited for laboratory micro-meteor simulation. Velocities up to 14 km/sec have been observed using spherical iron projectiles. A limited amount of work using carbon particles has been done. The lower density of the carbon results in larger charge to mass ratios and velocities up to 25 km/sec have been observed. Problems associated with handling of the carbon particles have prevented systematic studies as yet but work is continuing on this program.

# TWO MILLION VOLT ELECTROSTATIC ACCELERATOR

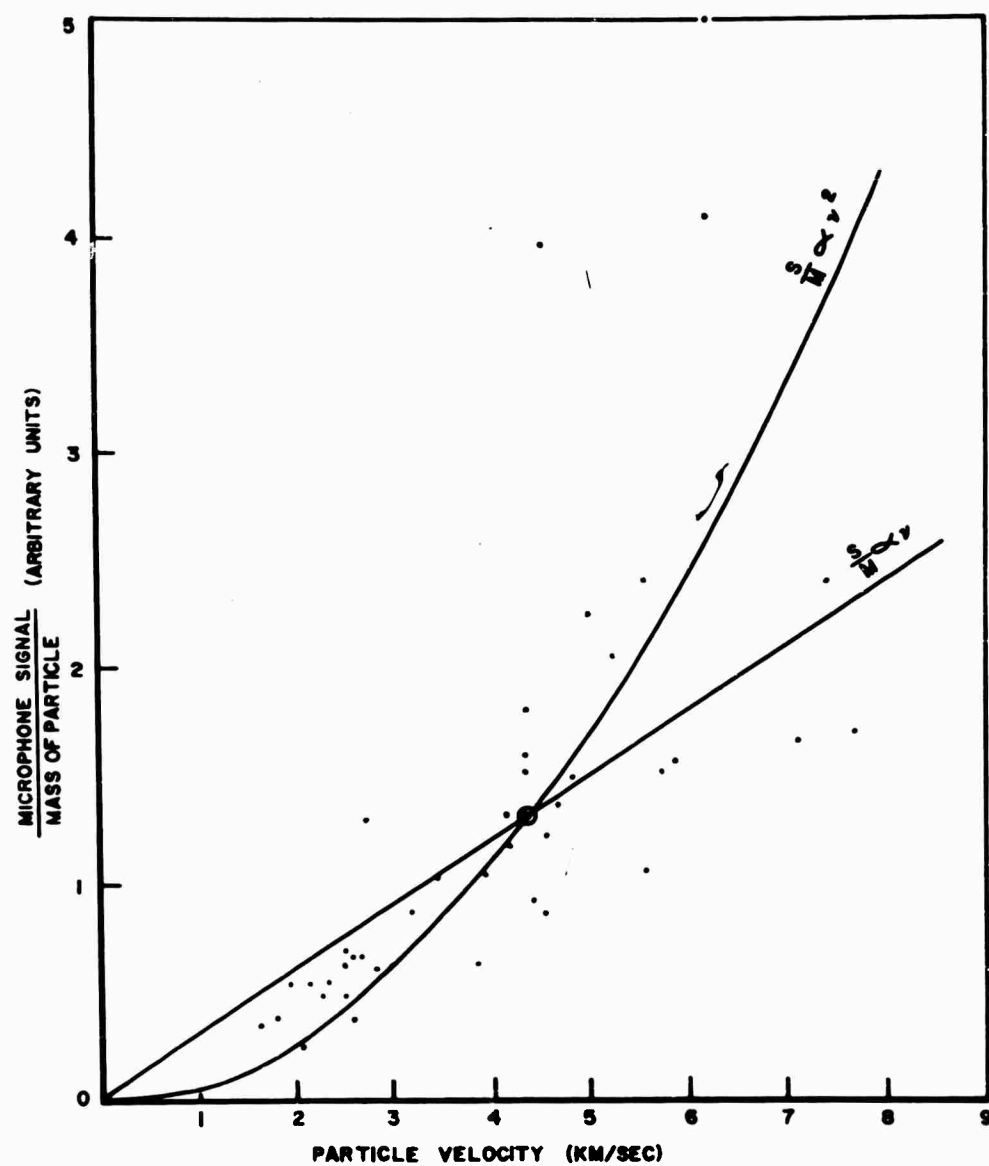


Figure 7 - Output of Crystal Transducer as a Function of Particle Impact Momentum

## TWO MILLION VOLT ELECTROSTATIC ACCELERATOR

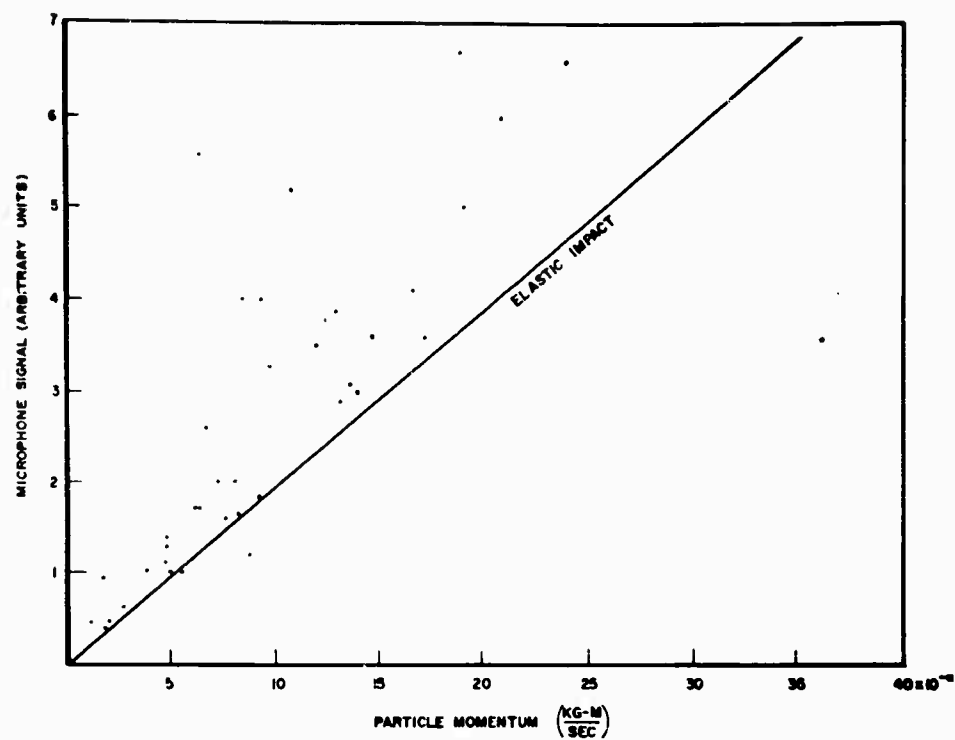


Figure 8. Crystal Transducer Output as a Function of Impacting Particle Momentum.

# TWO MILLION VOLT ELECTROSTATIC ACCELERATOR

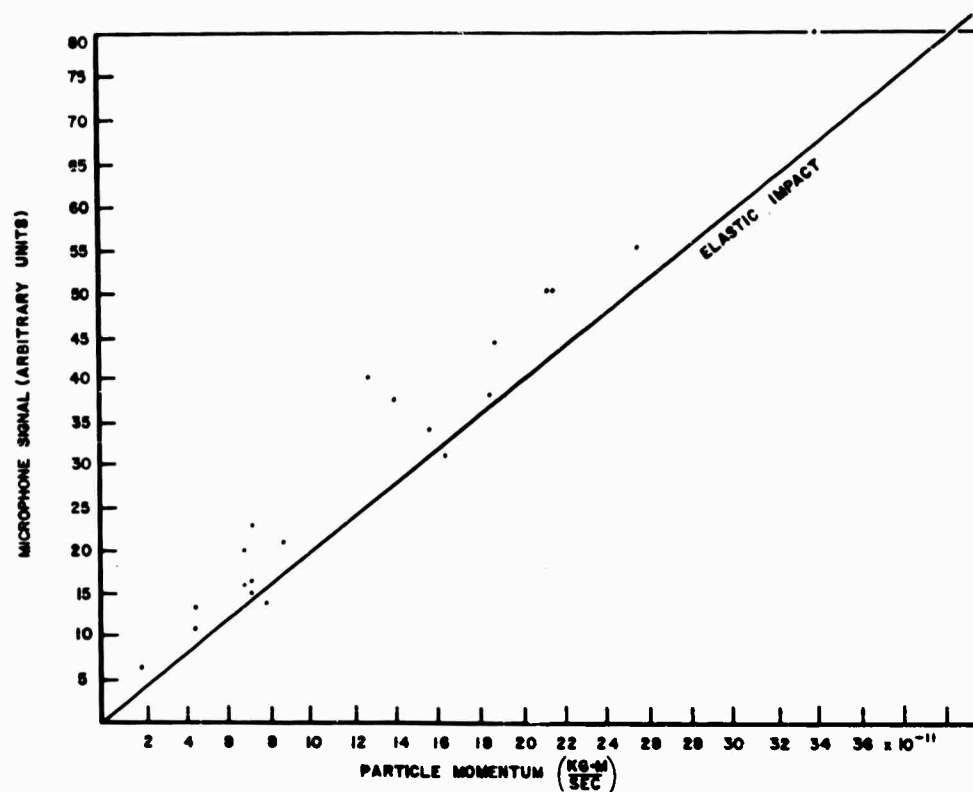


Figure 9. Crystal Transducer Output as a Function of Impacting Particle Momentum on a Polished Aluminum Surface.

## TWO MILLION VOLT ELECTROSTATIC ACCELERATOR

### REFERENCES

1. H. Shelton, C. D. Hendricks, Jr., and R. F. Wuerker, Journal of Applied Physics, Vol. 31, No. 7, July 1960.
2. C. D. Hendricks, Jr., H. Shelton, and R. F. Wuerker, Proceedings of the Third Symposium on Hypervelocity Impact, Vol. 1, Feb. 1959, pp. 33-43.
3. Maurice Dubin, Space Research, Proceedings of the First International Space Science Symposium, (Interscience Publishers, Inc., New York, 1960), p. 1042.

## CONCLUDING REMARKS

H. F. Swift

U. S. Naval Research Laboratory  
Washington 25, D. C.

During the past 18 months the maximum velocity capability of all major types of hypervelocity ballistic accelerators has been substantially increased. At present, gas guns are capable of accelerating small plastic cylinders to 10 km/sec, and explosive accelerators have launched beryllium rods to velocities above 20 km/sec.

The most direct advance in light-gas gun technology since the 4th Hypervelocity Impact Symposium has been the construction of a group of guns capable of accelerating small, low density projectiles to velocities between 7.5 km/sec and 10 km/sec. Advanced models of both shock heated and adiabatic compression guns have been developed to reach these performance levels, and a new concept of utilizing piston deformation for increasing peak compression ratios has been applied. Of more basic significance, however, has been the development of computational techniques capable of accurately predicting the performance of light-gas guns. These techniques have proven accurate over a very wide range of gun design and operation parameters. Since empirical data associated with a particular gun-firing situation are not required, these techniques can be used to estimate the results of firing situations not presently attainable with greater assurance than was possible in the past. Such computational techniques are presently being used for the design of gas guns with higher performance capability than is presently attainable, and for the evaluation of techniques that may increase maximum gas gun performance, such as pre-heating of the driver gas.

The biggest advances in explosive accelerator technology achieved during the last 18 months are the further perfection of the cavity charge, and the initial development of the cylindrical liner charge. At present, the explosive cavity charge may be considered as a research tool although considerable effort is being placed upon its additional development. The cylindrical liner charge is still in an early stage of development, but its presently demonstrated velocity capability with a limited number of materials assures its future importance. Techniques have also been developed for utilizing the train of hypervelocity pellets generated by a conical liner charge for the study of individual hypervelocity impacts.

A group of specialized ballistic accelerators has become increasingly important within the past 18 months. At present, many of the micrometeroid impact studies where single impacts must be considered are being conducted using electrically powered micrometeroid simulators. Other techniques presently under

## CONCLUDING REMARKS

development should find application for the launching of distributed mass projectile and low-strength projectile packages to hypervelocities using very low peak accelerations.

In the near future, the peak velocity capability of gas guns can be expected to increase. The maximum mass and density of projectiles being launched should also increase sharply as planned new facilities go into operation. The maximum velocities presently attainable with gas guns cover at least most of the velocity regimes of interest for several important ballistic applications. Therefore, a change in the main emphasis on accelerator development programs can be expected toward the development of techniques for accelerating as wide a range of models as possible to maximum velocities up to 10 km/sec. The major areas of effort for such programs will be the reduction of peak model acceleration during gun launch and the development of sabots capable of withstanding these accelerations.

Considerable future effort in explosive accelerator technology improvement programs may be expected in the further development of cylindrical liner charges to the point where various pellet materials can be accelerated to near their theoretical maximum velocities. Development of other explosive acceleration techniques should also continue, and more emphasis may be expected on the development of diagnostic instrumentation for the evaluation of explosive charge performance.

SESSION II

THEORY

CHAIRMAN

DR. C. H. LEE

OFFICE OF THE CHIEF  
OF ORDNANCE

## INTRODUCTION TO THE THEORY SESSIONS

Floyd E. Allison

Ballistic Research Laboratories  
Aberdeen Proving Ground, Maryland

One purpose of an introductory paper is that of defining the problem in its broad aspects. This has already been done in an excellent paper by Hopkins and Kolsky<sup>(1)</sup>, which was presented at the Fourth Hypervelocity Impact Symposium. Another purpose of an introductory paper could be to outline in a general way various approaches that have been suggested for solving the problem. In the case of hypervelocity impact, the approaches that have been suggested range from rigorous solutions based on fundamental mechanics with assumptions concerning the dominant forces to numerous theoretical models based on sweeping assumptions concerning the mode of deformation as well as the dominant forces. Of course, the degree of approximation introduced by such assumptions depends on how closely the dominant forces and assumed mode of deformation represent those actually encountered under impact conditions.

Historically speaking, the astronomers were the first scientists to become interested in the mechanics of hypervelocity impact. The problem of crater formation was considered in 1936 by Öpik<sup>(2)</sup>, who proposed a theoretical model for the problem of meteorite impact and proceeded to make calculations using basic principles of mechanics. In his analysis, Öpik assumed that:

1. The earth or rock into which the meteorite is penetrating behaves as an incompressible fluid with a finite yield strength: i. e., the pressure resisting the forward and radial motion each consist of two terms:

$$\begin{aligned} p &= 1/2 \rho z^2 + k \\ p' &= 1/2 \rho r^2 + k \end{aligned} \quad (1)$$

where  $\rho$  is the density of the material into which the meteorite is penetrating. The velocity dependent terms represent the inertial or hydrodynamic resistance and the parameter  $k$  represents the resistance to plastic flow or rupture.

2. The pressures resisting the forward and the radial motions are related by the strong form of Bernoulli's equation. (This is a definite assumption since the penetration by the meteorite is not a steady-state process.)

3. The meteorite is assumed to flatten at right angles to its direction of impact. The approximations introduced by each assumption could be a subject for discussion. However, the last assumption is probably the most controversial because it imposes a priori a specific flow pattern for the meteorite.

## INTRODUCTION

There appears to be no further work done on the problem of meteorite impact until the possibility of constructing space vehicles was seriously considered and possible damage due to collision with meteoroids became important. In 1947 Whipple (3) proposed that space vehicles could be protected by a meteor bumper, and, in 1948, Grimmer (4) published a paper in which he considered some aspects of the impact problem. With regard to the penetration of a meteoroid, Grimmer assumes:

1. The meteor is not deformed by the impact.
2. The force resisting the motion of the meteoroid is a dynamic pressure proportional to the square of its instantaneous velocity if the velocity is 5 times the velocity of a plastic wave: i. e.,

$$F = (1/8) C_D \rho D^2 V^2, \quad (2)$$

where  $D$  is the meteoroid diameter;  $\rho$ , the density of the material through which it is penetrating; and  $C_D$ , the drag coefficient.

3. For  $V$  less than 5 times the velocity of a plastic wave the penetration is given by one of the armor penetration formulae. Again, it should be noted that the mode of deformation for the meteoroid has been specified a priori, in this case zero deformation.

Although the penetration of a shaped-charge jet is not specifically applicable to the problem of meteorite penetration, the impact velocities encountered approach 10 km/sec during the initial stages of jet penetration. Because the theory of jet penetration has been verified by direct experimental observations, it is not inappropriate to examine the physical assumptions used to develop this theory and to note, in particular, the points at which the problem of meteorite penetration differs from that of a shaped-charge jet. It was realized during the early 1940's that the dynamic pressure produced by the impact of a shaped-charge jet greatly exceeded the yield strength of the metals involved and a hydrodynamic theory was proposed by Pugh (5). The basic assumptions of the theory were:

1. The target and jet behave as incompressible fluids.
2. The flow is assumed to be in a steady state when viewed from a frame of reference moving with the penetration velocity so that for the streamline along the axis of symmetry, the stagnation pressure is given by:

$$p_s = 1/2 \rho_t U^2 = 1/2 \rho_j (V-U)^2 \quad (3)$$

3. The penetration ceases when the jet velocity becomes sufficiently low that it cannot overcome the yield strength of the target material. The last assumption was necessary because it was realized that shaped-charge jets contain a complete spectrum of velocities ranging from about 10 km/sec at the front to somewhat less than 1 km/sec at the rear.

In order to apply the shaped-charge theory to hypervelocity impact problems it is necessary to modify the third assumption. One could, for example, assume that the projectile behaves as a short steady-state jet and that the penetration

## INTRODUCTION

ceases as soon as the rear surface of the jet comes in contact with the target. Under this assumption the penetration depth is given by  $P = \sqrt{\rho_j / \rho_t} l$ , where  $l$  is the length of the projectile. Rostoker<sup>(6)</sup> estimated the mass of the meteorite that produced the Barringer Crater using this approximation. However, he cautioned that his estimate should not be taken seriously because the assumed flow configuration would not necessarily be applicable to a meteorite. It is important to realize again that a specific flow configuration has been assumed. First of all, the assumption of steady-state hydrodynamics, which was known to be a good approximation for a long jet, is questionable because a meteorite is sufficiently short, relative to its diameter, that a steady flow configuration may not be established. More important, it has been demonstrated, at least for ductile materials, that assuming the penetration to cease as soon as the trailing edge of the projectile reaches the target surface introduces a very large error. It is now apparent that a short hypervelocity projectile imparts a sizable quantity of kinetic energy to the target material which ultimately must be carried away from the target as thermal and kinetic energy of the ejecta or transformed to thermal energy of the target itself by various dissipative mechanism. While the kinetic energy is being dissipated the crater continues to form by a process loosely described as secondary flow or cavitation. Of course, it had been realized that such an effect existed for shaped-charge jets, but the contribution of the secondary flow to the total penetration could be neglected in comparison with the primary penetration predicted from equation (3).

Thus far, all approaches to the hypervelocity impact problem have been based on incompressible hydrodynamics. However, experimental work initiated in 1945 by Goranson<sup>(7)</sup> and his co-workers has yielded much information concerning the compressibility of metals at high pressures<sup>(8)</sup>. The theory of jet penetration, which is based on incompressible fluid flow, is obviously an approximation; and, it is interesting to examine the degree of approximation involved. Equation (3) provides a relation between the penetration velocity  $U$  and the impact velocity  $V$ . The experiments reported by Eichelberger<sup>(9)</sup> have shown that this relation is a good approximation. However, the identification of  $1/2 \rho_t U^2$  or  $1/2 \rho_j (V-U)^2$  with the stagnation pressure is considerably less accurate. Theoretical estimates of the effect of compressibility on the calculated penetration velocity have been made by Rostoker<sup>(10)</sup> and perhaps others. Some estimates based on the more recent Los Alamos data indicate that, for steady-state penetration of a tungsten jet into a lead target with a penetration velocity of 3.26 km/sec, the impact velocity predicted from the incompressible theory will be 4 percent too low; the stagnation pressure, 22 percent too low; and the stagnation density, 40 percent too low. For hypervelocity impact in ductile materials, the steady-state situation described by equation (3) is a small fraction of the process. Therefore, effects of compressibility can be expected to play a much more important role, and may, in fact, be a dominant factor.

Further work on hypervelocity impact includes theoretical calculations of the initial pressure by Gilvarry and Hill<sup>(11)</sup> in 1956. Their calculations were based on a one-dimensional shock analysis using equation of state calculated from the Thomas-Fermi statistical model of the atom<sup>(12)</sup>. Unfortunately Gilvarry and Hill did not proceed to develop the mechanics of the impact process, but used the computed high values of the pressure and temperature as confirmation of the "explosion hypothesis"<sup>(13)</sup> for the origin of the lunar craters.

## INTRODUCTION

The development of high-speed digital computers with large memory capabilities opened the way for calculations based on non-steady compressible hydrodynamics in more than one space dimension. However, it was soon discovered that shock discontinuities were very difficult to handle even on the digital computers. This major obstacle was satisfactorily overcome by the introduction of the Von Neumann-Richtmyer<sup>(14)</sup> Q method, which introduces a pseudo-viscosity into the calculations. By this technique the shock discontinuity is "smeared out" over a few mesh points and the computations are carried out using the resulting continuous functions.

The first application of a hydrodynamic code to the problem of hypervelocity impact was reported in 1958 by Bjork<sup>(15)</sup> who made computations of the craters produced by hypervelocity impact of steel projectiles on steel targets. It should be noted that this approach eliminates the basic objection that the flow pattern has been either partially or wholly specified a priori. However, the flow pattern has been specified to the extent that it must satisfy the differential equations governing compressible fluid flow. Perhaps the biggest unanswered question revolves around whether or not the shear strength and viscous forces are important.

## REFERENCES

1. H. G. Hopkins and H. Kolsky, "Mechanics of Hypervelocity Impact of Solids," Proceedings of the Fourth Hypervelocity Impact Symposium, APGC-TR-60-39, Volume 1, (1960).
2. E. Öpik, "Theory of the Formation of Meteor Craters," Acta et Comm. Univ. Tartu., A30, (1936); "Meteor Impact on Solid Surface" The Irish Astronomical Journal, 5, 14 (1958).
3. F. Whipple, Astronomical Jour., 52, 131 (1947).
4. G. Grimminger, "Probability that a Meteorite Will Hit or Penetrate a Body Situated in the Vicinity of the Earth," Jour. Appl. Phys., 19, 947 (1948).
5. Garrett Birkhoff, Duncan P. MacDougall, Emerson M. Pugh, and Sir Geoffrey Taylor, "Explosives With Lined Cavities," Jour. Appl. Phys., 19, 563 (1948).
6. Norman Rostoker, "The Formation of Craters by High-Speed Particles," Meteoritics, 1, 11 (1953).
7. R. W. Goranson, D. Bancroft, B. L. Burton, T. Blechar, E. E. Houston, E. F. Gittings, and S. A. Landeen, "Dynamic Determination of the Compressibility of Metals," Jour. Appl. Phys., 26, 1472 (1955).
8. R. G. McQueen and S. P. Marsh, "Equation of State for Nineteen Metallic Elements from Shock-Wave Measurements to Two Megabars," Jour. Appl. Phys., 31, 1253 (1960). (Many other pertinent references are cited in this article.)
9. R. J. Eichelberger, "Experimental Test of the Theory of Penetration by Metallic Jets," Jour. Appl. Phys., 27, 63 (1956).

## INTRODUCTION

10. Norman Rostoker, Interim Report No. 1, Armour Research Foundation Project No. AO56, Subcontract DA-20-018-OED-13210, Michigan State University Contract DA-20-018-ORD-13210, April 1955. (Classified-Security Information.)
11. J. J. Gilvarry and J. E. Hill, "The Impact of Large Meteorites," *Astrophys. Jour.*, 124, 610 (1956).
12. L. H. Thomas, *Proceedings Cambridge Phil. Soc.*, 23, 542 (1927). E. Fermi, *Z. Physik*, 48, 73 (1928).
13. Ralph B. Baldwin, *The Face of the Moon*, University of Chicago Press (1949).
14. J. Von Neumann and R. D. Richtmyer, *Jour. Appl. Phys.*, 21, 232 (1949).
15. R. L. Bjork, "Numerical Solutions of the Axially Symmetric Hypervelocity Impact Process Involving Iron," *Proceedings of Third Symposium on Hypervelocity Impact*, Volume II (1959). (Classified-Security Information.)

MATHEMATICAL METHODS IN THEORETICAL MECHANICS OF  
HYPERVELOCITY IMPACT OF METALS

H. G. Hopkins

The War Office  
Armament Research and Development Establishment  
Fort Halstead, Sevenoaks, Kent, England

INTRODUCTION

The present series of Symposia on hypervelocity impact is characterized in a most striking manner by the variety of people taking part -- engineers, physicists, and mathematicians. However, this is by no means an uncommon situation in much of the current work in the general field of solid mechanics. It is of course a matter not only of intrinsic interest but also one of great importance, particularly for those who are responsible for the initiation and direction of research in the present subject, to be aware of and to appreciate the individual contributions possible by people of differing expertise and also the complementary relations between these contributions. Although I do not propose to discuss this matter, generally, I should like to direct attention to a particular aspect of it which I believe to be of crucial importance: namely, the place of mathematical methods. Discussion of this question is not only worthwhile in itself, but for my own purpose here it has the further merit of being the means of unifying the content of this paper as a whole.

The paper is summarized as follows. It gives a discussion of the place of mathematical methods in research into the theoretical mechanics of impact phenomenology of metals. The relevance of investigations of nonlinear stress-wave propagation to the mechanics of hypervelocity impact is made clear. In conclusion, reference is briefly made to some recent studies at A. R. D. E. of stress-wave propagation, which involve attention to rate-of-strain and nonlinear compressibility effects.

PLACE OF MATHEMATICS IN SCIENTIFIC RESEARCH

The place of mathematics in research into scientific subjects is often discussed, but nevertheless I do not feel that any apology needs to be made for giving some attention to this question in connection with the special interests of this Symposium. My concern is with applied mathematics rather than with pure mathematics, when the former discipline is taken to embrace quite generally all attempts to further our understanding of a science by mathematical methods. The essential difference between pure mathematics and applied mathematics is that the motivations and the objectives are different in the two cases, but this does not imply any difference in the standard of the mathematics per se involved. Naturally, the details of the approach made and the mathematics done vary widely with the

## MATHEMATICAL METHODS IN HYPERVELOCITY IMPACT

particular situation concerned, but nevertheless some general remarks may be made on the broader aspects of the role of the mathematics that is undertaken. There are two categories of situations distinguished by whether or not a fundamental mathematical-physical investigation is demanded. Thus, the situation may merely necessitate the development or application of a well-attested theory, such as elasticity theory. On the other hand, the situation may require the use of mathematics in first helping to understand the physical processes involved, attention naturally being focused on the design of experiments and on the interpretation of data obtained therefrom. This one is the more interesting and important, and it therefore merits some further discussion.

It is vital to recognize that experimental data bearing upon a physical situation, these data often being accumulated at the expenditure of much time and effort and money, generally have no long-term value except when they are finally integrated in the form of sound theoretical treatments. This remark is not to be taken to deny the fact that experiment is often not to be replaced as a means of answering some definite and specific questions. However, scientific progress is possible only when physical data are amenable to quantitative study, and mathematics is the natural language in which to express and to develop the processes involved. Thus, the essentials of the approach to physical situations lie in the interplay between physical ideas and mathematical methods -- the latter enable the former to be expressed in a precise quantitative form, and they may then be checked both theoretically and experimentally. A physical idea only becomes acceptable when this is done, and then, when cloaked in mathematical form, it provides the basis of a mathematical-physical theory. It now becomes possible to give attention to detailed theoretical examinations leading towards the derivation of specific results or predictions. Of course, it may well happen that the mathematics required is too difficult: in this event, it is not possible to attack directly some situations of interest, and these must therefore perforce be studied indirectly, often in terms of simpler but related situations. If the procedures just described can be successfully carried through, there is then confidence in applying a theory without the need to verify directly the results it predicts. Thus, the final outcome is a complete grasp and control of the physical situation with the allied result of being able to treat comparable situations with economy of data and effort. Clearly, much depends upon the skill of the mathematician. Engineering situations often involve a considerable degree of physical uncertainty as well as complexity, and they are notoriously difficult to deal with, but mathematical investigations of such situations are still of the utmost value, even when it is not possible to develop mathematical-physical theories of sufficient completeness.

I have deliberately limited the foregoing discussion on the place of mathematical methods in scientific and engineering research, only some of the more basic ideas being sketched. However, it may be noted that more extensive and highly illuminating discussion has been given by Lighthill (1), Taylor (2), and Biot (3), whose papers have provided the main source of inspiration for my own remarks. I shall now pass on to discuss more specifically the place of mathematical methods in studies of the theoretical mechanics of hypervelocity impact of metals.

## HYPERVELOCITY IMPACT OF METALS

The subject of impact in metals or other solid materials is extremely involved, due mainly to the complexity of mechanical behaviour and to the large number of physical and geometrical variables. At the Fourth Symposium, Hopkins and Kolsky (4) drew particular attention to the fact that hypervelocity impact results in the unsteady motion of the target and projectile materials occurring over combinations of fundamentally different physical regimes corresponding to different types of mechanical behaviour. In brief, hypervelocity impact is not a subject amenable to very precise theoretical treatment.

In experimental work on hypervelocity impact, there is still a need for collecting data on craters per se. But there is a far greater need now for collecting data on the actual particle motions occurring in the development of crater surfaces and also on the stress pulses propagated outwards from craters into targets, and more detailed studies of the permanent deformations surrounding craters would also be of much interest. The entire situation is a complicated one, and it is far too involved to permit unravelling as it stands in the absence of basic data relating to the pertinent mechanical behaviour of solids which must provide the starting point for a study of the integrated phenomena as a problem in the mechanics of continua. However, the experimental observations above could certainly provide a much improved picture of the events that take place, and their analysis would give some guide as to the levels of stress-amplitudes and rates-of-strain and perhaps to the overall partition of energy that are involved. It is possible of course often to correlate such data in terms of simple empirical formulae but this procedure in itself does not lead to improved physical understanding of the situation, and in fact, as I have already said, these data have no real permanent value save when assimilated into a sound physical theory.

Current progress in the proper interpretation and co-ordination of experimental data on hypervelocity impact is severely restricted by the almost complete lack of basic theoretical studies of the situation. The general reasons for this circumstance are not far to seek, and, with their appreciation, it becomes possible to make suggestions for the lines of research that appear most likely to be needed to help to achieve progress. Excluding certain aspects of material behaviour such as fracture and basic changes in metallurgical structure, problems of the mechanics of impact are described in terms of continuum theories for which the governing equations essentially represent the propagation of non-linear stress waves. Effectively, the physical and geometrical changes produced during impact are the result of the operation of complicated wave-type phenomena. Elsewhere (see Ref. 5), I have discussed the present state of research concerning nonlinear stress-wave propagation in metals, and I drew particular attention to the need for further work on the mechanical behaviour of metals under conditions of high rates-of-strain and high pressures. Such work is needed to lead to the construction of constitutive equations, which characterize sufficiently well the mechanical behaviour of metals under these conditions; and these equations are the most important single ingredient in continuum theories.

It should be noted that the construction of constitutive equations is itself an area in which mathematical methods have an important role to play (see Refs. 5 and 6). Broadly speaking, of the effects associated with high rates-of-strain

## MATHEMATICAL METHODS IN HYPERVELOCITY IMPACT

and high pressures, it is undoubtedly the former that are proving to be the more difficult ones to investigate in quantitative physical terms. Rate-of-strain effects are being actively studied (see, for example, Ref. 5), but there are still very considerable practical difficulties associated with the design of adequate mechanical-testing techniques and with the proper interpretation of the data obtained. For certain metals at least, there seems to be no reason to doubt that rate-of-strain effects are important even under quite moderate dynamic conditions, but precise quantitative data and sufficiently realistic and general constitutive equations embodying these data can scarcely be said to have yet been obtained. This is an important area of research in solid mechanics, and I feel that much more attention needs to be given to it.

The joint efforts of mathematicians and physicists may confidently be expected to lead ultimately to the construction of realistic constitutive equations describing quite complicated types of mechanical behaviour for metals, and indeed, this is well recognized to be one of the major objectives of plasticity theory (see, for example, Ref. 7). However, the power of the mathematician (even with the aid of modern computers) to solve problems of continuum theories, embodying even relatively simple constitutive equations, is still limited to comparatively simple situations. Unfortunately, it is not the case that hypervelocity impact is one of these situations. The circumstance of axial symmetry (assuming that this does apply) itself represents considerable complexity (in comparison say with that of spherical symmetry), and the presence of a deforming boundary is a major complication. It must therefore be recognized that a direct attack on the problem of crater formation is unlikely to be profitable, and much more progress is likely to result from an indirect attack. In my opinion, the most promising line of attack is to discuss first problems of the dynamic expansion of spherical cavities, and this appears to be quite feasible even when the assumed mechanical behaviour is relatively complicated, e. g., when shock waves occur (see Ref. 8). The result of this work would be a very comprehensive knowledge of the mechanics of the formation of spherical cavities in extended and finite media under dynamic conditions, which would, of course, include a quantitative assessment of the effects of high rates-of-strain and high stress-amplitudes. This knowledge could then be applied to suggest simplified treatments of the problem of crater formation, which in turn could be applied to the quantitative analysis of hypervelocity impact data. All this may seem to some of you to represent a rather long train of thought, but nevertheless the approach proposed does seem to represent a useful one for consideration at the present time. The success of any proposed approach depends ultimately upon the evolution of a simplified theory of crater formation, which is in accord with the salient known facts for hypervelocity impact, and which enables predictions to be made, particularly in respect of impact velocities higher than those that can be achieved at present under controlled laboratory conditions. Of course, one must be careful in adopting preconceived ideas in attacking a complicated physical situation, but the approach (or one closely similar to it) that I have outlined should enable a correct physical picture of the mechanics of hypervelocity impact to be gradually built up. I have not discussed approaches based upon fluid mechanical behaviour of the projectile and target materials, but their status is likely to resemble that of corresponding approaches made in the early work on shaped charges (see Ref. 5).

## MATHEMATICAL METHODS IN HYPERVELOCITY IMPACT

### STUDIES OF NONLINEAR STRESS-WAVE PROPAGATION

The foregoing discussion should, I think, have made clear the importance of studies of the propagation of nonlinear stress waves and of studies of the mechanical behaviour of metals in situations which are comparable in their time-scale with that of hypervelocity impact. It is appropriate therefore now to mention briefly some recent work of this kind that has been done at A. R. D. E. This work is of course of general interest in the mechanics of solids.

First, Kolsky and Douch (9) have made certain experimental studies of plastic wave propagation in specimens of pure copper, pure aluminium, and an aluminium alloy. They employed modified Hopkinson pressure-bar techniques, and the experimental data obtained were used to construct dynamic stress-strain curves, which were then used to test the validity of the rate-of-strain independent theory of longitudinal plastic wave propagation due to G. I. Taylor, Th. von Karman, and H. A. Rahmatulin (see Ref. 5). Second, Tupper (10) has made a theoretical study of the propagation of plane stress waves through a steel plate, of finite thickness but otherwise of unlimited extent, following the detonation of a uniform slab of high explosive placed in intimate contact with the plate. His study involved consideration of the nonlinear compressibility of the plate material under high pressures, and attention was given to the reflection of stress waves at the rear face of the plate.

Both the above studies are too detailed, in respect of either experimental or theoretical considerations, for it to be possible to give further adequate summary and discussion here. However, the important point to which I wish to draw attention is that a careful examination of the procedures followed in these studies shows clearly that mathematical methods are essential in attempting to elucidate the mechanical behaviour of metals when the physical situation unavoidably involves inertia effects associated with the propagation of stress waves.

### CONCLUDING REMARKS

In this paper, I have attempted to give a rather brief discussion of the place of mathematical methods in the theoretical mechanics of the hypervelocity impact of metals. In particular, attention has been directed towards the relevance of studies of nonlinear stress-wave propagation. For such studies, a prerequisite is adequate knowledge of the nonlinear mechanical behaviour of metals, this being incorporated into constitutive equations of sufficient realism and generality. This is a central field of work in the mechanics of solids, and many applied mathematicians are becoming increasingly aware of the importance of this field, which seems likely to receive much attention in future research.

### REFERENCES

1. M. J. Lighthill, "Mathematical methods in compressible flow theory", *Comm. Pure Appl. Math.* 7 (1954), 1-10.
2. Sir Geoffrey Taylor, "Rheology for mathematicians", *Proceedings of the Second International Congress on Rheology* (Edited by V. G. W. Harrison), Butterworth's Scientific Publications, London, 1954, pp. 1-6.

## MATHEMATICAL METHODS IN HYPERVELOCITY IMPACT

3. M. A. Biot, "Applied mathematics - an art and a science", J. Aero. Sci. 23 (1956), 406-410, 489
4. H. G. Hopkins and H. Kolsky, "Mechanics of hypervelocity impact of solids", Proceedings of the Fourth Symposium on Hypervelocity Impact (Edited by A. S. Galbraith), Air Proving Ground Center, Eglin Air Force Base, Fla., 1960, paper no. 12.
5. H. G. Hopkins, "Dynamic anelastic deformations of metals", Appl. Mech. Rev. 14 (1961), 417-431.
6. W. Prager, "Introduction to Mechanics of Continua", Ginn and Co., Boston, 1961.
7. R. Hill, "The Mathematical Theory of Plasticity", Clarendon Press, Oxford, 1950.
8. H. G. Hopkins, "Dynamic expansion of spherical cavities in metals", Progress in Solid Mechanics - Vol. I (Edited by I. N. Sneddon and R. Hill), North-Holland Pub. Co., Amsterdam, 1960, ch. III.
9. H. Kolsky and L. S. Douch, "Experimental studies in plastic wave propagation", unpublished War Office Report, 1961.
10. S. J. Tupper, "On the propagation of plane stress waves generated in a thick steel plate by a surface explosion", unpublished War Office Report, 1961.

## SOME THEORETICAL MODELS OF HYPERVELOCITY IMPACT

N. Davids, Y. K. Huang, and W. Jaunzemis

The Pennsylvania State University  
University Park, Pennsylvania

### 1. INTRODUCTION

#### Spatial Distribution of Cratering Effects

This paper offers some theoretical models of hypervelocity impact in order to investigate the penetration of metal projectiles into metal targets. The phenomena, and hence their analysis, are complex because different effects predominate in different parts of the crater. Thus, in a zone ahead of the projectile, the target material is under ultra-compression. This zone is bounded in front by an advancing shock wave and gradually shades off at the sides into another zone where the material, in some state of fluidity, deforms sideways along the crater. Ultimately, as the angle of deviation from the direction of impact is increased, the material has undergone permanent plastic deformation and hills up to form the lip of the crater. The zones described are depicted in Figure 1. The transition between the two zones is not meant to be exact in such a schematic picture.

As a first approximation, the impact crater will be considered to be hemispherical, as shown in Figure 2, and a simple model of spherical flow will be adopted. The direct aim of any penetration theory is, of course, to predict the shape and size of the crater. The spherical flow model does this by analyzing the state of the material in Zone I of Figure 1, (taking  $\theta = 90$  degrees) and leads to a value for the diameter and volume of the crater comparable with experimental data.

The flow effects in Zone II (Fig. 1) will be investigated by introducing a second model of axisymmetrically spherical flow. This naturally involves one more space variable in the basic equations, which means more mathematical complexity than that associated with the first model. However, we are in a position to be able to reach results which kinematically account for the formation of the crater lip.

### 2. SPHERICAL SHOCK WAVES

#### Distribution of Effects in Time

Just as the study of the problem is conveniently divided into zones, we can divide up the sequence of events in the cratering process for detailed analysis.

## THEORETICAL MODELS

### List of Notations

$r$	radius ( $r = a$ when $t = 0$ )	$p$	pressure
$\theta$	co-latitude ( $\theta' = b$ when $t = 0$ )	$\gamma$	adiabatic index
$t$	time	$\alpha$	progressing wave exponent
$u$	particle velocity	$\beta$	ditto
$a$	acoustic velocity	$\delta$	ditto
$c$	shock wave velocity	$\epsilon$	ditto
$m$	mass flow rate	$\xi$	progressing wave parameter
$M$	momentum	$U$	progressing wave function
$M^*$	impact Mach number	$D$	ditto
$E$	energy	$P$	ditto

$$\partial = d$$

i. Initial State - here the projectile at impact becomes imbedded just inside the target material and generates a region of excessively compressed material. The problem is to determine the nature of this zone.

ii. Expansion State - the compressed material, which might be in some state of fluidity and act in a manner similar to an explosion, expands further into the target, generating shock fronts and forming the crater.

iii. Final Phase - the shock wave decays, permanent deformation at the crater stops, secondary deformations appear at the back or other parts of the target. The main problem is to determine when this phase begins.

Of course it must be understood that these phases are not distinct events, nor may it be even possible in a given case to make the separation.

### 3. THE INITIAL STAGE

#### Fluid Impact

We lack direct data on the initial stage of crater formation. Headington and Jaunzemis <sup>(5)</sup> have made an analytical investigation of this stage based on the conservation laws and the known equations of state of the materials. Such a detailed study provides the initial and boundary conditions required for the expansion stage. However, we shall here make simpler assumptions about the initial stage during which the projectile becomes imbedded in the target material:

a) The impact is so rapid that the time required for the compression pressure to reach its maximum is negligible. This means that the problem may be treated essentially as one of an explosion at the impact center.

b) The shock-compression process is adiabatic.

c) The pre-impact shape of the projectile is unimportant for the case of semi-infinite target here.

These assumptions lead to the so-called "ballistic" model of fluid impact. See Charters and Summers <sup>(3, 4)</sup>. Here it is supposed that immediately on impact

## THEORETICAL MODELS

the projectile and some of the target material are converted to a fluid shell under ultra-pressure which propagates radially. In this analysis, however, we shall remove the assumption that the fluid shell be uniform -- part of our effort will be to determine the pressure profile and velocity distribution in it as functions of radius.

### 4. THEORY OF PROGRESSING SHOCK WAVES

We have previously, in Figure 1, considered the different angular zones in cratering. If we restrict the problem to spherically symmetric forces, and hence to radial velocities, we simplify it to a point capable of theoretical analysis. However, since edge effects are being neglected the results will be limited to some angle less than 90 degrees from the normal.

Our model is related to that of a spherical blast wave in a gas and may make the following assumptions about the medium during propagation of the shock wave:

- a) Changes of state are adiabatic, or entropy is constant along a particle path.
- b) The medium is a compressible fluid, with shear effects neglected.
- c) The entropic equation of state is such that the pressure is a function of the density alone, i. e., the medium is also barotropic.
- d) We also have two alternative possibilities, namely, constant total energy or constant total momentum for the cavity expansion process.

### 5. THE BASIC EQUATIONS FOR SPHERICAL FLOW

The conservation of mass, momentum, and entropy may be expressed as follows:

$$\frac{\partial u}{\partial t} + u \frac{\partial u}{\partial r} + \frac{1}{\rho} \frac{\partial p}{\partial r} = 0 \quad (5.1)$$

$$\frac{\partial \rho}{\partial t} + u \frac{\partial \rho}{\partial r} + \rho \frac{\partial u}{\partial r} + \frac{2u\rho}{r} = 0 \quad (5.2)$$

$$\frac{\partial (p\rho^{-\gamma})}{\partial t} + u \frac{\partial (p\rho^{-\gamma})}{\partial r} = 0 \quad (5.3)$$

with the equation of state

$$f(p, \rho) = p\rho^{-\gamma} = A = \text{const.} \quad (5.4)$$

where  $\gamma$  is the adiabatic index for a barotropic medium.

## THEORETICAL MODELS

### 6. PROGRESSING WAVE SOLUTIONS

We shall use a known general method which reduces the above basic equations to a succession of ordinary differential equations. By assuming a specific form for the equations, a set of particular solutions depending on one variable will be obtained. These are called "progressing waves" and are expressed in the form (1):

$$u = t^\beta \xi U(\xi) \quad (6.1a)$$

$$\rho = t^\delta D(\xi) \quad (6.1b)$$

$$\frac{p}{\rho} = t^\epsilon \xi^2 P(\xi) \quad (6.1c)$$

with  $\xi = r t^{-\alpha}$ , where  $\alpha, \beta, \delta, \epsilon$  are parameters, and  $U, D, P$  functions to be determined. By introducing the variable  $\xi$  we have defined geometrically a family of surfaces  $\xi = \text{constant}$  in the  $(r, t)$  plane, which play an important role in the analysis. Although these are not the trajectories of the particles of the medium, we shall see that the shock front belongs to this family of surfaces.

We now explore these solutions mathematically by substituting the expressions (6.1) into the equations (5.1) through (5.3), giving respectively:

$$\xi t^{\beta-1} \left\{ \beta U - \alpha(U + \xi U') + (U + \xi U') U t^{\beta-\alpha+1} + (2P + \xi P' + \xi P \frac{D'}{D}) t^{\epsilon-\alpha-\beta+1} \right\} = 0 \quad (6.2a)$$

$$t^{\delta-1} \left\{ \delta D - \alpha \xi D' + t^{\beta-\alpha+1} [3DU + \xi(D'U + U'D)] \right\} = 0 \quad (6.2b)$$

$$\begin{aligned} \xi^2 t^{\epsilon+\delta-1} \left\{ \gamma P(\delta - \alpha \xi D') - [DP(\delta + \epsilon) - \alpha(2DP + \xi DP' + \xi PD')] - \right. \\ \left. - U t^{\beta-\alpha+1} [(2DP + \xi DP' + \xi PD') - \gamma \xi PD'] \right\} = 0 \end{aligned} \quad (6.2c)$$

The sense in these equations is that it is possible to eliminate the explicit factor  $t$  by properly choosing the exponents, thereby leaving a system of functions of one independent variable  $\xi$ . This is accomplished by letting

$$\epsilon = 2\beta = 2(\alpha - 1) \quad (6.3)$$

so that  $t^{\beta-\alpha+1} = t^{\epsilon-\beta-\alpha+1} = 1$  and, after dividing by  $\xi t^{\beta-1}, t^{\delta-1}, t^{\delta-1+\epsilon}$

which are not zero for  $t > 0$ , we then have:

# THEORETICAL MODELS

$$\beta U - \alpha(U + \xi U') + U(U + \xi U') + (2P + \xi P' + \xi P \frac{D'}{D}) = 0 \quad (6.4a)$$

$$\delta D + \xi D'(U - \alpha) + D(3U + \xi U') = 0 \quad (6.4b)$$

$$\xi P'(U - \alpha) + P[2(U + \beta - \alpha) - \delta(\gamma - 1)] - \xi P(\gamma - 1)(U - \alpha) \frac{D'}{D} = 0 \quad (6.4c)$$

We now have a system of ordinary differential equations for the unknown functions  $U(\xi), D(\xi), P(\xi)$  and two free parameters  $\alpha$  and  $\delta$ . The substitutions (6.1), which may appear artificial, are thus justified.

We shall now reduce the number of variables further. Solving (6.4b) for  $\xi D'/D$  gives

$$\xi \frac{D'}{D} = -\frac{\delta + 3U + \xi U'}{U - \alpha} \quad (6.5)$$

When this is put into the remaining two equations, we obtain:

$$\beta U + \xi P' + (U - \alpha)(U + \xi U') + P(2 - \frac{\delta + 3U + \xi U'}{U - \alpha}) = 0 \quad (6.6a)$$

$$2\beta - \delta(\gamma - 1) + 2(U - \alpha) + \xi(U - \alpha) \frac{P'}{P} + (\gamma - 1)(\delta + 3U + \xi U') = 0 \quad (6.6b)$$

These equations (linear in  $\xi U'$  and  $\xi P'$ ) may be simultaneously solved, giving

$$\xi U' = \frac{-U(U - 1)(U - \alpha) + P(\delta + 2\beta + 3\gamma U)}{(U - \alpha)^2 - \gamma P} \quad (6.7a)$$

$$\xi P' = P \left\{ \frac{U(U - 1)(\gamma - 1) + (U - \alpha)[2 - U(3\gamma - 1)] + P[2\gamma + \frac{2\beta - \delta(\gamma - 1)}{U - \alpha}]}{(U - \alpha)^2 - \gamma P} \right\} \quad (6.7b)$$

From these we obtain

$$\frac{\partial P}{\partial U} = P \left\{ \frac{2\alpha + U(\alpha - 3) + \gamma U(2U - 3\alpha + 1) - P[2\gamma + \frac{2\beta - \delta(\gamma - 1)}{U - \alpha}]}{U(U - 1)(U - \alpha) - P(\delta + 2\beta + 3\gamma U)} \right\} \quad (6.8)$$

This is the basic differential equation for progressing waves. After the appropriate solution has been found for  $P = P(U)$ , the function  $\xi = \xi(U)$  is found by a quadrature of (6.7a) and the density function  $D(\xi)$ , from (6.5).

These progressing wave solutions, as we shall see, provide a general mathematical description of an expanding cavity reasonably consistent with the

## THEORETICAL MODELS

given conditions of initiation of the process. There remains the problem of choosing the two parameters  $\alpha$  and  $\xi$

### 7. BOUNDARY CONDITIONS AT SHOCK FRONT

We shall narrow down the number of parameters by examining the compatibility of our solution with the Rankine-Hugoniot conditions across a shock front. If the undisturbed and disturbed medium parameters are  $u_0$ ,  $\rho_0$ ,  $p_0$  and  $u_1$ ,  $\rho_1$ ,  $p_1$  respectively and the shock wave velocity is  $c$  then these relations are:

$$\rho_0(u_0 - c) = \rho_1(u_1 - c) = m \quad (7.1a)$$

$$\rho_1 u_1 (u_1 - c) - \rho_0 u_0 (u_0 - c) = p_0 - p_1 \quad (7.1b)$$

$$\rho_1 (u_1 - c) \left( e_1 + \frac{u_1^2}{2} \right) - \rho_0 (u_0 - c) \left( e_0 + \frac{u_0^2}{2} \right) = p_0 u_0 - p_1 u_1 \quad (7.1c)$$

where  $e = \frac{p}{(\gamma - 1)\rho}$

When the undisturbed medium is at rest, with  $u_0 = p_0 = 0$ , these reduce to:

$$\rho_1(c - u_1) - \rho_0 c = 0 \quad (7.2a)$$

$$\rho_1 u_1 (c - u_1) - p_1 = 0 \quad (7.2b)$$

$$\rho_1 (c - u_1) \left( \frac{u_1^2}{2} + \frac{p_1}{(\gamma - 1)\rho_1} \right) - p_1 u_1 = 0 \quad (7.2c)$$

Since  $\xi_1 = r t^{-\alpha}$  along the shock front, so  $c = \frac{\partial r}{\partial t} = \alpha \frac{1}{r} = \partial \xi_1 t^{\alpha-1}$

From (6.1) and (6.3) with  $c - u_1 = \xi_1 t^\beta (\alpha - \xi_1 U)$ , equations (7.2)

become:

$$t^{3+\beta} \xi_1 D(\alpha - \xi_1 U) - \alpha \rho_0 \xi_1 t^\beta = 0 \quad (7.3a)$$

$$t^{3+2\beta} \{ U(\alpha - \xi_1 U) - P \} D \xi_1^2 = 0 \quad (7.3b)$$

$$t^{3+3\beta} \left\{ (\alpha - \xi_1 U) \left( \frac{1}{2} U^2 + \frac{P}{\gamma - 1} \right) - P U \right\} D \xi_1^3 = 0 \quad (7.3c)$$

## THEORETICAL MODELS

To secure independence of  $t$  in these equations, it is necessary to make:

$$\delta = 0 \quad (7.4)$$

With this condition and the relation (6.3), the assumed form for the progressing waves reduces to:

$$u = \frac{r}{t} U(\xi) \quad (7.5a)$$

$$\rho = D(\xi) \quad (7.5b)$$

$$\frac{p}{\rho} = \left(\frac{r}{t}\right)^\epsilon P(\xi) \quad (7.5c)$$

$$p = \left(\frac{r}{t}\right)^2 P(\xi) D(\xi) \quad (7.5d)$$

with  $\xi = r t^{-\alpha}$ . These solutions show that on the shock front or free surface, where  $\xi$  is constant, the physical quantities such as velocity, pressure, density, and wave velocity are constant on the rays  $r/t = \text{constant}$ .

### 8. ENERGY CONDITION

The assumption of constant total energy for the cavity expansion process is now made, provided that certain secondary effects are neglected. With  $\xi = \xi_i$  representing the shock front at time  $t$ , the total energy in the fluid shell is given by

$$E(t) = 2\pi \int_{r_0}^{r_i} \left( \frac{1}{2} \rho U^2 + \frac{p}{\gamma-1} \right) r^2 dr \quad (8.1)$$

where  $r_i = \xi_i t^\alpha$  and  $r_0 = \xi_0 t^\alpha$  are the shell radii shown in Figure 2.

Substituting (6.1),  $r = \xi t^\alpha$ , and  $dr = t^\alpha d\xi$  for given  $t$ , the energy expression becomes:

$$E(t) = 2\pi t^{8+5\alpha-2} \int_{\xi_0}^{\xi_i} \left( \frac{1}{2} U^2 + \frac{P}{\gamma-1} \right) D \xi^4 d\xi \quad (8.2)$$

Since the integral is independent of  $t$ , we make the energy independent of time by satisfying the condition  $8+5\alpha-2=0$ . From (7.4) we obtain

$$\alpha = \frac{2}{5} \quad (8.3)$$

$$\beta = -\frac{3}{5} \quad (8.4)$$

$$\epsilon = -\frac{6}{5} \quad (8.5)$$

## THEORETICAL MODELS

### 9. EQUATION OF STATE FOR IRON

From data given by Walsh, Rice, McQueen, and Yarger, (2) the equation of state for iron can be formulated through Figure 3. It fits a polytropic law of the form (5.4), for two ranges of pressure:

a) Intermediate pressure range,  $.76 < V/V_0 < .85$

$$\rho \rho^{-16} = 1.3 \times 10^{-13} \quad (9.1a)$$

b) High pressure range,  $.85 < V/V_0 < .98$

$$\rho \rho^{-9} = 6.9 \times 10^{-7} \quad (9.1b)$$

where  $p$  is to be measured in kilobars ( $10^9$  dynes per sq. cm), and  $\rho$  in grams per cu. cm. Below about 80 kilobars we have a transition to elastic or elastoplastic behavior. The nature of this transition is considerably uncertain and will not be discussed here further. Unlike gases, the high value of  $\gamma$  (i.e., the comparatively small changes in density) shows up in that we do not have the strong shocks present as with gases, when the density changes by a factor of about 6.

### 10. P-U DIAGRAM FOR IRON UNDER PRESSURES IN INTERMEDIATE RANGE

If we assume constant total energy for the cratering process, the 2/5-power law holds and, with  $\gamma = 16$  and the numerical values given by (8.3) through (8.5), the differential equation (6.8) becomes:

$$\frac{\partial P}{\partial U} = 2P \left\{ \frac{0.4 + U(16U - 2.9) + P \left( \frac{3}{5U - 2} - 16 \right)}{U(U - 0.4)(U - 1) - 1.2P(40U - 1)} \right\} \quad (10.1)$$

A family of integral curves are sketched in the vector field of Figure 4. The vectors are oriented with slopes calculated from (10.1) on a grid network for  $U = 0$  to 0.05. Certain portions of the diagram have been amplified in finer intervals, in order to determine more accurately the initial behavior of the solution curve.

One type of solution is obtained by starting from the shock front and applying the known shock transition relations for pressure, density, and velocity. If we consider a small surface element of the shock front, we can neglect the sphericity in its immediate neighborhood and obtain the transition relations giving pressure, density, and velocity immediately behind it.

Equations (7.2) may be written:

$$c - u_1 = \frac{\rho_0}{\rho_1} c \quad (10.2a)$$

$$c - u_1 = \frac{\rho_1}{\rho_1 u_1} \quad (10.2b)$$

$$c - u_1 = \frac{\rho_1 u_1}{\frac{1}{2} \rho_1 u_1^2 + \frac{\rho_1}{(\gamma - 1)}} \quad (10.2c)$$

THEORETICAL MODELS

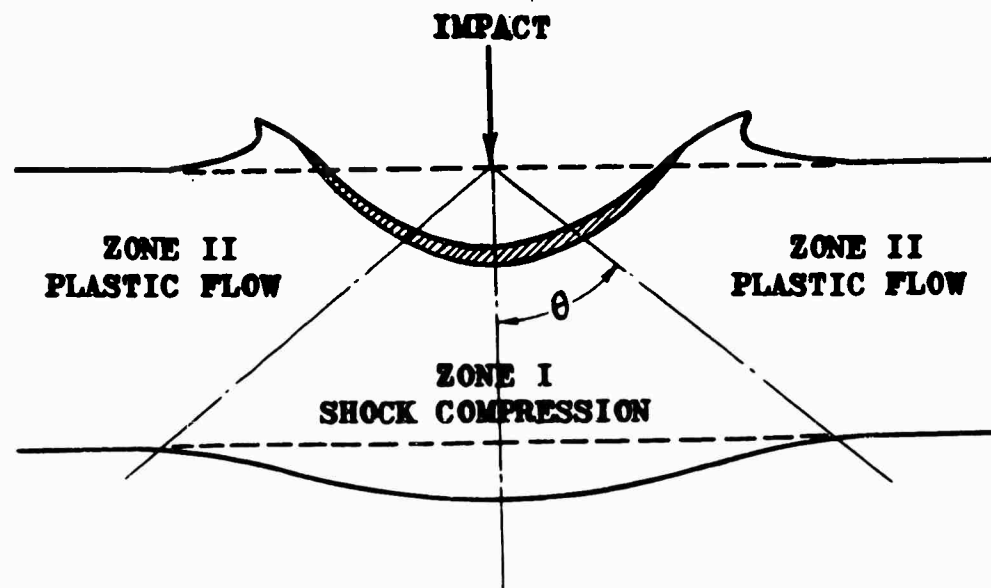


**FIG.1 REGIONS AROUND IMPACT CRATER**

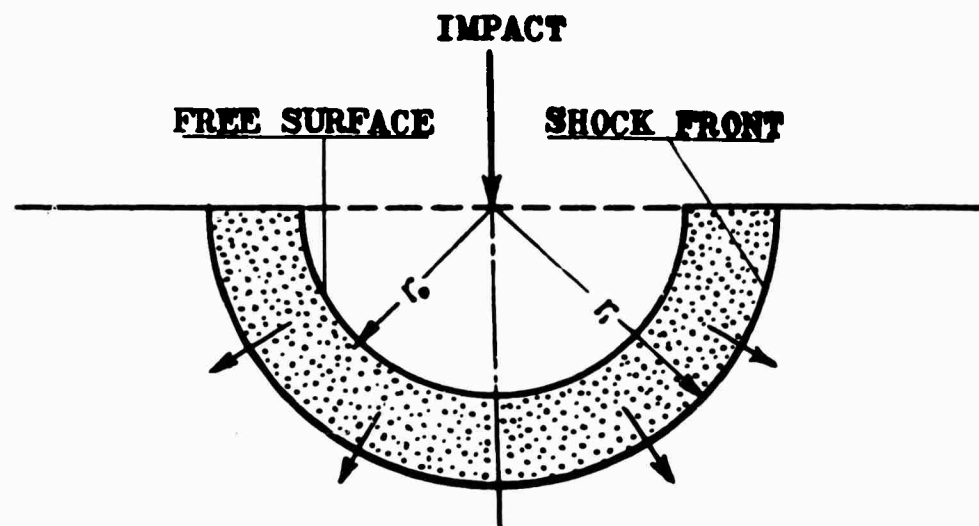


**FIG.2 SIMPLIFIED HEMISPHERICAL CRATER**

# THEORETICAL MODELS

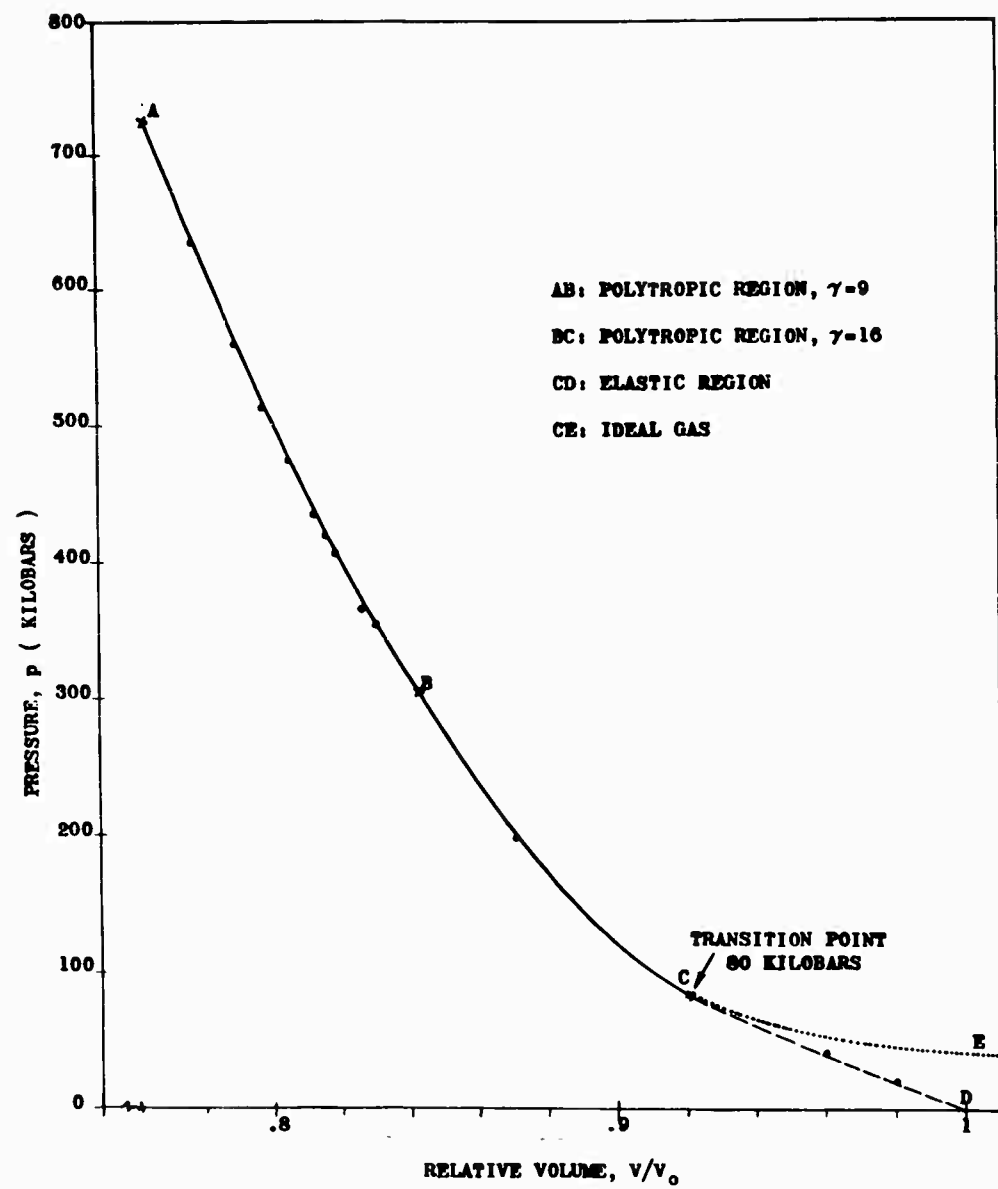


FIG.3 GRAPHICAL EQUATION OF STATE FOR IRON UNDER HIGH PRESSURE  
 ( Data from Walsh, Rice, McQueen, Yarger )

# THEORETICAL MODELS

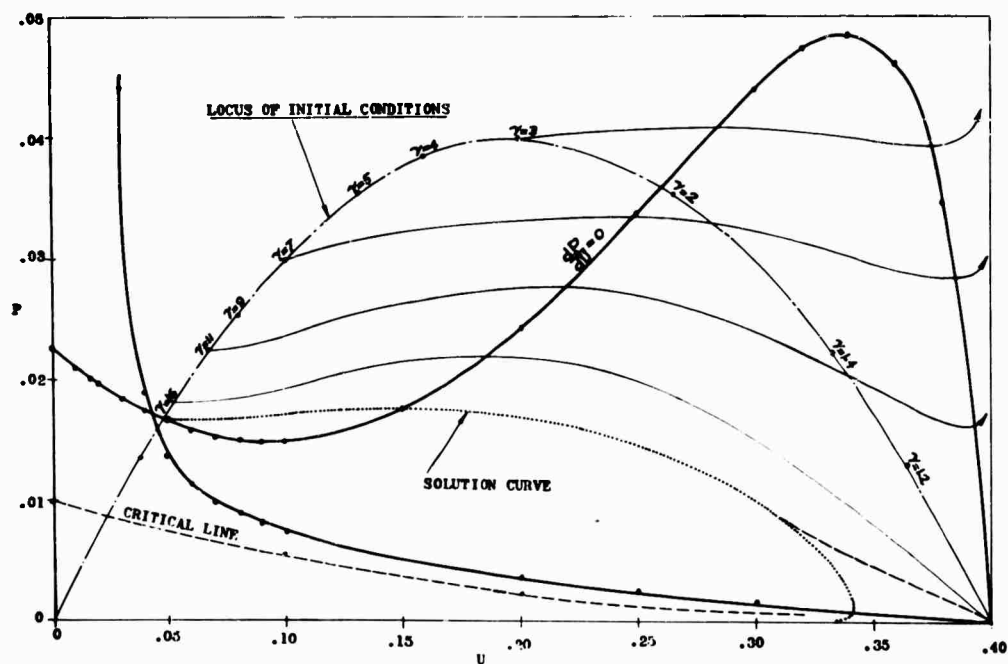


FIG.4 INTEGRAL CURVES ON P-U DIAGRAM FOR PROGRESSING WAVES

## THEORETICAL MODELS

Combining (10. 2b) and (10. 2c) gives  $u_1 = \sqrt{\frac{2p_1}{(\gamma-1)\rho_1}}$  ; (10. 2a) then gives

$c = \frac{\rho_1}{\rho_1 - \rho_0} u_1$       Equating (10. 2a) and (10. 2b) gives  $p_1 = c \rho_0 u_1$       which  
then leads to  $\frac{\rho_1}{\rho_0} = \frac{\gamma+1}{\gamma-1}$       Let  $\mu^2 = \frac{\gamma-1}{\gamma+1} = \frac{\rho_0}{\rho_1}$  , then

$$u_1 = c(1 - \frac{\rho_0}{\rho_1}) = c(1 - \mu^2) \quad (10. 3a)$$

$$p_1 = c \rho_0 u_1 = \rho_0 c^2 (1 - \mu^2) \quad (10. 3b)$$

$$a = \sqrt{\frac{\partial p}{\partial \rho}} = c \mu \sqrt{1 + \mu^2} \quad (10. 3c)$$

The last expression is obtained from the entropic equation of state (5. 4) and is conventionally referred to as "acoustic velocity" in Gas Dynamics.

Since  $\xi = \xi_1$  on the shock front,  $c = dr/dt = a r/t$  and, from (7. 5), we get:

$$U(\xi_1) = a(1 - \mu^2) \quad (10. 4a)$$

$$D(\xi_1) = \frac{\rho_0}{\mu^2} \quad (10. 4b)$$

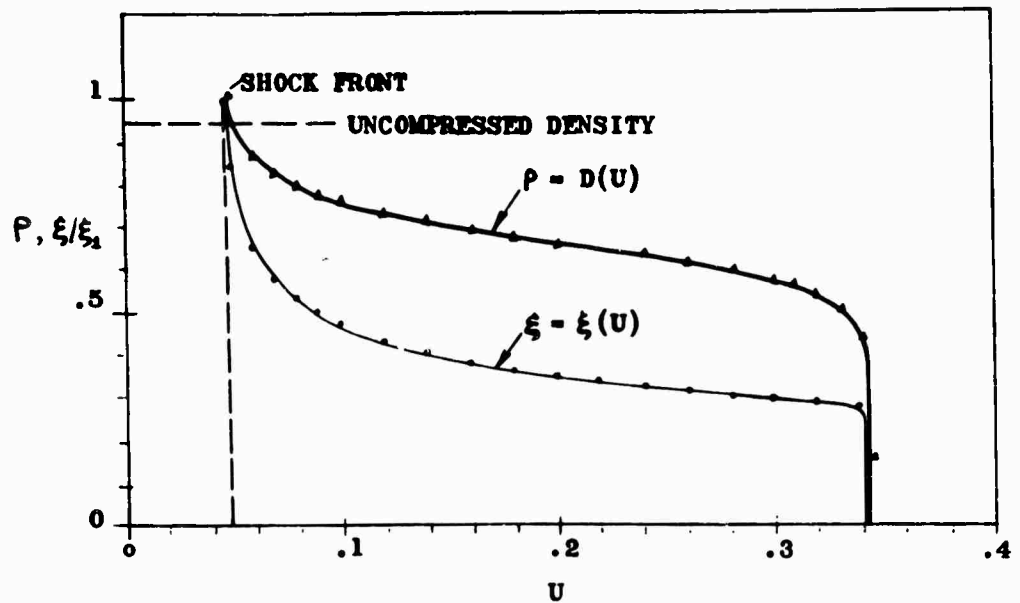
$$P(\xi_1) = a^2 \mu^2 (1 - \mu^2) \quad (10. 4c)$$

just behind the shock. The right side of (10. 4a) and (10. 4c) represent a definite point in the  $P - U$  plane, through which a particular solution curve is determined. We may refer to it as our "starting point," and proceed to draw the particular solution curve. It should be noted that the constant  $\xi_1$ , still undetermined, is not needed here. For iron with  $\gamma = 16$ ,  $\mu = 0.939$ , and  $a = 2/5$ , the starting point is located, in Figure 4, by  $U(\xi_1) = 0.04758$  and  $P(\xi_1) = 0.01661$ .

### 11. DETERMINATION OF $\xi$ and $D$ FUNCTIONS

Having determined the function  $P(U)$  as given by the solution curve in the  $P - U$  diagram, we have effected one quadrature. We now perform a second quadrature by referring to the differential equations (6. 5) and (6. 7a). In both of these the variables are separated, so a straightforward procedure leads directly to the  $\xi$  and  $D$  functions, shown graphically in Figure 5.

It should be noted that  $\xi$  is determined to within the multiplicative constant  $\xi_1$ , its value at the shock front. From the differential equation for the density function, we see that  $\rho$  also admits of a free multiplicative constant  $\rho = \rho_1$ , just behind the shock front. This value is given by  $\rho_1 = \frac{\rho_0}{\mu^2} = 8.9 \text{ gm/cm}^3$   
for iron with  $\rho_0 = 7.84 \text{ gm/cm}^3$ .

FIG.5 PROFILES OF DENSITY AND  $\xi$  PARAMETERS

From Figure 5 we see that the density of the material decreases after the shock front has passed, at first rapidly, then it levels off until  $U = 0.341$ , where it falls so rapidly to zero as to create almost a discontinuity there. The same occurs with the  $\xi$  function. The interpretation is this. Since  $\xi$  decreases with radius  $r$  when time  $t$  is held constant, the curves show that the density drops behind the shock front very rapidly at first, while the velocity increases. Ultimately there is a sudden density drop to zero, indicating a rather sharp boundary from the material to free space. In Figure 5 this is at  $U = 0.341$ , which would represent the crater boundary on the basis of the theory worked out here from the polytropic law. Unfortunately we can not use this discontinuity, as the computed density of the material has by this time dropped considerably from its free space value  $\rho_0$ . Since there is no evidence that any solid in these processes ever has a density less than  $\rho_0$ , we must find a way to deviate from the polytropic law at low pressures. The simplest way is to level off the density at  $\rho = \rho_0$ . The effect of this will be examined later.

## 12. THE PARTICLE TRAJECTORIES

In order to study the transient motion of the crater surface, there remains only one more construction to be made, i.e., that of  $r - t$  plane, showing the particle trajectories. (By "particle" we mean macroscopically all the particles on a shell surface of radius  $r$ .) From (7.5a) a vector field can be constructed on the  $r - t$  plane. Thus Figure 6 was made by substituting data for  $U(\xi)$  in

# THEORETICAL MODELS

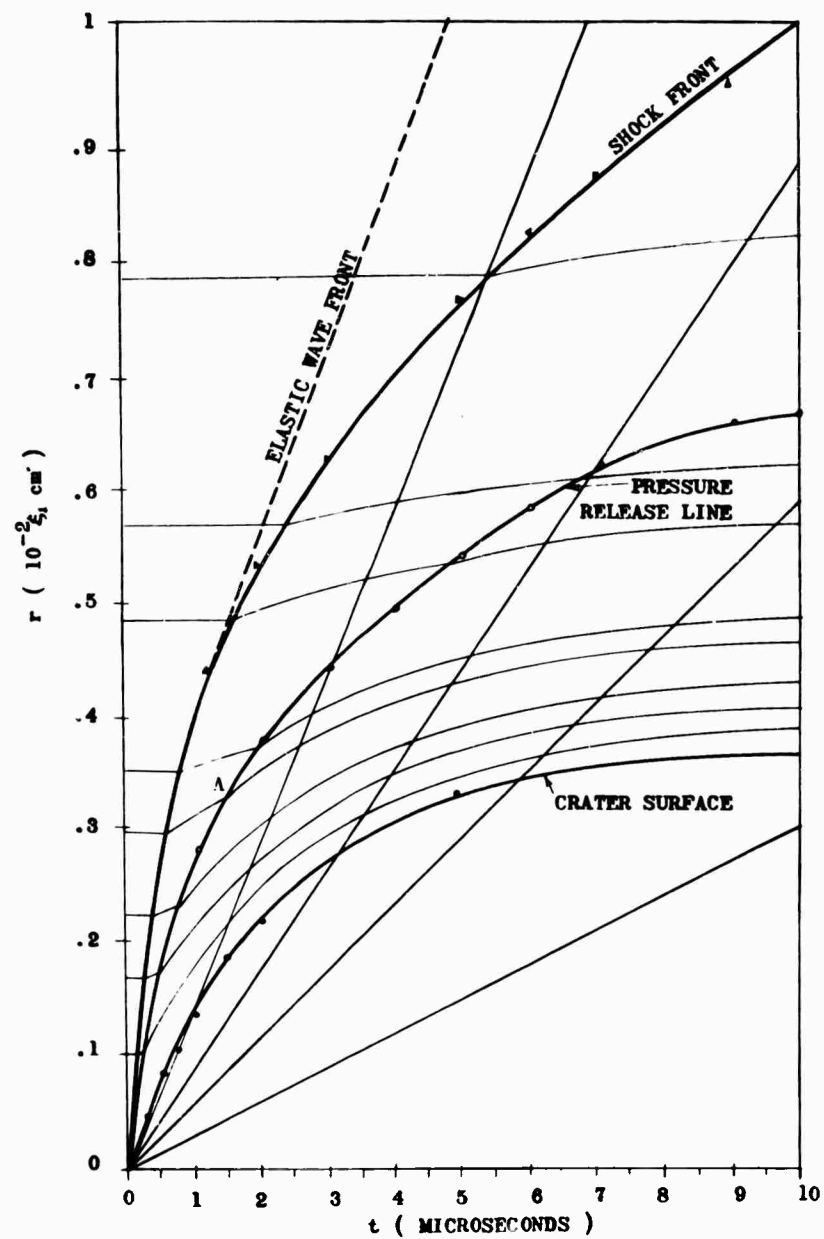


Figure 6. Motion of Fluid Shell and Crater Surface on r-t Diagram for Impact at 20,000 fps

# THEORETICAL MODELS

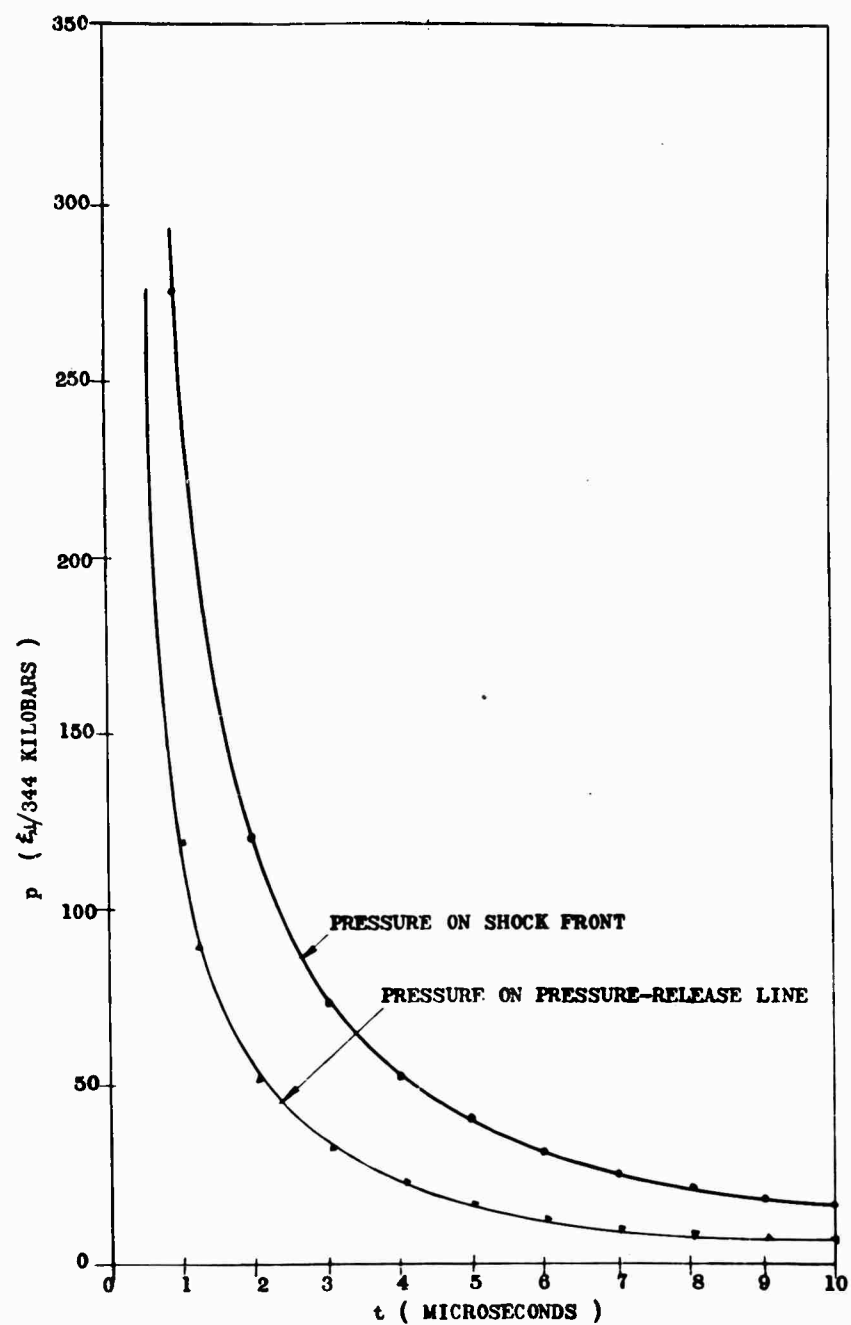


FIG.7 PRESSURE VARIATIONS ON FLUID SHELL

## THEORETICAL MODELS

$dr/dt = u(r, t) = \frac{r}{t} U(\xi)$ ,  $\xi = r t^{2/5}$ . It is convenient, because of the factor  $r/t$ , to plot the vectors along rays  $r/t = \text{constant}$ .

It is interesting to note that the shock front path is determined by the equation  $r = \xi_1 t^{2/5}$ , with  $\xi_1$  yet to be determined. The pressure release line is given by  $r = 0.704 \xi_1 t^{2/5}$ , showing the motion of the trailing surface. Finally, the crater surface is determined from volume conservation of the fluid shell enveloped by the shock front and trailing surface.

### 13. THE PRESSURE VARIATION

From Equation (7.5d) we see that the pressure variation in the medium shows the same discontinuity at the crater surface as the density function does. Inside the medium, the pressure, as given by

$$p = \left(\frac{r}{t}\right)^2 (0.0004) \rho_0 \xi_1^2 \quad (13.1)$$

is characterized by a non-zero variation, shown in Figure 7. This violates the constant energy condition (since some work is continually being done at the boundary due to the non-vanishing pressure), but it shows approximately the impulsive type of pressure to fit the impact problem. On the other hand, just beyond the jump, the vanishing of  $D$  function gives us zero pressure as the constant energy condition requires. We may regard this properly as a "free" surface.

The only way to come out exactly with a free surface, without having the discontinuity in pressure as just described, is for the solution  $v$  curve in Figure 4 to terminate at  $U = 0.4$  and  $P = 0$ . As the plotting of Figure 4 is very sensitive to the initial conditions, we can not say now for sure whether failure to reach this end point is due to inaccuracies, or whether the initial conditions need to be changed slightly. However, our solution approaches the required point closely enough to delineate the crater surface behavior, which is hardly sensitive at all to this discrepancy.

Physically, the pressure drops very rapidly with decreasing radius from the shock region. We are uncertain just how or just where it drops zero because we are neglecting the departure of the material from the polytropic law at low pressures. This does not appear to matter too much in locating the locus of the crater surface.

### 14. NUMERICAL RESULTS FOR STEEL-TO-STEEL IMPACT

We shall apply the foregoing analysis to an example of steel-to-steel impact. Consider a steel pellet 3/16 inches in diameter striking a thick steel plate with a velocity of 20,000 ft/sec. This velocity, which happens to be especially critical for terminal ballistic effects<sup>(6)</sup>, represents a Mach number  $M^* = u/c = 1.025$  in steel. With  $\rho_0 = 7.84 \text{ gm/cm}^3$ , the impact energy of the projectile is:

$$E = \frac{1}{2} (0.443 \text{ gm}) (6.1 \times 10^5 \text{ cm/sec})^2 = 8.25 \times 10^{10} \text{ ergs}$$

## THEORETICAL MODELS

If all this energy goes into the shock wave (no loss), the integration of (8.2) comes out to be:

$$E = 2\pi(3.8 \times 10^{-4})\rho_1 \xi_1^5 = 8.25 \times 10^{10} \text{ ergs}$$

Substituting  $\rho_1 = \frac{\rho_0}{\mu^2} = 8.9 \text{ gm/cm}^3$  gives  $\xi_1 = 329 \text{ cm/sec}^{2/5}$ . The pressure behind the shock front is given by:

$$p = 1.6 \times 10^{-5} t^{-6/5} \text{ kilobars}$$

with  $r$  in cm and  $t$  in sec. Thus,  $p = 582$  kilobars at  $t = 1/2$  microsecond;  $p = 254$  kilobars at  $t = 1$  microsecond. These show that the high pressure regime is over in about 1 microsecond (during which the crater is being formed and the material might be in some state of fluidity).

Figure 6 is a plot of radius versus time, showing the motion of the shock front, trailing surface, and some of the particle paths. We note that after the density has fallen to its free space values, the particles at the trailing surface still have a residual forward motion, which is effectively over at most by 10 microseconds. The crater surface is stopped at the value  $r = 0.37 \times 10^{-2}$   $\xi_1 = 1.2$  cm.

Following the notation of Charters (3), (4) and of Partridge (7), we get  $p/d = 1.63$  where  $p = 1.2$  cm = penetration depth,  $d = 0.738$  cm = projectile diameter. Referring to Charters' curve of  $p/d$  versus  $V/c$  (where  $V$  = velocity of the projectile,  $c$  = sound velocity), this point lies on the fluid impact curve (cf. 2/3-power law of Figure 8 in this paper). The experimental points for steel-to-steel impact, as obtained at the University of Utah, do not conform to the 2/3-power law. However, these points only go up to an Impact Mach number of 0.5. Our constant total energy analysis provides a 2/5-power law, with comparable results shown in Figure 8.

### 15. FURTHER REMARKS

The foregoing analyses appear to give reasonable results, in spite of the many assumptions needed and uncertain values of the parameters required. For the steel-to-steel impact at 20,000 ft/sec, the crater is formed in about 1 microsecond. The pressure is a maximum just behind the shock front. There is then a trailing wave in which the pressure drops rapidly. Just at crater, the material has been decompressed. From Figure 6 we see that the shock front starts out at about the impact velocity and slows down to the elastic wave velocity during the first microsecond, while the crater surface penetrates at a much slower speed. An interesting side feature is that if we had allowed the pressure-release line to stop suddenly at 1 microsecond, as marked by point A in Figure 6, we would come out with about the same value for the crater radius.

### 16. MOMENTUM CONDITION

If we base the progressing wave solutions on the constant total momentum instead of constant total energy condition, a different set of values will be obtained

# THEORETICAL MODELS

for the parameters  $\alpha$ ,  $\beta$ ,  $\delta$ , and  $\epsilon$ . The axial component of momentum of the moving shell is given by:

$$M(t) = 2\pi \int_{\xi_0}^{\xi} \int_0^{\pi/2} \rho u \cos \theta \cdot r^2 \sin \theta \, d\theta \, dr = \pi \int_{\xi_0}^{\xi} t^{\delta+\beta} DU \xi r^2 dr \quad (16.1)$$

With  $r = \xi t^a$ ,  $dr = t^a d\xi$ , this becomes:

$$M(t) = \pi t^{\delta+4a-1} \int_{\xi_0}^{\xi} DU \xi^3 d\xi \quad (16.2)$$

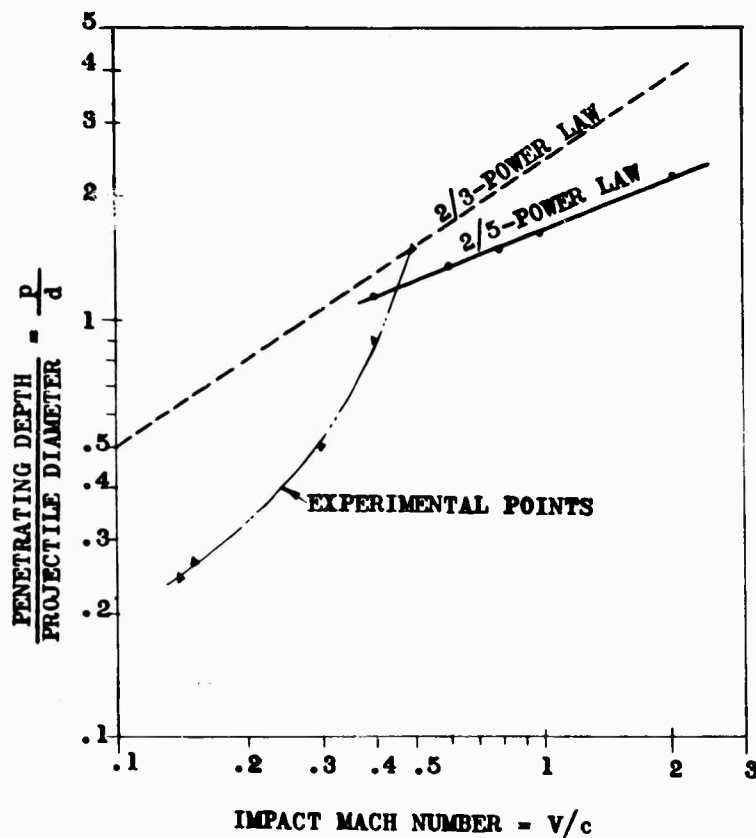


FIG.8 COMPARISON OF 2/5-POWER LAW WITH EXPERIMENTAL DATA FROM UNIVERSITY OF UTAH

# THEORETICAL MODELS

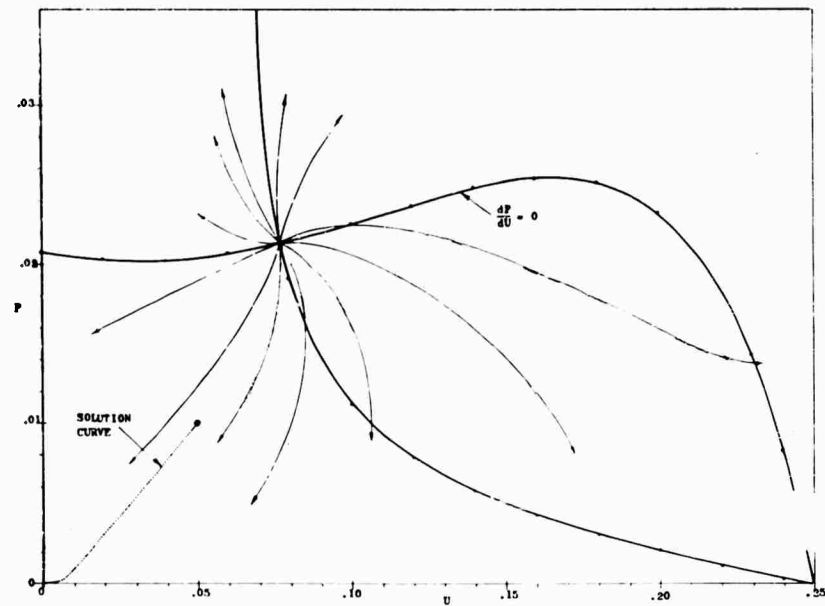


FIG.9 P-U DIAGRAM FOR PROGRESSING WAVES ON THE BASIS OF CONSTANT MOMENTUM

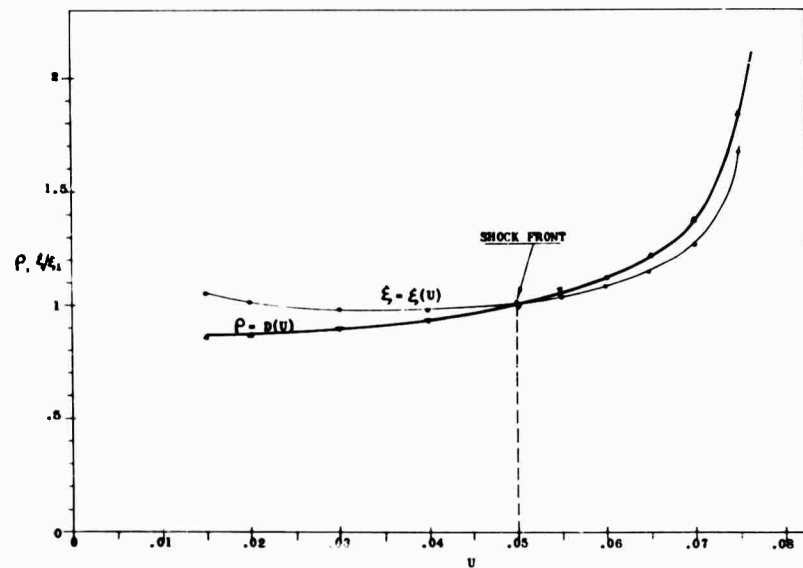


FIG.10 PROFILES OF DENSITY AND  $\xi$  PARAMETERS FOR CONSTANT MOMENTUM

## THEORETICAL MODELS

so that, from (7.4), time independence requires  $4\alpha - 1 = 0$ . Hence

$$\alpha = \frac{1}{4} \quad (16.3)$$

$$\beta = -\frac{3}{4} \quad (16.4)$$

$$\epsilon = -\frac{3}{2} \quad (16.5)$$

Thus, a  $1/4$ -power law holds for cratering process with momentum conserved.

It is of interest to examine the behavior of the material in the high-pressure range, with  $\gamma = 9$ . The basic differential equation (6.8) then becomes:

$$\frac{\partial P}{\partial U} = 2P \left\{ \frac{36U^2 - (U-1) - 12P(3 - \frac{1}{4U-1})}{U(U-1)(4U-1) - 6P(18U-1)} \right\} \quad (16.6)$$

from which the  $P - U$  diagram of Figure 9 is established. Here we obtain the particular solution curve, with the starting point given by  $U(\xi_1) = 0.05$  and  $P(\xi_1) = 0.01$ . It should be noted that this solution curve tends to end at the origin. This results in some uncertainty in the determination of  $\xi$  and  $D$  functions (beyond the limits  $U < 0.015$  and  $U > 0.05$ , see Fig. 10). In this connection, the motions of the shock front and trailing wave have not been understood so well as to reach any crater size from the  $1/4$ -power law. Yet we would not draw any conclusion here, although it is interesting to note that crater formation depends on the absorption of impact energy while the transfer of momentum effects rupture of the projectile and target.

## 17. THE AXISYMMETRIC FLUID IMPACT

So far, the edge effects of cratering have been neglected; further progress in the analysis of crater formation requires this to be taken into account. Let us consider the axisymmetrically spherical flow of an ideal fluid. The governing equations, as expressed in terms of Lagrangian material coordinates, are:

$$\left[ \frac{\partial^2 r}{\partial t^2} - r \left( \frac{\partial \theta}{\partial t} \right)^2 \right] \frac{\partial r}{\partial a} + \left[ 2 \frac{\partial r}{\partial t} \frac{\partial \theta}{\partial t} + r \frac{\partial^2 \theta}{\partial t^2} \right] r \frac{\partial \theta}{\partial a} + \frac{1}{\rho} \frac{\partial p}{\partial a} = 0 \quad (17.1)$$

$$\left[ \frac{\partial^2 r}{\partial t^2} - r \left( \frac{\partial \theta}{\partial t} \right)^2 \right] \frac{\partial r}{\partial b} + \left[ 2 \frac{\partial r}{\partial t} \frac{\partial \theta}{\partial t} + r \frac{\partial^2 \theta}{\partial t^2} \right] r \frac{\partial \theta}{\partial b} + \frac{1}{\rho} \frac{\partial p}{\partial b} = 0 \quad (17.2)$$

$$\left( \frac{\partial r}{\partial a} \frac{\partial \theta}{\partial b} - \frac{\partial r}{\partial b} \frac{\partial \theta}{\partial a} \right) \rho r^2 \sin \theta = \rho_0 a^2 \sin b \quad (17.3)$$

$$p = p(\rho) \quad (17.4)$$

# THEORETICAL MODELS

where  $a$  and  $b$  are the initial material coordinates. Semi-inverse methods have been employed to consider motions of the type:  $r = r(a, t)$ . The continuity equation (17.3) then becomes:

$$\rho r^2 \sin \theta \frac{\partial r}{\partial a} \frac{\partial \theta}{\partial b} = \rho_0 a^2 \sin b \quad (17.5)$$

For incompressible fluids,  $p$  is readily eliminated from equations (17.1) and (17.2). Motions of the type  $r = r(a, t)$  are then defined by:

$$r^2 \frac{\partial \theta}{\partial t} = T(t) \theta(\theta) \quad (17.6)$$

where  $T(t)$  and  $\theta(\theta)$  are arbitrary functions. Integrating this for  $r = \sqrt{a^2 + \frac{t^2}{a^6}}$ ,

$T(t) = kt$ , and  $\theta(\theta) = \sin \theta$ , gives  $\theta \approx 2 \tan^{-1}(1 + \frac{t^2}{2a^2})$ , provided  $t/a < 1$  (with  $b = \pi/2$ ). This particular solution shows up the deformation pattern of the surface layer of material (Fig. 11). It is to be noted that appropriate pressure boundary conditions are not satisfied here. Up to this stage of the study, we have attempted to account for the sidewise flow of crater formation, in the sense of a kinematic prediction only.

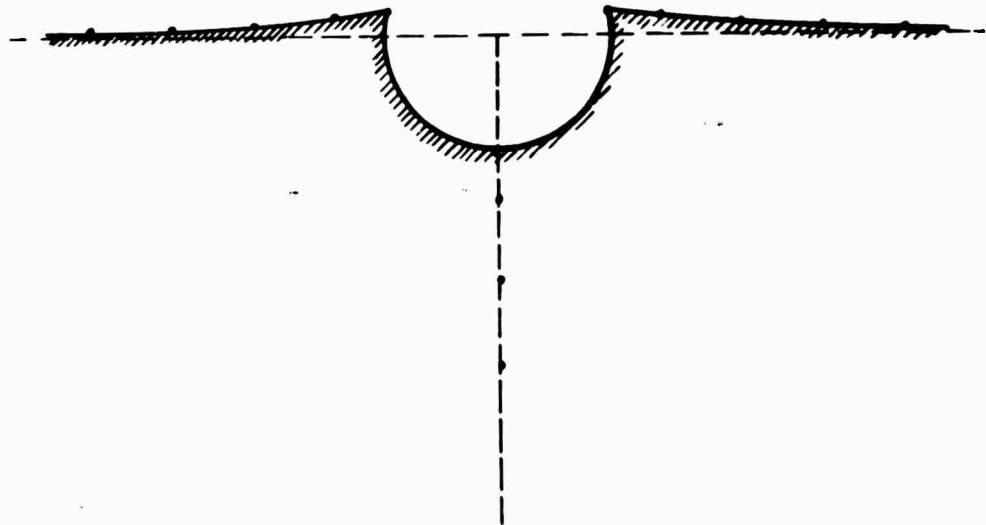


FIG.11 CRATER SHAPE PREDICTED BY ANALYSIS  
OF AXISYMMETRICALLY SPHERICAL FLOW

## THEORETICAL MODELS

### 18. CLOSURE

Generally speaking, the progressing wave analysis appears to give promise of reasonable agreement with experimental values. It also indicates an approach in favor of the dependence of crater formation on energy absorption. Yet the theoretical models proposed have to be referred to their pertinent governing effects, in order to avoid misunderstanding.

### REFERENCES

1. Courant, R., and Friedrichs, K. O., "Supersonic Flow and Shock Waves," Interscience Publishers, 1948.
2. Walsh, J. M., Rice, M. H., McQueen, R. G., and Yarger, F. L., "Shock Wave Compressions of Twenty-Seven Metals," Phys. Rev. 108 (1957).
3. Charters, A. C., and Summers, J. L., "Some Comments on the Phenomena of High-Speed Impact," Decennial Symposium (1959).
4. Charters, A. C., and Summers, J. L., "High-Speed Impact of Metal Projectiles in Targets of Various Materials," Proc. Third Symposium on Hypervelocity Impact (1958).
5. Headington, E., and Jaunzemis, W., "Large Amplitude Waves Generated by Pressure Pulses," Pennsylvania State University (unpublished).
6. Rogers, W. K., Jr., and Vikestad, W. S., "Hypervelocity Impact by Collision of Two Projectiles," BRL Tech. Note 1337, Aberdeen Proving Ground, August 1960.
7. Partridge, W. S., Van Fleet, H. B., and Whited, C. R., "An Investigation of Craters Formed by High-Velocity Pellets," University of Utah Contr. AF. 18(600)1217, Tech. Report OSR-9.

SESSION III

THEORY  
(continued)

CHAIRMAN

DR. H. G. HOPKINS

ARMAMENT RESEARCH AND DEVELOPMENT

ESTABLISHMENT, UNITED KINGDOM

#### CHAIRMAN'S REMARKS

I should like to thank Mr. F. E. Howard for his kind remarks introducing me as the Chairman of this Session.

There is little that I wish to say at the beginning of this morning's session on theoretical work relating to hypervelocity impact. However, I will draw attention to the fact that among the papers to be presented is one by A. E. Olshaker and R. L. Bjork of the RAND Corporation; in view of Dr. Bjork's earlier important work, I feel sure that this paper will be awaited by us all with much interest.

I have noted that different authors are using different systems of dimensional units in their papers presented at this Symposium. This practice is likely to cause unnecessary confusion, and I therefore wish to suggest that it would be worthwhile for some definite ruling to be given on the correct practice to be followed in the future.

# INERTIAL, VISCOUS, AND PLASTIC EFFECTS IN HIGH SPEED IMPACT

T. D. Riney and P. R. Chernoff

General Electric Company  
Philadelphia, Pennsylvania

## INTRODUCTION

When an ultra-high-speed projectile strikes a target a strain-rate which depends on the impact velocity is imposed on the projectile and target materials. The resulting flow of the materials will be resisted not only by the inertial forces, but also by the dynamic yield strength of the materials and by viscosity stresses with magnitudes which depend upon the strain-rate. The only serious attempt (1) to calculate the phenomenology of hypervelocity impact from basic principles has considered the medium to be a perfect fluid and, consequently, neglected the strength and viscosity effects. Since the predictions from the perfect fluid model are found to differ with the extrapolated results of hypervelocity impact tests, one is led to consider the problem anew in order to formulate a mathematical model which takes into account the inertial, viscous, and strength effects.

## VISCO-PLASTIC MODEL

Such a plastic solid (exhibiting visco-plastic flow) is most simply represented by a Bingham model. The material is considered rigid if stressed below its yield strength, whereas above this value the material acts like a Newtonian viscous liquid; a schematic representation of such a material is given in Figure 1a. In simple shearing flow, in which the velocity is  $q(y)$ , and  $dq/dy$  is a constant  $D$ , this means that

$$\begin{aligned} \tau - \tau_0 &= \mu_0 D & (\tau \geq \tau_0) \\ \tau + \tau_0 &= \mu_0 D & (\tau \leq -\tau_0) \\ D &= 0 & (|\tau| < \tau_0), \end{aligned} \quad (1)$$

where  $\tau_0$  is the yield value of the shearing stress and  $\mu_0$  is a constant. These equations may be written in the form

$$\tau = \mu(D) D, \quad (2)$$

# INERTIAL, VISCOUS, AND PLASTIC EFFECTS

where the strain-rate dependent viscosity coefficient  $\mu = \mu(D)$  is given by

$$\begin{aligned} \mu(D) &= \mu_0 + \frac{\tau_0}{|D|} & (|\tau| \geq \tau_0) \\ &= \infty & (|\tau| < \tau_0). \end{aligned} \quad (3)$$

This dependence of  $\mu$  on  $D$  is illustrated in Figure 1b. The viscosity coefficient decreases with increased strain-rate.

In order to extend this idealized visco-plastic model to a material subjected to hypervelocity impact the stress versus strain-rate relations, (2) and (3), must be generalized. As formulated above, only the properties of the material in simple shear flow are defined; corresponding relations for three dimensional flow are required. The expressions will be somewhat simplified by assuming that the projectile is axisymmetric in geometry and that it strikes a semi-infinite target normal to the axis of symmetry. Furthermore, the angular momentum of the projectile is assumed to be zero at impact. Under these hypotheses the total stress tensor becomes (2, 3)

$$\tau_{ik} = -p \delta_{ik} + \mu (D_{ik} - \frac{2}{3} \text{div } \bar{q} \delta_{ik}), \quad (4)$$

where the viscosity  $\mu$  is of the form (3) with  $D$  defined in terms of the strain-rate tensor  $D_{ik}$  according to

$$D^2 = D_{rz}^2 + \frac{1}{2} (D_{rr}^2 + D_{\theta\theta}^2 + D_{zz}^2) - \frac{2}{3} (\text{div } \bar{q})^2 \quad (5)$$

and the flow criterion is given in terms of

$$\tau^2 = \tau_{rz}^2 + \frac{1}{2} [(\tau_{rr} - p)^2 + (\tau_{\theta\theta} - p)^2 + (\tau_{zz} - p)^2] \quad (6)$$

The nonvanishing components of the strain-rate tensor are defined by

$$\begin{aligned} D_{rr} &= 2 \frac{\partial q_r}{\partial r} & D_{\theta\theta} &= \frac{2}{r} q_r & D_{zz} &= 2 \frac{\partial q_z}{\partial z} \\ D_{rz} &= D_{zr} & &= \frac{\partial q_r}{\partial z} + \frac{\partial q_z}{\partial r} \end{aligned} \quad (7)$$

Explicitly, the dependence of the viscosity on the strain-rate is given by the relation:

$$\begin{aligned} \mu &= \mu_0 + \frac{\tau_0}{\left[ D_{rz}^2 + \frac{1}{2} (D_{rr}^2 + D_{\theta\theta}^2 + D_{zz}^2) - \frac{2}{3} (\text{div } \bar{q})^2 \right]^{1/2}} & (\tau^2 \geq \tau_0^2) \\ \mu &= \infty & (\tau^2 < \tau_0^2). \end{aligned} \quad (8)$$

# INERTIAL, VISCOUS, AND PLASTIC EFFECTS

Actually this accounts for the viscous effect only approximately as  $\mu_0$  would be dependent upon local pressure, shear gradients, and temperature, since it must be far beyond Newtonian conditions.  $\tau_0$  would also depend on local conditions.

The usual Navier-Stokes equations of motion for viscous fluids are consequently complicated by replacing the constant coefficient of viscosity with this function. So too is the energy equation which may be derived under the assumption that no heat is transferred between neighboring particles of the material. These, together with the continuity equation and the equation of state give the following five relations (Eulerian formulation) for the five dependent variables  $q_r$ ,  $q_z$ ,  $p$ ,  $\rho$  and specific internal energy  $U$ :

$$\frac{d\rho}{dt} + \rho \operatorname{div} \bar{q} = 0 \quad (9) \quad \text{(Mass)}$$

$$\begin{aligned} \rho \frac{dq_r}{dt} = & - \frac{\partial p}{\partial r} + \frac{\partial}{\partial r} \left[ \mu(D) \left( 2 \frac{\partial q_r}{\partial r} - \frac{2}{3} \operatorname{div} \bar{q} \right) \right] \\ & - \frac{\partial}{\partial z} \left[ \mu(D) \left( \frac{\partial q_z}{\partial r} + \frac{\partial q_r}{\partial z} \right) \right] + 2 \frac{\mu(D)}{r} \left( \frac{\partial q_r}{\partial r} - \frac{q_r}{r} \right) \end{aligned} \quad (10) \quad \text{(Radial Momentum)}$$

$$\begin{aligned} \rho \frac{dq_z}{dt} = & - \frac{\partial p}{\partial z} + \frac{\partial}{\partial z} \left[ \mu(D) \left( 2 \frac{\partial q_z}{\partial z} - \frac{2}{3} \operatorname{div} \bar{q} \right) \right] \\ & + \frac{1}{r} \frac{\partial}{\partial r} \left[ r \mu(D) \left( \frac{\partial q_r}{\partial z} + \frac{\partial q_z}{\partial r} \right) \right] \end{aligned} \quad (11) \quad \text{(Axial Momentum)}$$

$$p = f(\rho, U) \quad (12) \quad \text{(State)}$$

$$\rho \left[ \frac{dU}{dt} + p \frac{d(1/\rho)}{dt} \right] = \mu(D) D^2. \quad (13) \quad \text{(Energy)}$$

The material time derivatives may be expanded according to the relation

# INERTIAL, VISCOUS, AND PLASTIC EFFECTS

$$\frac{d}{dt} ( \quad ) = \frac{\lambda ( \quad )}{\partial t} + \bar{q} \cdot \text{grad} ( \quad ) .$$

A discussion of our choice for the equation of state is given later in the paper.

## STUDY OF THE GOVERNING EQUATIONS

An examination of the momenta, continuity and energy equations shows that necessary conditions for dynamic similarity of two projectile-target systems, projectile and target of same material for a given system, are that they have the same values for the dimensionless ratios (4)

$$\begin{aligned} B_0 &= \frac{D_s \tau_0}{\mu_0 v_0} & R_0 &= \frac{D_s \rho_0 v_0}{\mu_0} \\ M^* &= \frac{v_0}{\sqrt{p/\rho_0}} & N &= \frac{U}{v_0^2} \end{aligned} \quad (14)$$

In these quantities the characteristic length,  $D_s$ , is the diameter of the sphere with mass equal to that of the projectile;  $v_0$  the impact velocity;  $\rho_0$  the

density of the undisturbed medium;  $p$  and  $U$ , represent the characteristic values of pressure and specific internal energy, respectively.

$B_0$  and  $R_0$  are the familiar Bingham-Oldroyd and Reynolds numbers which ordinarily arise separately in the theory of slow visco-plastic flow and the theory of viscous liquids respectively. Here both occur because the model includes the two types of flow.  $M^*$  is the generalized Mach number which for an ideal gas may be decomposed into two factors, the ratio of specific heat and the ordinary Mach number  $M$ . Since the fundamental equations of flow also include the equation of state, equality of numbers (14) is not sufficient to ensure that two geometrically similar flows are dynamically similar. The equation of state, an experimentally determined function, does not lend itself to this type of investigation since it is different for different materials.

The equations governing the flow can be written in dimensionless form by setting

$$\begin{aligned} \mathbf{r} &= L \mathbf{r}' & \mathbf{z} &= L \mathbf{z}' & \rho &= \rho_0 \rho' \\ q_T &= v q_T' & q_z &= v q_z' & U &= v^2 U' \\ p &= \rho_0 v^2 p' & t &= L v^{-1} t' \\ \mu_0 &= L \rho_0 v R^{-1} & \tau_0 &= \rho_0 v^2 B R^{-1} \end{aligned}$$

where  $D_s$  is replaced by  $L$  and  $v_0$  by  $v$  in the definitions of  $B$ ,  $R$ , and the dimensionless quantities are indicated by a prime. The governing equations then become

$$\frac{d\rho'}{dt} + \rho' \operatorname{div}' \bar{\mathbf{q}}' = 0$$

(15)

$$\begin{aligned} R \left\{ \rho' \frac{dq'_r}{dt'} + \frac{\partial p'}{\partial r'} \right\} = & \\ \left\{ \frac{\partial}{\partial r'} \left( 2 \frac{\partial q'_r}{\partial r'} - \frac{2}{3} \operatorname{div}' \bar{\mathbf{q}}' \right) + \frac{\partial}{\partial z'} \left( \frac{\lambda q'_r}{\lambda z'} + \frac{\lambda q'_z}{\lambda r'} \right) + \frac{2}{r'} \left( \frac{\partial q'_r}{\partial r'} - \frac{q'_r}{r'} \right) \right\} & \\ + B \left\{ \frac{\partial}{\partial r'} \frac{1}{|D'|} \left( 2 \frac{\partial q'_r}{\partial r'} - \frac{2}{3} \operatorname{div}' \bar{\mathbf{q}}' \right) + \frac{\partial}{\partial z'} \frac{1}{|D'|} \left( \frac{\partial q'_r}{\partial z'} + \frac{\partial q'_z}{\partial r'} \right) \right. & \\ \left. + \frac{2}{r'} \frac{1}{|D'|} \left( \frac{\lambda q'_r}{\partial r'} - \frac{q'_r}{r'} \right) \right\} & \end{aligned} \quad (16)$$

$$\begin{aligned} R \left\{ \rho' \frac{dq'_z}{dt'} + \frac{\partial p'}{\partial z'} \right\} = & \\ \left\{ \frac{\partial}{\partial z'} \left( 2 \frac{\partial q'_z}{\partial z'} - \frac{2}{3} \operatorname{div}' \bar{\mathbf{q}}' \right) + \frac{1}{r'} \frac{\partial}{\partial r'} r' \left( \frac{\partial q'_r}{\partial z'} + \frac{\lambda q'_z}{\partial r'} \right) \right\} & \\ + B \left\{ \frac{\partial}{\partial z'} \frac{1}{|D'|} \left( 2 \frac{\partial q'_z}{\partial z'} - \frac{2}{3} \operatorname{div}' \bar{\mathbf{q}}' \right) + \frac{1}{r'} \frac{\partial}{\partial r'} r' \frac{1}{|D'|} \left( \frac{\lambda q'_r}{\partial z'} + \frac{\partial q'_z}{\partial r'} \right) \right\} & \end{aligned} \quad (17)$$

$$p' = \frac{1}{\rho_0 v^2} f(\rho_0 \rho', v^2 U') \quad (18)$$

$$R \left\{ \rho' \left[ \frac{dU'}{dt'} + p' \frac{d(1/\rho)}{dt'} \right] \right\} = \left\{ D'^2 \right\} + B \left\{ |D'| \right\} \quad (19)$$

# INERTIAL, VISCOUS, AND PLASTIC EFFECTS

The momenta and energy equations are thus of the form

$$R \left\{ \dots \right\} + \left\{ \dots \right\} + B \left\{ \dots \right\} = 0,$$

where the inertial, viscous, and strength terms are associated with the factors  $R$ ,  $1$  and  $B$  respectively. The quantities in the brackets will be of order unity if  $L$ ,  $v$ ,  $\rho_0$  are truly representative values. If so, and if one of the three numbers  $R$ ,  $1$ ,  $B$  is much greater than the other two, a single set of terms in each equation predominates and the motion may be approximately described by equating the coefficient of the predominant number to zero. For example, if  $R \gg 1$ ,  $B$ , the equations (16), (17), (19) reduce to

$$\begin{aligned} \rho' \frac{dq'_r}{dt'} + \frac{\partial p'}{\partial r'} &= 0 \\ \rho' \frac{dq'_z}{dt'} + \frac{\partial p'}{\partial z'} &= 0 \\ \rho' \frac{dU'}{dt'} + p' \frac{d(1/\rho)}{dt'} &= 0, \end{aligned} \quad (20)$$

respectively.

Actually, these combined with (15) and (18) are the perfect fluid equations, and are seen to be valid when the inequalities  $R \gg 1$ ,  $B$  hold, i.e., only when the inertial effect predominates, i.e., by (14),

$$v \gg \text{maximum} \left( \sqrt{\tau_0 / \rho_0}, \mu_0 / L \rho_0 \right). \quad (21)$$

As the rate of flow decreases so does the characteristic velocity until eventually, when the flow ceases,  $v = 0$ . Clearly, in the late stages of flow the inequalities required for the perfect fluid approximation to be valid are reversed, i.e.,  $R \ll 1$ ,  $B$ . At other stages, two or possibly all three of the groups of terms may be equally important.

It is seen that the strength terms are insignificant during the early stages of flow but become predominant in the latter stages. The question arises as to the importance of the viscous terms. Clearly, they would always be negligible only if

$$\text{maximum} (R, B) \gg 1 \quad (22)$$

for the entire range of  $v$ ,  $(0, v_0)$ . Since  $R$  and  $B$  are respectively, monotone increasing and decreasing functions of  $v$  the left side of (22) is attained when  $R = B$ , i.e., when the flow velocity is given by

$$v^* = \sqrt{\tau_0 / \rho_0}.$$

## INERTIAL, VISCOUS, AND PLASTIC EFFECTS

The required inequality for the viscous terms to be negligible throughout the cratering process therefore becomes

$$\mu_0 \ll L \sqrt{\rho_0 \tau_0} \quad (23)$$

At the instant of impact an exceedingly large strain-rate gradient is imposed at the surface of contact. The use for example, of the diameter  $D_s$  for the representative length  $L$  cannot be justified; a much smaller value is actually required. Accordingly, the inequalities (21) and (23) are very restrictive. The viscosity is probably never really negligible in the time interval immediately after impact.

### CHOICE OF PARAMETERS

The principal difficulty in testing these conclusions, and a real difficulty in the application of the governing equations themselves, is in assuming the viscosity coefficients for structural materials such as steel, copper, or aluminum. The viscosity involved here has little relation to ordinary creep data. The choice of an appropriate value for the dynamic shear yield strength  $\tau_0$  is nearly as troublesome. It is known to increase with increasing strain-rate, but values are not known in the hypervelocity impact range. Therefore, to check the philosophy used in the construction of the mathematical model exploratory calculations had to be performed in which the values of  $\mu_0$  and  $\tau_0$  were varied over several orders of magnitude and the impact velocity  $v_0$  was allowed to assume a set of values in the range of interest.

In choosing trial values for  $\mu_0$  our starting point has been the values quoted by Perzyna (5). On the basis of the results of internal energy measurements by Kolsky (6) he computes the approximate values \*

$$\begin{aligned} \text{Steel: } \mu_0 &= 0.8 \text{ gm cm}^{-1} \text{ microsecond}^{-1} \\ \text{Copper: } \mu_0 &= 0.4 \text{ gm cm}^{-1} \text{ microsecond}^{-1} \end{aligned}$$

Our calculations have all been for iron and  $\mu_0$  is assumed to be within a factor of ten of 0.8.

For mild steel, Reiner (7) quotes the static yield stress to be approximately

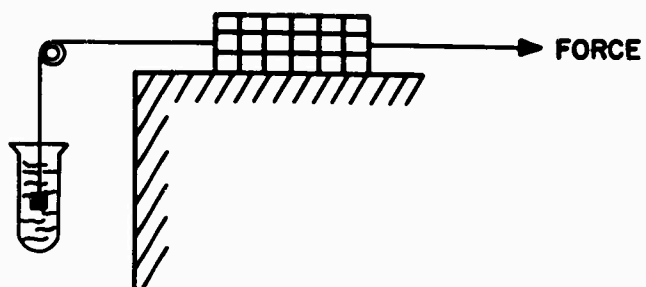
$$\tau_0 = 10^{-2} \text{ gm cm}^{-1} \text{ microsecond}^{-2},$$

i. e., ten kilobars. For our calculations it is the dynamic yield stress that is pertinent. The above value is assumed to be the lowest value likely, and  $\tau_0$  is varied up to one hundred times as large, i. e., one megabar.

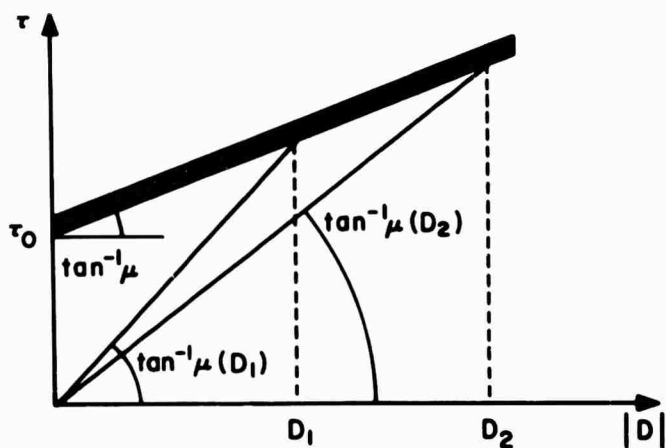
### ONE-DIMENSIONAL PROBLEM

For the exploratory calculations we will consider the one-dimensional impact of two semi-infinite bodies, Figure 2, and compare the results obtained with those given by the simple Rankine-Hugoniot equations (perfect fluid). In one

\* The gram-centimeter-microsecond system is used throughout this paper.



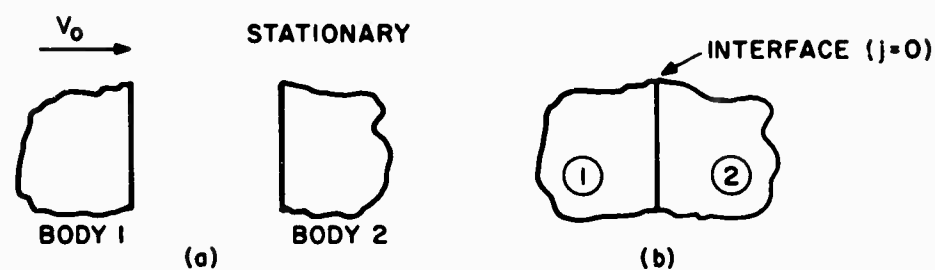
(a)



(b)

Figure 1. Schematic representations of the (a) forces in a Bingham body and (b) the dependence of the viscosity on the strain-rate.

# INERTIAL, VISCOUS, AND PLASTIC EFFECTS



STATION j QUANTITY	BODY 1		BODY 2	
	$-\infty$ TO $-1$	0	0	1 TO $\infty$
q	$V_0$	$q_H$	$q_H$	0
x	$j\Delta x$	0	0	$j\Delta x$
$v = 1/\rho$	$1/\rho$	$1/\rho_H$	$1/\rho$	$1/\rho$
U	0	$U_H$	$U_H$	0
p	0	$p_H$	$p_H$	0

(c)

Figure 2. Illustration of impact situation (a) just before impact, (b) at impact, and (c) a display of the initial and boundary data. The subscript H refers to the Rankine-Hugoniot values.

dimensional Lagrangian form the governing equations are as follows:

$$\left\{ \begin{array}{l} \frac{\partial q}{\partial x} = \frac{\lambda}{\lambda t} \left( \frac{\rho_0}{\rho} \right) \quad \text{or} \quad \frac{\partial X}{\partial x} = \frac{\rho_0}{\rho} \\ \rho_0 \frac{\partial q}{\partial t} = - \frac{\lambda p}{\lambda x} + \frac{4}{3} \mu_0 \frac{\lambda}{\partial x} \left( \frac{\rho}{\rho_0} \frac{\partial q}{\lambda x} \right) \\ p = f(\rho, U) \\ \frac{\lambda U}{\lambda t} + p \frac{\lambda}{\partial t} \left( \frac{1}{\rho} \right) = \frac{4}{3} \mu_0 \frac{\rho}{\rho_0^2} \left( \frac{\partial q}{\partial x} \right)^2 + \sqrt{\frac{4}{3}} \frac{\tau_0}{\rho_0} \left| \frac{\partial q}{\lambda x} \right| \end{array} \right. \quad (24)$$

The viscosity coefficient becomes, assuming flow,

$$\mu = \mu_0 + \sqrt{\frac{3}{4}} \frac{\rho_0}{\rho} \frac{\tau_0}{\left| \frac{\partial q}{\partial x} \right|} \quad (\tau^2 > \tau_0^2) \quad (25)$$

# INERTIAL, VISCOUS, AND PLASTIC EFFECTS

and the stress components become

$$\begin{aligned}\tau_{rr} = \tau_{\theta\theta} &= -p - \frac{2}{3} \mu_0 \frac{\rho}{\rho_0} \frac{\partial q}{\partial x} - \frac{\tau_0}{\sqrt{3}} \operatorname{sign} \left( \frac{\partial q}{\partial x} \right) \\ \tau_{zz} &= -p + \frac{4}{3} \mu_0 \frac{\rho}{\rho_0} \frac{\partial q}{\partial x} + \sqrt{\frac{4}{3}} \tau_0 \operatorname{sign} \left( \frac{\partial q}{\partial x} \right) \quad \tau_{rz} = 0 \\ \tau^2 &= \frac{4}{3} \mu^2 \frac{\rho^2}{\rho_0^2} \left( \frac{\partial q}{\partial x} \right)^2.\end{aligned}\tag{26}$$

Here  $X = X(x, t)$  is the instantaneous position of a section;  $x$  is the initial position of the section at time zero.

Analytical methods for solving these equations are not available, even for the one-dimensional formulation. It was therefore necessary to resort to finite difference techniques for the computations. The results reported here were obtained using a computer program based on an explicit difference scheme described in detail elsewhere (4, 9). An alternate implicit scheme utilizing the Eulerian formulation and requiring less machine time for large  $\mu_0$  and  $v_0$  values has also been developed (9).

To use either scheme of calculation the initial values (i. e., at time  $t = 0$  and at all points of the space mesh) must be assigned. The initial values that we have assumed at and away from the interface are displayed schematically in Figure 2c.

## NUMERICAL RESULTS

The various combinations of assumptions for  $\mu_0$ ,  $\tau_0$  and  $v_0$  for which calculations have been made are displayed in Table I. The values of the dimensionless parameters  $B_0$  and  $R_0$  are listed for each combination and are seen to cover a wide range. In computing these parameters the characteristic length is taken as unity. This choice is meaningful only after a stable pulse has been established.

To check the accuracy of the program the calculations for cases No. 1 ( $v_0 = 0.5$ ,  $\tau_0 = 0$ ,  $\mu_0 = 0$ ) and No. 49 ( $v_0 = 1.0$ ,  $\tau_0 = 0$ ,  $\mu_0 = 0$ ) have been examined in detail. The pressure profiles are depicted in Figures 3 and 15. It is seen that a stable shock front is established in 2 to 3 microseconds. For comparison the Rankine-Hugoniot solutions, applicable since here  $\mu_0 = \tau_0 = 0$ , are also shown at  $t = 1$  and  $t = 5$  microseconds. The other calculated dependent variables behind the stable shock may also be compared with the corresponding Rankine-Hugoniot values for cases No. 1 and No. 49, Table II. The computed quantities represent mean values about which there are small oscillations at the various mesh points behind the front.

The medium for each of the cases No. 1, 2, 3, 4 is a fluid since  $\tau_0 = 0$ . The manner in which an increase of the viscosity factor  $\mu_0$  affects the pressure profile is illustrated by comparing Figures 3, 4, 5, 6. In case No. 2 ( $\mu_0 = 0.08$ )

# INERTIAL, VISCOUS, AND PLASTIC EFFECTS

TABLE I

Enumeration of parameter combinations for which calculations have been made for one-dimensional iron impact. The units are in the gram-centimeter-microsecond system. The computed pressure profile characteristics are also listed ( $\Delta p$  = profile thickness, VP = profile velocity).

No.	Parameters			Numbers		Stable Profile		
	$v_o$	$\tau_o$	$\mu_o$	$B_o$	$R_o$	$p$	$\Delta p$	VP
1	0.5	0	C	-	$\infty$	1.541	.21	.534
2	0.5	0	.08	0	49	1.549	.25	.537
3	0.5	0	.8	0	4.9	1.560	.70	.545
4	0.5	0	8	0	.49	>5		
5	0.5	.01	0	$\infty$	$\infty$	1.545	.22	.537
6	0.5	.01	.08	.25	49	1.552	.25	.538
7	0.5	.01	.8	.025	4.9	1.563	.70	.545
8								
9	0.5	.1	0	$\infty$	$\infty$	1.581	.22	.548
10	0.5	.1	.08	2.5	49	1.572	.25	.549
11	0.5	.1	.8	.25	4.9	1.574	.72	.552
12								
13								
14	0.5	1	.08	25	49	1.758	.27	.643
15	0.5	1	.8	2.5	4.9	1.762	.78	.649
16								
49	1	0	0	-	$\infty$	4.601	.21	.673
50	1	0	.08	0	98	4.616	.22	.675
51								
52	1	0	8	0	.98	>4.6	3.5	

TABLE II

Rankine-Hugoniot values compared with finite-difference calculations for one-dimensional iron-iron impact ( $\mu_o = \tau_o = 0$ ). VP denotes velocity of stable profile relative to the interface.

		P	$1/\rho$	U	VP
Case 1 ( $v_o = .5$ )	Hugoniot	1.565	0.0873	0.0312	0.5466
	Computed	1.541	0.0867	0.0265	0.534
Case 49 ( $v_o = 1$ )	Hugoniot	4.646	0.0734	0.125	0.682
	Computed	4.601	0.0734	0.122	0.673

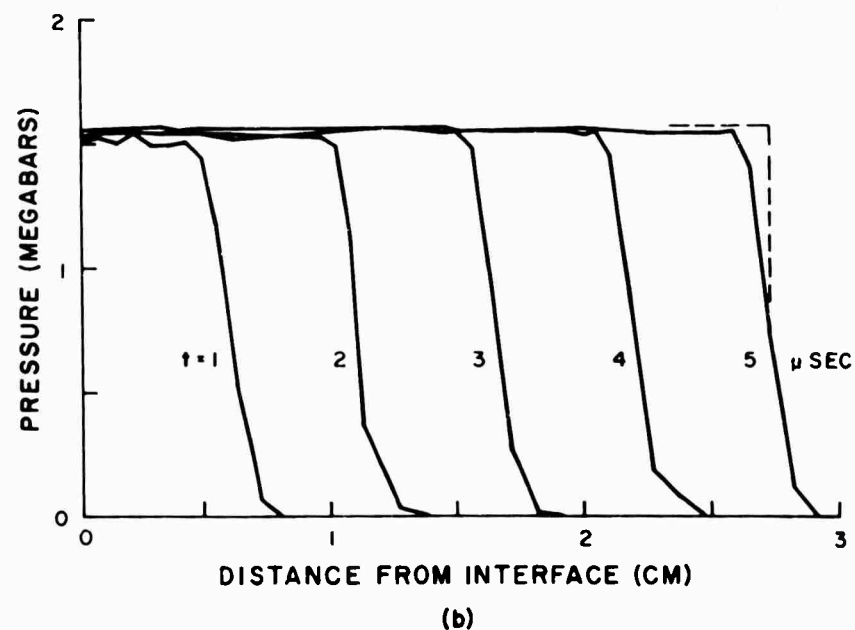
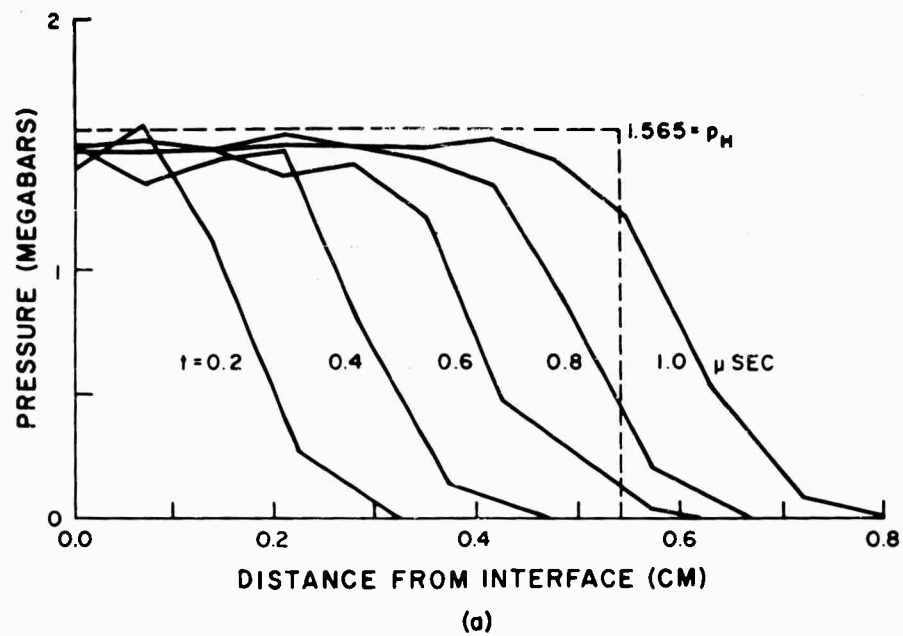


Figure 3. Calculated pressure profiles compared with the Rankine-Hugoniot solution (Case 1:  $v_0 = .5$ ,  $\tau_0 = \mu_0 = 0$ ).

# INERTIAL, VISCOUS, AND PLASTIC EFFECTS

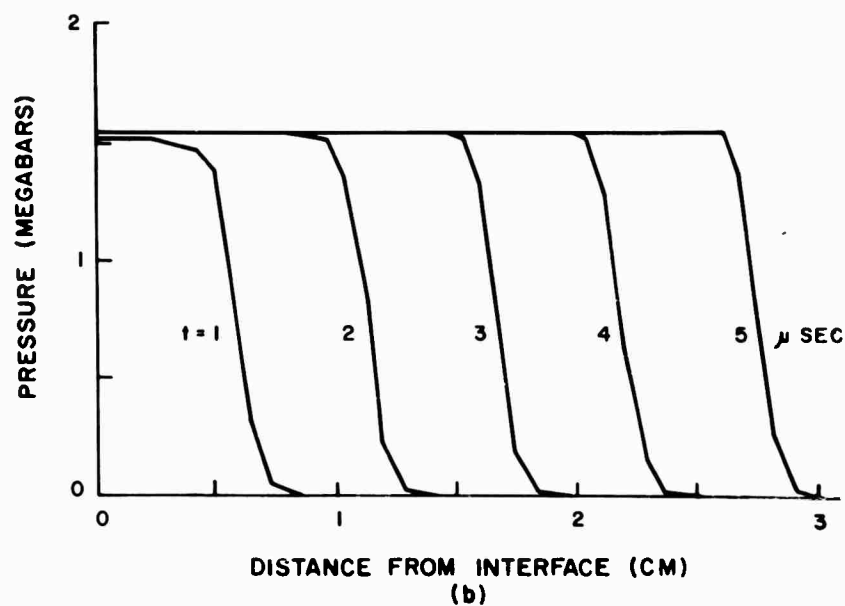
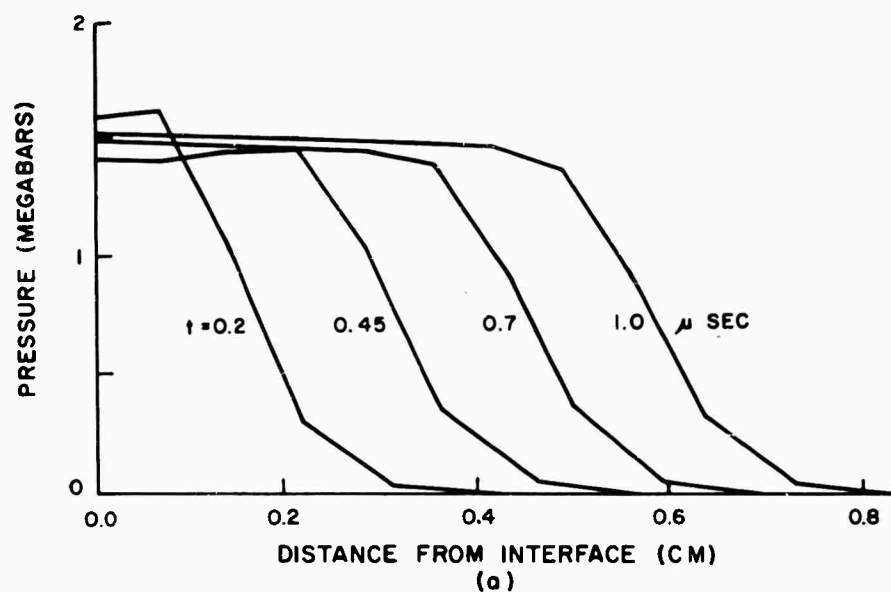


Figure 4. Pressure profiles (Case 2:  $v_0 = .5$ ,  $\tau_0 = 0$ ,  $\mu_0 = .08$ ).

# INERTIAL, VISCOUS, AND PLASTIC EFFECTS

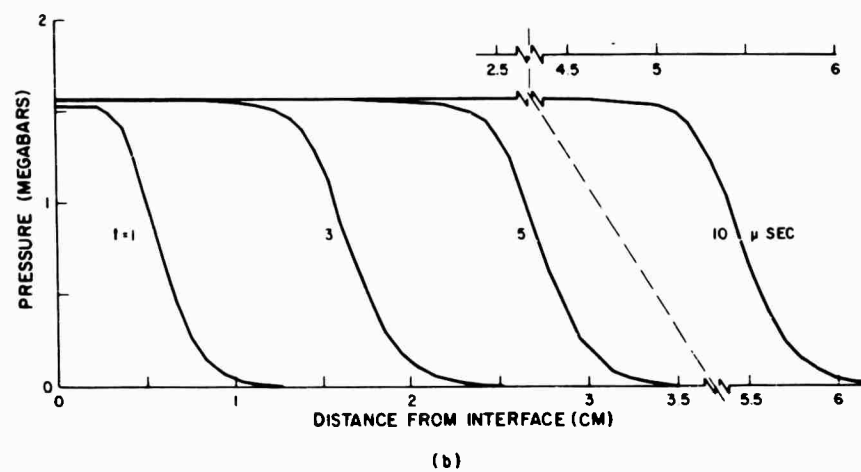
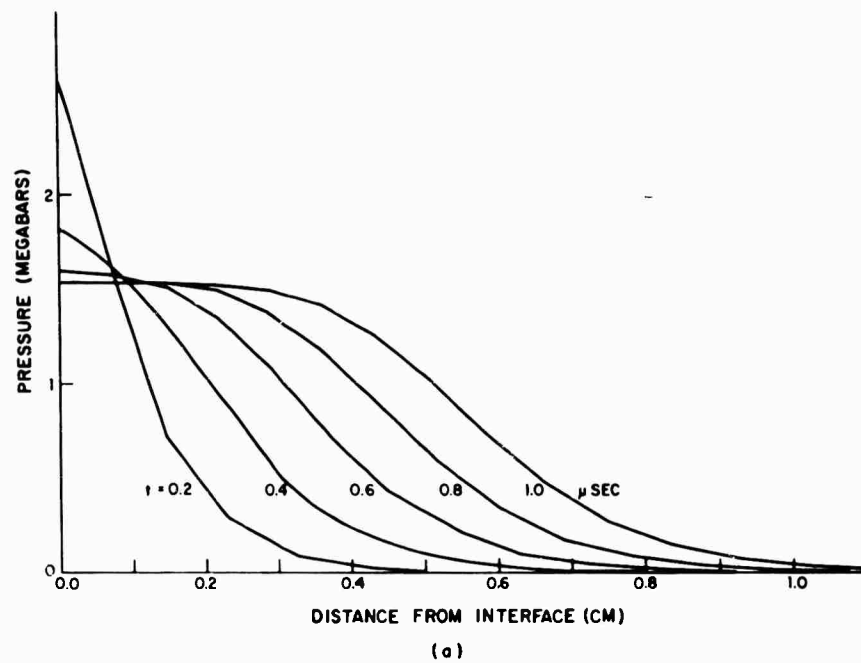


Figure 5. Pressure profiles (Case 3:  $v_0 = .5$ ,  $\tau_0 = 0$ ,  $u_0 = .8$ ).

# INERTIAL, VISCOUS, AND PLASTIC EFFECTS

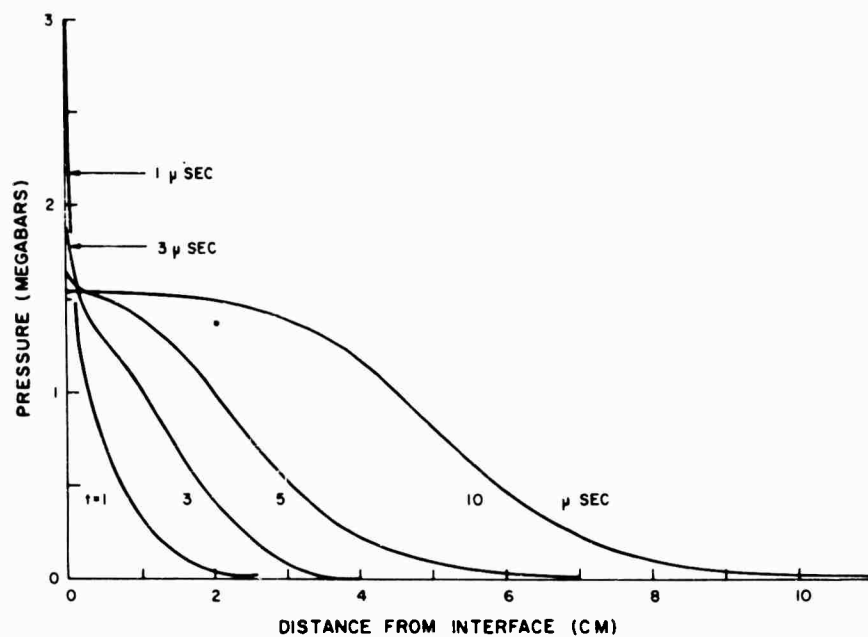


Figure 6. Pressure profiles (Case 4:  $v_0 = .5$ ,  $\tau_0 = 0$ ,  $u_0 = 8$ ).

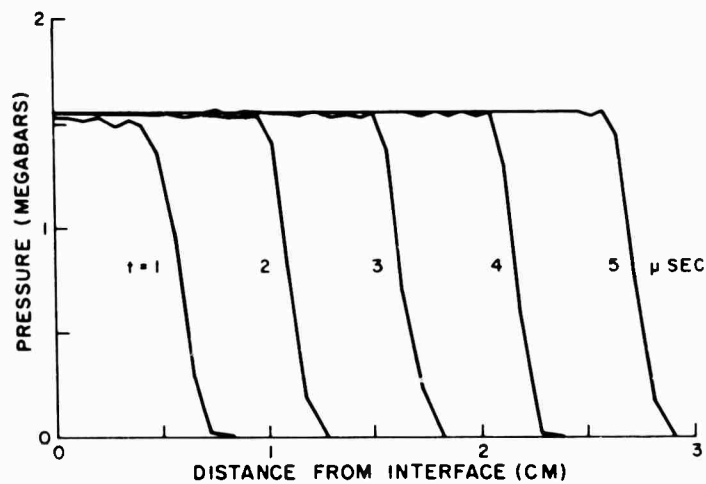


Figure 7. Pressure profiles (Case 5:  $v_0 = .5$ ,  $\tau_0 = .01$ ,  $u_0 = 0$ ).

# INERTIAL, VISCOUS, AND PLASTIC EFFECTS

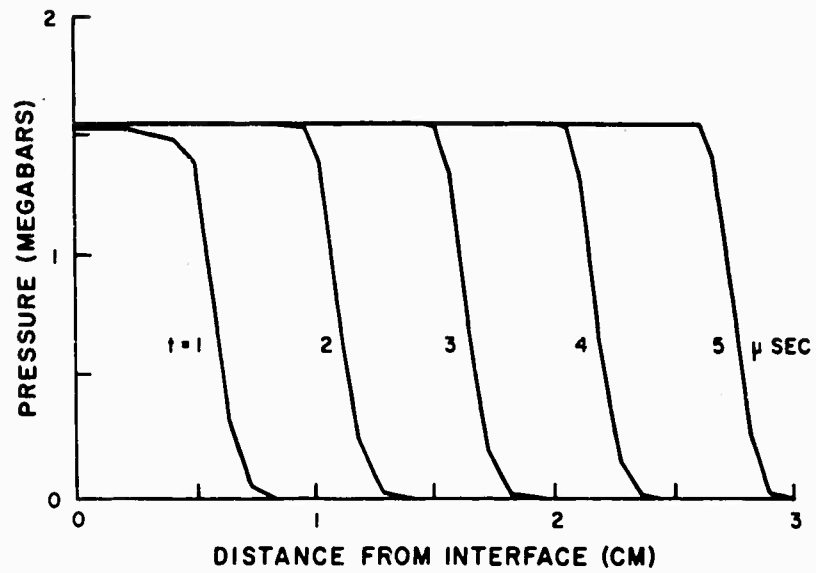


Figure 8. Pressure profiles (Case 6:  $v_0 = .5$ ,  $\tau_0 = .01$ ,  $\mu_0 = .08$ ).

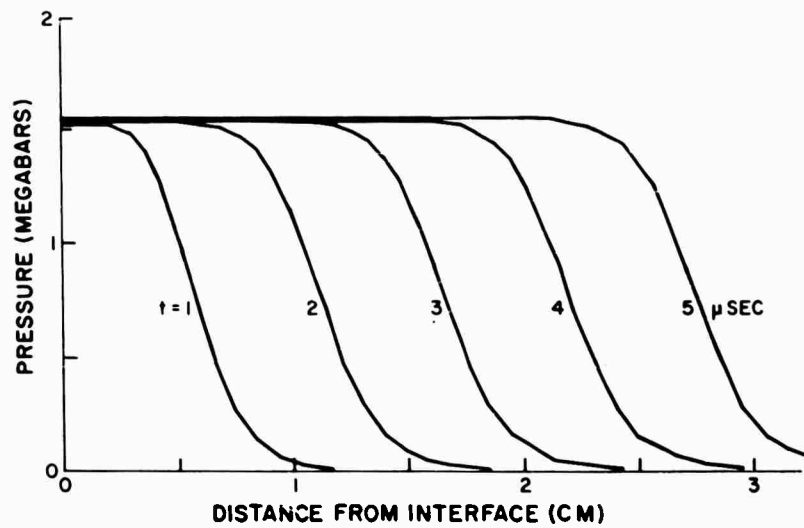


Figure 9. Pressure profiles (Case 7:  $v_0 = .5$ ,  $\tau_0 = .01$ ,  $\mu_0 = .8$ ).

# INERTIAL, VISCOUS, AND PLASTIC EFFECTS

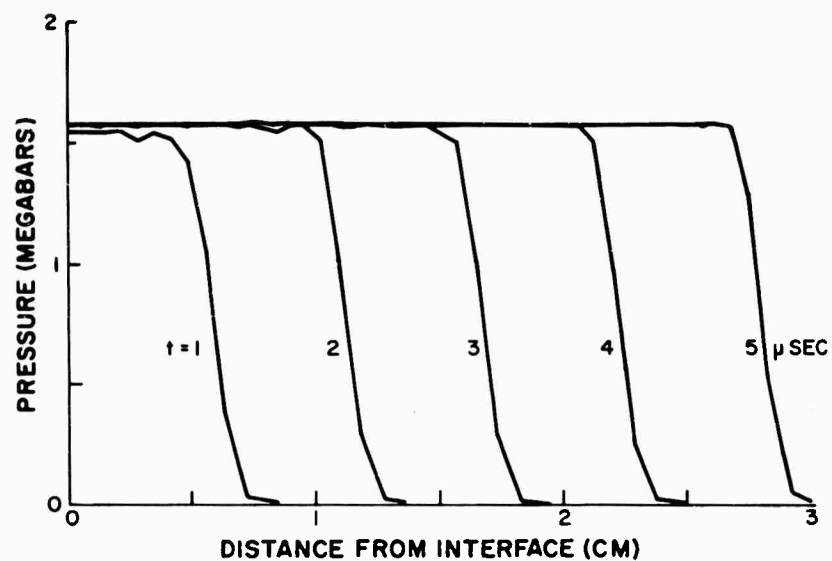


Figure 10. Pressure profiles (Case 9:  $v_o = .5$ ,  $\tau_o = .1$ ,  $\mu_o = 0$ ).

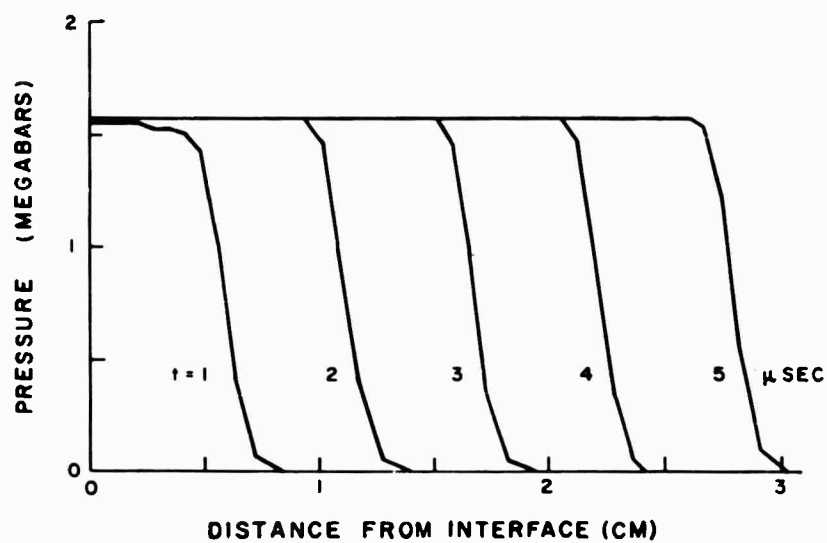


Figure 11. Pressure profiles (Case 10:  $v_o = .5$ ,  $\tau_o = .1$ ,  $\mu_o = .08$ ).

# INERTIAL, VISCOUS, AND PLASTIC EFFECTS

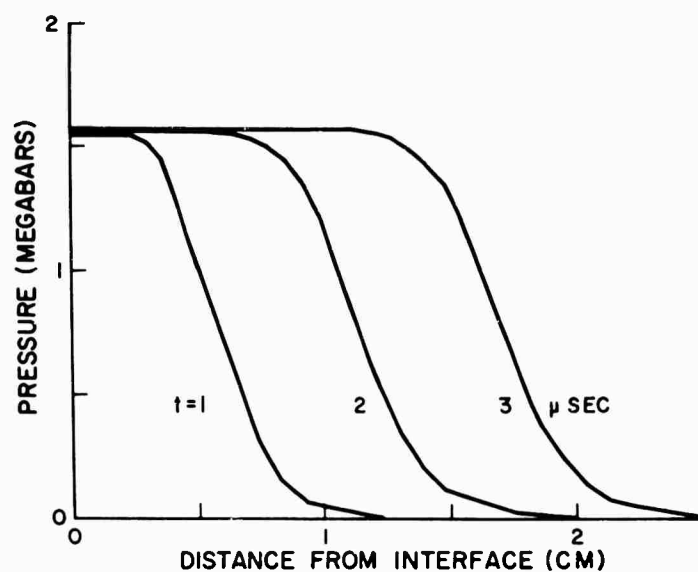


Figure 12. Pressure profiles (Case 11:  $v_0 = .5$ ,  $\tau_0 = .1$ ,  $\mu_0 = .8$ ).

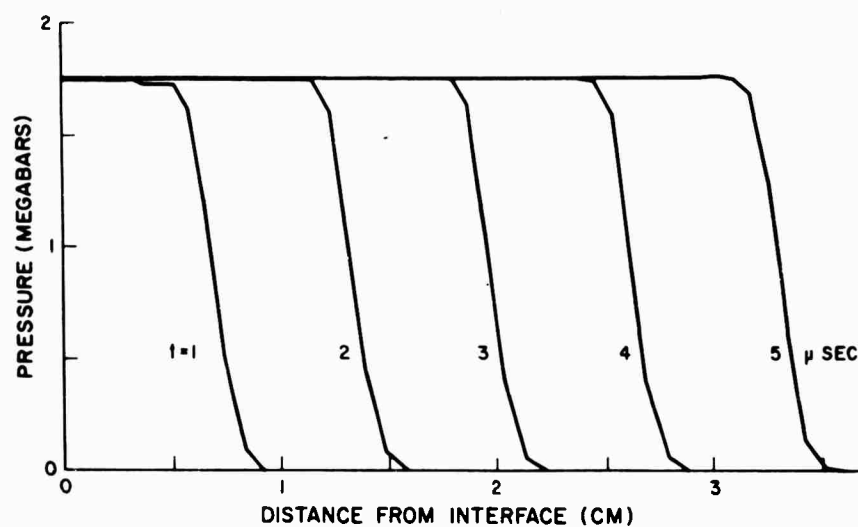
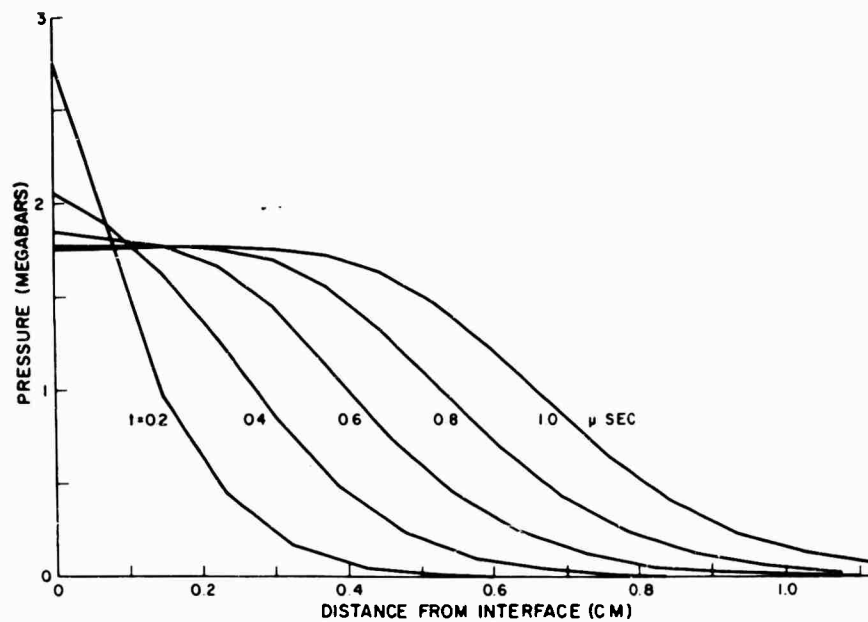
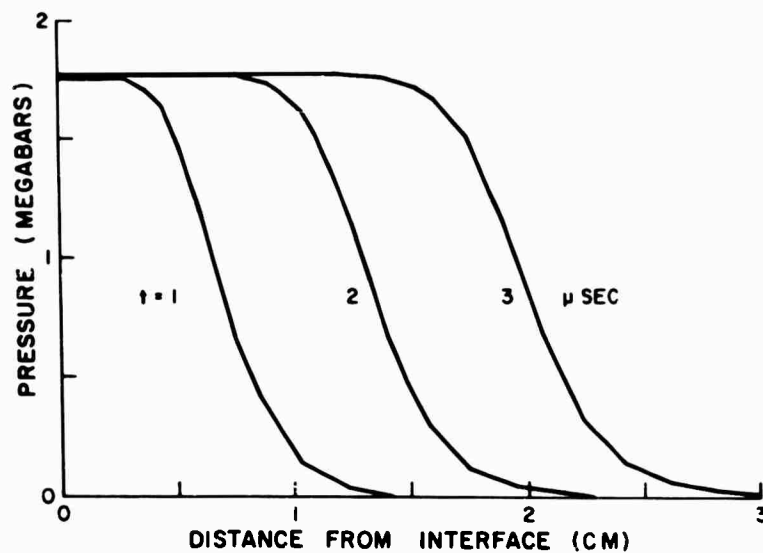


Figure 13. Pressure profiles (Case 14:  $v_0 = .5$ ,  $\tau_0 = 1$ ,  $\mu_0 = .08$ ).

# INERTIAL, VISCOUS, AND PLASTIC EFFECTS



(a)



(b)

Figure 14. Pressure profiles (Case 15:  $v_0 = .5$ ,  $\tau_0 = 1$ ,  $u_0 = .8$ ).

# INERTIAL, VISCOUS, AND PLASTIC EFFECTS

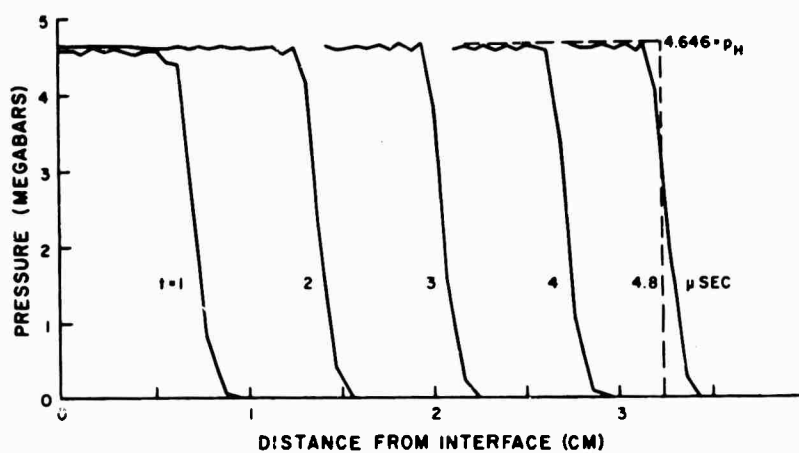


Figure 15. Pressure profiles (Case 49:  $v_0 = 1$ ,  $\tau_0 = 0$ ,  $\mu_0 = 0$ ).

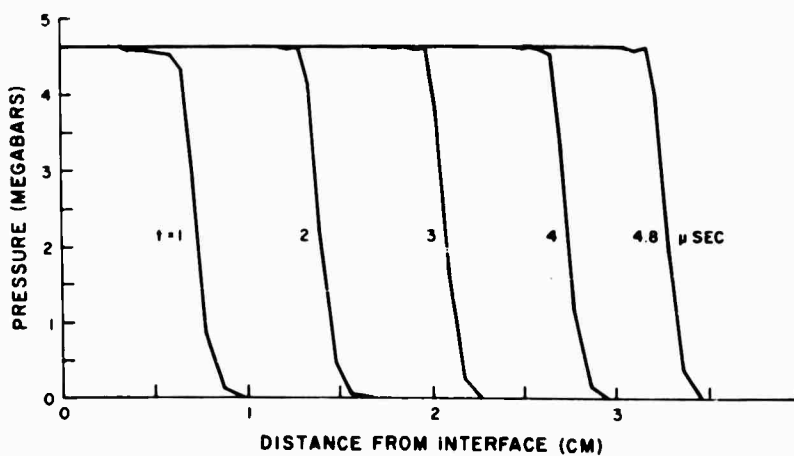


Figure 16. Pressure profiles (Case 50:  $v_0 = 1$ ,  $\tau_0 = 0$ ,  $\mu_0 = .08$ ).

# INERTIAL, VISCOUS, AND PLASTIC EFFECTS

a stable profile is obtained nearly as quickly for case No. 1 ( $\mu_0 = 0$ ), i. e., certainly in less than 5 microseconds. In case No 4 ( $\mu_0 = 8$ ), on the other hand, a stable profile requires more than 10 microseconds to be established. Case No. 3 ( $\mu_0 = 0.8$ ) is intermediate to these extremes and its pressure profile for times less than 1 microsecond are seen to be similar in form to those of case No. 4 for 1 to 10 microseconds.

In all cases that  $\mu_0 \neq 0$  the material near the interface is seen to be subjected to very large pressures in the first few tenths of microseconds. The amplitude and velocity of the stable profile, however, are only slightly increased by the inclusion of the viscosity, even for  $\mu_0 = 8$ .

It may also be observed from Figures 3, 4, 5 that as the viscosity is increased the front of the stable pressure profile is less abrupt. The effect is not noticeable for  $\mu_0 = 0.08$  (case No. 2) but is significant for  $\mu_0 = 0.8$  (case No. 3) and is even more pronounced for  $\mu_0 = 8$  (case No. 4). In the latter case  $R_0, B_0 < 1$  and it might be anticipated that the viscous terms would predominate.

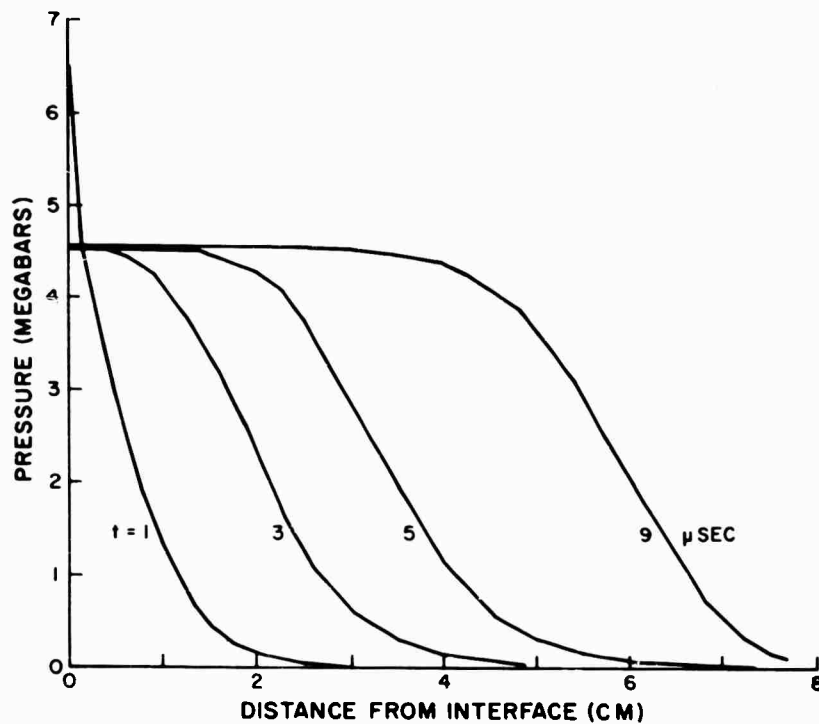


Figure 17. Pressure profiles (Case 52:  $v_0 = 1$ ,  $\tau_0 = 0$ ,  $\mu_0 = 8$ ).

# INERTIAL, VISCOUS, AND PLASTIC EFFECTS

Comparison of Figure 6 (case No. 4) with Figure 17 (case No. 52) shows that increasing the impact velocity from 0.5 to 1.0 causes the pressure profile to become more quickly stabilized. In the latter case the profile changes less after 5 microseconds elapsed than in the former case. Comparison of Figure 4 (case No. 2) with Figure 16 (case No. 50) illustrates the fact that the stable profile becomes more abrupt with an increase in  $v_0$ . The higher impact velocity also, of course, greatly increases the pressure and the velocity with which the stable front travels.

Now let us examine the results for cases where  $\tau_0 > 0$ . Substitution of (25) into the last of (26) yields

$$\tau^2 = \tau_0^2 + \frac{4}{\sqrt{3}} \mu_0 \tau_0 \frac{\rho}{\rho_0} \left| \frac{\partial q}{\partial x} \right| + \frac{4}{3} \mu_0^2 \left( \frac{\rho}{\rho_0} \right)^2 \left( \frac{\partial q}{\partial x} \right)^2. \quad (27)$$

In front of the disturbance  $\partial q / \partial x = 0$ , in the disturbance  $\partial q / \partial x < 0$  and, finally  $\partial q / \partial x$ , drops back to zero after the disturbance passes. Consequently,

$\tau^2 > \tau_0^2$  in the disturbance, but  $\tau^2$  drops to  $\tau_0^2$  after it passes. This means, in terms of our visco-plastic model, that there is flow only in that part of the medium through which the disturbance is currently passing; it again becomes rigid behind the disturbance. This phenomenon is illustrated in Figure 18 where the value of  $\tau^2$  is shown at various time intervals for two typical parameter combinations (Nos. 14 and 15). At each instant  $\tau^2 > \tau_0^2$  is seen only in a

finite region which represents the current position of the disturbance. Only in this moving region of disturbance does the medium behave as a viscous liquid. The region is more spread out the greater the value of  $\mu_0$ .

Comparison of Figures 7, 8, 9 (cases No. 5, 6, 7) and Figures 10, 11, 12 (cases No. 9, 10, 11) with Figures 3, 4, 5 (cases No. 1, 2, 3) respectively, shows that even with an impact velocity as low as  $v_0 = 0.5$  cm/microsecond there is little change effected on the stable profile by inclusion of the yield stress if it is as low as  $\tau_0 = 0.01$  or  $\tau_0 = 0.1$ . Only small increases in the pressure and in the disturbance velocity are apparent. This might be expected since for all these parameter combinations the ratios  $B_0: R_0$  and  $1: R_0$  are small, i. e., the inertial terms predominate. It must be kept in mind that in an actual cratering process the flow velocity must always decrease to the point where  $\tau_0$  is important.

On the other hand, comparison of Figures 13 and 14 (cases No. 14, 15) with Figures 4 and 5 (cases No. 2, 3) respectively, shows that both the amplitude and velocity of the pressure pulse are significantly increased by the inclusion of the strength term if it is as large as  $\tau_0 = 1.0$ . The shape of the pulse, however, is apparently not strongly affected, nor is the time required for the profile to be stabilized as may be seen by comparing Figure 5a with 14a. For these cases the inertial and strength terms are both important,  $R_0: B_0 = 1.97$ .

These characteristics of the stable profiles for the various cases are displayed in Table I. There  $p$  denotes the pressure behind the disturbance;  $\Delta P$  and  $VP$  denote the thickness and velocity (relative to the interface) of the stable pressure profile, respectively.

## DISCUSSION

In our model the medium is considered to act as a viscous liquid rather than a solid, provided  $\tau^2 \gg \tau_0^2$ . It is therefore consistent with ordinary viscous fluid theory that the equation of state be given in terms of a hydraulic pressure  $p$ , equal for all directions. We have, as usual, taken  $p = -(\tau_{rr} + \tau_{\theta\theta} + \tau_{zz})/3$  as the thermodynamic pressure. If the medium were to be considered a deformable solid and the material strength retained throughout, a tensorial equation of state would have to be used.

The particular equation of state employed in the calculations,  $p = f(\rho, U)$ , was determined by the Los Alamos group from measurements on pressure pulses induced by high explosive. The method is indirect in that the observed quantities are the pulse velocity and the free-surface velocity produced by normal reflection of the pulse from a free boundary. Pressure (strictly, stress normal to the wave front,  $-\tau_{zz}$ ) and corresponding values of internal energy and density were computed from these measurements by means of the Rankine-Hugoniot relations. An equation of state based on the assumption that  $\mu_0 = \tau_0 = 0$  has thus been employed to calculate the behavior of a model for the material which assumes

$|\mu_0| + |\tau_0| > 0$ . This certainly leads to errors but they are of second order and would not be expected to mask the effect of including the viscous and plastic terms in the other equations governing the model. The results have borne this out since, as physical reasoning would imply,  $\mu_0$  chiefly affects the shape of the stable disturbance and  $\tau_0$  has its main effect on its amplitude. At lower velocities,  $\tau_0$  would also affect the shape.

Other remarks on the equation of state are also relevant. In converting the measured velocities to pressure-energy-density states it was tacitly assumed that a stable, abrupt disturbance was obtained. Verification by direct measurement of the pressure profile has not been possible and justification for the assumption is based on the reasonable agreement with extrapolation of hydrostatic data. This should not be construed as proof that the viscosity and strength effects are negligible, however, since even with viscosity factors as large as  $\mu_0 = 0.8$  and yield stress as great as  $\tau_0 = 0.1$ ,  $v_0 = .5$ , the differences in the velocity and amplitude of the stable pressure would be difficult to observe by such measurements.

The fact that  $-\tau_{zz}$  and not  $p$  is the actual pressure reflected from the free surface in the experiments may not greatly affect the equation of state calculations since the shape, velocity, and amplitude of the stable  $p$  and  $-\tau_{zz}$  profiles are nearly identical. To see this compare Figures 5b, 6 and 14 with Figures 19, 20, and 21 respectively; these show the two corresponding profiles for three typical cases, Nos. 3, 4, 15.

Prior to the establishment of a stable profile, however, the components of the deformation stress tensor, of which  $\tau_{zz} + p$  is one, are not small. At the instant of impact between the two bodies a very large velocity gradient is imposed on the material near the interface. As the front of the disturbance propagates into the body the gradient at the interface decreases and the gradient at the front of the disturbance also decreases because of the smearing action of the viscosity. From (27) is seen that the von Mises statistic,  $\tau^2$ , which is a measure of the magnitude of the components of the deformation stress tensor, must act similarly.

# INERTIAL, VISCOUS, AND PLASTIC EFFECTS

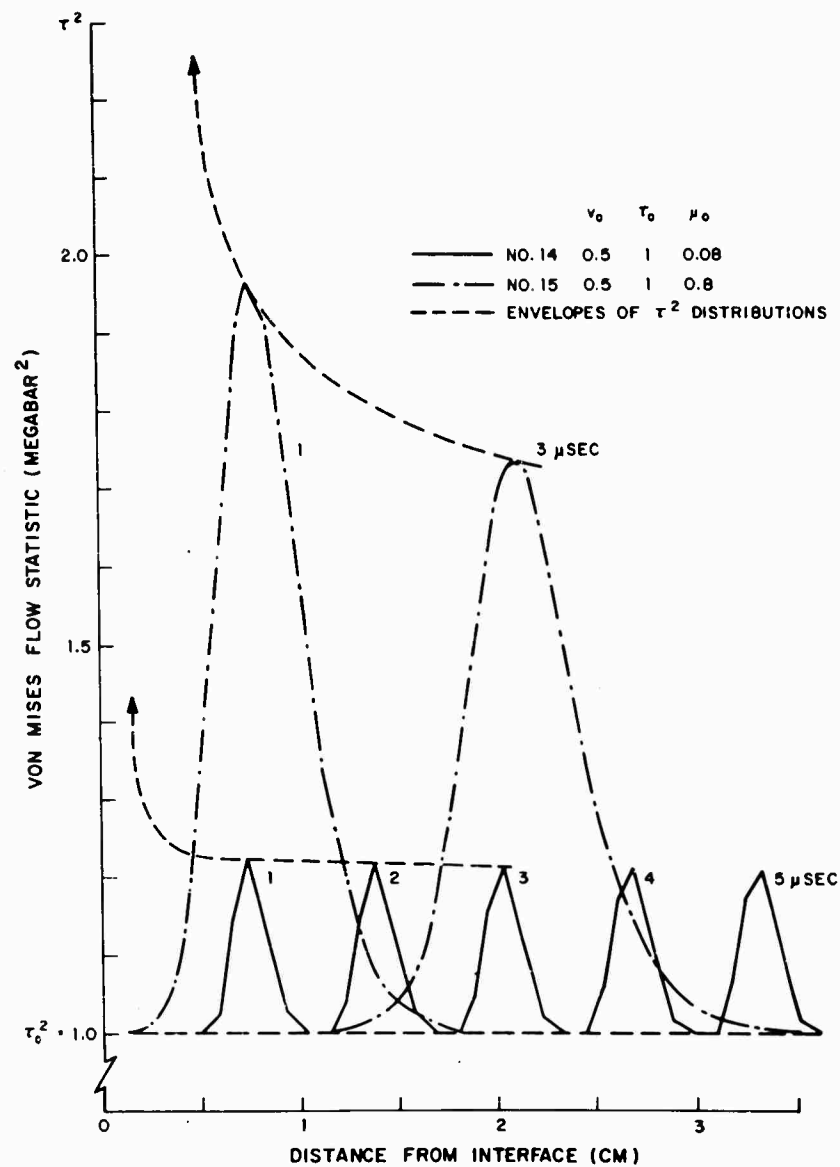


Figure 18. Von Mises flow statistic profiles and the envelopes of their maximum values.

# INERTIAL, VISCOUS, AND PLASTIC EFFECTS

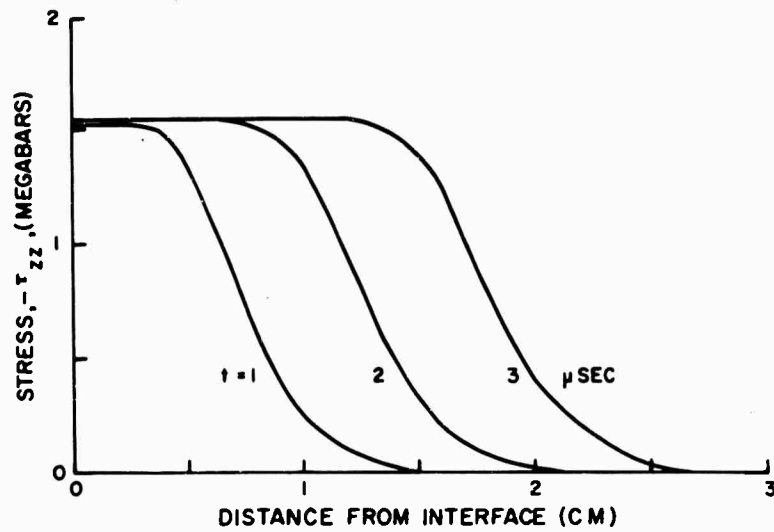


Figure 19. Profiles of stress normal to the wave front (Case 3:  $v_0 = .5$ ,  $\tau_0 = 0$ ,  $\mu_0 = .8$ ).

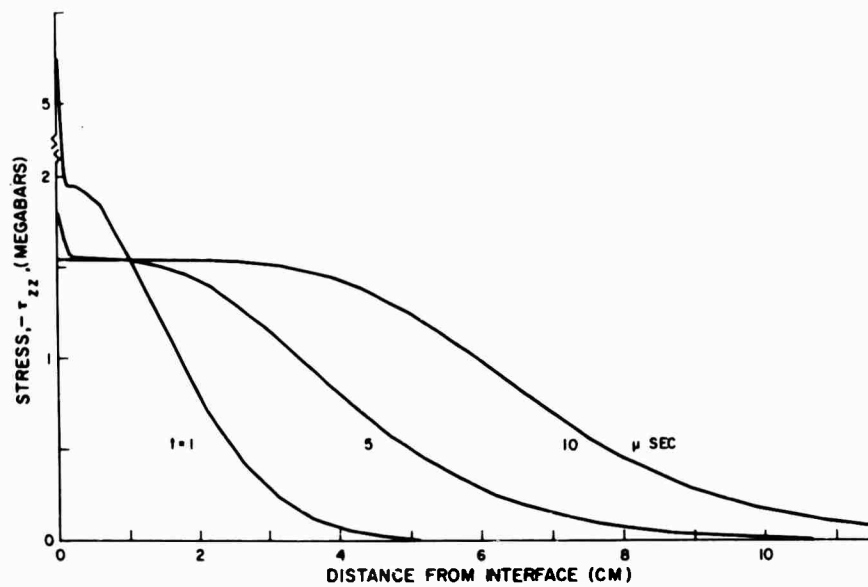


Figure 20. Profiles of stress normal to the wave front (Case 4:  $v_0 = .5$ ,  $\tau_0 = 0$ ,  $\mu_0 = .8$ ).

## INERTIAL, VISCOUS, AND PLASTIC EFFECTS

Thus when viscosity is present the material near the interface is subjected to a much greater distortion than material away from the interface. This is illustrated in Figure 18 by the envelopes of the  $\tau^2$  distributions.

These latter observations are consistent with experimental evidence that internal structural changes in a metal can be related to the distribution of stress that existed in an impulsively loaded body by plotting contours of equal hardness on sections of the body (10). The contours were found to coincide with the isochromatics obtained in photoelastic studies, i. e., the contours lie along lines of maximum shear stress. Recent microhardness studies (11) of one dimensional impacting plates have shown that indeed the microhardness near the impact interface is maximum, the value decreasing rapidly outside the interfacial zone.

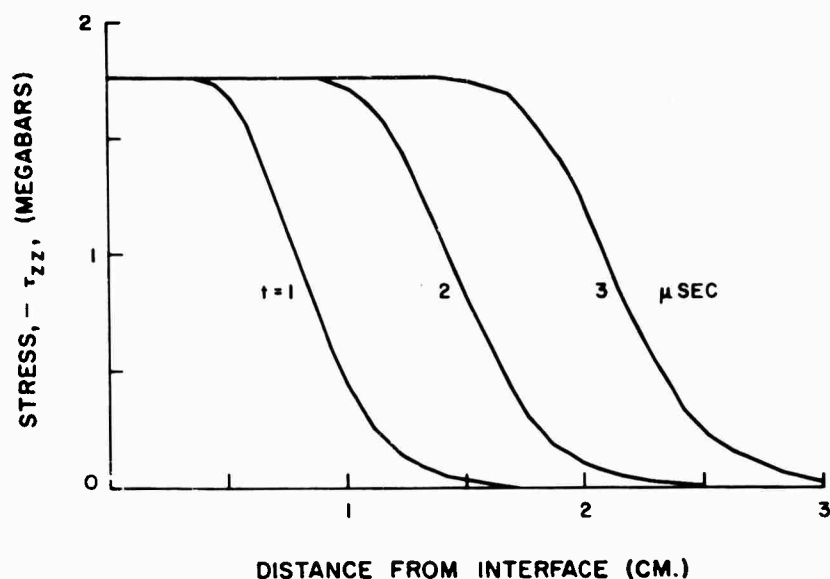


Figure 21. Profiles of stress normal to the wave front (Case 15:  $\nu_0 = .5$ ,  $\tau_0 = 1$ ,  $\mu_0 = .8$ ).

## CONCLUSIONS

A visco-plastic model for hypervelocity impact has been proposed which takes into account the inertial, viscous, and plastic effects. This was accomplished by introducing a viscosity factor  $\mu_0$  and a dynamic yield stress  $\tau_0$ . From an examination of the resulting system of equations several dimensionless parameters were found which control the relative importance of the three effects at the various stages of the cratering process. The inertial effect was found to

## INERTIAL, VISCOUS, AND PLASTIC EFFECTS

be important throughout the early stages while the strength of the medium is dominant during the final stages. Immediately after impact the viscous effect is large in the zone near the contact interface. Its magnitude decreases as the strain-rate gradient decreases, but it may remain important throughout the flow process.

In the absence of definitive data in the hypervelocity impact regime, computations were performed on a one-dimensional model in which the values of  $\mu_0$  and  $\tau_0$  were varied. The above qualitative conclusions were verified. Specifically, the following was found.

1) The assumption  $\mu_0 > 0$  results in large initial values for the pressure and deformation in a zone near the impact interface. As  $\mu_0$  is increased the effect becomes greater and the disturbance propagates a greater distance before reducing to its stabilized shape and amplitude. For impact velocity  $v_0 = 0.5$  cm/microsecond, the time the disturbance propagates before a stable profile is obtained varies from about 2 to 3 microseconds for  $\mu_0 = .08$  to more than 10 microseconds for  $\mu_0 = 8$ . The required time is less the greater the impact velocity; the value of  $\tau_0$  has little effect.

2) The amplitude and velocity of the stable pressure profile are only slightly increased as  $\mu_0$  is increased, but its width (shape) is significantly larger. Increasing the yield strength has little effect on the shape of the stable pressure wave; it significantly increases its amplitude and velocity only if  $\tau_0$  is as large as one megabar. The latter conclusion is valid for particle velocities of 0.25, 0.5 cm/microsecond and larger. At lower velocities  $\tau_0$  has a more significant effect on the viscosity coefficient, see (8), and thus more effect on the pressure wave.

These conclusions may be related to the qualitative model of crater formation that has evolved from experimental studies in which the actual cratering process has been monitored (12). It was found that though only five to ten microseconds are required to use up the projectile, the crater continues to enlarge for several hundred microseconds. The mechanism of crater formation is therefore essentially one of cavitation, the size and shape of the final crater being determined by (a) the shape and amplitude of the pressure wave established during the first five to ten microseconds by the action of the projectile on the target, and (b) the resistance of the target material to flow. (c) The flow continues until the amplitude of the wave decreases below the intrinsic yield strength of the material.

The calculations presented in this paper show that the shape and amplitude of the pressure wave, (a), are in turn strongly dependent on the viscosity of the medium. This is especially true during the first microsecond after impact when the strain-rate gradient is largest. Also, the resistance of the target material to flow, (b), depends on the viscosity factor  $\mu_0$  and, to a lesser degree, on the strength factor  $\tau_0$ ; the viscosity coefficient becomes larger and more dependent on  $\tau_0$  at the smaller strain-rates. Finally, (c), the strength factor  $\tau_0$  controls the instant when the flow ceases.

Thus, both  $\mu_0$  and  $\tau_0$  are important in determining how long the crater continues to expand. This may explain why a crater in Lucite stops expanding earlier than one in aluminum despite the relative magnitudes of their yield strengths.

## INERTIAL, VISCOUS, AND PLASTIC EFFECTS

### ACKNOWLEDGMENT

The authors wish to express their appreciation to Mr. M. H. Slud and Dr. F. W. Wendt for many interesting and helpful technical discussions. Thanks are also due to Mr. R. P. Supina for assistance in reducing the numerical results.

### BIBLIOGRAPHY

1. Bjork, R. L. , "Effects of a Meteoroid Impact on Steel and Aluminum in Space," Technical Report P-1662, Rand Corporation, Eng. Division, Dec. 16, 1958.
2. Riney, T. D. , "A Visco-Plastic Model for Hypervelocity Impact," General Electric Company, First Quarterly Report, Contract AF 08(635) - 1713, November 3, 1960-February 3, 1961.
3. Oldroyd, J. G. , "A Rational Formulation of the Equations of Plastic Flow for a Bingham Solid," Proc. Cambridge Phil. Soc. , Volume 43, (1947), pp. 100-105.
4. Riney, T. D. , "Study of Equations Governing the Visco-Plastic Model," General Electric Company, Second Quarterly Report, Contract AF 08 (635) - 1713, February 3, 1961-May 3, 1961, (APGC -TN-61-30).
5. Perzyna, P. , "Stress Waves in a Homogeneous Elastic-Visco-Plastic Medium," Arch. Mech. Stos. , Volume 11, No. 4, 1959.
6. Kolsky, H. , Stress Waves in Solids, Oxford, 1953.
7. Reiner, M. , Encyclopedia of Physics, Volume 6, Elasticity and Plasticity, Springer-Verlag, 1958.
8. Richtmyer, R. D. , Difference Methods for Initial-Value Problems, Interscience Publishers, Inc. , New York, N. Y. , 1957.
9. Riney, T. D. , "Numerical Investigation of One-Dimensional Visco-Plastic Model," General Electric Company, Third Quarterly Report, Contract AF 08 (635) - 1713, May 3, 1961-September 3, 1961.
10. Rinehart, J. S. , "Some Experimental Indications of the Stresses Produced in a Body by an Exploding Charge," Jour. Appl. Phys. , Volume 22, 1951.
11. Katz, S. , and Peterson, R. E. , "Study of Shock Propagation in Ferrous Metals," Poulter Laboratories. Technical Report 010-55, Stanford Research Institute, December 20, 1955.
12. Eichelberger, R. J. , and Gehring, J. W. , "Effects of Meteoroid Impacts on Space Vehicles ," ARS Space Flight Report to the Nation, New York, October 9, 1961.

A THEORETICAL STUDY OF DYNAMIC  
PLASTIC DEFORMATION UNDER IMPACT LOADS

L. E. Fugelso

American Machine and Foundry Company  
Niles, Illinois

I. INTRODUCTION

A theoretical treatment of dynamic plastic deformation under impulsive or impact loads is presented. Equations of motion based on dislocation theory are employed. The specific problem solved in this paper is the deformation of a semi-infinite half space which is struck suddenly by cylindrical projectile. The method of solution is based on a set of continuum equations derived from discrete-dislocation theory of plastic deformation. The basic physical assumption of this model of deformation is that the total deformation of the medium is composed of elastic deformation or distortion of the body accompanied by the motion of dislocations under the applied stress.

This problem was carried out as a portion of a theoretical study of light-armor penetration by subsonic-velocity projectiles in the velocity range of 300 to 6000 ft/sec. Excellent correlation with experimental data was found. It is believed that the theory is equally applicable to hypervelocity impact.

At the Fourth Hypervelocity Symposium Hopkins and Kolsky<sup>(2)</sup> presented a breakdown of the impact phenomena based on the predominant mode of deformation. Regions for predominantly elastic deformation, plastic deformation, shock propagation, etc., were estimated based on the stress generated at the surface by the impact. The bounds on the predominantly plastic region were, for the lower bound, the velocity such that the generated stress is the static yield stress, and for the upper bound the velocity is the impact velocity at which the decelerating force on the projectile is equal to the yield point of the material. In this regime, the plastic flow is estimated by quasi-static plasticity theory.

The foregoing discussion places extreme limitations on dynamic plastic deformation as a mode of impact deformation.

Little is known concerning the actual behavior of a body which is undergoing plastic deformation under non-steady or dynamic conditions. A characteristic feature of plastic deformation under static conditions is a sharp break or rapid change of slope in the stress-strain curve. For higher rates of loading or for loads of very short duration, the stress-strain curves obtained under the same

## DYNAMIC PLASTIC DEFORMATION

geometrical configuration are markedly different, passing in the limit of extremely short duration loads to the finite elastic stress-strain curves. Under experimental conditions the stress at which the stress-strain curve breaks over apparently increases with increasing strain rate. Thus a very complicated form of the stress curve must be a priori postulated to account for the experimental findings. Therefore, an extensive study was undertaken to investigate this behavior and to determine the magnitude and nature of plastic flow under impact.

In the process of plastic deformation a basic physical mechanism different than geometrical distortion of the specimen occurs. If this non-elastic mode of deformation occurs in single crystals, the most probable mechanism of deformation is dislocation movement. Similarly in polycrystalline metallic specimens, slip along the grain boundaries of the crystals may proceed in a step-wise fashion. For other materials where non-elastic deformation is of prime interest such as clays, soils, plastics, and organic compounds, this deformation proceeds by some micromechanism or combination of micromechanisms, which may be quite involved. Since the application of the present study is restricted to the impact of metallic plates, only one mechanism is utilized to describe the non-elastic deformation.

The total deformation in metallic specimens is then due to the action of two physically different mechanisms:

- (1) Geometric distortion or elastic strain,
- (2) Movement of dislocations under stress.

The deformation must be described in terms of these two mechanisms. This description was carried out in detail using the geometric theory of dislocations. By defining a continuum distribution of dislocations and deriving equations for the statistical transport of them under an applied stress, a set of continuum equations describing the deformation of the body were determined. <sup>(1)</sup>

The characteristic features of dynamic plastic deformation that may be deduced from solution of these equations include:

- 1) Once the stress wave has reached any given point in the medium two steps occur in the deformational sequence at that point: an instantaneous elastic deformation and a time-dependent plastic deformation.
- 2) Solution of the one-dimensional problem shows that the elastic strain propagates as a distinct wave while the plastic deformation is diffusive in the region behind the elastic wave front. There is no distinct plastic wave.
- 3) The stress-strain curve for any material is not unique, even though the relation between stress and elastic strain is unique and the mechanism for motion of dislocations is unique. The resulting total stress-strain relation is a derived curve and is dependent on strain rate, duration of stress, stress magnitude, and geometry.
- 4) The dynamic yield stress for plastic flow is explained simply. At early times, little plastic flow has occurred and the stress state may not yet

## DYNAMIC PLASTIC DEFORMATION

be stable with respect to plastic flow or dislocation movement. Use of a conventional definition for a yield stress, such as the stress at a 2 percent-offset from the linear infinitesimal elastic stress-strain curve will show an increase over static or long time values.

### II. GENERAL EQUATIONS

The solution of the plastic and elastic deformation of an elastic half space with a continuous distribution of dislocations will be studied. The problem will be restricted to cylindrical symmetry.

The general equations of motion are<sup>(1)</sup>

$$\frac{\partial \sigma_{ij}}{\partial x_j} + \frac{\partial s_{im}}{\partial x_m} = \rho \frac{\partial v_i}{\partial t} \quad 2.1$$

$$D_1 \nabla^2 \epsilon_{ij} = \frac{\partial}{\partial t} \epsilon_{ij} \quad 2.2$$

$$D_2 \nabla^2 d_{ij} = \frac{\partial}{\partial t} d_{ij} \quad 2.3$$

where

$D_1, D_2$  are stress dependent diffusion coefficients for the dislocations,

$s_{im}$  are the components of the plastic driving stress tensor.

Assume Hooke's law for the elastic part

$$\sigma_{ij} = \lambda \epsilon_{\kappa\kappa} \delta_{ij} + 2\mu \epsilon_{ij} \quad 2.4$$

$$\epsilon_{ij} = 1/2 (u_{i,j} + u_{j,i}) \quad 2.5$$

$$d_{ij} = \epsilon_{ij} - \epsilon_{\kappa\kappa} \delta_{ij} \quad 2.6$$

where  $\lambda, \mu$  are Lamé's constants.

Since the medium undergoing deformation is isotropic

# DYNAMIC PLASTIC DEFORMATION

$$s_{im} = q \delta_{im} + q_{im}$$

2.7

Restricting the equations to the case of cylindrical axisymmetry the equations of motion then are

$$\left\{ \nabla^2 - \frac{1}{r^2} \right\} u - \{ 2\eta - 1 \} \frac{\partial \Delta}{\partial r} + \frac{1}{\mu} \left[ \frac{\partial q}{\partial r} - \frac{\partial q_{rr}}{\partial r} + \frac{\partial q_{rz}}{\partial z} + \frac{q_{rr}}{r} \right] = \frac{1}{2} \frac{\partial^2 u}{c_2 \partial t^2} \quad 2.8$$

$$\nabla^2 w - \{ 2\eta - 1 \} \frac{\partial \Delta}{\partial r} + \frac{1}{\mu} \left[ \frac{\partial q}{\partial z} - \frac{\partial q_{rz}}{\partial r} - \frac{\partial q_{zz}}{\partial z} \right] = \frac{1}{2} \frac{\partial^2 w}{c_2 \partial t^2} \quad 2.9$$

$$D_1 \nabla^2 \epsilon_{ii} = \frac{\partial}{\partial t} \epsilon_{ii} \quad 2.10$$

$$D_2 \nabla^2 d_{ij} = \frac{\partial}{\partial t} d_{ij} \quad 2.11$$

Where  $u$ ,  $w$  are the displacements in the  $r$ ,  $z$  directions respectively,

$$\frac{\lambda + 2\mu}{\mu} = \eta \quad 2.12$$

and  $\Delta$  is the dilatation

$$\Delta = \left( \frac{\partial u}{\partial r} + \frac{u}{r} + \frac{\partial w}{\partial z} \right) \quad 2.13$$

These equations take on a more instructive form through the application of potential theory.

Introduce the potential functions  $\phi$ ,  $\psi$ ,  $s$ ,  $T$ , defined by

$$u = \frac{\partial \phi}{\partial r} - \frac{\partial \psi}{\partial z} + z \frac{\partial s}{\partial r} - z \frac{\partial T}{\partial z} \quad 2.14$$

# DYNAMIC PLASTIC DEFORMATION

$$w = \frac{\partial \phi}{\partial z} + \frac{\partial \psi}{\partial r} + z \frac{\partial S}{\partial z} + z \frac{\partial T}{\partial r} \quad 2.15$$

Differentiating the first equation with respect to  $z$  and the second with respect to  $r$ , it is readily observed that the plastic driving stresses are harmonic functions

$$q = \frac{\partial S}{\partial z} - \eta \nabla^2 \phi \quad 2.16$$

$$q_{rr} = \frac{\partial T}{\partial z} - \frac{\partial^2 \psi}{\partial z^2} \quad 2.17$$

$$q_{zz} = \frac{\partial T}{\partial z} - \frac{\partial^2 \psi}{\partial r^2} \quad 2.18$$

$$q_{rz} = \frac{\partial T}{\partial r} - \frac{\partial^2 \psi}{\partial r \partial z} \quad 2.19$$

Inserting these values into the equations, the equations reduce to the following

$$\frac{1}{c_1^2} \frac{\partial^2 S}{\partial t^2} = \nabla^2 S \quad 2.20$$

$$\frac{1}{c_2^2} \frac{\partial^2 T}{\partial t^2} = \nabla^2 T \quad 2.21$$

$$\left\{ c_2^2 \nabla^2 - \frac{\partial^2}{\partial t^2} \right\} \nabla^2 \psi + \left\{ D_2 \nabla^2 - \frac{\partial}{\partial t} \right\} \nabla^2 \psi = 0 \quad 2.22$$

$$\left\{ c_1^2 \nabla^2 - \frac{\partial^2}{\partial t^2} \right\} \nabla^2 \phi + \left\{ D_1 \nabla^2 - \frac{\partial}{\partial t} \right\} \nabla^2 \phi = 0 \quad 2.23$$

where

$$c_1^2 = \frac{\lambda + 2\mu}{\rho}, \quad c_2^2 = \frac{\mu}{\rho}.$$

From the nature of these equations, four boundary conditions must be prescribed for the free surface.

The first two equations indicate the propagation of two elastic waves. The

# DYNAMIC PLASTIC DEFORMATION

second pair of equations are the same form as the one dimensional plastic-elastic wave studied by the author <sup>(1)</sup>. We recall a theorem derived therein, the derivative of a term involving the dislocation parameters may be replaced by division by the average spacing of the dislocations

$$D_1 \operatorname{div} = V_1 \quad D_2 \operatorname{div} = V_2$$

where  $V$  is the dislocation velocity. Then the second pair of equations is identical in form to the one dimensional case

$$\left\{ c_2^2 \nabla^2 - \frac{\partial^2}{\partial t^2} \right\} \nabla^2 \psi + \left\{ v_2 \operatorname{grad} - \frac{\partial}{\partial t} \right\} \nabla^2 \psi = 0 \quad 2.24$$

$$\left\{ c_1^2 \nabla^2 - \frac{\partial^2}{\partial t^2} \right\} \nabla^2 \phi + \left\{ v_1 \operatorname{grad} - \frac{\partial}{\partial t} \right\} \nabla^2 \phi = 0 \quad 2.25$$

The nature of these solutions is recapitulated here. One part of the stress wave propagates at sonic velocity, the wave front being damped by the action of the dislocations. The dislocations move away from the wave front and further displacement occurs behind the wave front and at the same time, the stress state is relieved.

Here the only difference is that the non-elastic behavior occurs in both the shear and dilatational modes. Since the diffusion coefficient that appears in these equations is dependent on the maximum shear stress, more plastic deformation is to be expected in the shear wave.

The solution for the non-steady one-dimensional stress wave has been calculated <sup>(1)</sup>. A typical strain profile is shown in Figure 1. In this problem a constant stress is applied at the end of the rod and held. Since no locking mechanism has been assumed for the dislocation movement, the plastic flow continues at the end of the rod.

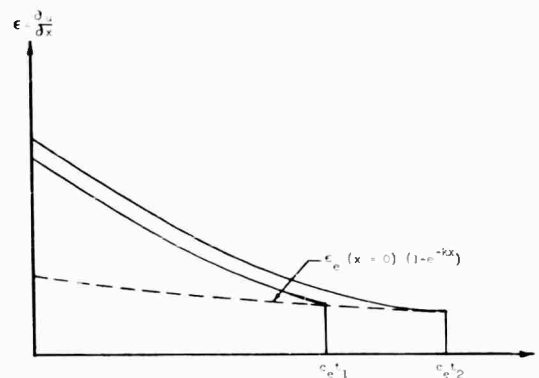


Figure 1. Elastic-Plastic Strain Profile in One-Dimensional Rod at Various Times.

## DYNAMIC PLASTIC DEFORMATION

### III. THE SOLUTION

A detailed solution is evaluated for a simple case. The dependence of the plastic driving force is assumed to be scalar, i.e., the tensor components of the driving force are all assumed to vanish with the exception of the scalar term.

Under this assumption, the equations of motion for elastic and plastic deformation of the half space are

$$\left\{ \nabla^2 - \frac{1}{r^2} \right\} u - \{ 2\eta - 1 \} \frac{\partial \Delta}{\partial r} - \frac{1}{\mu} \frac{\partial \sigma}{\partial r} = \frac{1}{c^2} \frac{\partial^2 u}{\partial t^2} \quad 3.1$$

$$\nabla^2 w - \{ 2\eta - 1 \} \frac{\partial \Delta}{\partial z} - \frac{1}{\mu} \frac{\partial \sigma}{\partial z} = \frac{1}{c^2} \frac{\partial^2 w}{\partial t^2} \quad 3.2$$

$$D(\tau) \nabla^2 (\Delta) = \frac{\partial (\Delta)}{\partial t} \quad 3.3$$

The boundary conditions are

$$\begin{array}{llll} \sigma_z & = P_0(r, t) & z = 0 & r \leq a & t \geq 0 \\ & = 0 & z = 0 & r > a & t \geq 0 \\ \sigma & = 0 & z = 0 & & t \geq 0 \\ \tau_{rz} & = 0 & z = 0 & & t \geq 0 \end{array}$$

These boundary conditions state that a surface traction normal to the surface, given by  $P_0$ , is applied to the surface, that the surface is free of shear tractions, and that the driving force for plastic deformation and dislocation movement vanishes at the free surface.

The thermodynamic treatment of dislocation movement indicates that the dislocations move at nearly a constant velocity when the shear stress is above the static yield stress. This fact is borne out by the elementary solution for the one-dimensional case. This solution indicates, that away from the wave front, the velocity does not depend on the magnitude of the stress above the yield stress, thus little dependence on the transient inertial forces is expected. Therefore, the inertial forces are taken as zero in the following development of the equation. These equations are similar to the equations of motion for deformation of a porous media. The following method of solution of these equations is by potential functions and the transform calculus. The methods of solution follow very closely that of McNamee and Gibson (3).

# DYNAMIC PLASTIC DEFORMATION

$$\frac{\partial^2 u}{\partial t^2} = 0$$

$$\frac{\partial^2 w}{\partial t^2} = 0$$

The equations to be solved for the plastic-elastic deformation are

$$\left\{ \nabla^2 - \frac{1}{r^2} \right\} u - \{ 2\eta - 1 \} \frac{\partial \Delta}{\partial r} - \frac{1}{\mu} \frac{\partial \sigma}{\partial r} = 0 \quad 3.4$$

$$\nabla^2 w - \{ 2\eta - 1 \} \frac{\partial \Delta}{\partial z} - \frac{1}{\mu} \frac{\partial \sigma}{\partial z} = 0 \quad 3.5$$

$$D(\tau_{max}) \nabla^2 \Delta = \frac{\partial \Delta}{\partial t} \quad 3.6$$

with

$$\Delta = - \left( \frac{\partial u}{\partial r} + \frac{u}{r} + \frac{\partial w}{\partial z} \right) \quad 3.7$$

and

$$2\eta = \frac{\lambda + 2\mu}{\mu}.$$

By differentiation of the first two equations

$$\nabla^2 \{ \sigma + 2\mu\eta \Delta \} = 0 \quad 3.8$$

so that, if  $S$  is a harmonic function of  $r$  and  $z$

$$\sigma = 2\mu \frac{\partial S}{\partial z} - \Delta\eta \quad 3.9$$

It may be shown that another potential function  $E$  may be introduced such that

$$\Delta = \nabla^2 E \quad 3.10$$

The displacements  $u$  and  $w$  are related to these potential functions by

$$u = \frac{\partial E}{\partial r} + z \frac{\partial S}{\partial r} \quad 3.11$$

# DYNAMIC PLASTIC DEFORMATION

$$w = \frac{\partial E}{\partial z} + z \frac{\partial S}{\partial z} - S \quad 3.12$$

and the potential functions satisfy the equations

$$D \nabla^4 E = \nabla^2 \frac{\partial E}{\partial t} \quad 3.13$$

$$\nabla^2 S = 0 \quad 3.14$$

Utilizing the linear stress-strain relations the components of stress may be written in terms of the potentials

$$\frac{\sigma}{2\mu} = \frac{\partial S}{\partial z} - \eta \nabla^2 E \quad 3.15$$

$$\frac{\sigma_r}{2\mu} = \left\{ \frac{\partial^2}{\partial r^2} - \nabla^2 \right\} E - \frac{\partial^2 S}{\partial z^2} + \frac{\partial S}{\partial z} \quad 3.16$$

$$\frac{\sigma_\theta}{2\mu} = \left\{ \frac{1}{r} \frac{\partial}{\partial r} - \nabla^2 \right\} E - z \frac{\partial^2 S}{\partial z^2} + \frac{\partial S}{\partial z} \quad 3.17$$

$$\frac{\sigma_z}{2\mu} = \left\{ \frac{\partial^2}{\partial z^2} - \nabla^2 \right\} E - z \frac{\partial^2 S}{\partial z^2} + \frac{\partial S}{\partial z} \quad 3.18$$

$$\frac{\tau_{rz}}{2\mu} = \frac{\partial^2 E}{\partial r \partial z} - z \frac{\partial^2 S}{\partial r \partial z} \quad 3.19$$

These expressions identically satisfy the equilibrium equation. It is more convenient to solve these equations in a non-dimensional form. The substitutions

$$r = br'$$

$$z = bz'$$

$$t = \frac{t' b^2}{D}$$

where  $b$  is the radius of the area that the pressure is applied. This substitution introduces a non-uniform time scale into the problem, but will not introduce any serious difficulties.

The equations for the potentials become

# DYNAMIC PLASTIC DEFORMATION

$$\nabla^4 E' = \nabla^2 \frac{\partial E'}{\partial t} \quad 3.20$$

$$\nabla^2 S' = 0 \quad 3.21$$

and similarly for the stress and displacement coefficients.

The superscripts will be dropped as no confusion will be encountered. The boundary and initial conditions become

$$\left. \begin{array}{l} \sigma = 0 \\ \sigma_{zz} = (r, t) \\ \tau_{rz} = 0 \end{array} \right\} \begin{array}{l} \text{on} \\ r < 1 \\ r > 1 \end{array} \quad \begin{array}{l} z = 0 \\ \\ z = 0 \end{array} \quad t > 0$$

Introducing the Laplace-Hankel transform of potentials

$$\hat{E} = \int_0^\infty e^{-pt} dt \int_0^\infty r J_0(\xi r) E(r, t) dr \quad 3.22$$

$$\hat{S} = \int_0^\infty e^{-pt} dt \int_0^\infty r J_0(\xi r) S(r, t) dr \quad 3.23$$

and utilizing the differential relations of this transform, the transforms of the stresses and displacements are

$$\frac{\hat{\sigma}_z}{2\mu} = \xi^2 \hat{E} - z \frac{\partial^2 \hat{S}}{\partial z^2} + \frac{\partial \hat{S}}{\partial z} \quad 3.24$$

$$\hat{\tau}_{rz} = -\xi \frac{\partial \hat{E}}{\partial z} + z \xi \frac{\partial \hat{S}}{\partial z} \quad 3.25$$

$$\hat{\sigma} = \frac{\partial \hat{S}}{\partial z} - \eta \left\{ \frac{\partial^2}{\partial z^2} - \xi^2 \right\} \hat{E} \quad 3.26$$

$$\hat{u} = -\xi (\hat{E}_1 + z \hat{S}_1) \quad 3.27$$

$$\hat{w} = -\frac{\partial \hat{E}}{\partial z} + z \frac{\partial \hat{S}}{\partial z} - \hat{S} \quad 3.28$$

and the differential equations are

$$\left\{ \frac{\partial^2}{\partial z^2} - \xi^2 - p \right\} \left\{ \frac{\partial^2}{\partial z^2} - \xi^2 \right\} \hat{E} = 0 \quad 3.29$$

$$\left\{ \frac{\partial^2}{\partial z^2} - \xi^2 \right\} \hat{S} = 0$$

3.30

subject to the initial and boundary conditions

$$\left. \begin{aligned} \hat{\sigma} &= 0 & \text{or} & & z &= 0 \\ \hat{\sigma}_{zz} &= \frac{P_0 J_1(\xi)}{p} & & & r > 1 \\ &= 0 & & & r > 1 \\ \hat{\tau}_{rz} &= 0 & & & z = 0 \\ \hat{u} &\rightarrow 0 & & & z \rightarrow \infty \end{aligned} \right\} z = 0 \quad t > 0$$

The general solutions of the potentials may be written

$$\hat{E} = A_1 e^{-z\xi} + A_2 e^{-z(\xi^2 + p)^{1/2}} \quad 3.31$$

$$\hat{S} = B_1 e^{-z\xi} \quad 3.32$$

The relations between the coefficients may be established by considering the values of the stresses at the boundary

$$\begin{aligned} A_1 (\xi^2) + A_2 (\xi^2) + B_1 (-\xi) &= \frac{P_0}{2\mu} \frac{J_1(\xi)}{p} & \text{for } \hat{\sigma}_{zz} = \hat{p} \text{ at } z=0 \\ A_1 (-\xi) + A_2 (\xi^2 + p)^{1/2} &= 0 & \text{for } \hat{\tau}_{rz} = 0 \text{ at } z=0 \\ A_2 (-\eta p) + B_1 (-\xi) &= 0 & \text{for } \hat{\sigma} = 0 \text{ at } z=0 \end{aligned}$$

Thus

$$A_1 = - \frac{P_0}{2\mu} \frac{\xi (\xi^2 + p)^{1/2}}{p \Delta} \quad 3.33$$

$$A_2 = + \frac{P_0}{2\mu} \frac{\xi^2 J_1(\xi)}{p \Delta} \quad 3.34$$

$$B_1 = - \frac{P_0}{2\mu} \frac{\eta J_1(\xi)}{\Delta} \quad 3.35$$

$$\Delta = \xi^3 [ - (\xi^2 + p)^{1/2} ] + \xi [ - \xi^3 - \eta p \xi ] \quad 3.36$$

 The change of scale  $p = \xi^2 s$ 

is made. (The inverse transform must also include this change.)

$$A_1 = - \frac{P_0 J_1(\xi) (1 + s)^{1/2}}{2\mu \xi^4 s \lambda} \quad 3.37$$

$$A_2 = \frac{P_0}{2\mu} \frac{J_1(\xi)}{\xi^4 s \lambda} \quad 3.38$$

$$B_1 = -\frac{P_0 \eta}{2\mu} \frac{J_1(\xi)}{\xi^3 \lambda} \quad 3.39$$

$$\lambda = (1+s)^{1/2} + 1 + \eta s \quad 3.40$$

The potential transforms may be written

$$\hat{E} = -\frac{P_0}{2\mu} \frac{J_1(\xi)}{\xi^4} \left[ \frac{(1+s)^{1/2}}{s \lambda} e^{-z\xi} - \frac{e^{-\xi z(1+s)^{1/2}}}{s \lambda} \right] \quad 3.41$$

$$\hat{S} = -\frac{P_0 \eta}{2\mu} \frac{J_1(\xi)}{\xi^3 \lambda} e^{-z\xi} \quad 3.42$$

Inverting the potentials, the following expressions are obtained

$$E = -\frac{P_0}{4\pi\mu i} \int_{Br} e^{st\xi^2} ds \int_0^\infty \frac{J_1(\xi) J_0(r\xi)}{\xi} \left[ \frac{(1+s)^{1/2}}{s \lambda} e^{-z\xi} - \frac{e^{-\xi z(1+s)^{1/2}}}{s \lambda} \right] d\xi \quad 3.43$$

$$S = -\frac{P_0 \eta}{4\pi\mu i} \int_{Br} e^{st\xi^2} ds \int_0^\infty \frac{J_1(\xi) J_0(r\xi)}{\lambda} e^{-z\xi} d\xi \quad 3.44$$

Due to the complexity of the ensuing integrals, for arbitrary position, they will be evaluated here for  $z = 0$ ,  $r = 0$ . By the boundary conditions  $\sigma_z = P_0$ ,  $\tau_{rz} = 0$ . By invoking symmetry arguments on the horizontal displacement  $u$ ,  $u = 0$ .

The other integrals to be evaluated are

$$w = \frac{P_0 \eta}{2\pi^2 \mu i} \int_{Br} \frac{e^{st\xi^2}}{\lambda} ds \int_0^\infty \frac{J_1(a\xi)}{\xi^2} d\xi \quad 3.45$$

$$\frac{\sigma_r}{2\mu} = \frac{P_0}{4\pi^2 \mu i} \int_{Br} \frac{[(1+s)^{1/2} + (\eta-1)s - 1]}{\lambda} e^{st\xi^2} ds \int_0^\infty \frac{J_1(a\xi)}{\xi} d\xi \quad 3.46$$

and

$$\frac{\partial w}{\partial z} = \frac{P_0}{2\pi^2 \mu i} \int_{Br} \frac{[(1+s)^{1/2} - (1+s)]}{\lambda} e^{st\xi^2} ds \int_0^\infty \frac{J_1(\alpha\xi)}{\xi} d\xi \quad 3.47$$

where Br denotes the Bromwich contour.

The Laplace inversion may be carried out

$$E = - \frac{P_0}{2\mu} \int_0^\infty \frac{J_1(\xi) J_0(r\xi)}{\xi} [I_1 - I_2] d\xi \quad 3.48$$

$$S = - \frac{P_0}{2\mu} \int_0^\infty J_1(\xi) J_0(r\xi) e^{-z\xi} I_3 d\xi \quad 3.49$$

where

$$I_1 = \frac{1}{2\pi i} \int_{Br} \frac{(1+s)^{1/2}}{s\lambda} e^{-z\xi} e^{st\xi^2} ds \quad 3.50$$

$$I_2 = \frac{1}{2\pi i} \int_{Br} \frac{e^{-z\xi(1+s)^{1/2}}}{s\lambda} e^{st\xi^2} ds \quad 3.51$$

$$I_3 = \frac{1}{2\pi i} \int_{Br} \frac{e^{st\xi^2}}{\lambda} ds \quad 3.52$$

Evaluation of  $I_1$  :

$$I_1 = \frac{1}{2\pi i} \int_{Br} \frac{(1+s)^{1/2} e^{-z\xi}}{s(\lambda)} e^{st\xi^2} ds \quad 3.53$$

If the factor  $\lambda$  is written in the form

$$\lambda = \frac{\eta^2 s^2 + (2\eta - 1)s}{(1 + \eta s) - (1 + s)^{1/2}} \quad 3.54$$

and substituting  $y = z\xi$ ,  $\tau = t\xi^2$

$$I_1 = \frac{1}{2\pi\eta^2 i} \int_{Br} \frac{[(1+s)^{1/2}(1+\eta s)^{-y} - (1+s)] e^{-y}}{s^2 (s + \frac{2\eta-1}{\eta^2})} e^{st} ds \quad 3.55$$

Substituting  $s = s - 1$ , the Laplace shift theorem implies

$$I_1 = \frac{e^{-y-\tau}}{2\pi\eta^2 i} \int_{Br} \frac{[s^{1/2}(1-\eta+\eta s) - s] e^{\tau s}}{(s-1)^2 (s - (\frac{\eta-1}{\eta})^2)} ds \quad 3.56$$

This integral has a branch point at  $s=0$ , a double pole at  $s=1$  and a pole at  $s = (\frac{\eta-1}{\eta})^2$ . Thus this integral reduces to the sum of the residues and a branch line integral from  $-\infty$  to  $0$ . The solution given by the residues is constant in time and corresponds to an instantaneous elastic displacement. The contribution from the branch integral determines the unsteady behavior. This integral may be readily evaluated. Substitute  $s = v^2$

$$I_1 = \frac{2e^{-y-\tau}}{2\pi\eta^2 i} \int \frac{e^{-\tau v^2} [\eta v^4 - v^3 + (1-\eta)v^2]}{(v^2 - 1)^2 (v^2 - (\frac{\eta-1}{\eta})^2)} dv \quad 3.57$$

Denoting  $\frac{1}{2\pi i} \int_0^\infty f(v) dv$  by  $K_1(\tau)$

$$I_1 = \frac{2e^{-y-\tau}}{\eta^2} K_1(\tau) \quad 3.58$$

Repeating the development for  $I_2, I_3$

$$I_2 = \frac{2e^{-\tau}}{2} K_2(\tau, y) \quad 3.59$$

$$K_2 = \frac{1}{2\pi i} \int_0^\infty \frac{e^{\tau v^2} e^{-yv} [\eta v^3 - v^2 + v(1-\eta)]}{(v^2-1)^2 (v^2 - (\frac{\eta-1}{\eta})^2)} dv \quad 3.60$$

$$I_3 = \frac{2e^{-\tau-y}}{\eta^2} K_3(\tau) \quad 3.61$$

$$K_3 = \frac{1}{2\pi i} \int_0^\infty \frac{e^{\tau v^2} (\eta v^2 - v + (1-\eta))}{(v^2-1)^2 (v^2 - (\frac{\eta-1}{\eta})^2)} dv \quad 3.62$$

Thus

$$E = -\frac{P_0}{\mu\eta^2} \int_0^\infty \frac{J_1(\xi) J_0(r\xi)}{\xi} \left[ e^{-\tau\xi^2} z\xi K_1(\tau\xi^2) - e^{-\tau\xi^2} K_2(\tau\xi^2, z\xi) \right] d\xi \quad 3.63$$

$$S = -\frac{P_0}{\mu\eta^2} \int_0^\infty J_1(\xi) J_0(r\xi) e^{-\tau\xi^2} z\xi K_3(\tau\xi^2) d\xi \quad 3.64$$

# DYNAMIC PLASTIC DEFORMATION

These integrals will not be evaluated at this time. The expressions for the displacements and stresses which involve derivatives of these expressions will be derived and the resulting expressions will be calculated.

The vertical displacement and the maximum shear stress at  $z=0$ ,  $r=0$  will be calculated.

The vertical displacement is

$$w = \frac{\partial E}{\partial z} + z \frac{\partial S}{\partial z} + S \quad 3.65$$

Inserting the transforms into this expression

$$w = + \frac{P_0}{\mu \eta^2} \int_0^\infty \frac{J_1(\xi) J_0(r\xi)}{\xi} \left[ -\xi e^{-\tau-z\xi} K_1(\tau) - e^{-\tau} \frac{\partial K_2}{\partial z}(\tau, z\xi) \right] d\xi \\ - \frac{P_0}{\mu \eta^2} \int_0^\infty J_1(\xi) J_0(r\xi) \left[ -\xi e^{-\tau-z\xi} K_3(\tau) \right] d\xi \quad 3.66$$

at  $z=0$  this reduces to

$$w = \frac{P_0}{\mu \eta^2} \int_0^\infty \frac{J_1(\xi) J_0(r\xi)}{\xi} \left[ -\xi e^{-\tau} K_1(\tau) - e^{-\tau} \frac{\partial K_2}{\partial z}(\tau, 0) \right] d\xi \\ - \frac{P}{\mu \eta^2} \int_0^\infty J_1(\xi) J_0(r\xi) \left[ -\xi e^{-\tau} K_3(\tau) \right] d\xi \quad 3.67$$

Taking the displacement at  $r=0$

$$w = \frac{P_0}{\mu \eta^2} \int_0^\infty \frac{J_1(\xi)}{\xi} \left[ -\xi e^{-\tau} K_1(\tau) - e^{-\tau} \frac{\partial K_2}{\partial z}(\tau, 0) + \xi^2 e^{-\tau} K_3(\tau) \right] d\xi \quad 3.68$$

with

$$K_1(\tau) = \frac{1}{2\pi i} \int_0^\infty \frac{e^{\tau v^2} (v^4 - v^3 + (1-\eta)v^2)}{(v^2-1)^2 (v^2 - (\frac{\eta-1}{\eta})^2)} dv \quad 3.69$$

$$\frac{\partial K_2}{\partial z}(\tau, 0) = \frac{-\xi}{2\pi i} \int_0^\infty \frac{e^{\tau v^2} (\eta v^4 - v^3 + v^2(1-\eta))}{(v^2-1)^2 (v^2 - (\frac{\eta-1}{\eta})^2)} dv \quad 3.70$$

$$K_3(\tau) = \frac{1}{2\pi i} \int_0^\infty \frac{e^{\tau v^2} (\eta v^2 - v + (1-\eta))}{(v^2-1)^2 (v^2 - (\frac{\eta-1}{\eta})^2)} dv \quad 3.71$$

Thus

$$w = \frac{P_0}{\mu \eta^2} \int_0^\infty \xi J_1(\xi) e^{-\tau} K_3(\tau) d\xi \quad 3.72$$

Similarly

$$\frac{\partial w}{\partial z} = \frac{P_0}{\mu \pi} \int_0^\infty \frac{J_1(\xi)}{\xi} [K_3 - (K_1 + K_2)] d\xi \quad 3.73$$

$$\frac{\sigma_r}{2\mu} = \frac{P_0}{2\mu\pi} \int_0^\infty \frac{J_1(\xi)}{\xi} (K_3 + (\eta-1)K_2 - K_1) d\xi \quad 3.74$$

Numerical solutions for the deformation were made on the surface at the center of the impact. The vertical and horizontal stresses, the maximum shear stress, the vertical displacement and the vertical strain were computed as a function of time (Fig. 2). These solutions indicate that the displacements due to plastic flow take a certain amount of time.

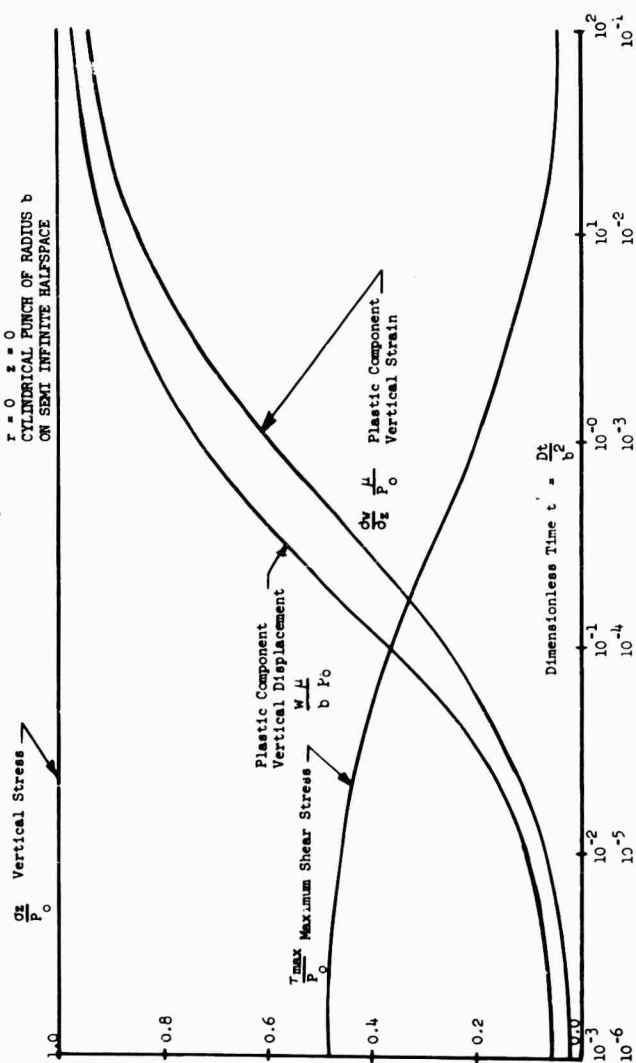
For short times after the impulse little plastic deformation has taken place. Around 100  $\mu$  sec the plastic deformation becomes appreciable and the decay of the shear stress becomes rapid. The horizontal stress rises rapidly approaching the value of the vertical stress. If the shear stress is allowed to decay all the way to zero, then the horizontal and vertical stresses are equal and a state of hydrostatic stress exists. The displacement reaches a maximum or-limiting value. The maximum shear stress decays rapidly as the dislocations move. Two factors arise to control the amount of plastic flow as are seen readily.

1. The maximum shear stress must exceed a certain level.
2. The duration of the load is such that the maximum shear stress is high governs the total amount of flow. Thus the duration of the high stress rather than the stress rate is the governing factor.

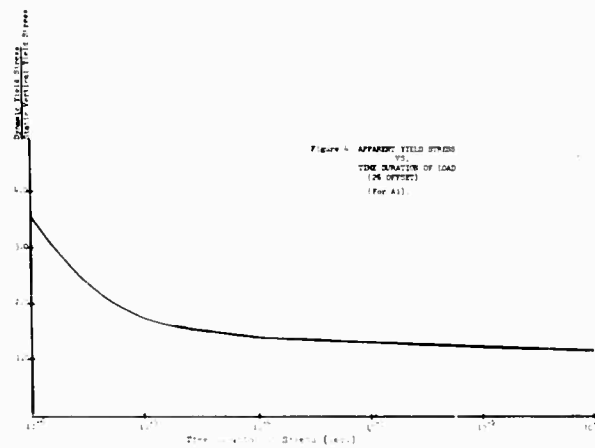
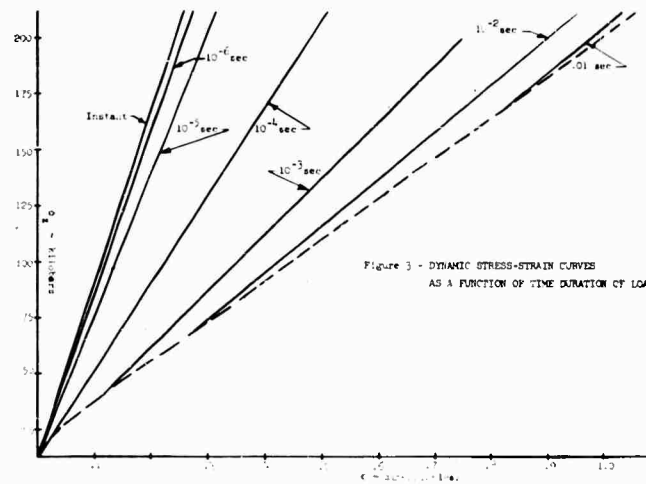
The stress-strain relationship that would be observed at the surface is computed for several durations of the applied load. The vertical stress as the vertical strain is plotted (Fig. 3). Because the boundary stress is maintained, the stress-strain curve does not flatten out to a horizontal position, but rather a limiting slope is approached as the time duration of load becomes infinite. This demonstrates another point. The observed total stress-strain curve is definitely a function of geometry and boundary conditions.

The stress at which a 2 percent offset of the total strain from the instantaneous elastic strain is plotted as a function of load duration (Fig. 4). The increase in this definition of the yield is quite marked.

Figure 2 - STRESSES AND STRAINS AT  
 $r = 0, z = 0$   
 CYLINDRICAL PUNCH OF RADIUS  $b$   
 ON SEMI INFINITE HALFSPACE



# DYNAMIC PLASTIC DEFORMATION



# DYNAMIC PLASTIC DEFORMATION

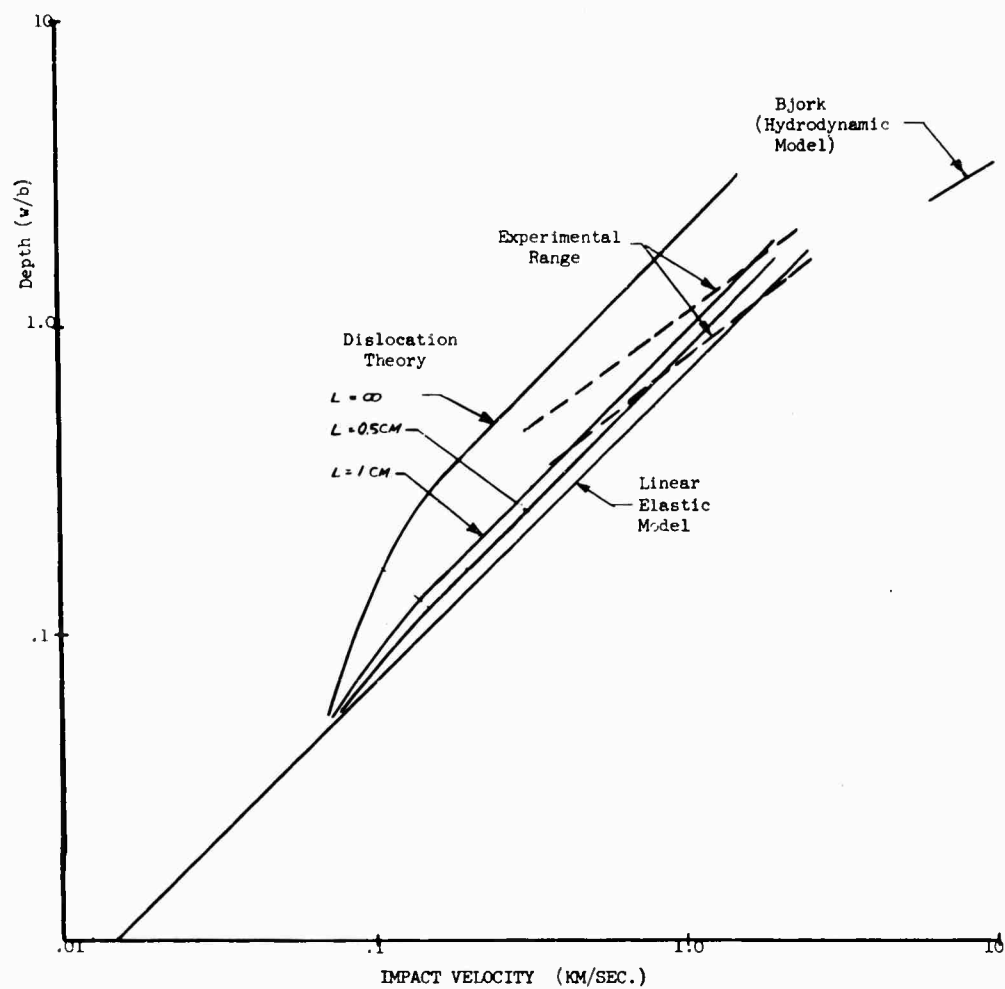


Figure 5  
DEPTH OF PENETRATION  
VS  
IMPACT VELOCITY FOR  
CYLINDRICAL PROJECTILE

## DYNAMIC PLASTIC DEFORMATION

The vertical displacement at the center of impact is, of course, the depth of the crater that will be formed. To compare these results with experimental data this displacement must be calculated as a function of depth. To accomplish this, the pressure on the surface must be found and the duration of the load must be calculated. A cylindrical projectile is assumed. The vertical applied stress is related to the incident velocity by the Beltrami equation for projectile and target of the same material

$$\sigma_z = \rho \frac{c v_i}{2}$$

where

$$\begin{aligned}\rho &= \text{density} \\ c &= \text{compressional wave velocity} \\ v_i &= \text{impact velocity}\end{aligned}$$

For similar target and projectile materials, this stress is maintained for a period while a compressive stress wave is sent back into the projectile and a tensile is reflected from the near surface of the projectile. Thus the time duration is twice the length of the projectile divided by the sonic velocity  $\Delta t = \frac{2L}{c}$

Figure 5 shows the vertical displacement as impact velocity for several lengths of projectile. Then deformation curves are compared with other theoretical approaches, linear elastic(5) and hydrodynamic (4) and experimental values. Reasonable agreement is shown for the range computed.

### SUMMARY

The time dependent elastic-plastic deformation problem for impact has been solved, utilizing continuum equations derived from a two mechanism model of deformation. The two basic physical processes used were elastic distortion and movement of dislocations under stress.

This two-mechanism model gives reasonably accurate quantitative prediction of dynamic plastic deformation, specific qualitative information about the course of dynamic plastic deformation, and information of engineering interest.

Notable among the information on the course of the plastic deformation is the derivation and computation of the observed stress-strain curve. This study also indicated that yielding begins instantaneously, but that the full effect of yielding occurs over a period of time at a rate dependent on stress and on material properties.

The magnitude of the plastic deformation under impact conditions is governed by two features of the impact: (1) the magnitude of the stress, which may be related to the incident velocity, and (2) the duration of the stress, which may be related to the material properties of the target and projectile and to the geometry of the projectile.

## DYNAMIC PLASTIC DEFORMATION

### BIBLIOGRAPHY

1. Fugelso, L. E. , American Machine and Foundry Company, Final Technical Report Contract, AF 29(601)-2533, 1961.
2. Hopkins, H. G. , and Kolsky, H. , Fourth Symposium on Hypervelocity Impact Proceedings, Volume 1, 1960.
3. McNamee, J. , and Gibson, R. E. , Mech. and Appl. Math. Quart. Jour. 13, 210-227, 1960.
4. Bjork, R. L. , Rand Corporation, Report P-1662, 1958.
5. Fugelso, L. E. , and Arentz, A. A. , American Machine and Foundry Company, Final Technical Report Contract, DA-19-129-QM-1542, 1961.

# HYDRODYNAMICS APPLIED TO HYPERVELOCITY IMPACT

## I. SCALING LAWS FOR DISSIMILAR MATERIALS

A. E. Olshaker and R. L. Bjork

The RAND Corporation  
Santa Monica, California

### I. FUNDAMENTAL SHOCK RELATIONS

#### Shock Waves

It is an interesting property of fluids and gases that any compression wave, even if started with a continuous form, will become discontinuous as it propagates, with this discontinuity or shock wave moving supersonically with respect to the overtaken medium. For an elastic-plastic solid under certain conditions an elastic disturbance may precede the shock wave, but its particle displacements and pressures are usually small compared to the shock pressures and particle velocities, and will not be considered here. A rough but simple physical justification of the discontinuous compression in fluids is obtained by noting that in general the more compression any given matter undergoes, the stiffer it becomes, with the resulting greater bulk "force constant" giving a higher "frequency," or disturbance propagation velocity. Therefore, the more compressed part of the waveform will propagate faster than the less compressed part, overtaking it until a shock is formed in which the pressure jump approximates a mathematical discontinuity. This is sketched in Figure 1.

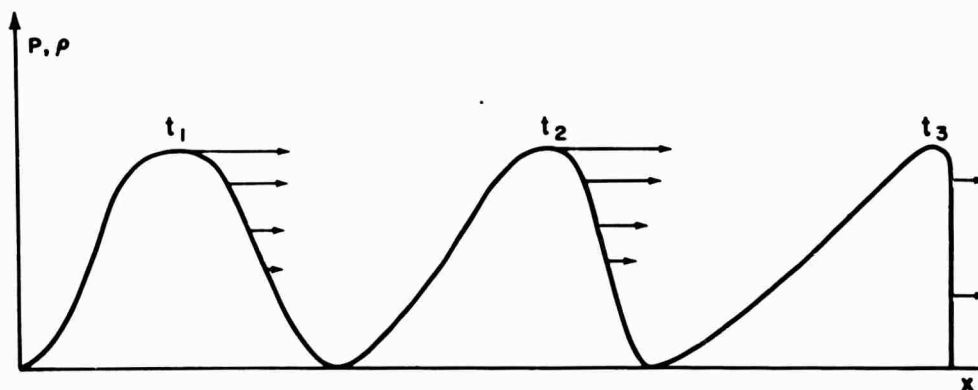


Figure 1. Steepening of Compressive Wave Fronts with Time.

## SCALING LAWS

By the same argument one would expect a tensile, or rarefaction wave-form, even if initially discontinuous, to become increasingly smoothed out as it propagates, with its front traveling at the speed of sound in the undisturbed material, and this is in fact the case.

### One-Dimensional Shock Conservation Relations

Shock relations are derived by considering the shock as a mathematical discontinuity across which irreversible processes occur. Hugoniot showed in 1889 that, in the absence of viscosity and heat conduction outside the shock, conservation of energy implies conservation of entropy in continuous flow and also implies a change of entropy across shock. <sup>(2)</sup> To quote a current textbook, Courant and Friedrichs, "In reality very considerable changes of velocity and temperature occur across such surfaces; thus the assumption of sharp discontinuities is indeed an idealization which agrees with the facts rather better than we might hope." <sup>(3)</sup> The simple but important relation of pressure, density and energy across a shock was first derived by him and still bears his name.

Let us first review all the relations which must hold across a one-dimensional shock before bringing in any material properties. It is important not to think of a three-dimensional cratering process initially, so that the important points of shock systems can be seen from these one-dimensional arguments.

Consider a column of fluid in a tube (Fig. 2) where  $a_0(t)$  and  $a_1(t)$  denote the positions of the moving particles that form the ends of the tube. At

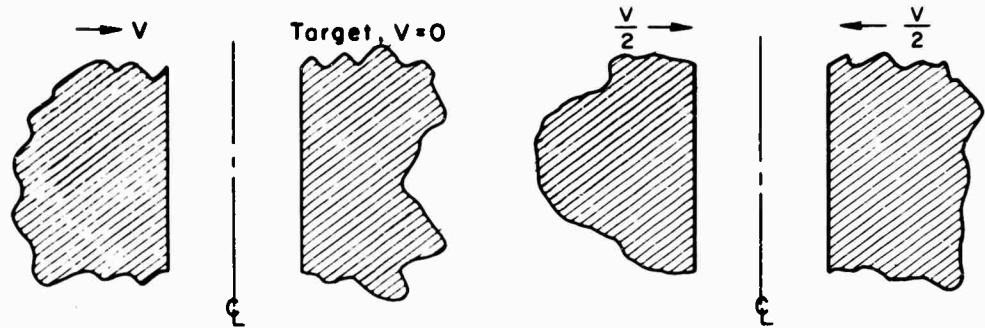


Figure 2. Sample Volume for Deriving Shock Conservation Relations

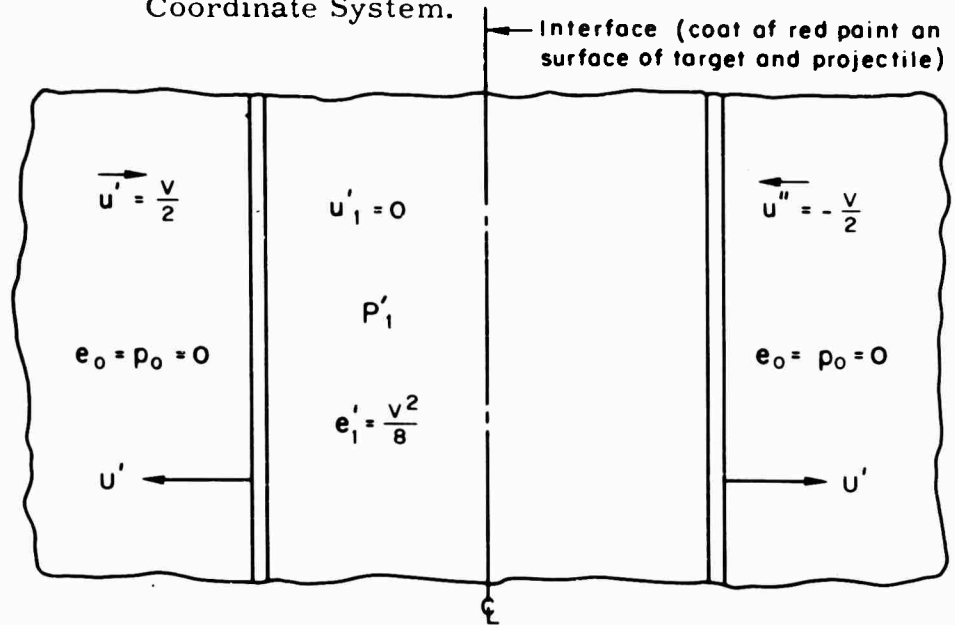
first let the tube interior be completely general. The absolute particle velocities at the tube ends are then  $\dot{a}_0 = u_0$  and  $\dot{a}_1 = u_1$  respectively. The dot over the

# SCALING LAWS

## (B) Velocities in the Center of Mass Coordinate System



## (A) Velocities in the Laboratory Coordinate System.



## (C) Shock Parameters in the Center of Mass Coordinate System.

Figure 3. Shock Relations for a One-dimensional Impact Between Similar Materials.

## SCALING LAWS

symbol denotes differentiation with respect to time. The three conservation relations are:

Conservation of mass

$$\frac{d}{dt} \int_{a_0(t)}^{a_1(t)} \rho \, dx = 0 \quad (1)$$

Conservation of momentum

$$\frac{d}{dt} \int_{a_0}^{a_1} \rho \, u \, dx = p_0 - p_1 \quad (2)$$

This simply says that the only forces acting are pressure forces, and that consequently the rate of change of momentum of the column equals the total resultant force exerted on the column.

Conservation of energy

$$\frac{d}{dt} \int_{a_0}^{a_1} \rho \left( \frac{1}{2} u^2 + e \right) dx = p_0 u_0 - p_1 u_1 \quad (3)$$

$e$  is here the internal energy of the material per unit mass, so that the total energy per unit mass is  $e + 1/2 u^2$ . The equation then says that the change in net energy is due to the "power input", or the work done in unit time by the end pressures. A fourth implied relation is that entropy either increases or remains constant, but this is automatically taken care of by Hugoniot's arguments when the shock is introduced.

In Appendix A the three so-called jump conditions across a shock are derived from Equations 1-3 by permitting a mathematical discontinuity within the tube, and then letting the tube shrink to just include material immediately in front of and behind the shock. The resulting relations are:

Conservation of mass

$$\rho_0 (u_0 - U) = \rho_1 (u_1 - U) = m, \text{ the mass flux} \quad (4)$$

where  $U$  is the absolute velocity of the shock.

Conservation of momentum

$$\rho_0 u_0 (u_0 - U) + p_0 = \rho_1 u_1 (u_1 - U) + p_1 \quad (5)$$

Conservation of energy

$$m \left\{ \frac{1}{2} u_0^2 + e_0 \right\} + p_0 u_0 = m \left\{ \frac{1}{2} u_1^2 + e_1 \right\} + p_1 u_1 \quad (6)$$

## SCALING LAWS

where  $m$  is the mass flux in (4).

The Hugoniot relation is derived from these three jump conditions in Appendix B, after a moderate amount of algebraic manipulation, and is:

$$\frac{1}{2} (p_0 + p_1) (v_0 - v_1) = e_1 - e_0 \quad (7)$$

where  $v$  is the specific volume,  $= \frac{1}{\rho}$ .

This is an important equation in shock dynamics because it refers only to thermodynamic quantities. It can be interpreted as saying that the increase in internal energy across the shock front is due to the work done by the mean pressure in performing the compressions.

Note that Equations 4-7 are completely general for any one-dimensional shock system in which the only noteworthy force is a pressure. This will be seen to be well verified for metallic solids above one or two hundred kilobars.

In these equations it is important to distinguish between the shock velocity  $U$ , which is the absolute velocity of propagation of the interface between the compressed and uncompressed zones, and  $u$ , which is the absolute velocity of the material particles. Courant and Friedrichs (3) gives an analogy of the shock system which is perhaps familiar. Imagine a single file row of speeding automobiles coming upon a long row stopped at a traffic light. The particle velocity is that to which the stopped cars are abruptly bumped in sequence, which is the same velocity as that to which the speeders are equally abruptly decelerated. Two shocks result. One is the interface between the stopped cars and those which have been bumped, and this is evidently a rapidly advancing forward facing shock whose velocity depends on the car spacing and "particle velocity," which in turn depends on the mass and bumper design of the cars. It is not obvious which way the second shock, which represents the discontinuity between the speeding and slowed cars, moves, and in Reference 4 and below it is shown that it can be either way, depending on relative properties of the two columns. This, of course, is of interest in impact, since sometimes the projectile material can go deep into the target before it overtakes the rear shock and is decelerated.

It is shown in Reference 3 that particle velocities always decrease across a shock from left to right, and also that the shock propagation velocity is always supersonic with respect to the material before it, and subsonic with respect to the compressed region behind. In the limit of very weak shocks, the material in front and behind the shock is indistinguishable; therefore, the disturbance is sonic with respect to both, and this is a sound wave.

In the auto column, the deceleration from left to right, and compression behind the shock are evident, and if driver agitation is considered an analogy for thermal motion, so is the increase of temperature.

### Shock Relations for One-dimensional Hypervelocity Impact (Target at Rest)

Using the jump conservation relations 4-7, we will now show some properties of the initial impact shock front. That is, the following equations

## SCALING LAWS

are one-dimensional, which is for the case of projectiles as well as target being semi-infinite. The condition of interest for hypervelocity impact is target material at rest and under no pressure in front of the shock, or  $p_0 = u_0 = 0$ . For convenience, we define  $e_0 = 0$  also. The quantities behind the shock in the high pressure and density region have the subscript 1.

Conservation of mass, Equation (4) becomes, with  $u_0 = 0$ ,

$$\rho_1 (U - u_1) = \rho_0 U \quad (8)$$

or

$$\frac{\rho_1}{\rho_0} = \frac{U}{U - u_1} \quad (9)$$

Conservation of momentum, Equation (5) becomes, with  $p = u = 0$ ,

$$P_1 = \rho_1 (U - u_1) u_1$$

or using Equation (8),

$$P_1 = \rho_0 U u_1 \quad (10)$$

Equations (9) and (10) show that across a shock, the pressure rise and density increase are completely determined by two velocities, the particle velocity behind the shock  $u_1$ , and the shock velocity  $U$ . This fact will be referred to again, since in experimental determination of shock pressures and densities the actual measurements made are of these velocities, and it also will turn out to be very useful in some applications to plot material shock properties in the pressure versus particle velocity form for this case of stationary material before the shock.

If the impacting material is the same as that of the target, then the particle velocity behind the shock is exactly one-half of the impact velocity. This interesting fact is a consequence of symmetry, and is apparent with the help of Figure 3 which is taken from Reference 4.

There it was explained that in the "center of mass" coordinate system the interface is brought to rest by symmetry. This coordinate system is referred to a point halfway between the impacting surfaces, and moving at  $V/2$ . But the entire shock system may then be translated to the right at  $V/2$ , after which Figure 3C will become equivalent to the target coordinate system after impact, Figure 4. It is now seen that the particle velocity after impact is  $V/2$ . This is plausible by the automobile analogy if one considers inelastic collisions of equal mass cars.

Figure 3C can also be used to show how the similar material impact pressure can be calculated. Using the center of mass coordinate system, conservation of energy requires that the specific kinetic energy of the material in the two moving zones outside the shock becomes specific internal energy of the compressed material in the shocked region, where there is no velocity,

# SCALING LAWS

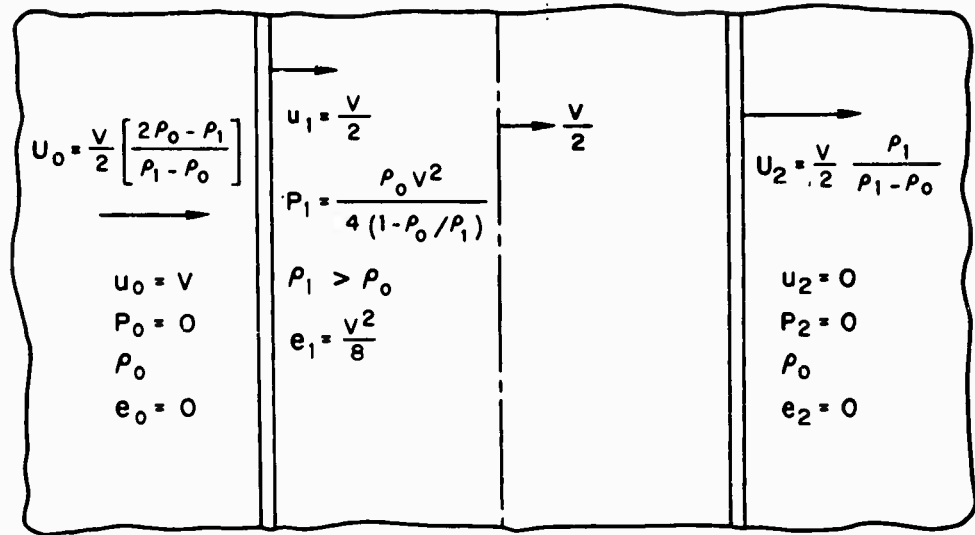


Figure 4. Shock Parameters for a One-dimensional Impact Between Similar Materials Referred to the Laboratory Coordinate System.

independent of any conditions upon increase of entropy. Therefore, the Hugoniot relation, (7) becomes:

$$\frac{1}{2} p_1 (v_0 - v_1) = \frac{V^2}{8}$$

since  $p_0$  and  $e_0$  are taken to be zero, and

$$e_1 = \frac{1}{2} \left( \frac{V}{2} \right)^2 = \frac{V^2}{8}.$$

Then

$$\frac{V^2}{4} = p_1 \left( \frac{1}{\rho_0} - \frac{1}{\rho_1} \right) = p_1 \left( \frac{\rho_1 - \rho_0}{\rho_0 \rho_1} \right)$$

and multiplying by  $\rho_0$  and dividing by  $1 - \rho_0/\rho_1$ ,

# SCALING LAWS

$$p_1 = \frac{\rho_o v^2}{4(1 - \rho_o/\rho_1)} = \frac{\rho_o v^2}{4(1 - v_1/v_o)} \quad (11)$$

Since the pressure does not depend on the coordinate system, this equation holds for either two semi-infinite slabs approaching at  $V/2$  each, or for one approaching the other at  $V$ . Therefore, if one knows the experimental shock pressure versus density ratio,  $p$  versus  $v/v_o$ , one can calculate the similar material impact pressure by plotting Equation 11 for a constant value of  $V$ , and reading the pressure at the intersection of the two curves. (If the density is taken in  $\text{grams/cm}^3$ , then velocity in  $(\text{KM/sec})/10$  will give the pressure in megabars.)

A more general and convenient method will be given in the following sections for identification of maximum impact pressures for either dissimilar or similar material collisions.

The velocity of the shock moving into the target is obtained from Equation (10):

$$U_2 = (p_1) \left( \frac{1}{\rho_o u_1} \right) \quad (12)$$

The pressure is substituted in from (11), so

$$U_2 = \left( \frac{\rho_o v^2}{4(1 - \rho_o/\rho_1)} \right) \frac{1}{\rho_o u_1} \quad (13)$$

But for similar material impact,

$$U_1 = \frac{V}{2}$$

therefore

$$U = \frac{v}{2(1 - \rho_o/\rho_1)} = \frac{\rho_1 v}{2(\rho_1 - \rho_o)} \quad (14)$$

for the shock advancing into the target.

The only difference between the shock facing the target and that facing the projectile is in the translation  $V$ , so the velocity of the rear shock is expression (12),

$$U_o = v \left[ \frac{\rho_1}{2(\rho_1 - \rho_o)} - 1 \right] = v \left[ \frac{2\rho_o - \rho_1}{2(\rho_1 - \rho_o)} \right] \quad (15)$$

## SCALING LAWS

This shows that the shock moves to the left if  $2\rho_0 > \rho_1$ , and to the right if  $\rho_1 > 2\rho_0$ . Whether these conditions are fulfilled or not depends on the particular materials and impact velocity.

### Hugoniot Curves and Equations of State

In the above three conservation relations the four unknowns are pressure, density, internal energy, and velocity, all of which must be determined as functions of time and position. One more equation is needed to determine the four unknowns, and since the first three are general, the fourth must bring in the relevant material properties. This is the equation of state of the material. In this formulation the natural choice is pressure as a function of density, and internal energy,  $p(\rho, e)$ . (Other forms such as  $p(v, T)$  or  $p(v, S)$  are equally valid but less convenient.) With these four relations, any fluid dynamic process is theoretically determined. The difficulties involved in realizing the solution are 1) the actual calculation of this unsteady, non-linear problem in the presence of discontinuities, or shocks, and 2) specification of the equation of state in the relevant pressure ranges.

Calculations of this problem are handled by large computers and numerical finite-difference techniques. Since machines cannot handle discontinuities, a method of approximating shocks by rapid but continuous variations which satisfy the conservations and still give the necessary entropy increase is used. Axially symmetric projectiles are used, which reduce the number of space variables from three to two. (Even with this reduction, the mountain of data which the machine spews forth is monumental. One compensating advantage of this lies in the fact that the detailed step by step records of the impact process give valuable insight into the mechanisms at work.)

The determination of the equations of state up into the hydrodynamic regimes is the major problem in the field of high pressure physics. Again, it should be mentioned that the  $p(\rho, e)$  equations only have the essential parameters of the fluid regimes, which are felt to be the most important in hypervelocity impact. To obtain a more complete impact problem solution, the relations of displacements as functions of pressures, shears, and time would have to be known. When one considers how little is known about such a relative simplification of this general case as work hardening under static loadings, the inclusion of general rate and loading effects is impressive. This is also true for the same problem in tension, which is of interest for problems of spallation and dynamic fracture. However, the hydrodynamic equation of state,  $p(\rho, e)$ , must be known first before other refinements can be added for the "low" pressures toward the end of the impact.

Measuring densities as functions of temperature and pressure by static loadings is inadequate for hypervelocity impact, since static pressures cannot be made sufficiently high. Bridgeman<sup>(5)</sup> has conducted isothermal compressibility studies on many materials to pressures as great as 100 kilobars, or almost one-and-one-half million pounds per square inch, but this appears to be about the practical limit for static methods.

On the other hand, theoretical equations of state calculated by quantum-statistical mechanics are not valid until pressures of 10 to 20 megabars or more,

## SCALING LAWS

which is fairly high even for meteoroid impacts.

What has finally begun to make this information available in the ranges of greatest interest for hypervelocity impact has been dynamic measurement methods including the use of hypervelocity impact itself. Shock waves induced explosively or by impact generate the pressures required, and Equations (9) and (10) show that for any one shock strength, measurement of both the shock and particle velocities determine the pressure and density jump across this shock, and so give one point on a pressure versus volume or density ratio plot. The locus of these points obtained for different shock strengths is known as the Hugoniot curve of the material. This is because the Hugoniot equation, Equation (7), is identically satisfied between any point on this curve and the foot of the curve, where  $p = 0$ . (On these scales, one atmosphere is indistinguishable from zero pressure.) It should be emphasized that such a plot does not show a continuous compression process of the material, but rather the series of points to any one of which the material is discontinuously compressed across the shock of that particular strength.

It is only within the last five years that these curves have been measured and placed in the unclassified literature, and recently there seems to have developed a characteristic competition between American and Soviet scientists to obtain higher experimental pressures. Our workers at Los Alamos have investigated Hugoniot curves for 27 metals to about 0.4 megabars,<sup>(6)</sup> and 19 metals up to two megabars,<sup>(7)</sup> while Al'tshuler, et al., in Russia have published curves of nine elements to 4 megabars,<sup>(8)</sup> and iron up to 5 megabars.<sup>(9)</sup> (One megabar, or one million bars, equals 14,502,000 pounds per square inch or approximately one million atmospheres.)

Some typical Hugoniot curves are shown in Figure 5 taken from the Los Alamos data. The relative softness, or compressibility of lead is apparent, while, surprisingly, copper is seen to be stiffer or less compressible than iron. The kink at the bottom of the iron curve is due to the phase transition discussed in Reference 1.

The results shown in Figure 5 were obtained by measuring shocks induced by explosives detonated against the material. By explosive detonation alone it is not possible to obtain pressures much over the one-half megabar shown. With use of impact, however, the data was extended beyond this limit. Los Alamos employed explosively accelerated brass plates to achieve impact pressures in target specimens of two megabars, and the Russians allude to impact methods, although without specifications of details, in discussion of their five megabar results.

There are several different techniques used in measuring the particle and shock velocities which are needed to determine the pressures and density ratios of Hugoniot loci. It is encouraging that in general the agreement between these techniques is excellent and such reported data are reliably known to within a very few percent. In original explosive Los Alamos work, shock and particle velocities were determined by electrical contact pins placed in holes drilled in the metal or spaced at small distances from the back surface. Oscillograph records of concentric arrays of 60 pins were used to correct for any nonplanarity and tilt of the shock wave. Control of the shock wave strength was obtained by varying the type of explosive, the thickness of the targets, and placement of intermediate

# SCALING LAWS

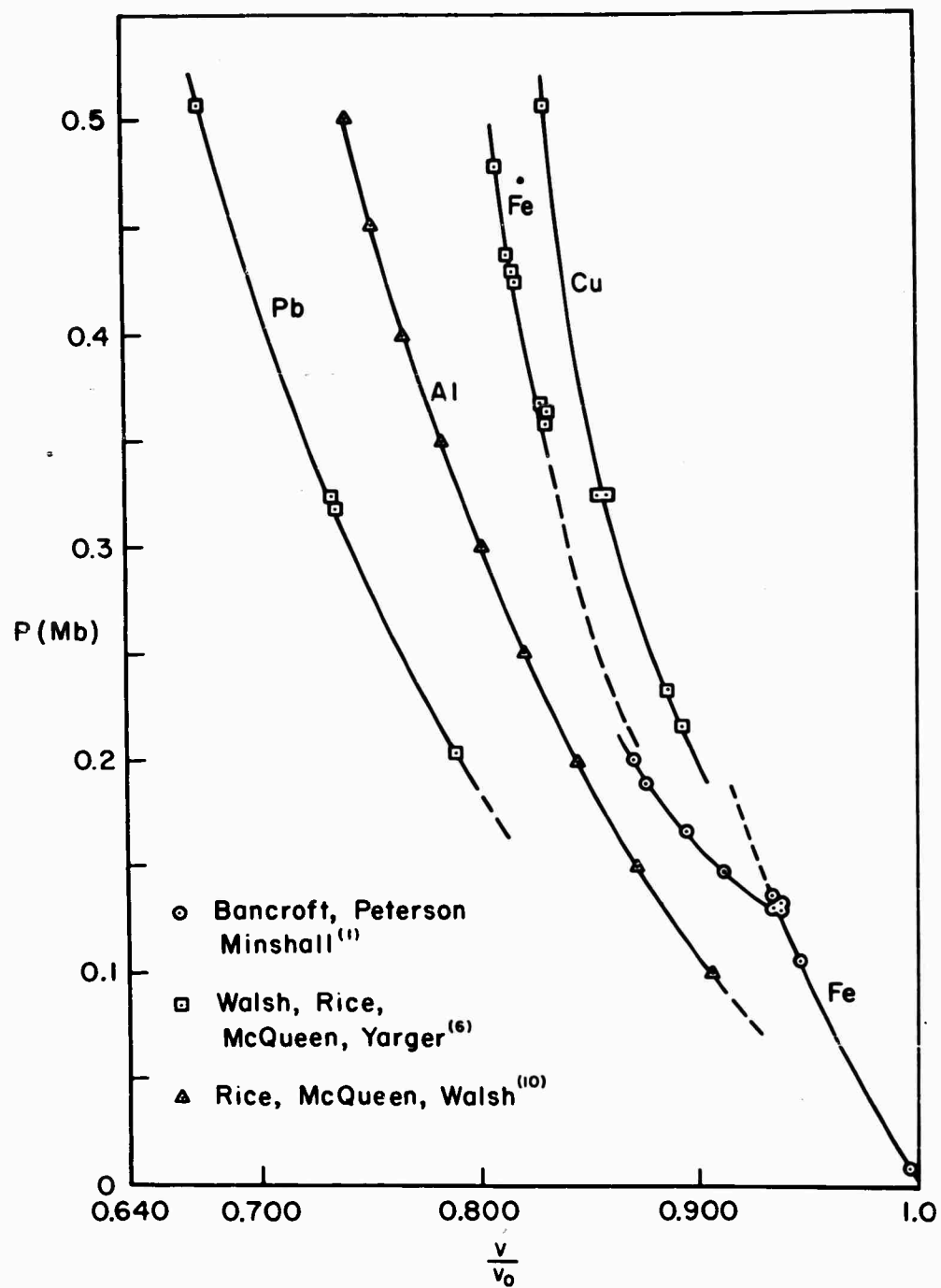


Figure 5. Hugoniot Curves for Four Common Metals.

## SCALING LAWS

metal between the explosive and target. Another successful independent check was obtained from agreement between target Hugoniot calculated from these mechanical, conservation measurements and those obtained from compatibility relations at the interface of the target and intermediate standard using the known Hugoniot of the standard.

The more recent velocity measurements at Los Alamos use photographic methods based on the fact that confined gases become brilliantly luminescent when excited by multiple shock reflections. (6), (10) A series of spaced argon-filled flash gaps are mounted at various positions behind the back of the targets and swept by a moving image camera located in a remote bunker. Both the velocities of the target shock wave and the particle velocities at the target free surface are then measured. The average disagreement between this method and the pin contact technique is less than one percent in velocity. (10) Attempts at direct measurement of pressures by piezoelectric crystals have confirmed the velocity-measured results.

Of particular interest is an experiment in which three different orientations of zinc single crystals were explosively shocked two times in order to investigate whether observed compressions were dependent upon crystal orientation. For a shock strength of 0.414 megabars, the spread in measured velocities was 1 percent, and at 0.200 megabars it was 1.5 percent. Since this is approximately the amount of experimental error, and also similar to the results of polycrystalline zinc, it is concluded that at these pressures there is no dependence of shock velocity, hence compressibility, upon crystallographic orientation. (6) However, these shock wave results differ from Bridgeman's lower pressure static measurements, which show a several-fold difference in compressibility between the same axes, the *c* and the *a*. (5)

Another typical characteristic of Hugoniot curves is that they are almost independent of small-percentage alloying. Figure 6 shows points for both 1100 aluminum, which is known as commercially pure, and 2024 alloy, which is 4.5 percent Cu, 1.5 percent Mg, and 0.6 percent Mn. (11) There is no discernible difference in compressibility above approximately 130 kilobars, which is what might be expected for slight amounts of impurities in such pure hydrostatic compressions.

While obtaining the Hugoniot curve of a material is the first step in describing its dynamic high pressure behavior, it is insufficient for determining a complete flow problem. The compression jump across the shock is determined, but the expansion back to zero pressure is not. This expansion is adiabatic and reversible in contrast to the irreversible shock compression. This is just saying that what is desired is the general thermodynamic equation of state of the material, which would encompass any conceivable process. For example, the equation of state is some function  $p = p(\rho, e)$ . If the energy,  $e$ , is eliminated from the expression by the relation which must hold across the shock, Hugoniot relation,

$$e - e_0 = \frac{p + p_0}{2} \left( \frac{1}{\rho_0} - \frac{1}{\rho} \right) \quad (16)$$

then the resulting expression,  $p' = p'(\rho)$  is the Hugoniot curve. But since what is obtained experimentally is the Hugoniot curve, a major concern is to use the Hugoniot as a basis for calculating the complete thermodynamic equation of state.

## SCALING LAWS

This is done by combining theoretical results from statistical mechanics with known thermodynamic properties at standard conditions, and an approximate equation of state valid in the vicinity of the Hugoniot is obtained. (More details are given in Reference 16.) Since the impact problems are necessarily expanding down to zero pressure from points on the Hugoniot, this region is the one of greatest interest. These results are then combined with the quantum mechanical theoretical results which are valid in the very high pressure ranges, and curves are faired in between. The Los Alamos presentation of this resulting equation is given in the following form

$$P(\rho, \epsilon) = \frac{a_1 \mu + a_2 \mu \mu + \epsilon (b_0 + b_1 \mu + b_2 \mu^2) + \epsilon^2 (C_0 + C_1 \mu)}{\epsilon + \epsilon_0} \quad (17)$$

where  $\epsilon = \rho_0 e$ ,  $\mu = \frac{\rho}{\rho_0} - 1$

and  $p$  is in megabars. The constants for two elements are given in Table 1. <sup>(12)</sup>  $\mu$  is used simply because  $p$  versus  $\mu$  starts at the origin while  $p$  versus  $\rho/\rho_0$  starts at  $\rho/\rho_0 = 1$ .

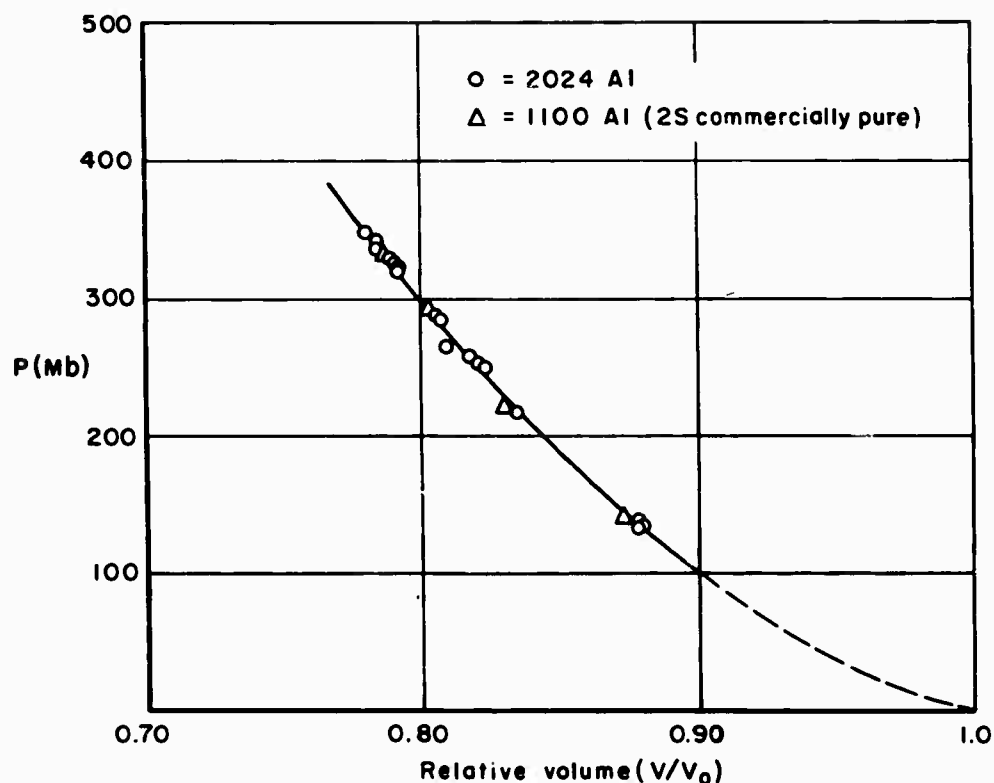


Figure 6. Hugoniot Curve for Aluminum, Comparing Points for the 1100 and 2024 Alloys.

## SCALING LAWS

Figure 7 shows the Hugoniot curves of iron and aluminum which result from the following Los Alamos equation of state. For the maximum meteoroid velocities of 72 km/sec, iron to iron impact reaches a pressure of 143 megabars and aluminum to aluminum 47 megabars.

TABLE 1

Los Alamos Equation of State Constants for Two Elements

	<u>Aluminum</u>	<u>Iron</u>
$a_1$	1.1867	7.780
$a_2$	0.7630	31.18
$b_0$	3.445	9.591
$b_1$	1.545	15.676
$b_2$	0.9643	4.634
$c_0$	0.4338	0.3984
$c_1$	0.5487	0.5306
$\epsilon_0$	1.5	9.0
$p_0$	2.702	7.86

### p-u Form of the Hugoniot and Graphical Determination of Maximum Dissimilar Material Impact Pressure

It was seen in Equations (9) and (10) that the pressure and density jumps across a shock are determined by the particle and shock velocities. Therefore, since all four of these quantities must be determined in obtaining the Hugoniot curve, the shock pressure versus particle velocity behind the shock may be plotted instead of pressure versus density ratio for the case of material in front of the shock at rest. This p-u form of the Hugoniot is referred to below as  $p_H(u)$  and enables the identification of dissimilar material impact pressures. Figure 8 shows that p-u plot for iron. As illustrated in Figure 9, consider material 1 moving at velocity V striking material 2, which is at rest. The shock pressure, which is constant within the entire compressed zone, is necessarily some point on the Hugoniot curve of each material, by definition of the Hugoniot. The problem is to determine what pressure is consistent with both materials, since each will be compressed a different amount by any given shock pressure. Using the p-u form of the Hugoniot the impact shock pressure for material 1 can be expressed as  $p_{H1}(u)$  where u is now the particle velocity within the compressed zone. Next, change coordinate systems so that material 2 appears at rest, and material 1 is impacting at velocity V. The magnitude of the particle velocity is now (V-u), because this second collision differs from

# SCALING LAWS

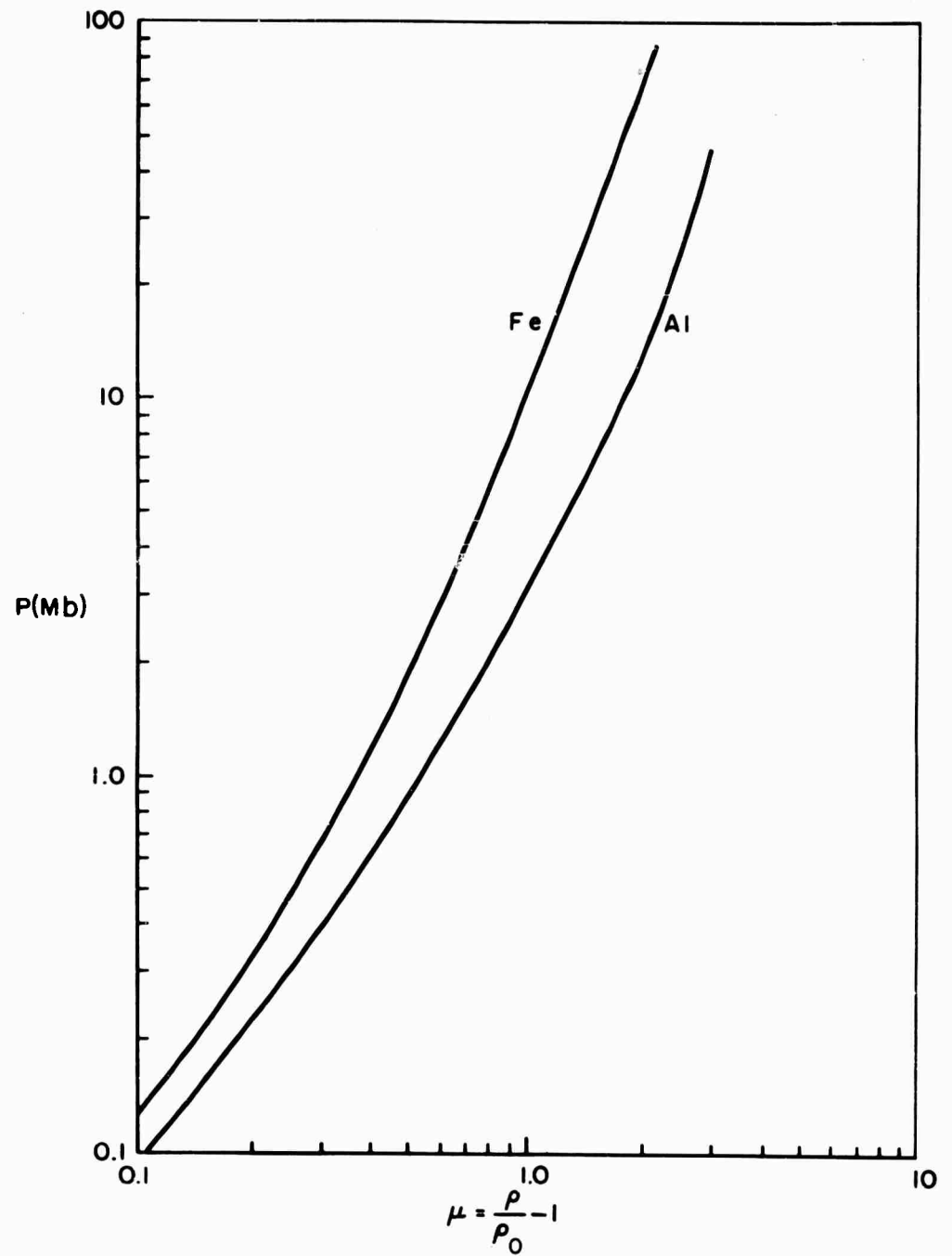


Figure 7. Hugoniot Curves for Iron and Aluminum Derived from the Los Alamos Equations of State.

# SCALING LAWS

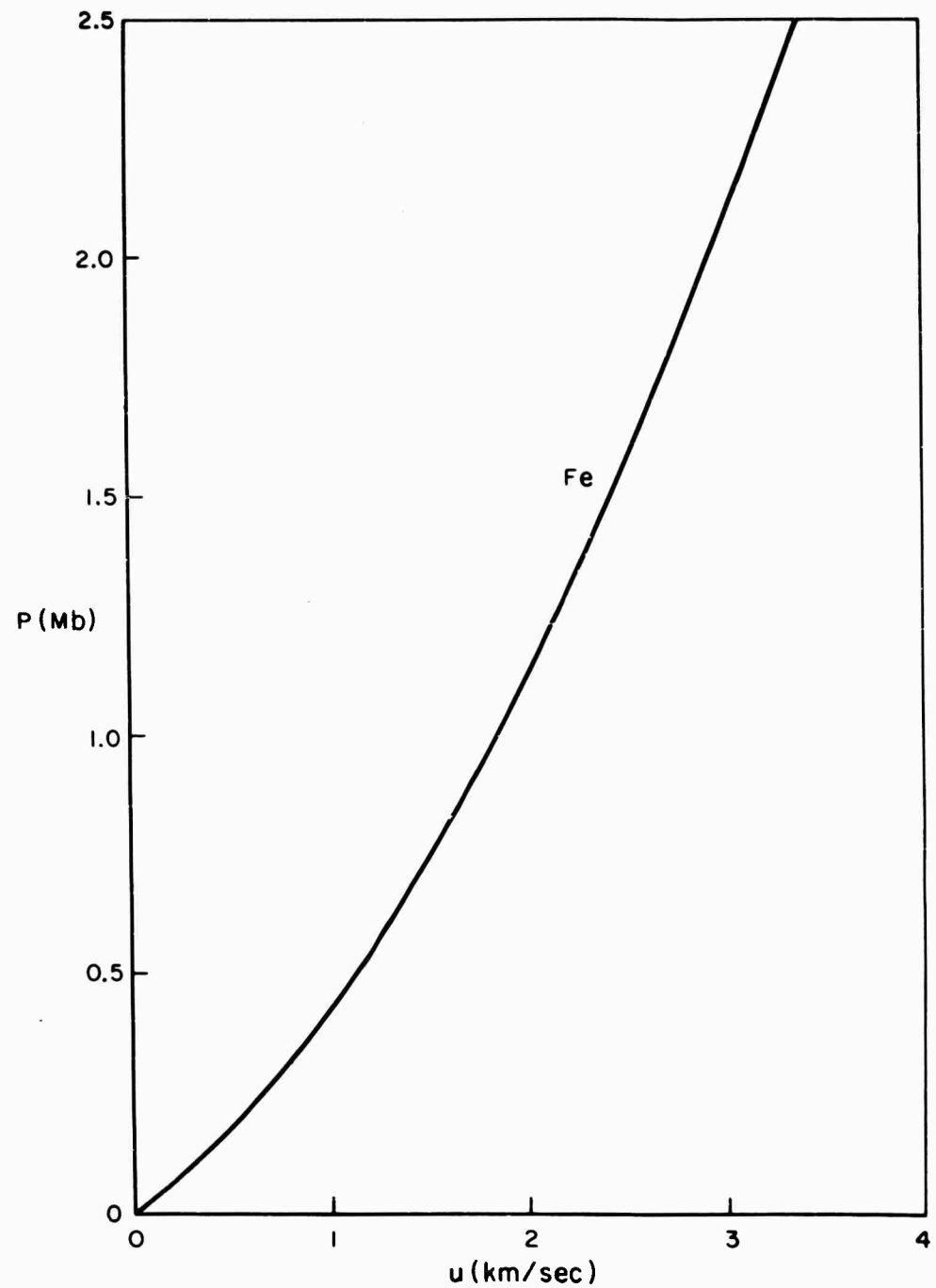


Figure 8. Pressure Versus Particle Velocity for Shocks Moving into Stationary Iron. (P-u Form of the Hugoniot Curve.)

## SCALING LAWS

the first only by the translation of the coordinate system at velocity  $V$ , and the particle velocity must be constant within the compressed zone. So relative to the now "resting" material 2, the shock pressure versus particle velocity behind the shock in material 2 is expressed by  $p_{H_2}(V-u)$ . But in the compressed zone the pressure is the same no matter what coordinate system is used to observe it. Therefore,

$$p_{H_1}(u) = p_{H_2}(V-u) \quad (18)$$

This result shows how the maximum, one-dimensional, impact pressure may be found for any dissimilar material impact. First the  $p$ - $u$  Hugoniot for the target material, the one actually at rest, is plotted in the normal way from the origin, as in Figure 10. Then the mirror image of the projectile material

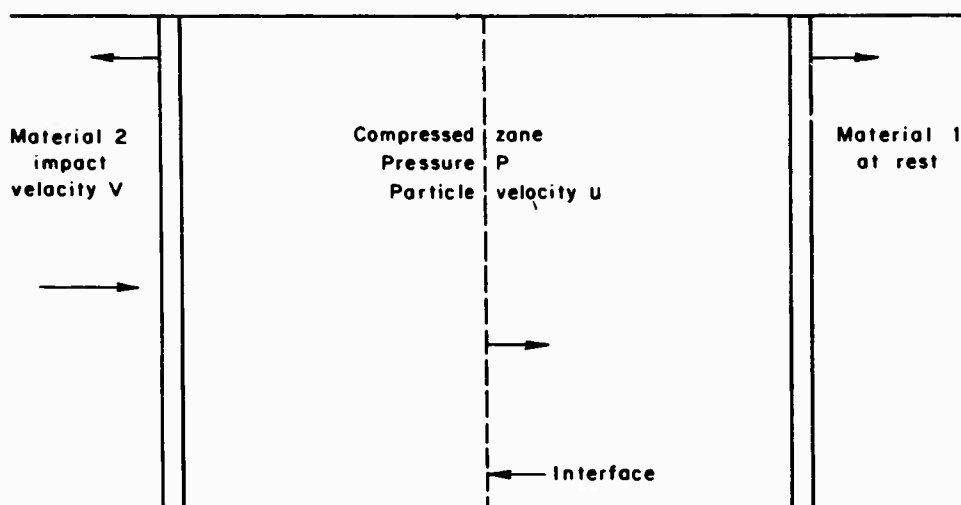


Figure 9. Sample Volume to Illustrate Solution of Shock System for Dissimilar Material Impact

$p$ - $u$  Hugoniot is drawn starting up from the point  $u = V$  instead of  $u = 0$ , and the intersection of the curves is the point  $p_{H_1}(u) = p_{H_2}(V-u)$ . Figure 10 shows this point for the case of iron impacting lead at 2.1 kilometers per second. It is seen that if the projectile material is the same as the target, then the two  $p$ - $u$  Hugoniots are symmetric about the intersection and the particle velocity is just half the impact velocity, which is the condition required of similar material impact by the symmetry argument of Section III. Figure 11 shows a collection of  $p$ - $u$  Hugoniots to moderate pressures, and Table 2 tabulates compression and  $p$ - $u$  Hugoniots for several metals and one rock, taken from References 6, 7, 10, 12, and 13.

By sliding the "backwards" plot of a projectile  $p$ - $u$  Hugoniot up to the desired impact velocity on the abscissa of Figure 11, the maximum impact

## SCALING LAWS

pressure is read at the intersection with the Hugoniot of the target material.

In these tables and figures the iron and aluminum Hugoniots are generated from the complete equations of state of Table 1, which was the result of the combined high pressure theory and moderate pressure experiment. The other Hugoniots were extrapolated above the experimental ranges of 2-5 megabars using the experimentally observed fact that for every measured metal with the single exception of aluminum, the shock velocity is very accurately related to the particle velocity by the linear relation,

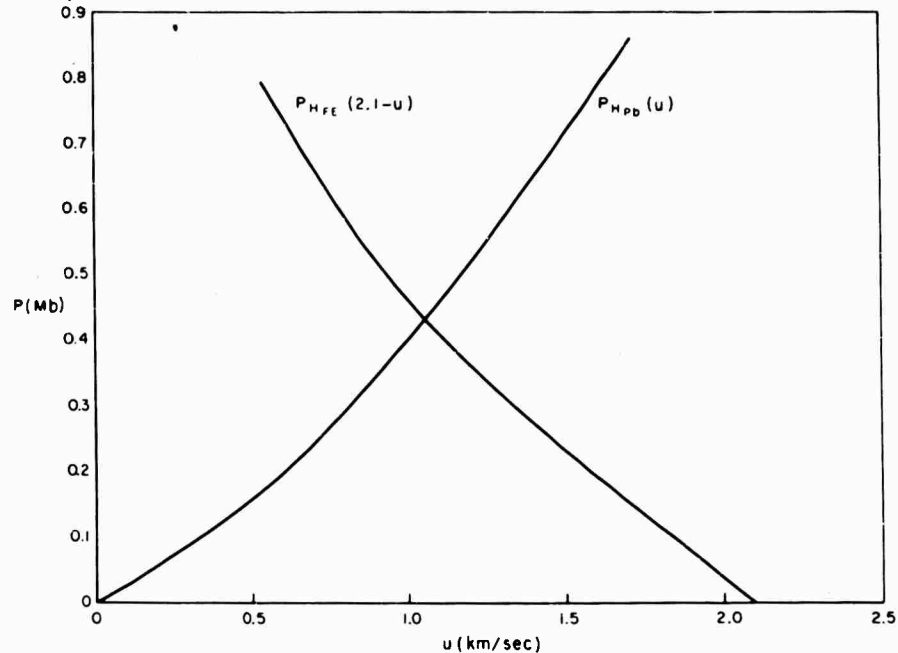


Figure 10. Shock Solution for Iron on Lead at 2.1 km/sec.

$$U = a + b u. \quad (19)$$

This makes the Hugoniot pressure Equation (10),

$$p = \rho_0 U u \quad (20)$$

become

$$p = \rho_0 u (a + b u) \quad (21)$$

for the  $p$ - $u$  Hugoniots, where the  $a$ 's and  $b$ 's are tabulated in References 7 and 9. The extrapolations were made from measured pressures of .5 to 5 megabars up to those in the range of 3 to 7 megabars. This was felt to be a conservative extrapolation because in comparing the iron Hugoniot extrapolated by this linear  $U$  versus  $u$  relation with that obtained from the complete equation of state (Table 1), the pressures did not begin to depart until a similar material impact velocity of 30 kilometers per second, which corresponds to a pressure of over 30 megabars.

# SCALING LAWS

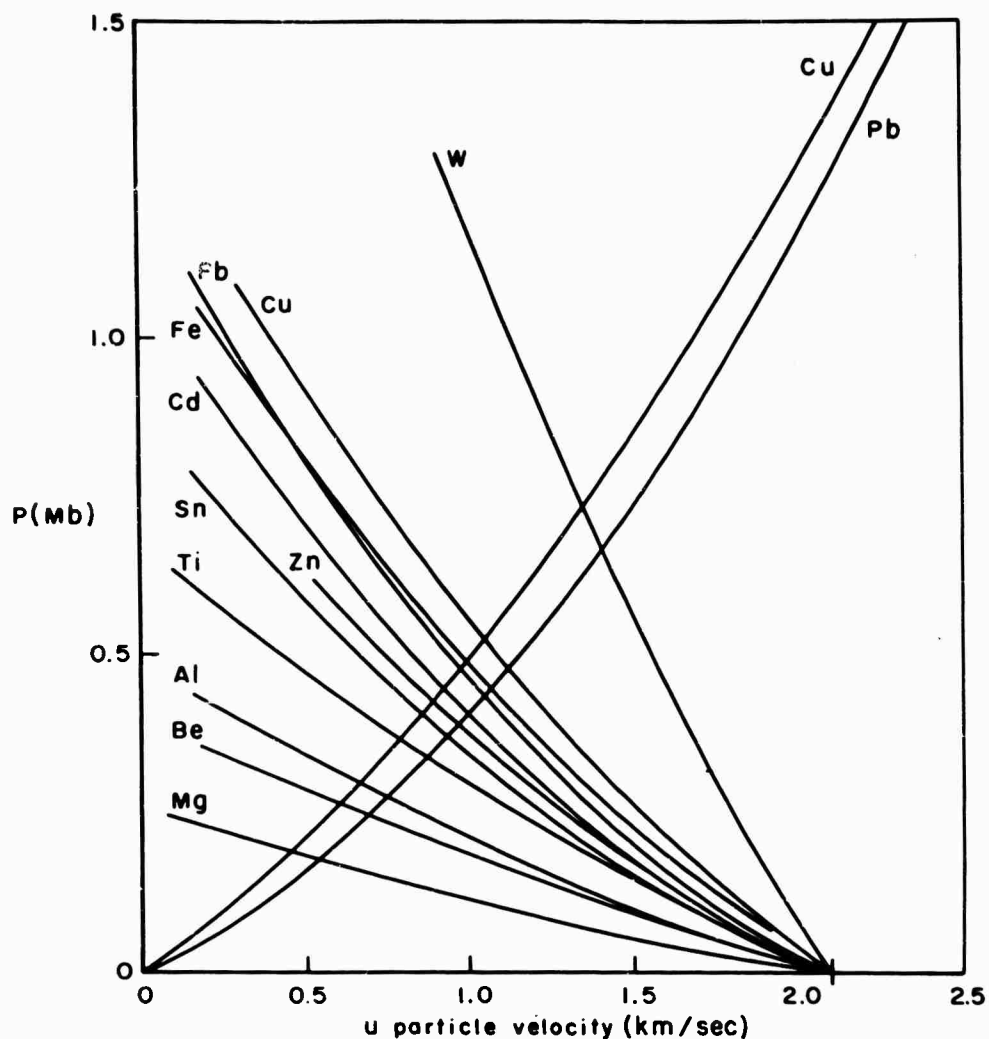


Figure 11. Shock Solutions for Several Metals on Copper and Lead at 2.1 km/sec.

The curve labeled "Tuff" refers to a soft volcanic rock of density  $1.7 \text{ gms/cm}^3$ , in which some underground explosions at the Nevada test site were shot. It is shown because its Hugoniot was the only non-metal one available; however, because its complete equation of state has been estimated including the theoretical high pressure end, hydrodynamic predictions can be made showing the effect of at least this one non-metal up into the meteor velocity range. In Figure 11 it is very interesting to note that both the steepness and magnitude of the Hugoniots generally increase with increasing density. In the cases where this is not true in some regions, it becomes so if a high enough pressure is

# SCALING LAWS

TABLE 2  
p-u Hugoniot Values

Pressure	Particle Velocity, u(km/sec)							
Mb	Fe	Cu	Cd	Pb	Sn	Al	W	Tuff
.2	.535	.481	.654	.600	.737	1.06	.241	2.33
.4	.96	.858	1.09	.998	1.23	1.83	.453	3.68
.6	1.3	1.18	1.44	1.32	1.63	2.48	.645	4.66
.8	1.6	1.46	1.74	1.59	1.98	3.04	.825	5.50
1.0	1.86	1.72	2.00	1.83	2.28	3.55	.987	6.25
1.2	2.1	1.95	2.24	2.06	2.57	4.14	1.14	6.88
1.4	2.32	2.15	2.47	2.26	2.82	4.66	1.29	7.52
1.6	2.55					5.10	1.43	8.08
2.0	2.94					5.64	1.69	9.15
2.5	3.39					6.49		10.3
3.0	3.81					7.29		11.32
3.5	4.20					8.02		12.3
4	4.56					8.70		13.2
5	5.22					10.2		14.88
10	7.93					15.1		21.4
20	11.9					22.3		30.5
30	15.0							
50	20.1							
100	29.6							
140	35.6							

TABLE 2(a)  
p-u Hugoniot Calculated from  $p = \rho_0 u(a+bu)$

Particle Velocity km/sec	Pressure (Mb)					
	Mg	Be	Cu	Pb	W	Ti
1	.1	.167		.402	1.02	.628
2	.244	.375	1.24	1.15	2.53	1.09
3	.431	.623	2.26	2.24	4.52	1.65
4	.663	.911	3.54	3.67	7.01	2.31
5	.939	1.24	5.09	5.45	9.98	3.06
6	1.26	1.61	6.91	7.57		3.92
7	1.62	2.02	8.99	10.0		4.87
8	2.03	2.47	11.3			5.92
9	2.48	2.96				7.07
10	2.98	3.48				9.66
12	4.10	4.66				
14	5.40	6.01				

## SCALING LAWS

considered. At the lower velocities lead exhibits lower pressures than its density (11.34) warrants, however at .75 megabars it rises above iron (7.84), at 2.5 megabars it crosses over copper (8.90), and in the vicinity of 7.5 megabars it appears to be finally crossing molybdenum; (10.20). Even more striking is the fact that gold (19.24) becomes stiffer, or has a higher pressure for a given particle velocity, than tungsten (19.17) at 5 megabars.

### II. SCALING LAW FOR DISSIMILAR MATERIAL IMPACTS

In a beautifully conceived series of hypervelocity impact experiments, Summers and Charters<sup>(15)</sup> varied only the projectile material. The impact velocity, target material, projectile mass and projectile geometry were held fixed. The range of projectile density covered was from 17.1 to 1.75 specific gravity, corresponding to tungsten alloy and magnesium respectively.

One of the principal results was that penetration correlated well with density, the relation being essentially linear on a log-log plot of penetration versus density. This implies an analytical relation of the form

$$p \sim \rho_p^\beta \quad (22)$$

where  $p$  = penetration  
 $\rho_p$  = projectile density  
 $\beta$  = slope of log-log plot

$\beta$  was different for the two targets treated, viz., copper and lead.

The constant projectile mass implies that  $\rho_p d^3 = \text{constant}$ , where  $d$  is the diameter of the spherical projectiles used. Thus in the experiments

$$d \sim \rho_p^{-1/3} \quad (23)$$

which emphasizes the surprising fact that the deepest craters were made by the smallest spheres.

Since it is most common for experimenters to report values of  $p/d$  we shall have occasion to define  $\alpha$  through

$$p/d \sim (\rho_p)^\alpha \quad (24)$$

and it may be seen from Equations (22) and (23) that  $\alpha = \beta + 1/3$ .

An early objective of our investigation was to calculate the values of  $\alpha$  (or  $\beta$ ) from equation of state data. This would permit an extension of the Summers and Charters relation to velocities and materials not covered by their experiments. However, from the outset, this aim was beclouded by the question of compressibility. It is easy to convince oneself that there should be a correction for the compressibility of the material in addition to the correction for the density which Summers and Charters had found.

Summers and Charters had attempted the inclusion of compressibility

## SCALING LAWS

effects through the use of the target sound velocity. In principle we cannot agree with this use. To begin with, the sound velocity is determined by the very low pressure elastic properties of materials. For example, a detailed plot of the steel Hugoniot has the features shown in Figure 12. The sound velocity is fixed by the slope of the straight portion up to point A, which Minshall<sup>(14)</sup> has shown to occur at about 11 kilobars for steel. Above 11 kilobars, the material behavior is radically inelastic, and it is the properties of the inelastic region which will govern impact phenomena. It should be pointed out that Summers and Charters were well aware of the limitations involved in using a sound velocity to scale the impact process, and presented it only as a first cut at a scaling law. A less serious objection is that the compressibility of the projectile is not taken into consideration.

Both the density and compressibility enter into the determination of the Hugoniot, so that these effects are both included if one formulates a scaling law based on the Hugoniot. In addition, physical intuition leads one to expect that the initial velocity imparted to the target material on impact will have a direct bearing on the crater produced. Accordingly, we set out to find whether or not the crater dimensions were some function of the initial target particle velocity in dissimilar-material impacts.

In correlating the experimental data available, it turned out that the crater dimensions were indeed a beautifully simple function of particle velocity, namely, they were linearly proportional to it. More explicitly, for projectiles of the same mass striking a given target at the same velocity, the penetration is proportional to the particle velocity initially produced in the target. It will be shown that this single relation leads to the density dependence found by Summers and Charters for both lead and copper targets, and predicts how the density dependence will change with impact velocity. Moreover, the relation may be applied to other projectile-target systems if the equations of state are known.

The initial particle velocity may be calculated from the one-dimensional model treated in the first section. We re-emphasize here that our empirical relation is based on this one-dimensional particle velocity. In the case of similar material collisions, the particle velocity is always half the impact velocity, so that our result may be expressed as

$$\frac{p_{B-A}}{p_{A-A}} = \frac{2u_{B-A}}{V} = \frac{u_{B-A}(V)}{V/2} = \frac{2u_{B-A}}{V} \quad (25)$$

The subscript, B-A, denotes cases where a projectile of material B is incident on a target of material A,  $p$  is the penetration depth,  $V$  is the impact velocity, and  $u_{B-A}(v)$  is the one dimensional particle velocity, or maximum particle velocity, for an impact at  $V$ , of the target material behind the shock, and this depends on the impact velocity,  $V$ .

By including the fact that the penetration is proportional to the size of the projectile, we can remove the restriction of identical-mass projectiles. Together with Equation (23), this fact leads to

# SCALING LAWS

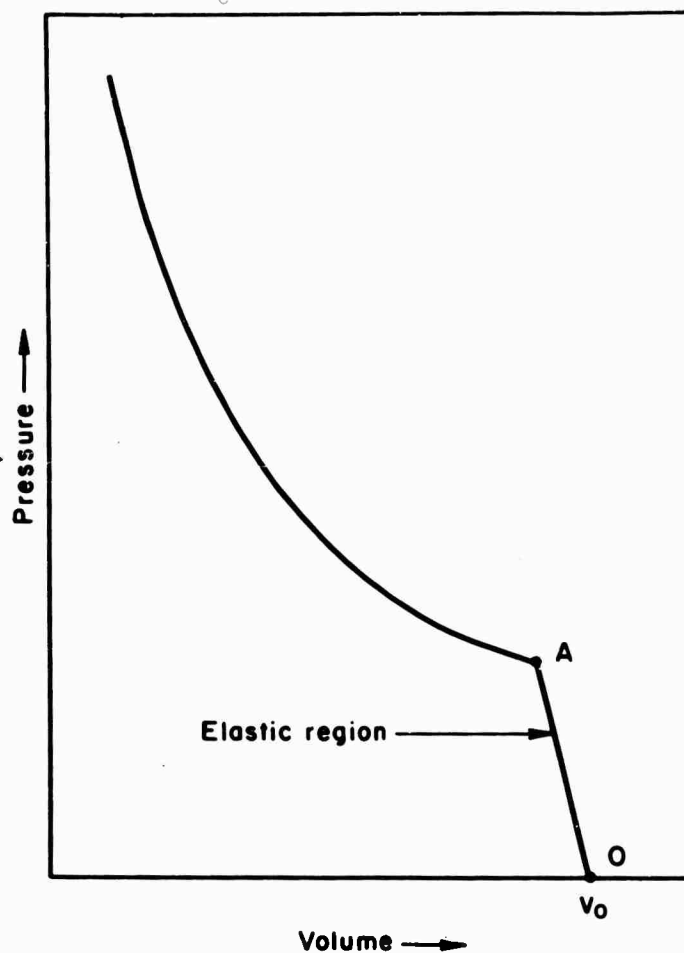


Figure 12. Details of the Hugoniot Curve at Low Pressures

$$\left(\frac{p}{d}\right)_{B-A} = F_{B-A} \left(\frac{p}{d}\right)_{A-A} \quad (26)$$

where

$$F_{B-A} = \frac{2u_{B-A}(V)}{V} \left(\frac{\rho_B}{\rho_A}\right)^{1/3} \quad (27)$$

will be called the normalized penetration ratio. Here,  $d$  is the characteristic dimension of the projectile.

Equation (26) refers the B-A penetration to the A-A one. However, suppose one knows the B-A penetration at a given velocity, and wishes to calculate that for the combination C-A. It is easy to deduce from two applications

# SCALING LAWS

of Equation (26) that

$$\left(\frac{p}{d}\right)_{C-A} = \frac{F_{C-A}}{F_{B-A}} \left(\frac{p}{d}\right)_{B-A} \quad (28)$$

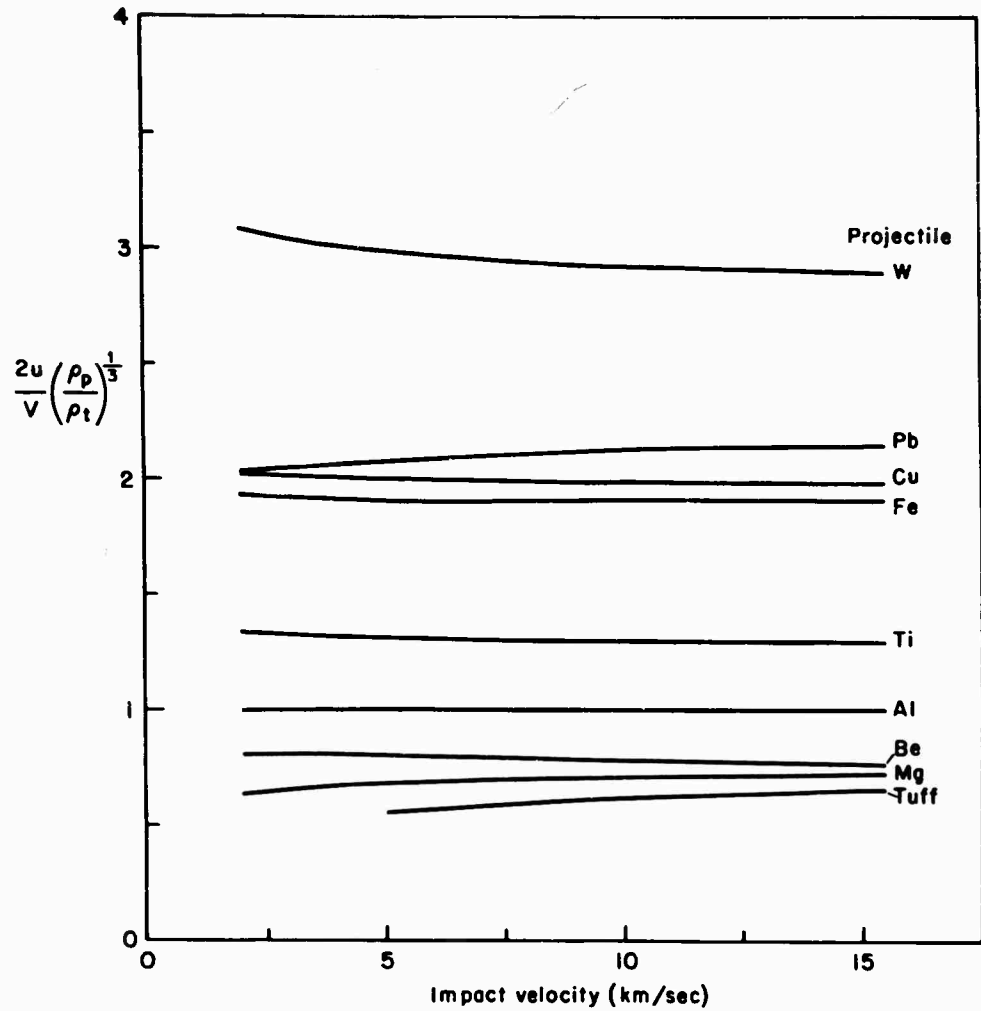


Figure 13. Normalized Penetration Ratios as a Function of Impact Velocity for Aluminum Targets.

# SCALING LAWS

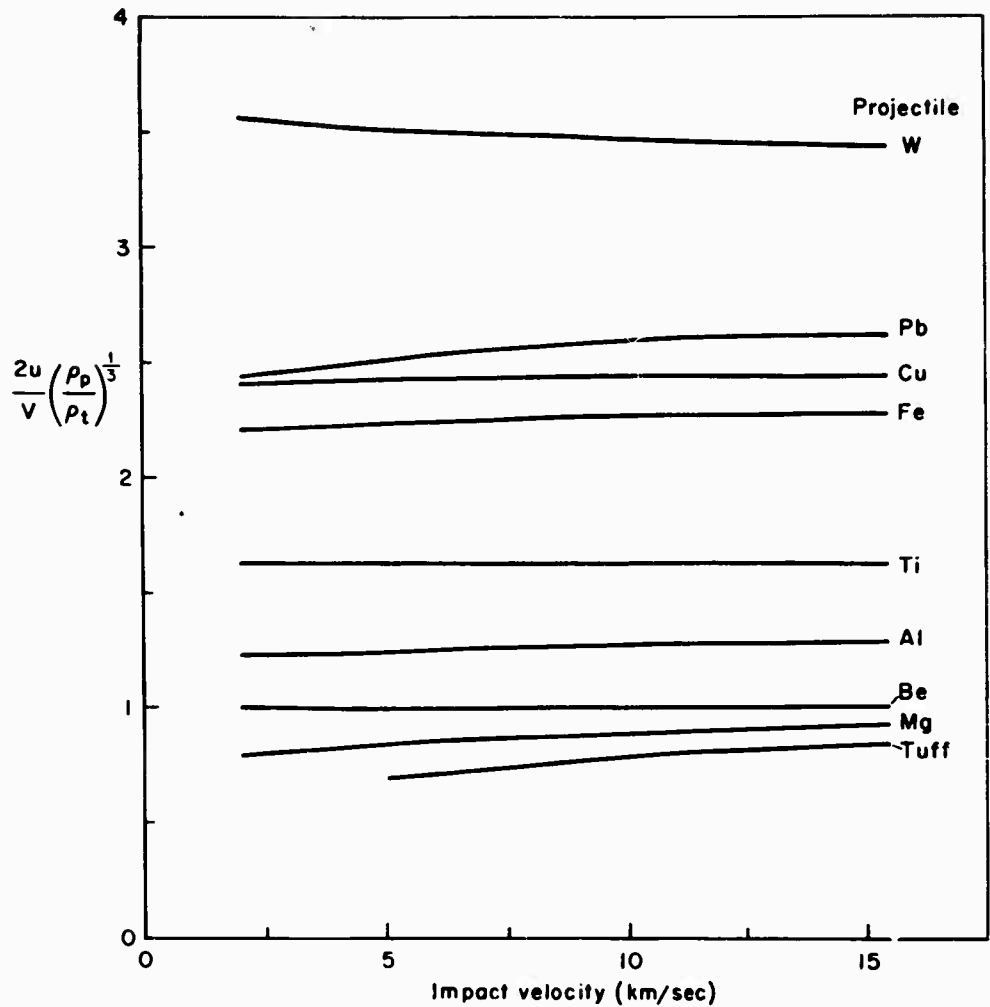


Figure 14. Normalized Penetration Ratios as a Function of Impact Velocity for Beryllium Targets

Of course, all of the factors in Equation (28) must pertain to the same impact velocity. Thus, when the normalized penetration,  $p/d$ , is known for any projectile on target A at the velocity of interest, one can use Equation (28) to calculate the normalized penetration for any other projectile incident on A at the same velocity.

# SCALING LAWS

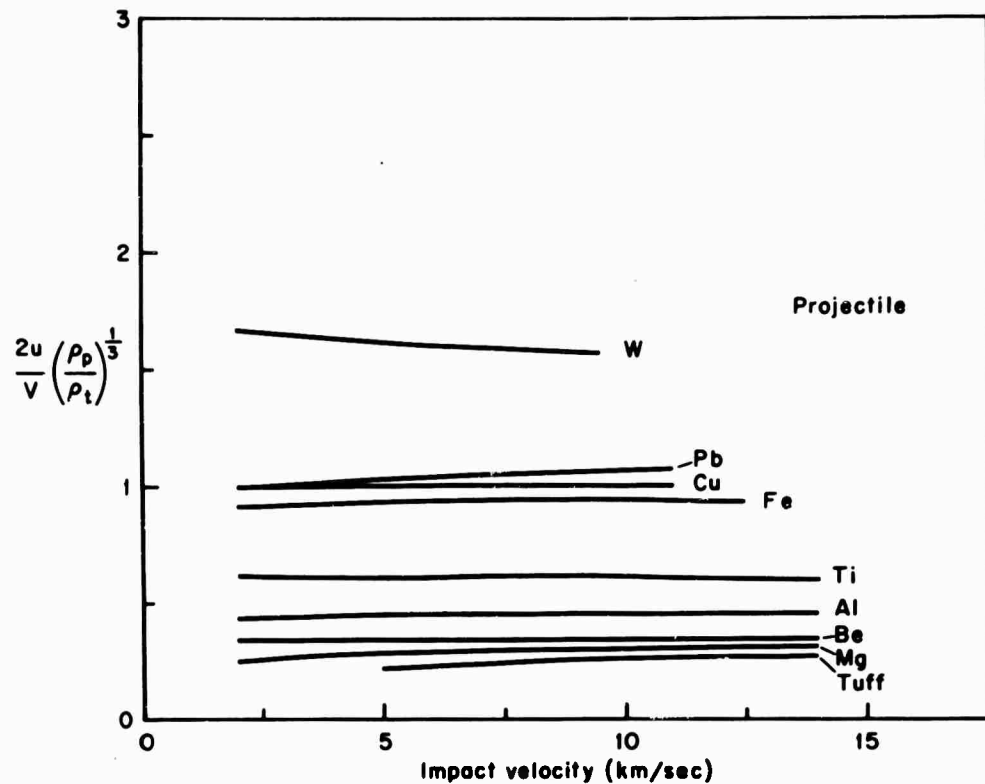


Figure 15. Normalized Penetration Ratios as a Function of Impact Velocity for Copper Targets.

The normalized penetration ratios,  $F$ , have been calculated for eight metals and tuff from known equation of state data, and are presented in Figures 13 to 21. Each figure pertains to a given target material, and gives the factors as a function of impact velocity over the range where there is good confidence in the equation of state data. Since the curves characteristically flatten out at the high velocity end, they may be extrapolated to obtain rough approximations of penetrations in the meteor velocity range.

For the three materials, iron, aluminum, and tuff, equation of state data were available up to the highest meteor velocities. These were formulated from a composite of theoretical and experimental data. Figure 22 shows the six combinations of these three materials as both targets and projectiles up to the higher velocities. The fact that these remain roughly constant throughout the high velocity range lends some substance to the extrapolation of the others.

If one considers a particular target material from among Figures 13 to 21, and calculates the penetration given by constant-mass projectiles at a given velocity on the basis of the graphs, and then plots the penetrations versus

# SCALING LAWS

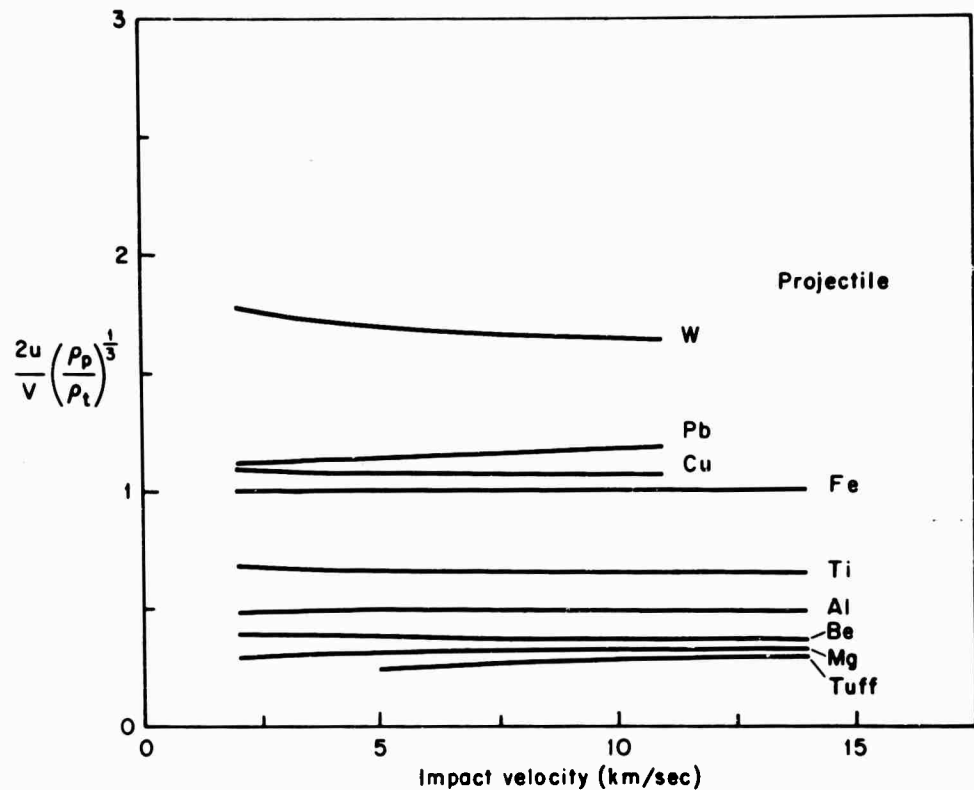


Figure 16. Normalized Penetration Ratios as a Function of Impact Velocity for Iron Targets.

the projectile density on log-log paper, he will find that the plot is always well fit by a straight line of slope  $\beta$ . This fact implies exactly the relation found by Summers and Charters, as given in Equation (22). In other words, if our scaling law is correct, they would have obtained the same qualitative result if they had used any of the target materials and velocities we have considered. Only the value of  $\beta$  would have been changed, since the slope of the line which best fits our calculated points changes with both impact velocity and material. The values of  $\beta$  so derived are presented in Figure 23.

The reason that a  $\beta$ -fit may be obtained is because at any impact velocity  $u_{B-A}(V)$  is roughly proportional to some power of  $\rho_B$ . As might be expected, there are some systematic deviations from this rule due to the character of the Hugoniot involved. These may be partially corrected by the correction factors shown in Figure 24. The  $\beta$ -law penetration is to be modified by the factor  $(K_p/K_t)$ , where  $K_p$  is the factor for the projectile material, and  $K_t$  that for the target. Thus

# SCALING LAWS

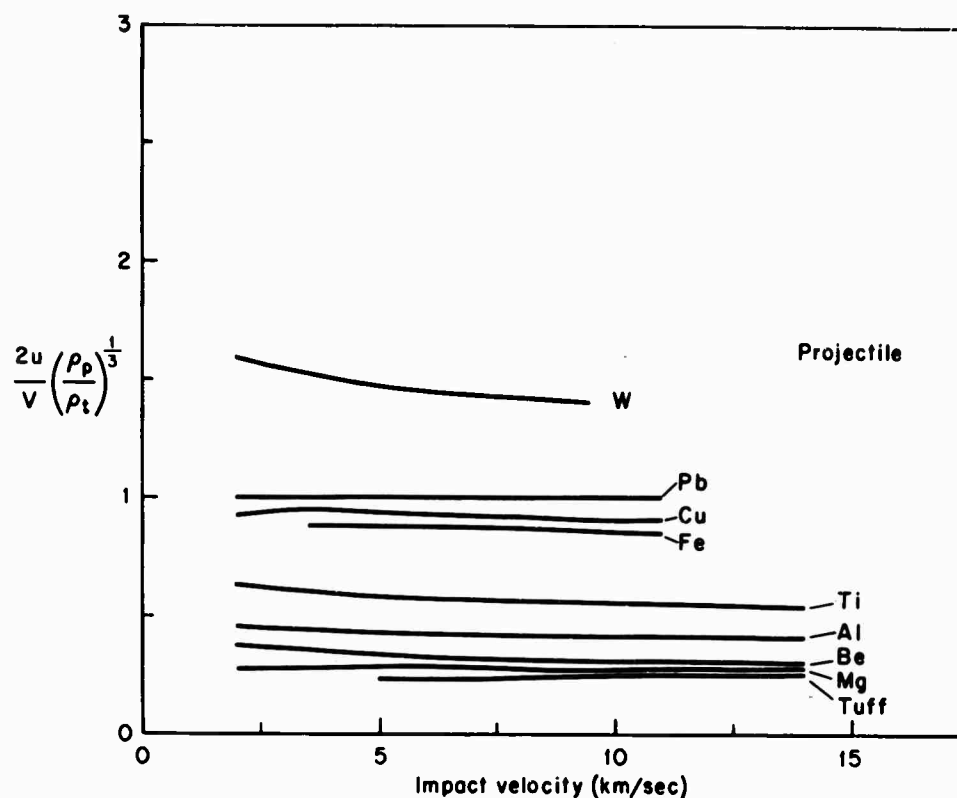


Figure 17. Normalized Penetration Ratios as a Function of Impact Velocity for Lead Targets.

$$p \sim (\rho_p / \rho_t) (K_p / K_t) \quad (29)$$

The notion that the penetration is directly proportional to the particle velocity is physically pleasing, and possibly applies to all materials over a wide velocity range. This is particularly so when contrasted with previously proposed scaling laws, which involved unusual powers of the density (and which we believe vary with velocity) and treated compressibility effects poorly. However, despite this aesthetic appeal, it should be emphasized that the idea is still an empirical correlation, having been given no sound theoretical basis as yet. We hope that experimentalists will be stimulated to make further checks on the validity of the notion, and that theorists will find it a fruitful area to apply their talents.

# SCALING LAWS

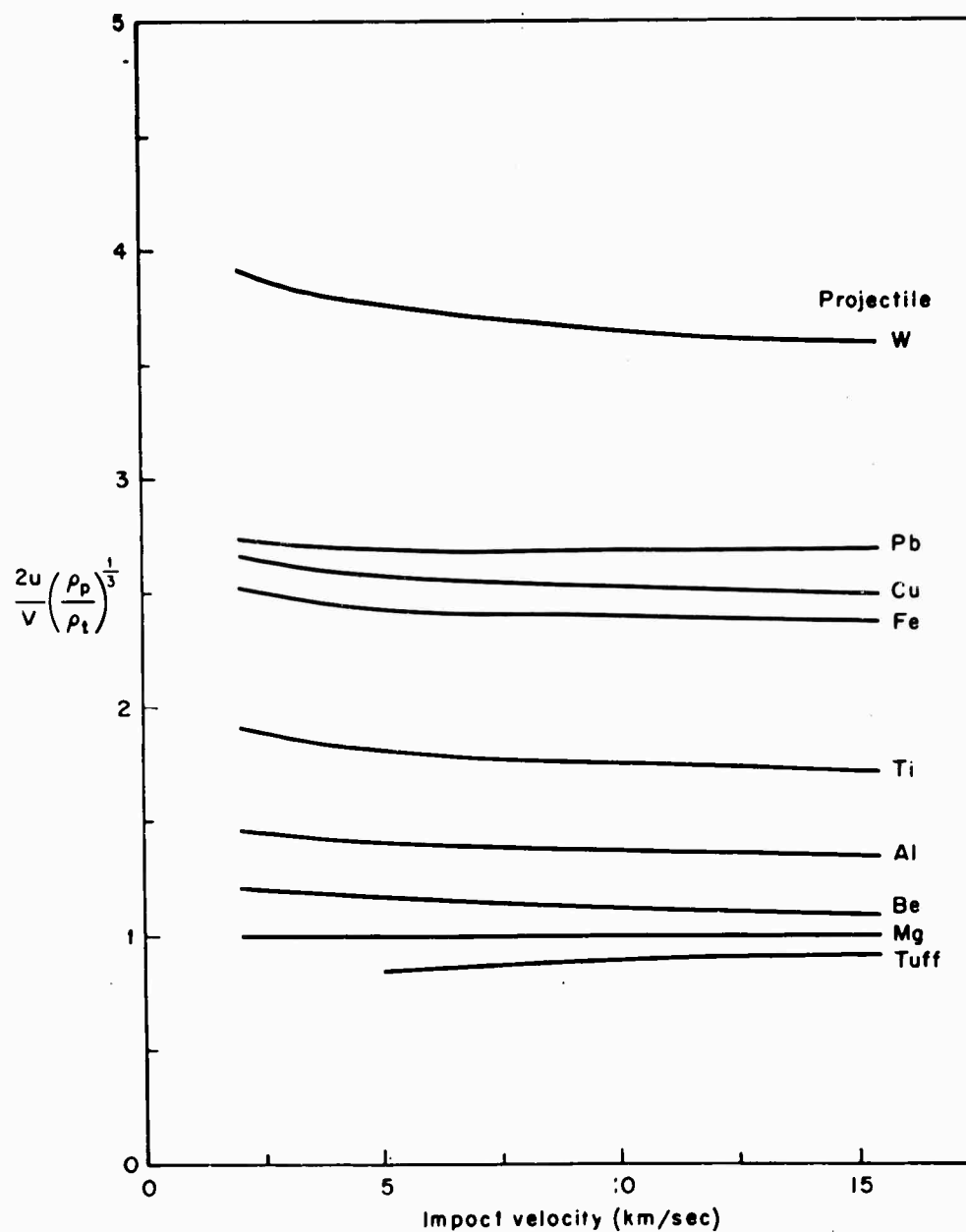


Figure 18. Normalized Penetration Ratios as a Function of Impact Velocity for Magnesium Targets.

# SCALING LAWS

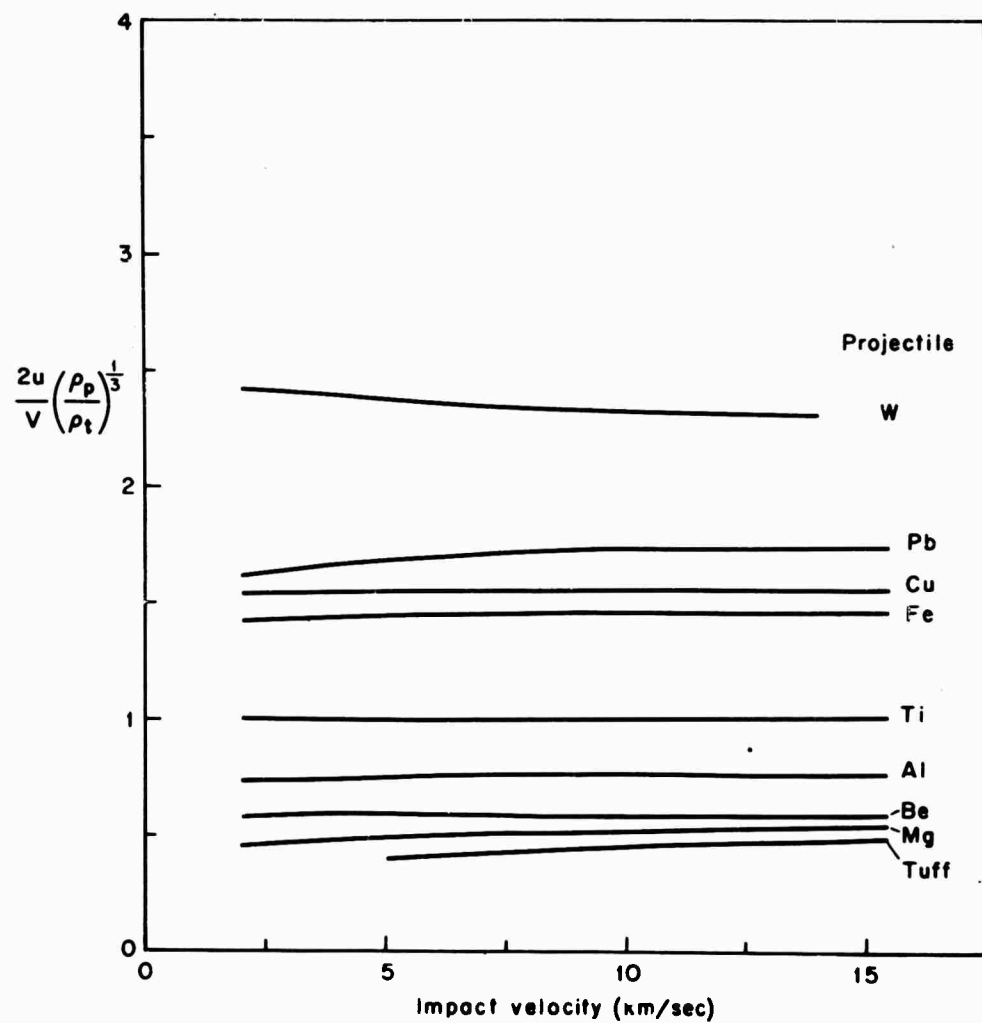


Figure 19. Normalized Penetration Ratios as a Function of Impact Velocity Titanium Targets.

# SCALING LAWS

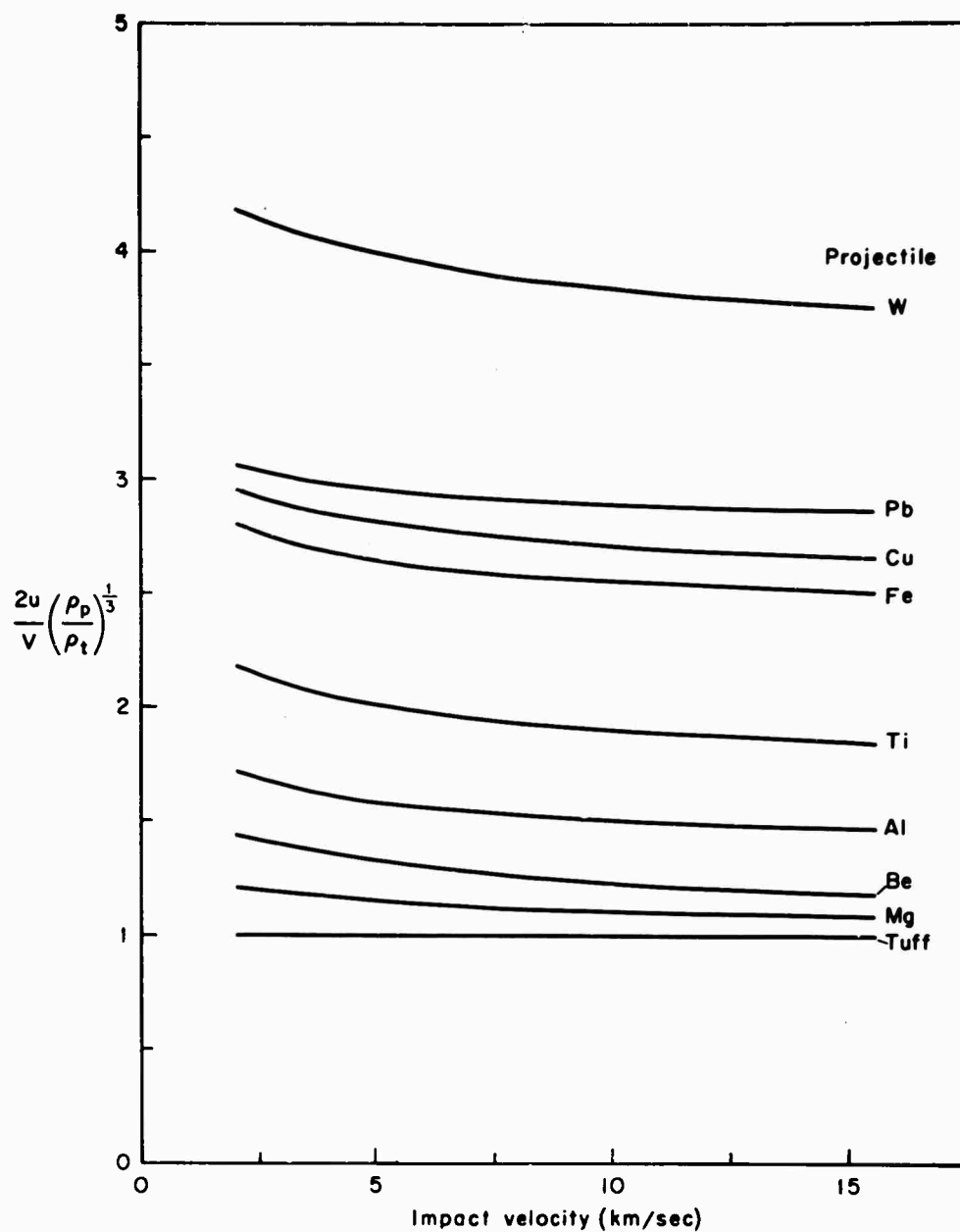


Figure 20. Normalized Penetration Ratios as a Function of Impact Velocity for Tuff Targets.

# SCALING LAWS

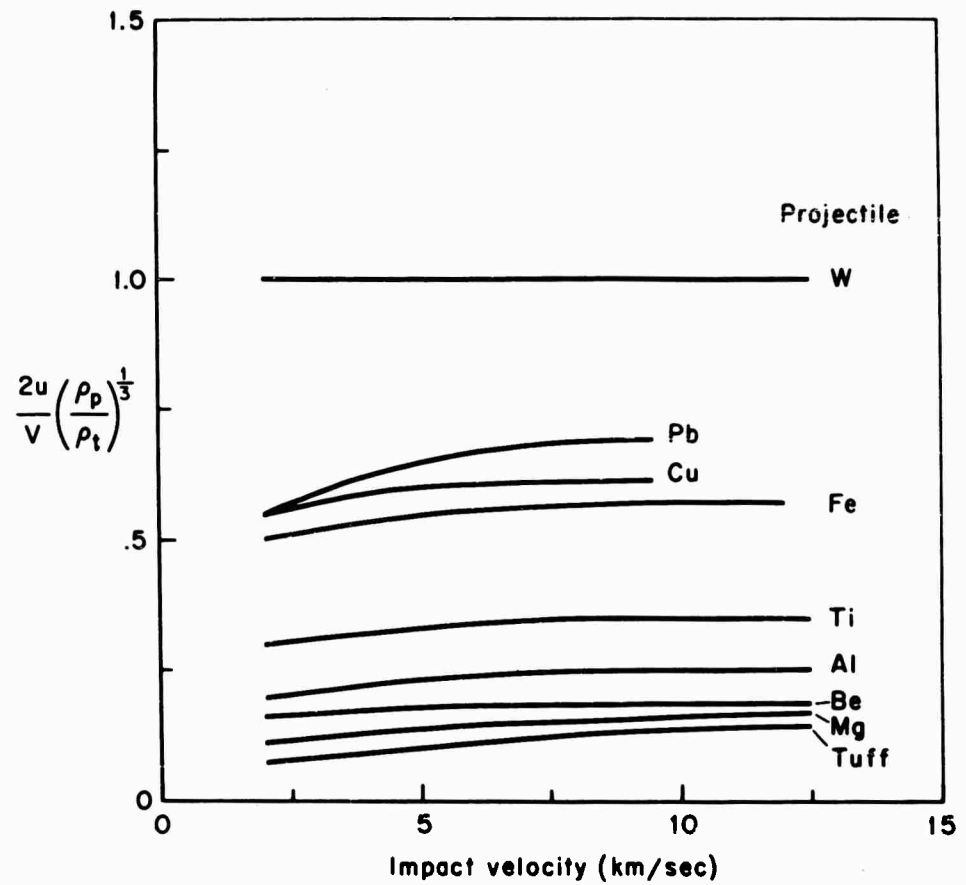
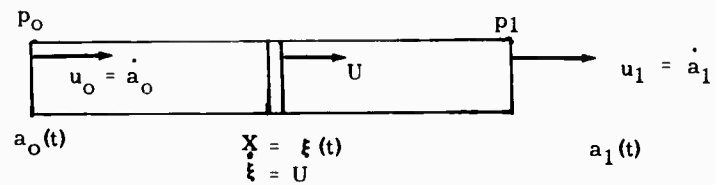


Figure 21. Normalized Penetration Ratios as a Function of Impact Velocity for Tungsten Targets.

## APPENDIX A



# SCALING LAWS

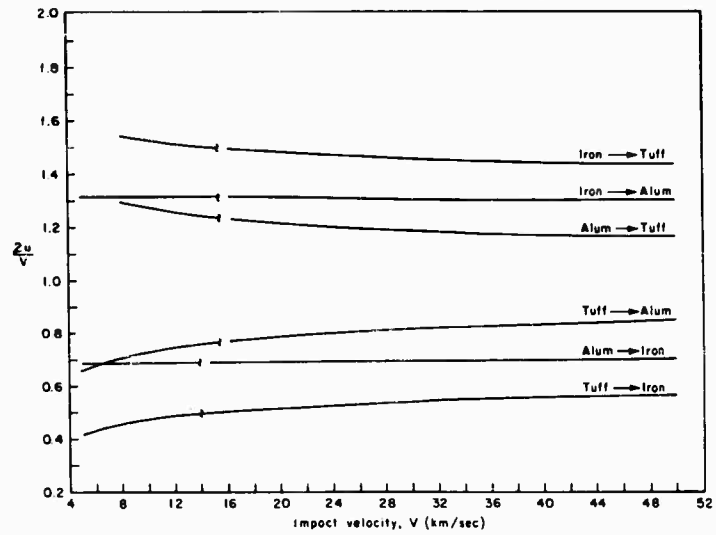


Figure 22. Penetration Ratios for Iron, Tuff, and Aluminum at High Impact Velocities.

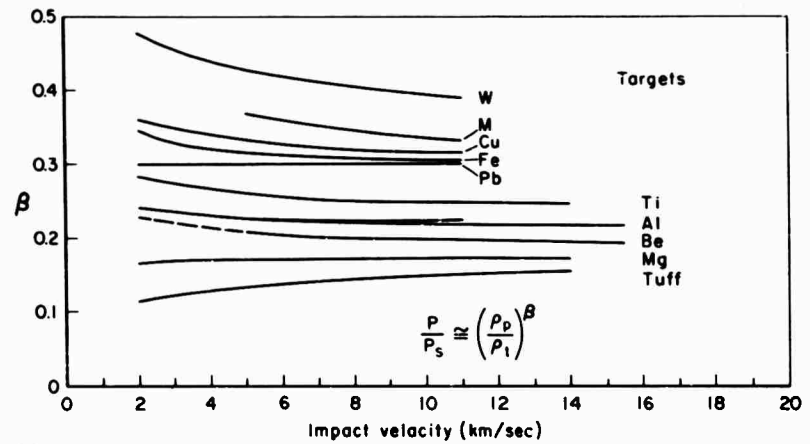


Figure 23. Values of  $\beta$  Deduced from the Normalized Penetration Ratio Curves.

# SCALING LAWS

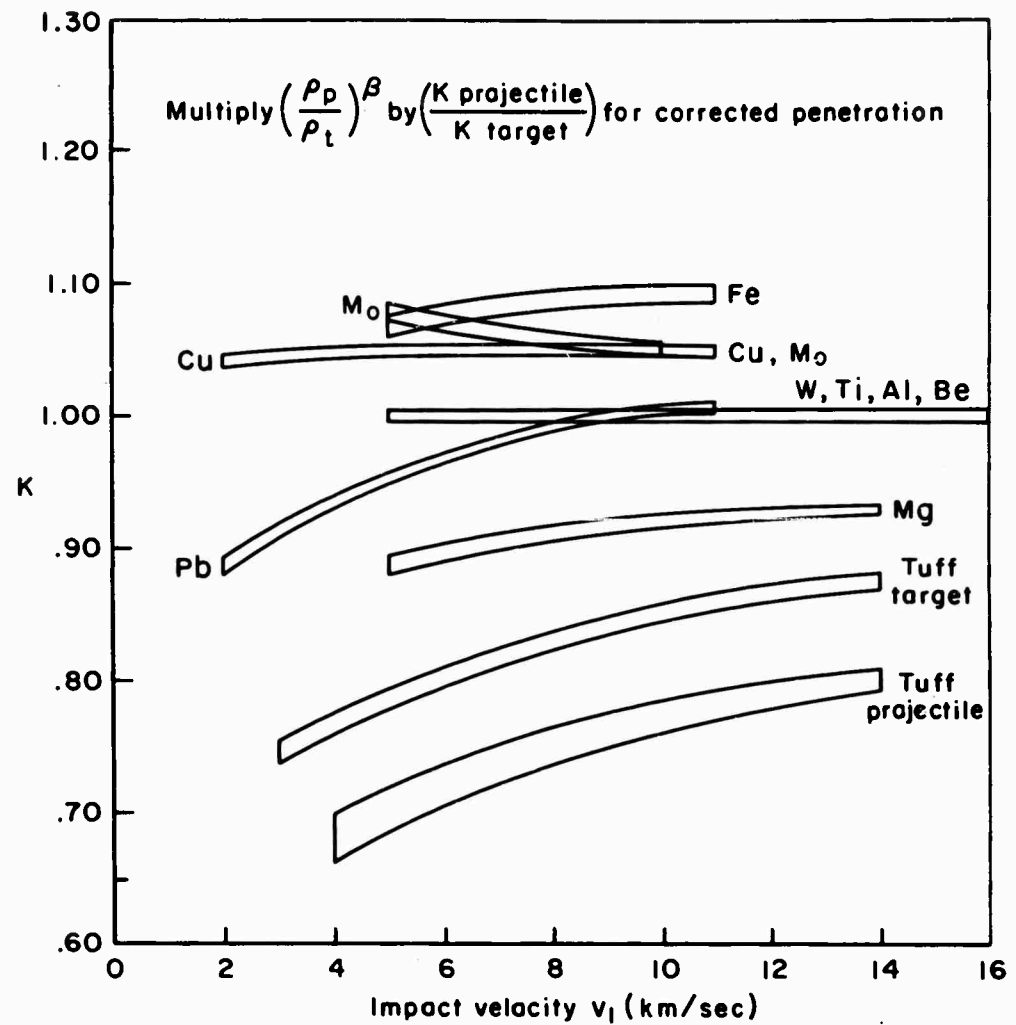


Figure 24. Correction Factors on  $\beta_1$ -Law

The three conservation laws

$$\frac{d}{dt} \int_{a_0(t)}^{a_1(t)} \rho \, dx = 0 \quad (A-1)$$

# SCALING LAWS

$$\frac{d}{dt} \int_{a_0}^{a_1} \rho u dx = p_0 - p_1 \quad (A-2)$$

$$\frac{d}{dt} \int_{a_0}^{a_1} \rho \left\{ \frac{1}{2} u^2 + e \right\} dx = p_0 u_0 - p_1 u_1 \quad (A-3)$$

are all integrals of the form

$$J = \int_{a_0(t)}^{a_1(t)} \psi(x, t) dx$$

Now say that there is a discontinuity in the column at  $x = \xi(t)$  which moves at an absolute velocity (shock velocity)  $u(t) = \dot{\xi}(t)$ . Then

$$J = \int_{a_0}^{\xi} \psi dx + \int_{\xi}^{a_1} \psi(x, t) dx.$$

To differentiate these integrals we use the identity,

$$\frac{d}{dt} \int_{A(t)}^{B(t)} F(t, x) dx = \int_{A(t)}^{B(t)} \frac{\partial F}{\partial t} dx + F(B) \frac{dB}{dt} - F(A) \frac{dA}{dt}$$

Therefore,

$$\begin{aligned} \frac{d}{dt} J &= \frac{d}{dt} \int_{a_0}^{\xi} \psi dx + \frac{d}{dt} \int_{\xi}^{a_1} \psi dx \\ &= \int_{a_0}^{a_1} \frac{\partial \psi}{\partial t} dx + \psi_0 \dot{\xi} - \psi(a_0) u_0 \\ &\quad + \psi(a_1) u_1 - \psi_1 \dot{\xi} \end{aligned}$$

where  $\psi_0$  and  $\psi_1$  are the limits of  $\psi$  as  $x$  approaches  $\xi$  from the respective ends, and  $u_0$  and  $u_1$  are  $\dot{a}_0$  and  $\dot{a}_1$ , the particle velocities at either end.

We now perform the limiting process, letting the length of the column

# SCALING LAWS

approach zero. The first integral then approaches zero, and  $\Psi(a_1) \rightarrow \Psi_1$ ,  $\Psi(a_0) \rightarrow \Psi_0$ , so

$$\lim_{a_1 \rightarrow a_0} \frac{d}{dt} J = \Psi_1 (u_1 - U) - \Psi_0 (u_0 - U) \quad (A-4)$$

since  $\xi = U$ . Putting the  $\Psi$  from the three conservation conditions will now give us the three jump conditions.

The mass conservation, (A-1) becomes, with  $\Psi_1 = \rho_1$ ,

$$\rho_1 (u_1 - U) - \rho_0 (u_0 - U) = 0 \quad (A-5)$$

Since the quantity  $\rho_0 (u_0 - U) = \rho_1 (u_1 - U)$  remains constant across the shock,

we will denote it by  $m$ , which is the mass flux through the surface. For momentum conservation,  $\Psi_2 = \rho u$ , so equation (A-4) becomes

$$\rho_1 u_1 (u_1 - U) - \rho_0 u_0 (u_0 - U) = p_0 - p_1 \quad (A-6)$$

or using the mass flux  $m = \rho (u - U)$

$$m u_1 + p_1 = m u_0 + p_0 \quad (A-7)$$

Finally, for energy conservation,

with  $\Psi_3 = \rho \left\{ \frac{1}{2} u^2 + e \right\}$ , Equation (A-4) becomes,

$$\rho \left\{ \frac{1}{2} u_1^2 + e_1 \right\} [u_1 - U] - \rho_0 \left\{ \frac{1}{2} u_0^2 + e_0 \right\} [u_0 - U] = p_0 u_0 - p_1 u_1 \quad (A-8)$$

or, again using the mass flux,

$$m \left\{ \frac{1}{2} u_1^2 + e_1 \right\} + p_1 u_1 = m \left\{ \frac{1}{2} u_0^2 + e_0 \right\} + p_0 u_0 \quad (A-9)$$

# SCALING LAWS

## APPENDIX B

Derivation of Hugoniot relation  $e_1 - e_0 = \left( \frac{p_1 + p_0}{2} \right) (v_0 - v_1)$  from the three conservation jump conditions.

Conservation of mass, Equation (4), is

$$m = \rho_0(u_0 - U) = \rho_1(u_1 - U) \quad (B-1)$$

$$\text{or } u_0 - U = \frac{m}{\rho_0} = m v_0$$

$$\text{since } (v = \frac{1}{\rho})$$

$$\text{so, } u_0 = m v_0 + U$$

$$u_1 = m v_1 + U \quad (B-2)$$

the momentum Equation (A-7) then becomes

$$p_1 - p_0 = m(u_0 - u_1) = m[(m v_0 + U) - (m v_1 + U)] \quad (B-3)$$

or

$$p_1 - p_0 = m^2 [v_0 - v_1]$$

multiplying by  $[v_0 + v_1]$

$$[p_1 - p_0] [v_0 + v_1] + m^2 [v_0^2 - v_1^2]$$

$$\text{but } m^2 = \rho_0^2 (u_0 - U)^2 = \rho_1^2 (u_1 - U)^2$$

$$\text{so } = \frac{1}{v_0} (u_0 - U)^2 \dots$$

$$(p_1 - p_0) (v_0 + v_1) = [(u_0 - U)^2 - (u_1 - U)^2] \quad (B-4)$$

The energy Equation (6) is

$$m \left\{ \frac{1}{2} u_0^2 + e_0 \right\} + p_0 u_0 = m \left\{ \frac{1}{2} u_1^2 + e_1 \right\} + p_1 u_1$$

by using  $u^2 = [(u - U) + U]^2$  and  $u = m v + U$  this becomes

$$\begin{aligned} & m \left\{ e_0 + \frac{1}{2} (u_0 - U)^2 + (u_0 - U) U + \frac{1}{2} U^2 \right\} + p_0 [m v_0 + U] \\ & = m \left\{ e_1 + \frac{1}{2} (u_1 - U)^2 + (u_1 - U) U + \frac{1}{2} U^2 \right\} + p_1 [m v_1 + U] \end{aligned}$$

## SCALING LAWS

but by conservation of momentum (A-7)

$$U [m u_o + p_o] = U [m u_1 + p_1]$$

leaving only

$$m \left\{ \frac{1}{2} (u_o - U)^2 + e_o + p_o v_o \right\} = m \left\{ \frac{1}{2} (u_1 - U)^2 + e_1 + p_1 v_1 \right\}$$

or

$$\frac{1}{2} [(u_o - U)^2 - (u_1 - U)^2] = [e_1 - e_o] + [p_1 v_1 - p_o v_o]$$

But the first term is known in terms of thermodynamic variables by the above relation (B-4), so,

$$-\frac{1}{2} [p_1 - p_o] [v_o + v_1] = [e_1 - e_o] + p_1 v_1 - p_o v_o$$

by multiplying out and collecting terms this becomes

$$\frac{p_1}{2} (v_o - v_1) + \frac{p_o}{2} (v_o - v_1) = e_1 - e_o$$

or, finally,

$$\frac{p_1 + p_o}{2} (v_o - v_1) = e_1 - e_o \quad (B-5)$$

## SCALING LAWS

### REFERENCES

1. Bancroft, D. , et al. , Journal of Applied Physics 27, (1956), 291.
2. Hugoniot, H. , Journal de l'ecole Polytechnique 58, (1889), 1-125.
3. Courant, R. , and K. O. Friedrichs, Supersonic Flow and Shock Waves, Interscience Publishers, Inc. , New York, 1948.
4. Bjork, R. L. , "Effects of a Meteoroid Impact on Steel and Aluminum in Space," P-1662, The RAND Corporation, 1700 Main Street, Santa Monica, California, 1959.
5. Bridgeman, P. W. , Proceedings of the American Academy of Arts and Sciences 77, (1949), 189.
6. Walsh, J. M. , et al. , Physical Review 108, (1957), 196.
7. McQueen, R. G. , and S. P. Marsh, Journal of Applied Physics, 31, (1960), 1253.
8. Al'tshuler, L. V. , et al. , Soviet Physics JETP 34(7), (1958), 606.
9. Al'tshuler, L. V. , et al. , Soviet Physics JETP 34(7), (1958), 606.
10. Rice, M. H. , et al. , Solid State Physics, Advances in Research and Applications, Academic Press, Inc. , New York, (1950), V. 6, p. 58.
11. Walsh, J. M. , and R. H. Christian, Physical Review 97, (1955), 1544.
12. Personal communication, F. Harlow.
13. Brode, H. L. , and R. L. Bjork, "Cratering by a Megaton Surface Burst," Research Memorandum, RM-2600, The RAND Corporation, Santa Monica, California, June 1960.
14. Minshall, S. , Journal of Applied Physics 26 (1955), 463.
15. Summers, J. L. , and A. C. Charters, Proceedings of the Third Symposium on Hypervelocity Impact, Armour Research Foundation, Chicago (1959).
16. Olshaker, A. E. , and R. L. Bjork, "Hydrodynamics Applied to Hypervelocity Impact II. The Role of Melting and Vaporization in Hypervelocity Impact," The Rand Corporation, Paper P-, October 1961.

## HYDRODYNAMICS APPLIED TO HYPERVELOCITY IMPACT II. THE ROLE OF MELTING AND VAPORIZATION IN HYPERVELOCITY IMPACT

A. E. Olshaker and R. L. Bjork

The RAND Corporation  
Santa Monica, California

### I. INTRODUCTION

During the portion of the hypervelocity impact wherein the material is severely compressed and under tremendous pressures, the state of the material does not play a very important role. The material strength is so small compared with the pressures generated, and the heats of fusion and vaporization are so small compared with the specific internal energies which appear, that these factors cannot affect the process in an important way. However, in the later stages of the process, when the pressures and specific internal energies fall to low levels, the condition of the material can become important. One should focus his attention on the state to which the material reverts after the severe compression is over, and expansion back to low pressure has occurred. It is not necessary to devote much attention to the precise point at which phase changes occur during the expansion, which is fortunate, since the determination of this information is very difficult.

If the material were compressed adiabatically, and then expanded adiabatically there would be little residual heating. However, the material is first compressed by a shock, and in this process the entropy is raised. In the subsequent adiabatic expansion the entropy is unchanged, so that on return to low pressure the material has a greater entropy than it began with. It can be shown quite generally that the entropy excess increases rapidly with shock strength, depending on the third and higher powers of shock strength. <sup>(1)</sup> Shocks of low strength will leave the material in the solid state, but heated to some degree. Stronger and stronger shocks lead to fusion, heated liquid, vaporization, and superheated vapor as the final state. The aim of this paper is to discuss the final condition of the material as a function of shock strength, and to illustrate some effects on the hypervelocity impact process.

### II. EQUATION OF STATE AND THERMODYNAMIC CONSIDERATION

The thermodynamic equation of state which is employed by the Los Alamos workers is the Mie-Gruneisen approximation, calculated in the vicinity of the experimentally measured Hugoniot curves. For this case the equation takes the form

# MELTING AND VAPORIZATION

$$P - P_H = \frac{\gamma}{v} (e - e_H) \quad (1)$$

where  $P$  is the pressure,  $v$  is the specific volume,  $e$  the specific internal energy, the subscript  $H$  denotes points on the Hugoniot, and  $\gamma$  is the Gruneisen ratio, which relates the change in frequency of the thermally oscillating atoms in a crystal to its compression. (2,3,4) The variation in  $\gamma$  with volume can be obtained experimentally. Since  $P_H$  and  $e_H$  are on the Hugoniot, they are functions of volume only, as is  $\gamma$  by definition. Therefore, differentiating with respect to temperature,

$$\left(\frac{\partial P}{\partial T}\right)_v = \frac{\gamma}{v} \left(\frac{\partial e}{\partial T}\right)_v \quad (2)$$

But  $\left(\frac{\partial e}{\partial T}\right)_v = C_v$ , the heat capacity at constant volume, and  $\left(\frac{\partial P}{\partial T}\right)_v = \beta/K$ , where  $\beta = \frac{1}{v} \left(\frac{\partial v}{\partial T}\right)_P$ , the volume coefficient of expansion of constant pressure, and  $K = -\frac{1}{v} \left(\frac{\partial v}{\partial P}\right)_T$ , the isothermal compressibility. (See any thermodynamics text.) Therefore,  $\frac{\gamma}{v} = \frac{\beta}{KC_v}$  is the relation between the

statistical mechanics and bulk thermodynamics of a crystal. Based on these values at standard conditions and the theoretical variations of  $\gamma$  with volume, Los Alamos presentations of two typical  $\gamma$ 's versus  $v/v_0$  are shown in Figure 1. The curvature of the copper  $\gamma$  arises from the theoretical variation, while the straight line for the lead is a result of the assumption that  $\gamma/v$  is constant. This assumption is made for the following reason. For the case of zero pressure, the theoretical variation of  $\gamma$  can be combined with the experimental Hugoniot data to furnish an absolute value of  $\gamma$  which can then be compared to the zero pressure value known to be correct from the experimental thermodynamic values. For copper this theoretical-Hugoniot  $\gamma$  is 1.99 while the thermodynamic value is 2.00, and for most other metals the agreement is within 14 percent. (3) This agreement at zero pressure gives some justification for the use of the theoretical variation at the higher compressions. However, for the three elements gold, thorium, and lead, the zero pressure values do not agree; e. g., for lead the theoretical-Hugoniot  $\gamma$  is 2.03 while the experimental-thermodynamic value is 2.77. For these three materials  $\gamma/v$ , which is also equal to  $\left(\frac{\partial P}{\partial e}\right)_v$  by differentiation of Gruneisen's

equation, is assumed to be constant at the thermodynamic zero pressure value, and in fact this is not too far from what the theoretical variations amount to on the other metals. To quote: "it is, of course, clear that the calculated values of  $\gamma$ , at high pressures, are not very accurate. In regard to calculated  $P$ - $v$  curves, on the other hand,  $\gamma$  is used only to estimate the small offsets (typically one percent in volume) from the experimental Hugoniot and errors as large as 25 percent in the offsets (i. e., approximately 25 percent in  $\gamma$ ) lead to uncertainties which are only comparable to probable errors in the experimental curves. Temperature increases, calculated along constant-entropy curves, reflect an error which is roughly proportional to the volume average error in  $\gamma$ . The use of the correct  $\gamma$  at normal

# MELTING AND VAPORIZATION

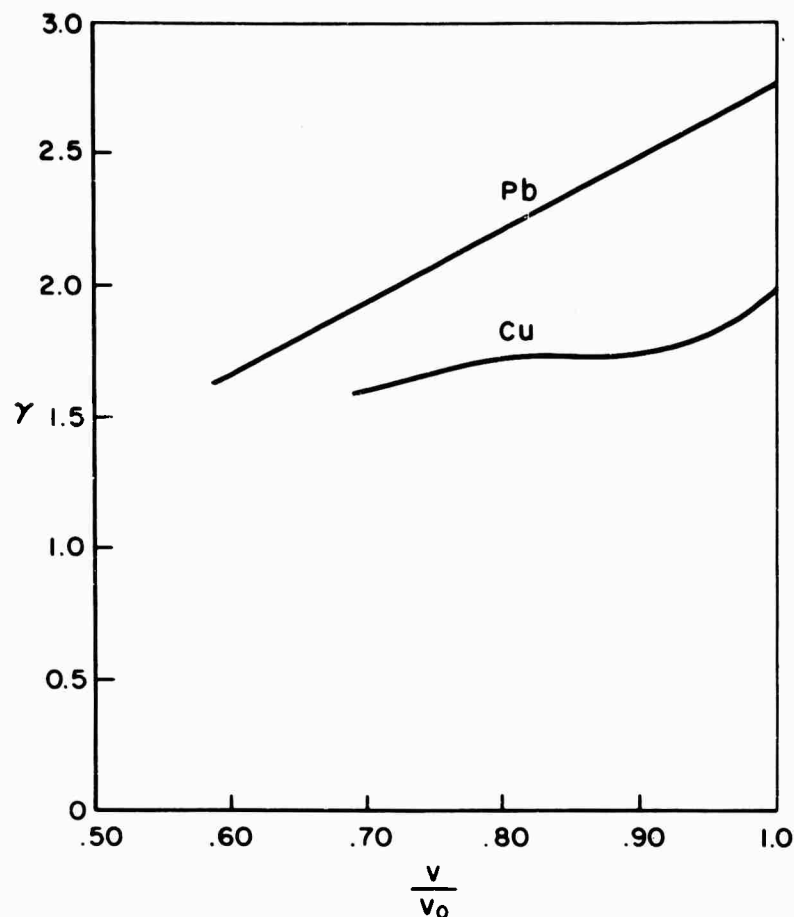


Figure 1. Gruneisen Ratio as a Function of Volume for Lead and Copper.

volume and an experimental additive term in the listed temperature ( $T = 0$  at  $P = 0$  on the adiabat through the point) then lead to temperatures which should be reliable to 10 percent or less of their centigrade values. <sup>(6,2)</sup> Following is the method used to calculate the excess internal energy imparted by a shock and adiabatic expansion. In Figure 2 point 1 is a point on the Hugoniot having coordinates  $P_H$  and  $v_1$ . Note that for the case of material at rest and with zero energy before being shocked, the Hugoniot relation,

$$e_H = \frac{P_H}{2} (v_0 - v_H) \quad (3)$$

shows that the specific internal energy of the shock compressed material is equal to the area of the dashed triangle. The energy that is returned by the material in  $P - v$  work is the area under the adiabat, and because of the irreversible losses in the shock this is less than the area  $A$ . It is evident from this figure

# MELTING AND VAPORIZATION

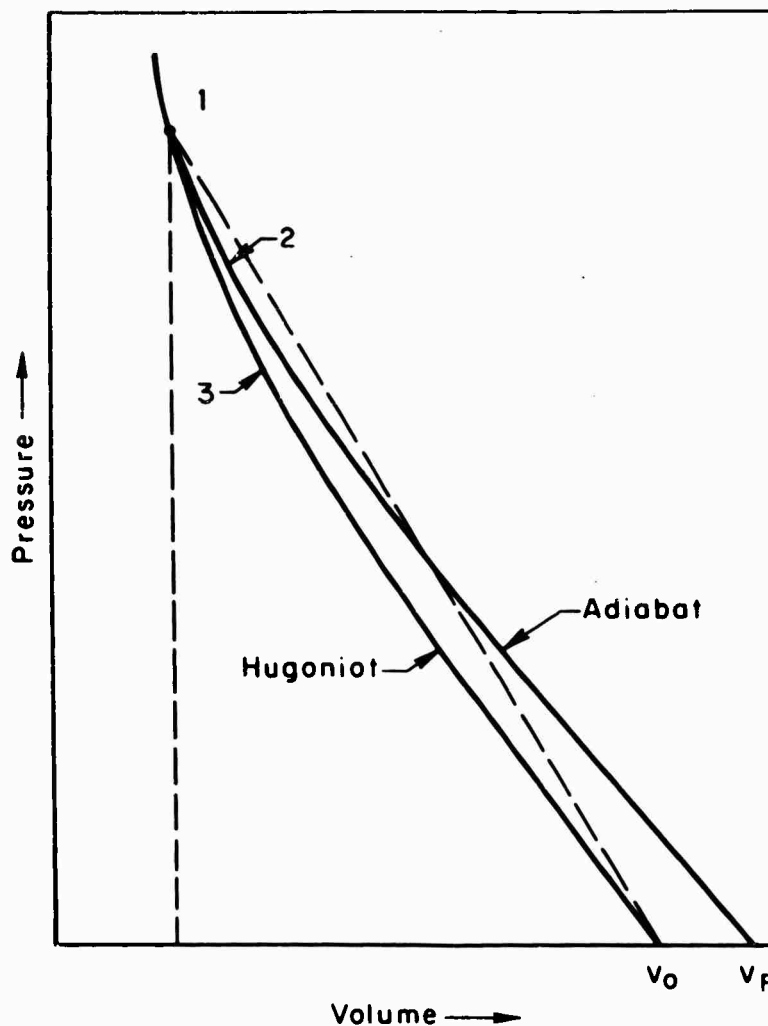


Figure 2. Qualitative Relationship of Hugoniot and Adiabot, Illustrating Method of Calculating Internal Energy after Shock Release.

that the differences between these areas are small compared to the total areas, and that the theories which postulate kinetic energy of impact going entirely into melting, or "breaking of chemical bonds," are over-estimating the transference of energy into residual heating since the return of the work of expansion is neglected.

In order to calculate an adiabat from the Hugoniot, one simply integrates numerically from any desired initial shock point, using the Gruneisen equation and

the known  $\gamma$ . Starting at point 1, where  $e_1 = \frac{P_{H1}}{2} (v_0 - v_{H1})$

by the Hugoniot relation, one desires the value of internal energy at some expanded

# MELTING AND VAPORIZATION

incremental volume above  $v_1$ . Gruneisen's equation gives  $P_2 = P_{H_3} + \frac{\gamma_{2-3}}{v_{2-3}} (e_2 - e_{H_3})$ . But since the expansion is along an adiabat, or constant entropy process, the first law of thermodynamics gives

$$dQ = de + Pdv = 0 \quad (4)$$

or

$$\Delta e_{1 \rightarrow 2} = \bar{P}_{1 \rightarrow 2} \Delta v_{1 \rightarrow 2} \quad (5)$$

and so

$$e_2 = e_1 - \bar{P}_{1 \rightarrow 2} \Delta v_{1 \rightarrow 2} \quad (6)$$

This fixes  $v_2$  and  $e_2$ , so that  $P_2$  may be calculated from the equation of state. In this manner, by extrapolating the adiabat ahead of each point so that  $\bar{P}$  for the next increment can be evaluated, the entire adiabat is calculated and one obtains a final internal energy at zero pressure after the entire process is completed and the material has become over-expanded to  $v_f$  by the irreversible heating. Since the heat capacity at constant (zero) pressure is known versus temperature, this resulting internal energy is readily converted to a final temperature. That is, since the state at  $v_f$  could be reproduced by either the illustrated shock-expansion process, or simple heating at zero pressure from  $v_0$  to  $v_f$ , the expression

$$e_f - e_0 = \int_{T_0}^{T_f} C_P(T) dT \quad (7)$$

permits the evaluation of  $T_f$  from the computed  $e_f$ .

For the calculation of the rise in temperature along the adiabat going back up from  $T_f$  @  $v_f$  and  $P = 0$  to a point 1 on the Hugoniot, one uses the TdS identity in terms of  $T$  and  $v$ ,

$$TdS = C_v dT + T \left( \frac{\partial P}{\partial T} \right)_v dv = 0 \quad (8)$$

or

$$\left( \frac{\partial T}{\partial v} \right)_S = - \frac{1}{C_v} \left( \frac{\partial P}{\partial T} \right)_v T \quad (9)$$

if phase changes are neglected. But from the Gruneisen equation

$$\left( \frac{\partial P}{\partial T} \right)_v = \frac{\gamma}{v} C_v \quad (10)$$

## MELTING AND VAPORIZATION

so

$$\left(\frac{\partial T}{\partial v_s}\right) = - \frac{\gamma}{v} T \quad (11)$$

or

$$T = T_f \exp \left\{ - \int_{v_f}^v \frac{\gamma}{v} dv \right\} \quad (12)$$

along an adiabat, or constant entropy process. By these methods, Los Alamos workers have calculated in detail the values of the shock pressures which are just great enough to result in expansion back to melting.<sup>(3)</sup> Figure 3 illustrates some zero pressure temperatures (after shock and subsequent expansion) versus the shock pressures which they have expanded from. The flat portions of the curves are where the excess energy is going into the fusion, or melting, instead of the raising of temperature, and therefore the shock pressure at the start of the flat portion is that which causes incipient, or beginning of, melting, while that at the end of the flat portion is that which causes complete melting. (It appears, incidentally, that in this pressure range the temperature versus shock pressure after fusion is linear for everything but lead.) For those metals for which this Los Alamos information is available, Table 2 shows the shock pressures for both incipient and complete melting, as well as the minimum impact velocities which just cause these pressures with similar material, steel, and aluminum projectiles. For tungsten, molybdenum, titanium, beryllium, and magnesium, incipient melting has not occurred in the pressure ranges tested, and probably will not occur until a similar material impact velocity of at least five kilometers per second, by considerations of melting temperature and density.

For iron and aluminum, less detailed thermodynamic data is available for this calculation. The final zero pressure energies resulting from the complete equations of state are not known with as much confidence as other variables which are needed for the flow problem. To symbolize this, the aluminum curve is dashed in Figure 3. Also, the lower energies are known less accurately than higher ones, so an attempt is made to calculate only complete melting in these two metals, and not incipient melting. The liquidus temperature of 2024 aluminum is 660° C at one atmosphere. The internal energy required to achieve complete melting is the integral of the specific heat times the differential temperature, added to the heat of fusion. For this analysis, assuming the specific heat is constant is more than adequate. Therefore, using data from Metals Handbook, 1939,

$$e_{\text{melt}} = (.24) (640^\circ) + 93 = 247 \frac{\text{calories}}{\text{gram}} = 10^{10} \text{ ergs/gram.}$$

This corresponds to a shock pressure in aluminum of roughly .9 of a megabar. A similar analysis for iron gives a shock pressure of two megabars to cause complete melting, and this is compatible with approximate thermodynamic data published in Reference 2. Table 3 gives the impact velocities for estimated complete melting in aluminum and iron.

# MELTING AND VAPORIZATION

TABLE 2  
Melting Properties

Material	Density	Melting Temp. (°K)	Incipient Melting				Complete Melting			
			Shock Pres- sure (Mb)	Sim. Mat. Impact Velocity (km/sec)	Fe Proj. (km/sec)	Al Proj. (km/sec)	Shock Pres- sure	Sim. Mat. Impact Velocity	Fe Proj.	Al Proj.
Gold	19.24	1340	1.46	2.9	3.8	6.0	? (over 1.6)	---	---	---
Lead	11.34	600	0.25	1.4	1.3	2.0	0.35	1.8	1.8	2.6
Silver	10.49	1230	0.98	3.2	3.4	5.1	1.27	3.8	4.1	6.1
Copper	8.90	1360	1.40	4.4	4.5	6.6	? (over 1.5)	---	---	---
Cadmium	8.64	590	0.33	1.9	1.8	2.5	0.46	2.4	2.3	3.2
Tin	7.28	505	0.21	1.5	1.3	1.8	0.35	2.2	2.0	2.8
Zinc	7.14	690	0.50	2.7	2.5	3.5	0.70	3.4	3.2	4.5

## MELTING AND VAPORIZATION

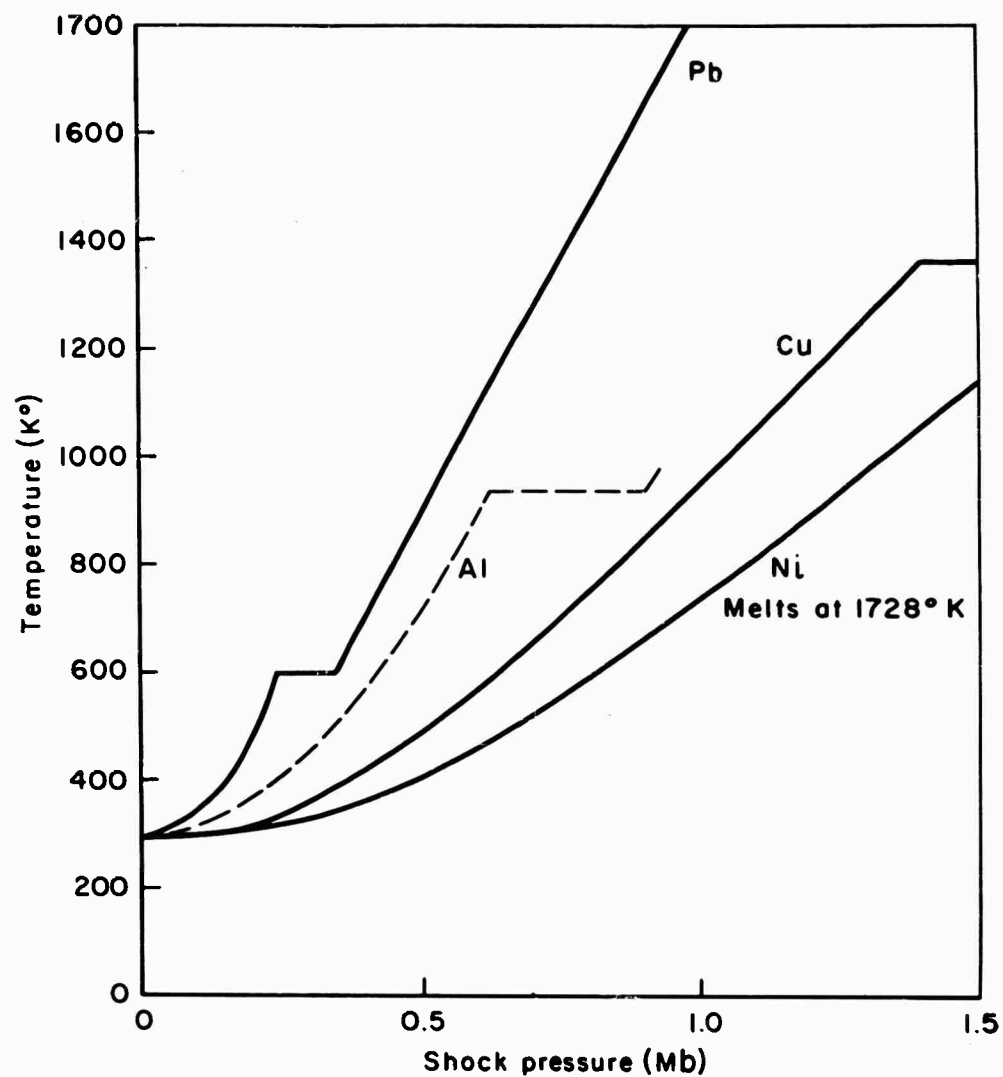


Figure 3. Temperatures After Shock Release for Four Metals.

### III. INFLUENCE OF VAPORIZATION AND MELTING ON HYPERVELOCITY CRATERING

As discussed in the 1958 paper, (5) the hypervelocity cratering process proceeds in two stages:

- (1) The shock generated on initial impact races through the target with diminishing intensity.

## MELTING AND VAPORIZATION

TABLE 3  
Impact Melting Fe, Pure Al

Target Material	Density	Liquidus Temp. ( $^{\circ}$ K)	Shock Pressure Complete Melting (Mb)	Similar Material Impact Velocity	Fe. Proj. Impact Velocity	Al Proj. Impact Velocity
Iron	7.84	1810	2.0	5.9	5.9	8.6
Aluminum	2.78	660	0.9	6.6	5.0	6.6

Incipient Melting of Pure Aluminum

	Shock Pressure	Similar Material	Fe Projectile
Pure Aluminum	.6Mb	5.0 km/sec	3.8 km/sec

(2) The material behind the shock then flows and generates the crater on a much longer time scale.

As a result, the material flow which generates the crater always occurs in a medium which has been conditioned by the shock, and it is this conditioning which we will now discuss.

As an example, consider the case of a square cylinder (length equals diameter) which moves along its axis and strikes a semi-infinite target at normal incidence. This problem has cylindrical symmetry, and we shall consider conditions along the axis of symmetry. Figure 4 shows the peak pressures produced by the shock along the axis as a function of depth. The units of depth are given in terms of the characteristic dimension of the projectile,  $d$ , and we shall call this the scaled depth.

The initial impact of aluminum on aluminum at 20 km/sec produces a pressure of about 4.9 Mb. This pressure persists along the axis to a scaled depth of about 0.7, at which time a rarefaction wave overtakes the shock. Under the influence of the rarefaction wave and the lateral expansion which also begins at that time, the shock pressure subsequently drops with about the -1.2 power of depth. At a scaled depth of 4.5, which is somewhat greater than the final crater depth in Reference 5, the peak shock pressure is about 0.5 Mb. Although the graph is terminated at this point, the shock does propagate beyond this depth, and is in fact the agent which would cause spallation were it to encounter a free surface.

Also shown in Figure 4 is an estimate of the temperature to which the target material comes upon expansion back to zero pressure after the shock has passed.

## MELTING AND VAPORIZATION

At scaled depths less than 2.8 the material returns to a liquid state which is hotter than the melting temperature of  $930^{\circ}\text{K}$ . Between the scaled depths of 2.8 and 3.4 the material will be a mixture of solid and liquid, and below a depth of 3.4, it is a solid, heated to the temperature shown in the graph.

At the instant of time when the shock reaches a scaled depth of 2.8, the bottom of the forming crater is at a scaled depth of about 1.7. Consequently, the subsequent material flow is into a target having the temperature distribution shown in Figure 4. Some important implications may be derived from these considerations:

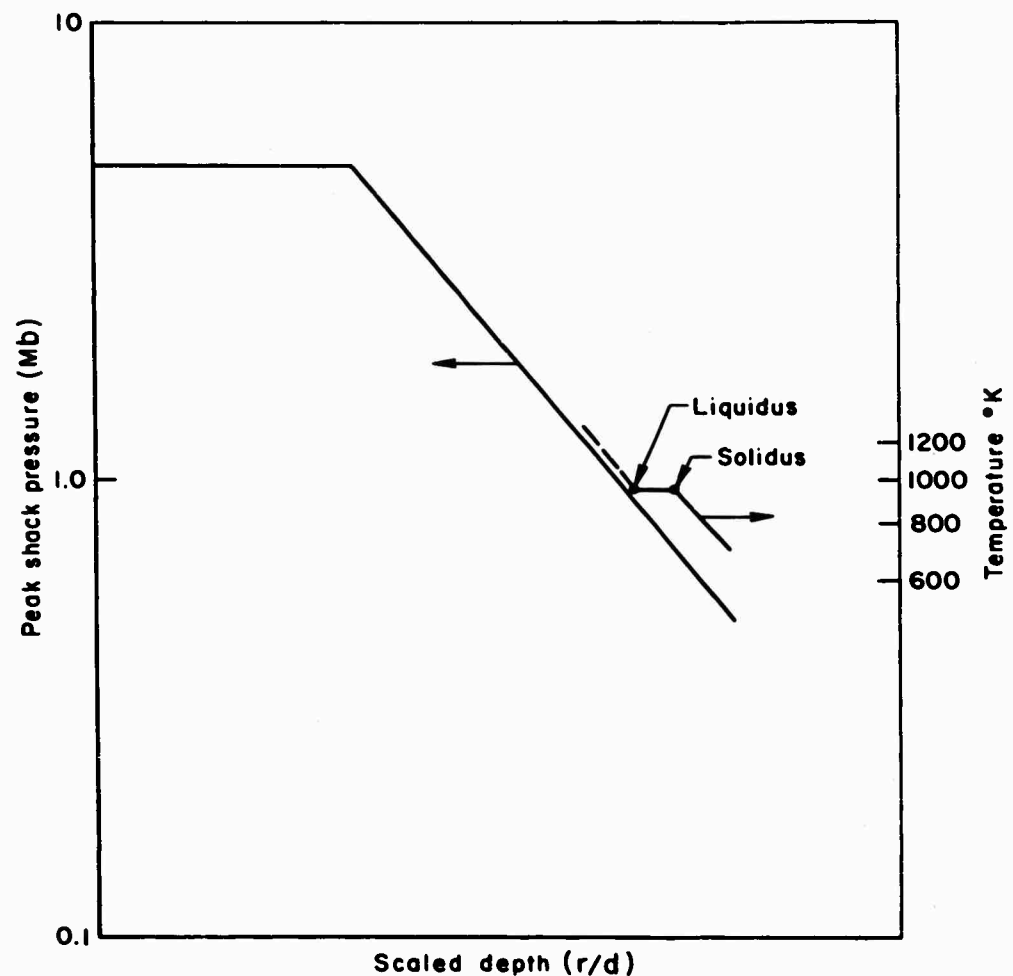


Figure 4. Peak Shock Pressure and Temperature After Shock Release as a Function of Depth Along the Axis for Aluminum on Aluminum at 20 km/sec.

## MELTING AND VAPORIZATION

- (1) The process is truly hydrodynamic to a scaled depth of 3.4, and below this the validity of the hydrodynamic approximation is enhanced by the fact that the target material has been intensely heated. A comparison of recent experimental data and the crater estimates on the hydrodynamic model<sup>(6)</sup> are given in Appendix A.
- (2) Theories which seek to include the role of material strength without including these heating effects seem doomed to failure at the higher velocities.
- (3) Those theories which attempt to assess the effects of material strength and viscosity by calculating their effects on the initial shock wave seem incorrectly oriented for two reasons: (a) the dynamic yield strength can have little effect on shocks of greater than 0.5 Mb, and (b) the viscosity of the actual material is orders of magnitude less than the artificial viscosities which are used in the numerical calculations, yet the inclusion of these (hopefully) still leads to the correct shock strength and position. Thus, reasonable values of dynamic yield strength and viscosity cannot have much influence on the initial shock in this problem. The important physical quantity is the strength of the material after conditioning by the front-running shock, and its influence will be felt in governing the material flow which finally forms the crater.
- (4) The "energetic" theories of hypervelocity cratering which assumed that all of the projectile's kinetic energy was absorbed in bringing the crater and projectile material to exactly a state of fusion are seen to be on an incorrect physical basis. Figure 4 illustrates well the fact that a great deal of the crater material has been given much more internal energy than is necessary to melt it. In fact, at 72 km/sec, an appreciable amount is vaporized. In general, the average specific internal energy imparted to the crater material increases rapidly with impact velocity. Consequently a penetration theory based on energetics cannot lead to a "2/3 law" (crater volume proportional to projectile kinetic energy). When the increase of average specific internal energy is taken into account, the value of 2/3 will be reduced.

### APPENDIX A

#### Comparison of Hydrodynamic Crater Calculations with Recent Experimental Data

The comparison is made in Figure A-1, wherein the abscissa is the impact velocity and the ordinate is  $P/d$ , the ratio of the penetration to the characteristic dimension of the projectile. All of the information pertains to impact of aluminum projectiles on aluminum targets.

The upper group of experimental data representing craters made in commercially pure (1100) aluminum is all due to Atkins.<sup>(7)</sup> Atkins had previously concluded that an unsaboted aluminum projectile loses an important fraction (up to 45 percent) of its mass by ablation in the gun barrel, and so regards his point

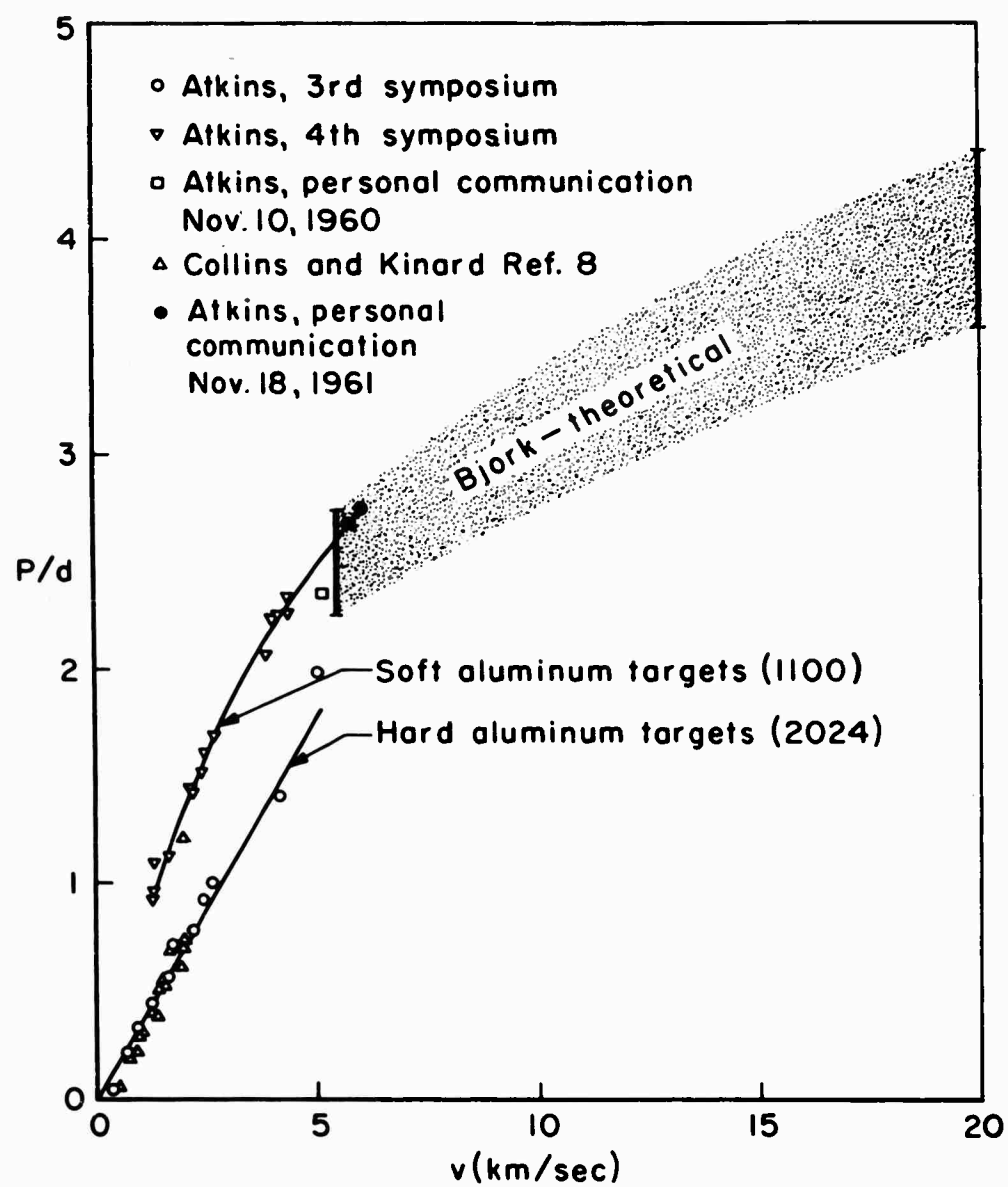


Figure A-1. Cartesian Comparison of Theoretical and Experimental Penetration - Aluminum on Aluminum.

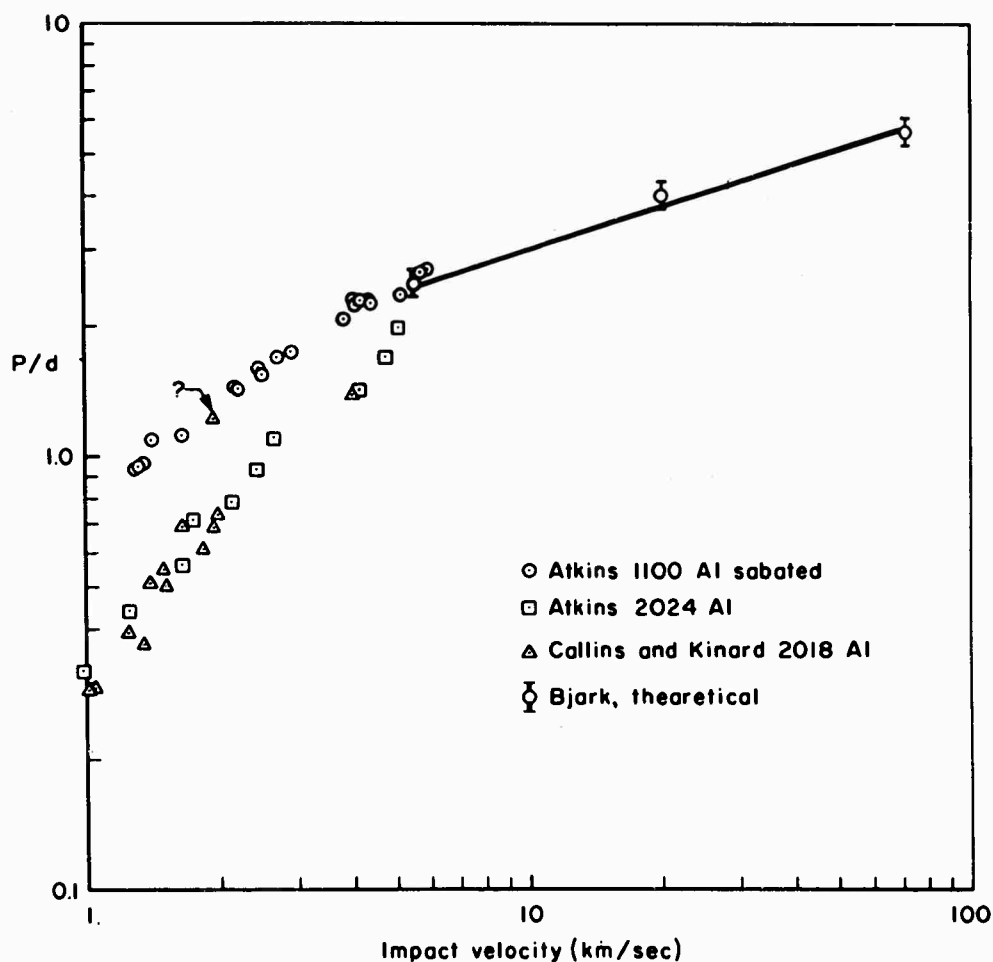


Figure A-2. Log-Log Comparison of Theoretical and Experimental Penetration - Aluminum on Aluminum.

cited in Reference 6 as questionable. The data shown here were all taken using sabot spherical projectiles. The theoretically predicted craters (6) are shown as the shaded region in Figure A-1, and the experimental points appear to be entering this region in a satisfactory way.

The lower group of experimental data represents craters made in stronger aluminum alloys (2024, 2018). (7, 8) As one would expect on intuitive grounds, these craters are smaller than those made in the 1100 alloy at the same impact velocity. Some of these data were taken with spherical projectiles and some with square cylinders (length equals diameter). In all cases, the projectile diameter was chosen as the characteristic dimension. Treating the data in this way resulted

## MELTING AND VAPORIZATION

in good agreement, in spite of the fact that a cylinder weighs fifty percent more than a sphere having the same characteristic.

The data on the cartesian graph of Figure A-1 is replotted on a log-log graph in Figure A-2. The two groups of experimental data are obviously converging on the new plot, which implies that the percentage-wise difference in crater depth is decreasing at higher velocities. For example, at 2 km/sec, the craters in 1100 aluminum are almost twice as deep as those in the stronger alloys, whereas at 5 km/sec they are only deeper by a factor of about 1.25. When one considers that the strong alloys have strengths about a factor of 5 higher than the 1100 alloy, and that this results in only a 25 percent change in crater dimension, it is clear that the penetration is quite insensitive to strength. Summers<sup>(9)</sup> has reported on the same effect, viz., the decrease in strength effects with increasing impact velocity, for copper.

Since the hydrodynamic model neglects the material strength, it is only natural that the 1100 data should come into agreement with it at a lower impact velocity than the stronger alloys.

If one were to naively fit the two sets of experimental data by straight lines on the log-log plot and then extrapolate these lines to high velocities, he would see that the two lines would cross. This would lead to the questionable conclusion that a larger crater is produced in the 2024 alloy than in pure aluminum, for the same projectile at impact velocities above the crossing point. Besides illustrating the dangerous risks incurred in this type of empiricism, this construction indicates that the behavior of one set of data must change with increasing velocity. It is our belief that the hard aluminum data will exhibit a negative second derivative on the log-log plot and ultimately fare into the theoretical region just below the soft aluminum data.

## REFERENCES

1. Courant, R., and K. O. Friedrichs, *Supersonic Flow and Shock Waves*, Interscience Publishers, Inc., New York, 1948, p. 142.
2. Walsh, J. M., et al., *Physical Review*, **108**, 1957, p. 196.
3. McQueen, R. G., and S. P. Marsh, *Journal of Applied Physics*, **31**, 1960, p. 1253.
4. Rice, M. H., et al., *Solid State Physics, Advances in Research and Applications*, Academic Press, Inc., New York (1958), Vol. 6, p. 58.
5. Bjork, R. L., *Proceedings of the Third Symposium on Hypervelocity Impact*, Vol. II, edited by F. Genevieve, Armour Research Foundation of Illinois Institute of Technology, Chicago, Illinois, 1958.
6. Bjork, R. L., "Effects of a Meteoroid Impact on Steel and Aluminum in Space," The RAND Corporation Paper, P-1662, 1959.
7. Atkins, W. W., "Proceedings of the Third and Fourth Symposia on Hyper-

## MELTING AND VAPORIZATION

velocity Impact." (Also personal communication.)

8. Collins, R. D., Jr., and W. H. Kinard, "The Dependency of Penetration on the Momentum Per Unit Area of the Impacting Projectile and the Resistance of Materials to Penetration, NASA TN D-238, Langley Research Center, Langley Field, Va., May, 1960.
9. Summers, J. L., "Investigations of High Speed Impact: Regions of Impact and Impact at Oblique Angles," NASA TN D-94, Ames Research Center, Moffett Field, California, October, 1959.

## PENETRATION BY HYPERVELOCITY PARTICLES

M. Zaid

Technik Incorporated  
Garden City, New York

### INTRODUCTION

In a previous paper<sup>1</sup> a rational theory of penetration by ultra high-speed penetrators was presented. To summarize; the ultra high-speed process was defined as one in which stress waves do not radiate significant distances from the penetrator during its primary penetration stages. Because of this, large amounts of energy are transferred to the particles in the neighborhood of the particle-target interface; resulting in a "fluidizing" of these particles. These particles are then swept radially out of the path of the penetrator, between two essentially rigid members (undeformed regions of target and penetrator). Large shear forces can be associated with this high radial velocity of the "fluid" layer, and these forces will in turn dissipate large amounts of energy into the neighboring undeformed regions. Consequently, the fluid-zone region can be thought of as advancing through the target, together with the projectile. In general this zone may change its size and shape during the process. Further, it should be understood that even though the fluid-zone will advance through the target with the projectile, the particles associated with it at any instant will not; they will be swept radially out of the zone by the unbalanced radial forces.

Based on the above mechanism the equation of motion for a rigid-penetrator deformable-target combination was derived; and two auxiliary relationships were examined in some detail. Once these are completely formulated it is possible to proceed with the complete solution of penetration problem, and to obtain experimental correlation and/or evaluation of any undetermined material or fluid-flow constants.

In the present paper several different fluid-zone "growth" laws are formulated and the equations of motion are solved using a particularly simple viscous relationship. Based on these solutions it is possible to obtain a rather detailed understanding of the penetration process. Additionally, coefficients to be determined by additional experimental and/or analytical work are indicated, so that absolute values can be assigned to the associated time and distance scales.

The work of this paper indicates that much more remains to be done in the refinement of input data from both an experimental and analytical point-of-view. However, even in the absence of accurate material information, the theory is capable of predicting order-of-magnitude results. Based on this it will be fruitful

## PENETRATION BY HYPERVELOCITY PARTICLES

to extend the concepts contained herein to the case which also allows a deformable penetrator, and to additionally examine the secondary penetration phenomenon.

### ABSTRACT

In this paper additional equations are presented for the solution to the problem of a non-deformable ultra high-speed penetrator striking a semi-infinite deformable target. These, together with the ones of a previous paper, provide a complete mathematical description of a penetration model. Based on these equations, and on an assumed stress-velocity relationship, various "growth" laws are postulated and solutions for penetration distance, velocity and time history are obtained. From these it is seen that although the phenomenon is sensitive to the exact magnitude of physical parameters, it is much less sensitive to a variation in the formulation of the "growth" law.

The paper suggests many areas in which experimental work would be fruitful, and additionally provides a model capable of extension to the deformable-penetrator deformable-target problem.

# PENETRATION OF HYPERVELOCITY PARTICLES

## NOMENCLATURE

$a$  = radius of penetrator

$F_{rod}$  = radial shear force

$h$  = instantaneous fluid-zone thickness

$h_{\infty}^*$  = quasi-steady state fluid-zone thickness

$\dot{h}$  = instantaneous rate of growth of fluid-zone thickness

$H^*$  = dimensionless fluid-zone thickness (  $h/h_{\infty}$  )

$\left. \begin{matrix} k_1 \\ k_2 \\ k_1' \\ k_2' \end{matrix} \right\}$  = shear law coefficients

$l$  = length of penetrator

$M_f$  = fluid-zone mass

$M_p$  = penetrator mass

$r$  = radial coordinate of element in fluid-zone

$t$  = time

$\bar{u}_0$  = average radial velocity of fluid "particle"

$x$  = axial penetration distance

$\dot{x}, \ddot{x}$  = penetrator velocity, acceleration

$\dot{x}'$  = fluid-zone front velocity, into target

$\dot{x}_0$  = penetrator striking velocity

$X^*$  = dimensionless penetration distance (  $x/h_{\infty}$  )

$X_{tot.}^*$  = maximum dimensionless penetration distance (  $x_{tot.}/h_{\infty}$  )

$\beta$  = coefficient associated with velocity profile

$\mu$  = viscosity of material in fluid-zone, in its instantaneous state

\* Additional subscript indicates case under consideration.

## PENETRATIONS BY HYPERVELOCITY PARTICLES

$\rho_{**}$  = mass density

$T_L$  = shear stress on lower interface

$T_U$  = shear stress on upper interface

---

\*\* Subscript  $p$  ,  $f$  refers to penetrator and fluid, respectively.

# PENETRATIONS BY HYPERVELOCITY PARTICLES

## ANALYSIS

### I. Basic Equations

The basic equations were derived and discussed in Reference 1; so that they will be introduced with little further discussion in the present paper.

#### A - Equation of Motion

The equation of motion can be written as

$$M_p \ddot{x} + \frac{2\pi\beta}{h} \left[ \frac{1}{2} \int_0^a T_u r^2 dr + \frac{\rho a^4}{16} \left( \ddot{x} + \frac{3}{2} \frac{\dot{x}^2}{h} \right) \right] = 0 \quad (1)$$

Using the shear-velocity equations indicated in the following section, this equation becomes,

$$\ddot{x} \left[ \frac{M_p}{M_f} + \frac{\beta}{8} \left( \frac{a}{h} \right)^2 \right] + \frac{3}{16} \beta \left( \frac{a}{h} \right)^2 \frac{\dot{x}^2}{h} + \beta \frac{k^2}{8h^2\rho} \left( \frac{a}{h} \right)^2 \dot{x} + \frac{\beta}{3\rho} \left( \frac{a}{h} \right) \frac{k_1}{h} = 0 \quad (2)$$

#### B - Shear-Velocity Equation

We will take a shear-velocity relationship on the upper interface of the type

$$T_u = k_1 + k_2 \frac{\dot{u}_a}{h} \quad (3)$$

and that on the lower interface to be,

$$T_L = k'_1 + k'_2 \frac{\dot{u}_a}{h} \quad (4)$$

which accounts for a constant and a simple viscous term. It is felt that additional terms or further refinement is not warranted at the present stage of the investigation; although modifications and generalizations can be made later, as experimental evidence indicates the need.

#### C - Fluid-Zone "Growth" Relationship

Growth laws of the type

$$\dot{x}' = b_n \bar{T}_L^n \quad (5)$$

# PENETRATIONS BY HYPERVELOCITY PARTICLES

are investigated. As discussed in the referenced paper, they have physical justification. In addition we have also investigated a growth law of the type

$$\dot{x}' = C_m \bar{u}_a^m \quad (6)$$

which, although it is closely related to laws of the type indicated in equation (5), has some additional mathematical simplicity.

In the usage of "average" shears or velocities one has a choice; subject to experimental verification. For purposes of mathematical simplicity and physical reasonableness we have defined these as the average shear stress or velocity acting radially outward between the center and outside radius, over an incremental element; that is

$$F_{rad.} = \bar{T}_L \frac{a^2 d\phi}{2} = \int_0^a T_L r d\phi dr \quad (7)$$

$$\bar{u}_a \frac{a^2 d\phi}{2} = \int_0^a u_a r d\phi dr \quad (8)$$

Using the relationship for  $\dot{u}_a$  from the referenced paper,

$$\dot{u}_a = \frac{r}{2h} \dot{x} \quad (9)$$

and equation (4) as required in equations (7) and (8), there results:

$$\bar{T}_L = k'_1 + k'_2 \frac{a}{3h^2} \dot{x} \quad (10)$$

$$\bar{u}_a = \frac{a}{3h} \dot{x} \quad (11)$$

Thus in the present paper we will introduce the basic growth laws, represented by equations (5) and (6), in the form

$$\dot{x}' = b_n (k'_1 + k'_2 \frac{a}{3h^2} \dot{x})^n \quad (12)$$

## PENETRATION BY HYPERVELOCITY PARTICLES

or

$$\dot{x}' = C_m \left( \frac{a}{3h} \dot{x} \right)^m \quad (13)$$

### D - Fluid-Front Motion

The relationship between the fluid-front velocity, the fluid region growth and penetrator velocity is given by<sup>1</sup>,

$$\dot{x}' = \dot{x} + \dot{h} \quad (14)$$

### E - Limitation of Present Investigation

For the purposes of the present investigation we will limit ourselves to the cases of  $k_1 = k_1' = 0$ ,  $n = 1, 2$ ,  $m = 1$ . This serves to sufficiently simplify the mathematics so that the investigation can be completed without recourse to extensive numerical equation-solving, with its associated limiting to special cases; thus the overall physical phenomena can be simply understood from both a quantitative and qualitative viewpoint. The generalization of these results is the subject of future work. Thus the basic equations to be used in this paper are,

#### General

$$\ddot{x} \left[ \frac{M_p}{M_f} + \frac{\beta}{8} \left( \frac{a}{h} \right)^2 \right] + \frac{3}{16} \beta \left( \frac{a}{h} \right)^2 \frac{\dot{x}^2}{h} + \beta \frac{k_2}{8h^2 \rho} \left( \frac{a}{h} \right)^2 \dot{x} = 0 \quad (15)$$

#### Special

##### Case I

$$\dot{x}' = \dot{x} + \dot{h} = b_1 k_2' \frac{a}{3h^2} \dot{x} \quad (16)$$

##### Case II

$$\dot{x}' = \dot{x} + \dot{h} = b_2 k_2'^2 \frac{a^2}{9h^4} \dot{x}^2 \quad (17)$$

# PENETRATION BY HYPERVELOCITY PARTICLES

## Case III

$$\dot{x}' = \dot{x} + \dot{h} = C_1 \frac{a}{3h} \dot{x} \quad (18)$$

## II - Fluid-Zone Build-Up

### A - x-h relationship

In both cases I and III we can eliminate time directly from the associated equations (16) and (18), and obtain solutions for the relationship between  $h$  and  $x$ . Defining dimensionless penetration distance and fluid-zone thickness  $x/h_\infty = X$ ,  $h/h_\infty = H$ , and taking initial conditions of  $X(0) = H(0) = 0$ , there results:

### Case I

$$X = -H_I + \frac{1}{2} \ln \left( \frac{1+H_I}{1-H_I} \right) \quad (19)$$

where

$$h_{I\infty} = \sqrt{\frac{b_1 k_2' a}{3}}$$

### Case III'

$$X = -H_{III} + \ln \left( \frac{1}{1-H_{III}} \right) \quad (20)$$

where

$$h_{III\infty} = \frac{C_1 a}{3}$$

The interpretation of  $h_\infty$  becomes very clear when we evaluate the maximum value that  $H$  can take. Examining equations (19) or (20) it can be shown that  $H$  is a monotonically increasing function of  $X$ , for non-negative  $X$ . Further its maximum occurs at  $X = \infty$ , and is  $H = 1$  or  $h = h_\infty$ . Thus  $h_\infty$  is the maximum fluid-zone thickness that can exist.

In Figure 1 we have plotted the relationship between  $X$  and  $H$  for the two cases under consideration.

## PENETRATION BY HYPERVELOCITY PARTICLES

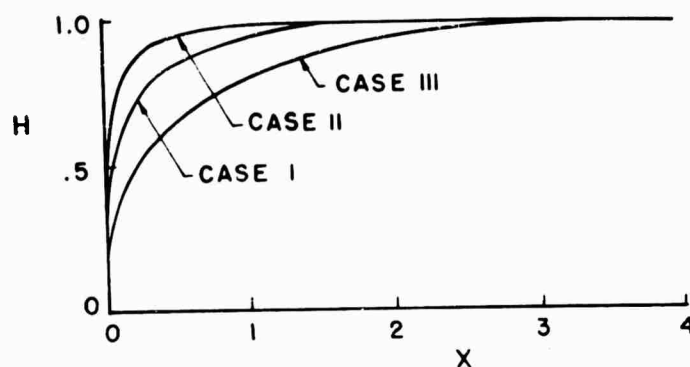


FIG. 1

It is particularly useful and important to note that the fluid-zone build-up is quite rapid; reaching 83% or 96% of its maximum possible thickness by the time the penetrator has traversed one fluid-zone thickness.

### B - x - h - t relationship

In both the above considered cases it has been possible to eliminate time ( $t$ ) and directly obtain the  $x - h$  relationship; but this will not generally be possible. Since it will be most useful in the work that follows, a technique will be presented for evaluating the nature of the fluid-zone build-up, in a specific situation. This result will form the basis for an "a priori" assumption which greatly reduces the complexity, and increases the understanding of the final solution. Finally the validity of this assumption is subject to an "a posteriori" verification. The evaluation technique will be illustrated in all three cases under consideration. For Cases I and III the technique can be immediately evaluated by comparison with the solutions already obtained; at the same time providing a standard against which Case II results can be compared.

The basis for the above mentioned technique is to evaluate the fluid-zone build-up for a penetrator moving at constant velocity. \* Then, if it can be shown "a posteriori" that this full fluid-zone build-up occurs before there are appreciable velocity changes, it is valid to assume that a quasi steady-state process dominates; so that there is a unique relationship between instantaneous fluid-zone thickness and velocity. Assuming that it is valid and introducing this relationship, the equation-of-motion can be integrated. This procedure neglects the effects of the transient initial fluid-zone build-up as compared to those of maintaining of the full zone. In some cases it is possible that the transient build-up may be important; especially with a short deformable penetrator. As indicated, these are subject to an "a posteriori" check; a complete coupled-solution being

---

\*See Appendix for a more accurate technique that verifies this approach.

## PENETRATION BY HYPERVELOCITY PARTICLES

required only in those cases where this simplified approach fails. However, it should be noted that this coupled solution of the equations can always be obtained by recourse to numerical integration techniques.

### Case I

Introducing  $\dot{x} = \dot{x}_0$  we can integrate equation (16) directly to obtain  $H$  as an implicit function of  $t$ ,

$$\dot{x}_0 t = -H_I + \frac{1}{2} \ln \left( \frac{1+H_I}{1-H_I} \right) \quad (21)$$

where  $H$ ,  $X$  are defined in conjunction with equation (19). Equation (21) also follows trivially from equation (19), since

$$X = \dot{x}_0 t \quad (22)$$

### Case III

In a similar fashion we can show

$$\dot{x}_0 t = -H_{III} + \ln \left( \frac{1}{1-H_{III}} \right) \quad (23)$$

where  $H$  is defined in conjunction with equation (20).

### Case II

In this case, introducing  $x = \dot{x}_0$  into equation (17) we obtain

$$\dot{x}_0 t = -H_{II} + \frac{1}{4} \ln \left( \frac{1+H_{II}}{1-H_{II}} \right) + \frac{1}{2} \tan^{-1} H_{II} \quad (24)$$

where

$$h_{\infty} = \left( \frac{b_2^{\frac{1}{2}} k_2' a}{3} \right)^{\frac{1}{2}} \dot{x}_0^{\frac{1}{4}} \quad (25)$$

Using equation (22) it is possible to plot all three cases on the  $X-H$  graph; bearing in mind that Case II is only exact for the case of  $\dot{x}_0 = \text{constant}$ . The other cases have no such restriction. These results are shown in Figure 1. From these it is seen that for Case II, essentially 97% of the steady-state fluid-zone is built up within the time the penetrator has traversed one-half the distance of that

## PENETRATION BY HYPERVELOCITY PARTICLES

zone. This is much faster than for Cases I and III. Thus, with the exception of the transient effects that occur in the short time of this build-up, it is reasonable to base further analysis on the quasi steady-state condition:

$$h = h_{\infty} \quad (26)$$

To understand the reason for this rapid build-up we need only examine equations (16) to (18) inclusive, in the region of  $h \sim 0$ ; i.e., at the start of the process. Since  $\dot{x} \leq \dot{x}_0$  at that time we see that

$$\dot{h} \propto \frac{\dot{x}^n}{h^m} \quad (27)$$

where

$$\text{Case I} \quad n = 1, \quad m = 2$$

$$\text{Case II} \quad n = 2, \quad m = 4$$

$$\text{Case III} \quad n = 1, \quad m = 1$$

Thus, initially the rate of film build-up is infinite and remains quite high until  $h \rightarrow h_{\infty}$ . Further, at any specified  $x$  this initial rate of build-up is highest for Case II, second for Case I and least for Case III; because of the exponent  $m$ .

The quasi steady-state solution is adequate if  $\dot{x}$  does not fall off too rapidly, compared to the build-up rate. However, it must be carefully understood that this does not imply that the initial build-up stage can not be important; it only implies that its consideration adds additional mathematical complexities. For the purpose of understanding the qualitative behavior of the penetration process, this transient behavior is not essential to the present paper and will be neglected. The main effect of this transient build-up will be to increase the shear forces during the time interval associated with the decreased zone thickness. This will increase the force tending to retard the forward motion of the penetrator during this time interval. Hence, the results of this paper would be modified by an additional velocity decrease during the time of fluid-zone build-up. The magnitude of this decrease and conditions for its neglect or inclusion to the present work is a subject of a later paper.

### III - Penetrator Motion

#### A - Discussion

In the following work we will investigate only those cases in which the fluid-zone build-up is rapid compared to the velocity decay in the same interval. More precisely, in this paper we will consider, in detail, cases where  $X_{tot} \gg 1$  and  $\Delta \dot{x} \ll \dot{x}_0$  over the region  $0 \leq x \leq 1$ . This is shown in Figure 2.

# PENETRATION BY HYPERVELOCITY PARTICLES

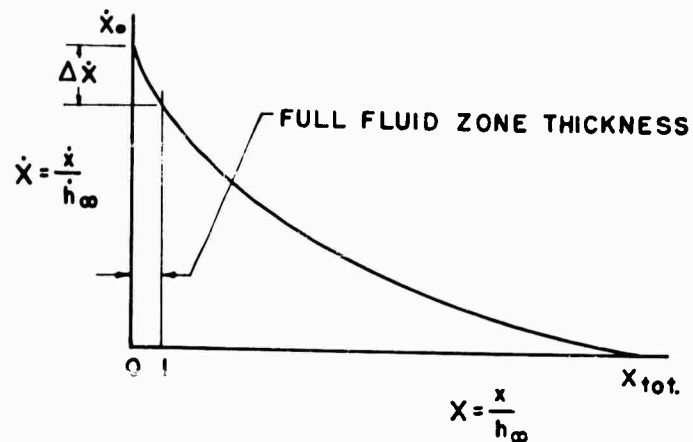


FIG. 2

Associated with this requirement we have the corollary, that for the significant part of the penetration,  $H = 1$ ; independent of  $X$ . In Figure 3 we represent the actual and ideal  $H$ - $X$  relationships.

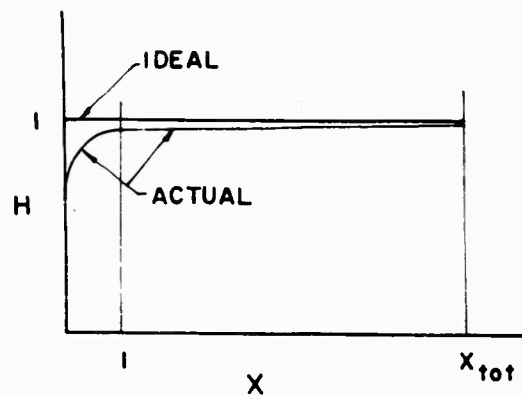


FIG. 3

Further, even though  $H = 1$  throughout the penetration process,  $h$  need not be constant because of the variation in  $h_\infty$ .

In particular, Cases I and III have  $h_\infty$  defined in conjunction with equations (19) and (20), Case II has an  $h_\infty$  which is generalized from equation (25) to become

$$h_{II\infty} = \left( \frac{b_2^{\frac{1}{2}} k_2 a}{3} \right)^{\frac{1}{2}} \dot{x}^{\frac{1}{4}} \quad (28)$$

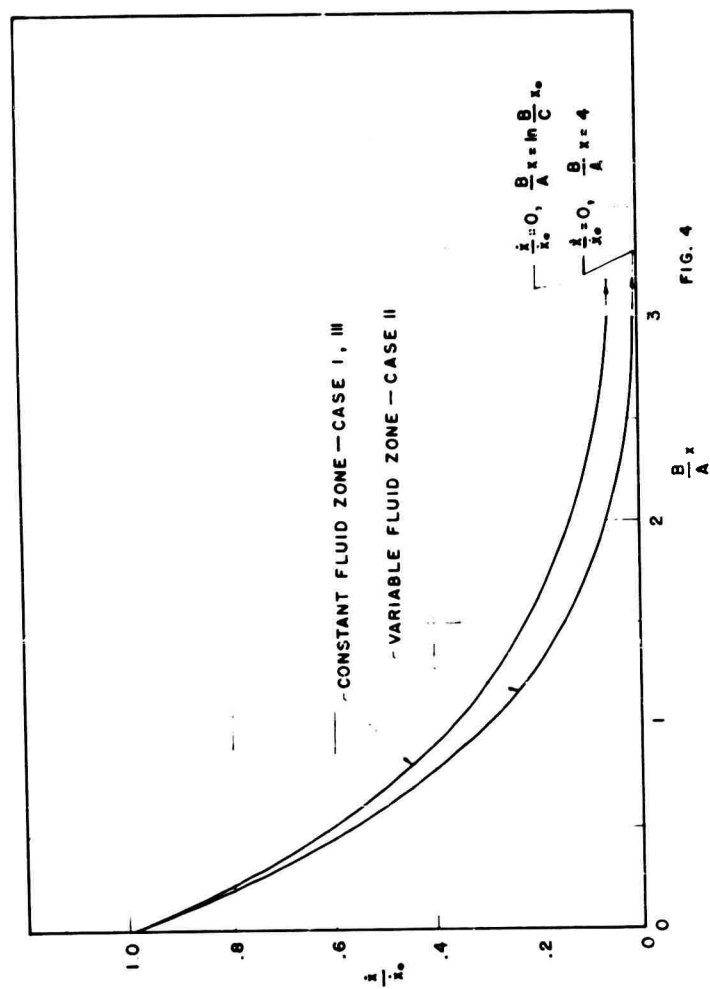


FIG. 4

# PENETRATION BY HYPERVELOCITY PARTICLES

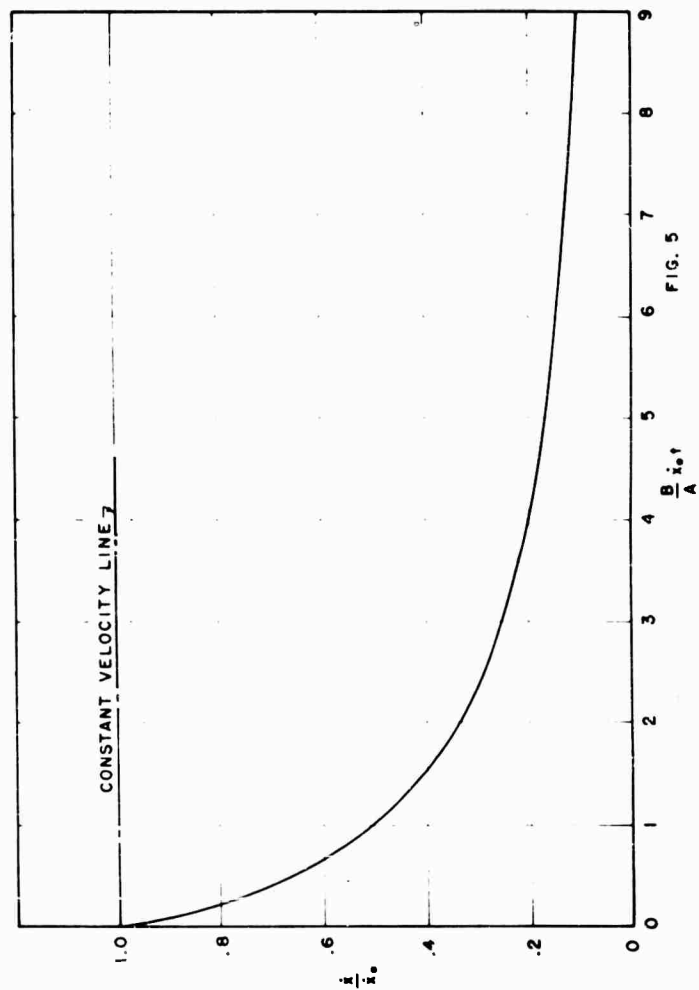
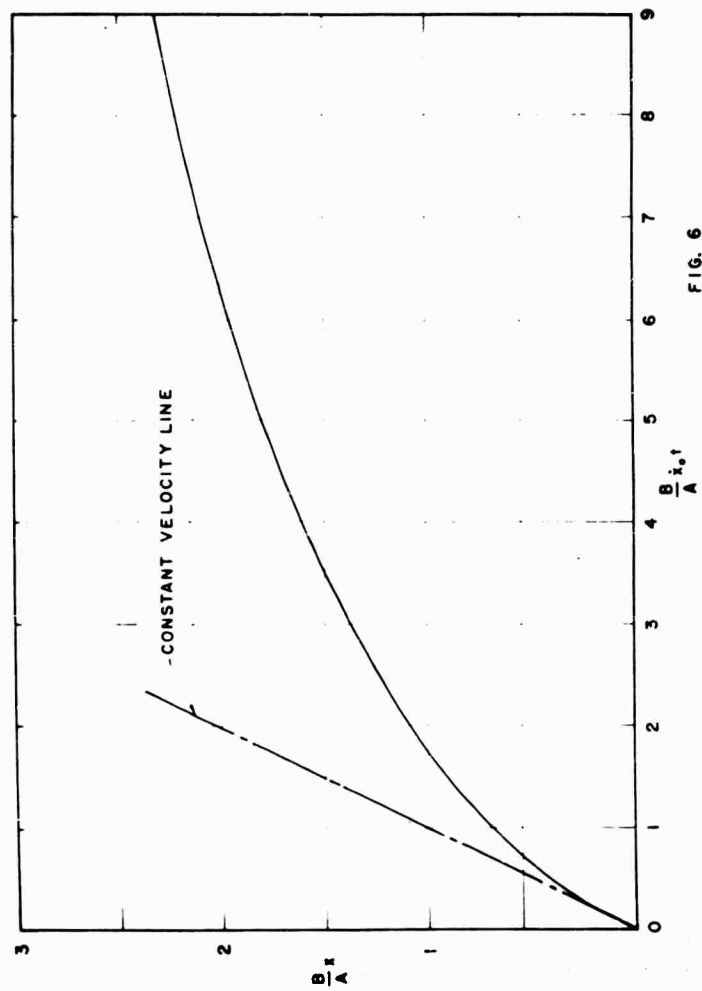


FIG. 5

# PENETRATION BY HYPERVELOCITY PARTICLES



# PENETRATION BY HYPERVELOCITY PARTICLES

Because of its increased mathematical complexity we will treat Case II in detail only for the case of

$$\beta \frac{M_f}{M_p} \left( \frac{a}{h} \right)^2 \gg 8 \quad (29)$$

which appears reasonable for a wide class of penetrators.

As an alternate approach, it can be noted that since  $h_{\pi\infty}$  varies quite slowly with changes in  $\dot{x}$ , that it is quite reasonable to consider  $h_{\pi\infty}$  constant over a range of  $\dot{x}$  and then, to simply integrate the equation of motion over that region. The motion of the penetration being found by suitably combining several such adjacent regions, matching end points.

## B - Constant Fluid-zone Thickness (h)

For constant  $h$ , equation (15) can be written as

$$A\ddot{x} + B\dot{x}^2 + C\dot{x} = 0 \quad (30)$$

where

$$\left. \begin{aligned} A &= \frac{M_p}{M_f} + \frac{\beta}{8} \left( \frac{a}{h} \right)^2 \\ B &= \frac{3}{16} \beta \left( \frac{a}{h} \right)^2 \frac{1}{h} \\ C &= \beta \frac{k_2}{8h^2\rho} \left( \frac{a}{h} \right)^2 \end{aligned} \right\} \quad (31)$$

which can be integrated in terms of "t" to yield

$$\frac{\dot{x}}{\dot{x}_0} = \left[ \frac{1}{1 + \left( \frac{B\dot{x}_0}{C} \right) \left( 1 - e^{-\frac{C}{A}t} \right)} \right] e^{-\frac{C}{A}t} \quad (32)$$

which for very small  $\frac{C}{A}t$  can be represented as

$$\frac{\dot{x}}{\dot{x}_0} \approx \frac{1}{1 + \frac{B}{A} \dot{x}_0 t} \quad (33)$$

or in terms of "x"

$$\frac{\dot{x}}{\dot{x}_0} = \frac{1}{\frac{B\dot{x}_0}{C}} \left[ \left( 1 + \frac{B\dot{x}_0}{C} \right) e^{-\frac{Bx}{A}} - 1 \right] \quad (34)$$

# PENETRATION BY HYPERVELOCITY PARTICLES

which for

$$\frac{B\dot{x}_0}{C} \gg 1$$

and

$$\frac{Bx}{A} \neq \theta(0)$$

becomes

$$\frac{\dot{x}}{\dot{x}_0} \sim e^{-\frac{Bx}{A}} \quad (35)$$

or

$$\frac{Bx}{A} \sim \ln \frac{\dot{x}_0}{\dot{x}} \quad (36)$$

for all

$$\frac{\dot{x}}{\dot{x}_0} \gg \frac{1}{\frac{B\dot{x}_0}{C}}$$

Further

$$\frac{x_B}{A} = \ln \left[ 1 + \frac{B\dot{x}_0}{C} (1 - e^{-C/A t}) \right] \quad (37)$$

or

$$\frac{x_B}{A} = \ln \left[ 1 + \frac{B}{A} \dot{x}_0 t \right] \quad (38)$$

for

$$\frac{C}{A} t \ll 1$$

Equation (34) can be used to estimate the maximum depth that the penetrator can reach. At this maximum

$$x = x_{\max}$$

$$\dot{x} = \dot{x}_{\min}$$

Introducing these conditions into equation (34) we obtain the penetration associated with the cut-off velocity:

$$\frac{B}{A} x_{\max} = \ln \frac{1 + \frac{B\dot{x}_0}{C}}{1 + \left(\frac{B\dot{x}_0}{C}\right) \left(\frac{\dot{x}_{\min}}{\dot{x}_0}\right)} \quad (39)$$

which reduces to equation (36) with the substitution of  $\dot{x}_{\min}$  for  $\dot{x}$ , under the condition:

$$\frac{B\dot{x}_0}{A} \frac{\dot{x}_{\min}}{\dot{x}_0} \gg 1$$

# PENETRATION BY HYPERVELOCITY PARTICLES

and to

$$\frac{B}{A} x_{\max} \approx \ln \frac{B}{C} \dot{x}_0 \quad (40)$$

when

$$\frac{B}{A} \dot{x}_0 \frac{\dot{x}_{\min}}{\dot{x}_0} \ll 1$$

This leads to the solution for maximum depth of penetration, or a useful relationship to aid the experimental evaluation of the parameters A, B, and C.

## C - Variable Fluid-zone Thickness (h) - Case II

We will limit our Case II considerations to small fluid-zone thickness; in addition we will only examine those cases for which inequality (29) is satisfied. This, in essence, does not allow the condition of  $\rho \rightarrow 0$  which is generally not useful. In this case equation (15) can be reduced to

$$\ddot{x} + \frac{3}{2} \frac{\dot{x}^2}{h} + \frac{k_2}{h^2 \rho} \dot{x} = 0 \quad (41)$$

Introducing  $h$  as defined in equation (28) we have

$$\ddot{x} + \frac{3}{2} D \dot{x}^{7/4} + \frac{k_2}{\rho} D^2 \dot{x}^{1/2} = 0 \quad (42)$$

where

$$D = \left( \frac{3}{b_2 k_2' a} \right)^{1/2} = \frac{\dot{x}_0^{1/4}}{h_\infty} \quad (43)$$

Equation (42) can be solved to yield

$$x = \int_{\dot{x}}^{\dot{x}_0} \frac{d\dot{x}}{\frac{3}{2} D \dot{x}^{3/4} + \frac{k_2}{\rho} D^2 \dot{x}^{-1/2}} \quad (44)$$

The integration of equation (44) can be performed in full generality by analytical or experimental means. However, because of the order-of-magnitude of the parameters for the actual class of problems under consideration the integrand will simplify. It will be shown later that

$$\frac{k_2}{\rho} D^2 \dot{x}^{-1/2} \ll \frac{3}{2} D \dot{x}^{3/4}$$

for the range of interest. Hence for this case

$$x = \frac{8\dot{x}_0^{1/4}}{3D} \left[ 1 - \left( \frac{\dot{x}}{\dot{x}_0} \right)^{1/4} \right] \quad (45)$$

or from equation (43)

$$x = \frac{4}{\frac{3}{2a} \left( \frac{a}{h} \right)} \left[ 1 - \left( \frac{\dot{x}}{\dot{x}_0} \right)^{1/4} \right] \quad (46)$$

Considering a thin film and using equation (64), which defines B/A for this case, we have

$$\frac{B}{A} x = 4 \left[ 1 - \left( \frac{\dot{x}}{\dot{x}_0} \right)^{1/4} \right] \quad (47)$$

Now we can compare this thin, but variable, fluid-zone solution with that for the non-variable fluid-zone; as given in equation (36). A plot of these two solutions, which are more fully discussed in a later section is presented in Figure 4. From this plot we can see that both solutions are sufficiently close, so that within the framework of the existing theory the additional refinement given by Case II is probably unwarranted where the fluid-zone is thin. Additionally, it is reasonable to expect that the variable fluid-zone velocity drop is greater than the constant (for the same initial fluid-zone thickness). This follows from equation (28) which shows a fluid-zone decrease in thickness with decrease in velocity. Hence, shear effects will be greater than those associated with the constant "h" case, and the velocity will drop off faster.

#### D - Evaluation of Parameters - Order-of-Magnitude

It is useful to estimate the magnitude of the various ratios so that  $\dot{x} - t$ , and  $x - t$  can be plotted over a reasonable range of values. It is important to note that these are estimates only; the exact values of the various physical constants being subject to experimental and/or more detailed analytical determination.

##### 1. Estimate of $k_2$ , h

For estimating purposes, we will assume parabolic flow for which,

$$\tau_u = \mu \frac{6\dot{u}_0}{h} \quad (48)$$

where  $\mu$  is the viscosity.

# PENETRATION BY HYPERVELOCITY PARTICLES

Comparing equations (3) and letting  $k_1 \neq 0$ , we have

$$k_2 = \theta(6\mu) \quad (49)$$

where  $\theta$  signifies "order of".

Considering that the absolute minimum  $T_u$  is the ultimate shear stress of the material, at the raised temperature, we have

$$T_u \geq T_{ult.} \quad (50)$$

Combining equations (9) and (48) and inequality (50) we have

$$h^2 \leq \frac{3\mu \dot{\gamma}}{T_{ult.}} \quad (51)$$

We should note that actually  $h = f(r)$ , since  $\dot{\gamma}_a \sim 0$  at  $r = 0$ , we expect  $h \sim 0$  there; increasing with increasing  $r$ . However, this variation in  $h$  was neglected in the original detailed equation derivation, so it will not be considered here. Instead we will consider an average  $\bar{h}$  in the sense defined in equation (7) or (8). Thus

$$\begin{aligned} \text{or} \quad \frac{a^2 \bar{h}}{2} &\leq \int_0^a \left( \frac{3\mu \dot{\gamma}}{T_{ult.}} \right)^{1/2} r^{3/2} dr \\ \bar{h} &\leq \frac{\bar{h}_{app.}}{a} \end{aligned} \quad (52)$$

where

$$\frac{\bar{h}_{app.}}{a} = \frac{4}{5} \left( \frac{3\mu \dot{\gamma}_0}{a T_{ult.}} \right)^{1/2} \quad (53)$$

## 2. Estimate of B/C

From equation (31) and (49)

$$\frac{B}{C} = \frac{a\rho}{4\mu} \left( \frac{\bar{h}}{a} \right) \quad (54)$$

# PENETRATION BY HYPERVELOCITY PARTICLES

Introducing inequality (52)

$$\frac{B}{C} \leq \frac{\sigma \rho}{4\mu} \left( \frac{\bar{h}_{app}}{a} \right) \quad (55)$$

## 3. Estimate of C/A

From equation (31) the relationship C/A is

$$\frac{C}{A} = \frac{\beta \frac{k_2}{8h^2 \rho} \left( \frac{a}{h} \right)^2}{\frac{M_p}{M_f} + \frac{\beta}{8} \left( \frac{a}{h} \right)^2} \quad (56)$$

Now we should note that

$$\frac{M_p}{M_f} = \left( \frac{\rho_p}{\rho_f} \right) \left( \frac{l}{h} \right) \quad (57)$$

where  $l$  is the "length of" the penetrator.

Thus

$$\frac{C}{A} = \frac{\frac{k_2}{\rho a^2}}{\left( \frac{\bar{h}}{a} \right)^2 \left[ 1 + \frac{8}{\beta} \frac{\rho_p}{\rho_f} \left( \frac{l}{a} \right) \left( \frac{\bar{h}}{a} \right) \right]} \quad (58)$$

Introducing inequality (52) we obtain

$$\frac{C}{A} \geq \frac{\frac{k_2}{\rho a^2}}{\left( \frac{\bar{h}_{app}}{a} \right)^2 \left[ 1 + \frac{8}{\beta} \frac{\rho_p}{\rho_f} \left( \frac{l}{a} \right) \left( \frac{\bar{h}_{app}}{a} \right) \right]} \quad (59)$$

For the "thin" fluid-zone, defined by

$$\frac{\bar{h}}{a} << \frac{\beta}{8} \frac{\rho_f}{\rho_p} \frac{a}{l} \quad (60)$$

C/A can be simply represented as

$$\frac{C}{A} = \frac{6\mu}{\rho a^2} \left( \frac{a}{h} \right)^2 \quad (61)$$

or

$$\frac{C}{A} \geq \frac{6\mu}{\rho a^2} \left( \frac{a}{\bar{h}_{app}} \right)^2 \quad (62)$$

## PENETRATION BY HYPERVELOCITY PARTICLES

### 4. Estimate of B/A

From equation (31)

$$\frac{B}{A} = \frac{\frac{3}{2a}}{\left(\frac{\bar{h}}{a}\right) \left[ 1 + \frac{8}{\beta} \frac{\rho_p}{\rho} \left(\frac{\bar{h}}{a}\right) \left(\frac{l}{a}\right) \right]} \quad (63)$$

or

$$\frac{B}{A} \geq \frac{\frac{3}{2a}}{\left(\frac{\bar{h}_{app.}}{a}\right) \left[ 1 + \frac{8}{\beta} \frac{\rho_p}{\rho_f} \left(\frac{\bar{h}_{app.}}{a}\right) \left(\frac{l}{a}\right) \right]} \quad (64)$$

For the "thin" fluid-zone defined by equation (60)

$$\frac{B}{A} = \left(\frac{3}{2a}\right) \left(\frac{a}{\bar{h}}\right) \quad (65)$$

or

$$\frac{B}{A} \geq \left(\frac{3}{2a}\right) \left(\frac{a}{\bar{h}_{app.}}\right) \quad (66)$$

### 5. Note on evaluation of parameters

In the following evaluation we will make assumptions on  $\bar{h}/a$  on the basis of reasonable upper and lower bounds. This way we can set an expected range for penetration distance, as a function of velocity or time. As more information becomes available, these limits will be able to be set more closely.

#### E - Numerical Evaluation

Although there is a paucity of information available on the viscosity of metals in the fluid or gaseous state (especially at the associated temperatures and pressures) an order-of-magnitude estimate of the various parameter ratios will be made. These will provide a reasonable range of values over which solutions to the penetration motion can be plotted. In these we have estimated ranges of material and other properties as follows:

$$(3 \times 10^{-3}) (.06 \times 10^{-3}) \frac{\text{slug}}{\text{ft. sec.}} \leq \mu \leq (.06 \times 10^{-3}) \frac{\text{slug}}{\text{ft. sec.}}$$

$$\rho = 15.2 \frac{\text{slug}}{\text{ft.}^2} = \rho_p \quad a = \frac{1}{4} \text{ inch} = .021 \text{ ft.} = l \quad T = ? \quad \beta = 1$$

## PENETRATION BY HYPERVELOCITY PARTICLES

The upper value of  $\mu$  is based on molten iron and the lower on water vapor, at standard conditions. Actually much better values of  $\mu$  must be obtained for an accurate evaluation. In addition, since we have no clearcut evaluation of  $T$  we will take a range of  $h/a$

$$1.0 \geq \frac{h}{a} \geq 10^{-3}$$

The upper limit is taken as that beyond which the unmodified simplified theory apparently ceases to have validity.

Based on this we have a range of

$$.437 \times 10^6 \geq \frac{B}{C} \geq 1.31 \quad (\text{sec./ft.})$$

$$18.2 \times 10^{-6} \leq \frac{C}{A} \leq 54.7 \times 10^3 \quad (1/\text{sec.})$$

$$\text{Constant} - h \quad 8.04 \leq \frac{B}{A} \leq 72.3 \times 10^3 \quad (1/\text{ft.})$$

The motion for the penetration is described by equations (32), (34) and (37). However, since  $\frac{B}{C} \dot{x}_0$  is generally quite large compared to 1, it is necessary to use reduced equations. These are represented by equations (33), (35), (36) and (38) and are obtained by using the consideration that  $\frac{B}{C} \dot{x}_0 \gg 1$  and correspondingly  $\frac{C}{A} t \ll 1$ .

Figures 5 and 6 present the velocity-time and penetration distance-time relationships. These are graphed in a general form so that they apply for the entire range of target-penetrator parameters; subject only to the requirement that  $\frac{B}{C} \dot{x}_0 \gg 1$ , which is satisfied in any real situation.

In the application of these graphs to actual situations, it is important to recall that the fluid flow phenomena is assumed valid only for the higher velocities; so that the process, as described in this and the previous paper<sup>1</sup>, is no longer valid for velocities below the cut-off velocity.

From these figures we see that the percentage drop-off in velocity is greatest during the first instants after impact. This is physically reasonable, since the process is such that high retarding viscous and dynamic forces are associated with the high radial velocities; so that initially the axial retarding forces are great and they drop off rapidly with the decline in velocity.

We should further note that, for the time intervals of interest, the viscosity doesn't appear to enter directly into the problem, since all results are obtained in terms of  $B/A$ . However, it does enter indirectly since the film thickness is, itself, a function of viscosity and  $B/A$  varies almost inversely with this film thickness. Thus, by having experimental or analytical information on film thickness, it might be possible to eliminate the viscosity dependence requirement or else deduce viscosity information.

It is interesting to compare some specific numerical results obtainable from Figures 4 to 6. For this we will take  $\dot{x}_0 = 10^5$  ft/sec and will examine the extremes of parameters presented earlier, together with a mid-range value.

# PENETRATION BY HYPERVELOCITY PARTICLES

$B/A \cdot (\frac{1}{ft.})$	$\frac{B}{A} \dot{x}_0 (\frac{1}{sec.})$	$\dot{x}_{min}/\dot{x}_0 = .1$		$\dot{x}_{min}/\dot{x}_0 = .05$	
		$x_{max.} (in.)$	$t_{max.} (sec.)$	$x_{max.} (in.)$	$t_{max.} (sec.)$
8.04	$8.04 \times 10^8$	3.44	$1.1 \times 10^{-5}$	4.46	$2.3 \times 10^{-5}$
$10^2$	$10^7$	.277	$.9 \times 10^{-5}$	.36	$.19 \times 10^{-5}$
$72.3 \times 10^3$	$72.3 \times 10^8$	$.38 \times 10^{-3}$	$.12 \times 10^{-8}$	$.496 \times 10^{-3}$	$.25 \times 10^{-8}$

Where the above tabulated results were obtained from

$\frac{\dot{x}}{\dot{x}_0}$	$\frac{B}{A} x$	$\frac{B}{A} \dot{x}_0 t$
.1	2.303	9
.05	2.996	19

We should note that it takes just as much time to change the velocity 5000 ft/sec near the end of the travel as it takes to drop it the initial 90,000 ft/sec; which confirms our previous discussions. We see that these results will predict perforation depths anywhere from a  $3.8 \times 10^{-4}$  to 4.5 inches depending on the viscosity and film thickness assumed.

## Variable - h

It was shown earlier (Figure 4) that this case does not differ too greatly from that for constant h; in the former case the integration was straightforward and given by equation (46) when,

$$\frac{3}{2} \dot{x}^{5/4} \gg \frac{k_2}{\rho} D$$

which, using equations (43) and (49) becomes

$$\dot{x} \gg \left( \frac{\dot{x}_0}{\dot{x}} \right)^{1/4} \frac{4\mu}{\rho} \frac{1}{\left( \frac{h_0}{a} \right) a}$$

This imposes the requirement, on the simplified solution, that the penetrator radius must be,

$$a \gg \left( \frac{4\mu}{\rho} \right) \left( \frac{\dot{x}_0}{\dot{x}} \right)^{5/4} \frac{1}{\left( \frac{h}{a} \right) \dot{x}_0}$$

Now let us consider values for  $\mu$ ,  $\rho$ , etc., which make the right hand side of the inequality as large as possible, giving the maximum requirement on "a"; that is

$$\begin{aligned} \mu &= .06 \times 10^{-3} \\ \rho &= 15.2 \\ \dot{x}_0 &= 10^5 \\ \dot{x}_0/\dot{x} &= 10 \\ h/a &= 10^{-3} \end{aligned}$$

## PENETRATIONS BY HYPERVELOCITY PARTICLES

Then we have,

$$a \gg 3.3 \times 10^{-6} \text{ inches}$$

which is always satisfied in the range of interest.

### APPENDIX

#### Fluid-zone build-up

It is useful to consider a more accurate technique for evaluating non-integrable cases, such as Case II. In this approach we allow for a variation in  $\dot{x}$  but treat the velocity component of the growth term ( $\dot{x}^2$ ) as  $\dot{x} \dot{x}_0$ . This makes the growth term, in equation (17), slightly greater than might actually exist for variable  $\dot{x}$ . However, if  $\dot{x}$  does not decrease more than, let us say, 25% during the time the penetrator traverses one fluid-zone, then the use of  $\dot{x} \dot{x}_0$  instead of  $\dot{x}^2$  will initially lead to an exact  $h$ , and will at the most introduce a 25% error in  $\dot{h}$  (at the time of minimum  $\dot{x}$ ). However, because of the use of the correct value of  $\dot{x}$  in the other term of the same expression, this error should be reduced. Finally since

$$h = \int \dot{h} dt \quad (A-1)$$

and  $h_{\text{approximate}}$  departs gradually from the  $\dot{h}_{\text{actual}}$  over the range of interest, we can expect that  $h_{\text{approximate}}$  will deviate from  $h_{\text{actual}}$  by considerably less than the 25%. This estimate on the accuracy of our approximation and the range of usefulness is subject to an "a posteriori" verification in the manner indicated earlier.

Subject to the above considerations, equation (17) reduces to

$$\dot{h} = \dot{x} \left[ b_2 k_2'^2 \frac{a^2 \dot{x}_0}{9h^4} - 1 \right] \quad (A-2)$$

which can be integrated to yield

$$x = -H_{\infty} + \frac{1}{4} \ln \left( \frac{1+H_{\infty}}{1-H_{\infty}} \right) + \frac{1}{2} \tan^{-1} H_{\infty} \quad (A-3)$$

where  $h_{\infty}$  is defined in equation (25).

This result is identical to that previously indicated on Figure 1, so that the previously mentioned technique based on the use of a constant velocity penetrator, is less restricted than would appear. Further, in other cases that we might investigate in later work, both techniques will be of value.

## PENETRATION BY HYPERVELOCITY PARTICLES

### ACKNOWLEDGMENTS

I wish to acknowledge the helpful discussions concerning this work with Messrs. Bill Fleischer and Jim Kymer and the additional moral and financial support of these scientists and of the Hyperdynamics Section and Physics laboratories at Frankford, all of which made this work possible.

### REFERENCES

1. Zaid, M. , An Analytical Approach to Hypervelocity Impact Mechanics: Proceedings 4th Symposium of Hypervelocity Impact, Eglin Air Force Base, April 1960.
2. Opik, Ernest, J. , Physics of Meteor Flight in the Atmosphere: Interscience Tracts on Physics and Astronomy No. 6.

## A MODEL OF NON-EXPLOSIVE IMPACT

J. F. Schipper

Avco Corporation  
Wilmington, Massachusetts

The model of impacting to be constructed here consists, essentially of a sequence of time regimes, not always nonoverlapping. The target is assumed semi-infinite in extent, with a flat face presented to the oncoming projectile. The projectile itself is assumed to be traveling normal to this face. The effect of the shock accompanying the projectile in its flight (before impact) is neglected here as it appears that this effect is likely to be infinitesimal as far as useful energy transfer is concerned.

The first time regime  $0 \leq t \leq T_1$ , begins at the moment the projectile first encounters the target. At  $t = 0$ , both target and projectile begin to deform, according to the relation between their respective densities and compressibility factors. If the impact velocity were subsonic (i. e., less than the longitudinal velocity of sound in one or the other or both of the materials of which the projectile and the target are composed), then the shock waves generated would immediately begin to move away from the "advancing front" of impact in said material and will travel through this material; as a tension wave in both the projectile and the target. If the impact velocity is greater than or equal to the longitudinal sound speed in either material, the shock waves will not begin to move away from this "advancing front" until the velocity of this front relative to some point fixed in said material has become subsonic. The deceleration experienced by this front is due to the increasing resistance to deformation offered by the two bodies; and the energy lost by the projectile is partly absorbed in overcoming this resistance, the remainder being transferred into heat, which then diffuses through the two bodies and/or is dissipated into the surrounding atmosphere.

In this latter case, the second time regime is taken to begin at the instant  $T_1$  at which the velocity of the advancing front has just become sonic in the projectile. In the case where the impact velocity is already subsonic relative to this material,  $T_1$  is taken to be zero. Within this time regime, two processes are of interest. The first is the motion of the (tension) shock waves back through the projectile, their reflection from the back boundary, and their subsequent return to the front of the projectile. The second is the heating of the region surrounding surface of contact of the two bodies, due to the loss of kinetic energy of the projectile, which ultimately can lead to melting.

The third regime, (and also the fourth) is taken to begin at the time  $T_2$  at which the temperature in at least one local domain is "just sufficient" for melting

## A MODEL OF NON-EXPLOSIVE IMPACT

to begin locally. It is possible that within this time regime, the shock waves reflected from the rear boundary of the projectile will return, adding to the complexity of the reaction. However, it is expected that the disturbance caused by these reflected waves will be very small (see the assumption on damping of the waves in the treatment of regime 2), so that these residual effects may be neglected in this first treatment. Because of the high pressure present, this melted material will be extruded, flowing along the small space between the boundaries of the respective unmelted parts of the bodies and up the sides of the crater produced. This flow will act to conduct more heat along this boundary, causing additional melting to occur there. A certain amount of heat will also be generated by the friction caused by the viscous behavior of this melted mass. The material will cool rapidly as it approaches the end of this boundary, and so will solidify (partly) along this boundary.

### THE CASE OF NO EXPLOSION

#### First Time Regime

Within this regime, only the mechanics of the compression suffered by each of the two bodies is of interest. Only a cylindrical bar, of infinitesimal physical extent normal to the cylindrical axis is considered. If a one-dimensional coordinate system(s) is introduced such that  $s = 0$  defines the face of the target initially and (such that)  $s \geq 0$  defines the domain of the target material, and if it is assumed that the resulting compressed area in each bar is homogeneously compressed and thus sharply defined, then the following picture presents itself:

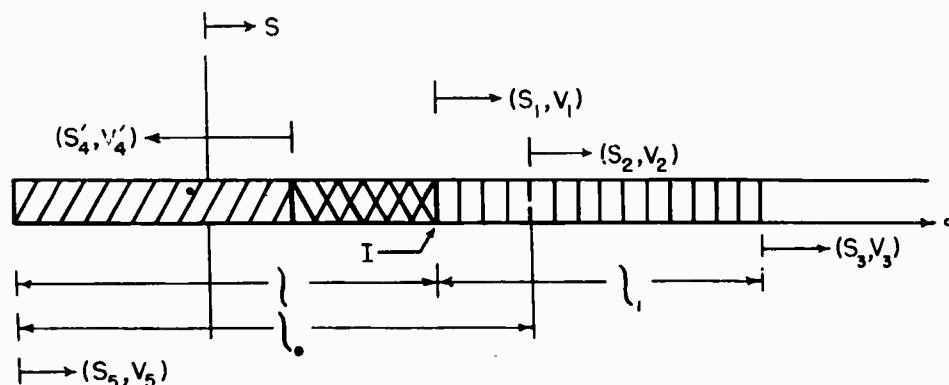


FIGURE 1

The notation  $(s'_4, v'_4)_P$  is to be interpreted as follows:  $(-s'_4)$  is the physical extent of the compressed region of the target material here, and  $(-v'_4)$  is its time-rate-of-growth, of this region, both taken relative to the target-projectile interface (defined by  $s' = 0$  and/or  $s = s_1$ , and denoted by  $I$  in Figure 1). Similarly, the region defined by  $s_1 \leq s \leq s_3$  is the compressed region with the bar of target material. The "point"  $s = s_2$  denotes where the target-projectile interface would be if only the target suffered compression. The following quantities will be of interest:

# A MODEL OF NON-EXPLOSIVE IMPACT

Initial length of projectile:  $l_0$   
 Foreshortening of projectile:  $l_0 - l = \Delta s$   
 Rate-of-growth of compressed area within projectile relative to interface (I):  $-v'_4$   
 Foreshortening of target:  $s_1$   
 Rate-of-growth of compressed area within target relative to I:  $v_3 - v_1$   
 Rate-of-progression of compression front within target:  $v_3$   
 $v_5 = v_2 = v_0$  = initial impact velocity  
 $s_2 = s_5 + l_0$   
 $s_3 = s_5 + l + l_1$   
 $s_1 = s_5 + l$

The forces exerted across the interface (I) by the projectile and target upon each other may be expected to determine the time-rate-of-change of  $v_1 = \dot{s}_1$  to a large extent, though not completely since dissipation effects (of energy) due to heating and crystal irregularities will also contribute. Let  $F_1$  and  $F_2$  denote the deformation forces exerted across I by the projectile and target, respectively, upon each other. Then, for example,  $F_1$  represents the magnitude of the gradient of the potential function of the projectile material which arises due to a compression (here, assumed homogeneous) of part of the projectile. That portion of initial energy of the projectile, which will go into a deformation of the lattices of the two materials at any time after impact but before appreciable "melting" takes place, may be expected to be divided equally between  $F_1$  and  $F_2$ ; i. e.,  $F_1 = F_2$ .

In order to simplify the following description, it will be assumed that each of the crystal lattices considered here has cubic structure, with the direction of the rows of the lattice assumed normal to the (original) face of the target. The necessary modifications to other structures should be clear from the following treatment. The row-direction above then coincides with that of the  $s$ - and  $s'$ -axes in Figure 1. Choosing any one of these rows, assign the number 1 to the first molecule in that row, the number 2 for the next, and so on (for increasing  $s$ , from  $s = 0$ ). Considering any two distinct molecules (i) and (j) in the same row, let  $R_{ij}$  denote the distance between them. It will now be assumed that the potential associated with the  $i$ th molecule in any row may be written as

$$V_i = \sum_{j \neq i} V(R_{ij}),$$

where the "effective potential"  $V(R_{ij})$  depends only on the magnitude of the argument  $R_{ij}$ . It is thus assumed that the potential associated with any molecule in the lattice may be found by considering only the effective contributions to this quantity arising from the other molecules in the same row; the effects of molecules from other rows being assumed to be accounted for indirectly by the "effective potentials"  $V(R_{ij})$ .

Kittel<sup>1</sup> suggests that the potential in a crystal arising from the interaction of particles located at positions  $\underline{r}_i$  and  $\underline{r}_j$  within the lattice ( $\underline{r}_i \neq \underline{r}_j$ ) may be given by

<sup>1</sup>Kittel, Introduction to Solid State Physics.

# A MODEL OF NON-EXPLOSIVE IMPACT

$$\tilde{V}(|\underline{r}_i - \underline{r}_j|) = \frac{e^2}{|\underline{r}_i - \underline{r}_j|} + \frac{\lambda}{|\underline{r}_i - \underline{r}_j|^n}$$

in this case, the effective potentials alluded to above might take the form

$$V(R_{ij}) = \frac{A}{R_{ij}} + \frac{B}{(R_{ij})^n}, \quad (1)$$

where the empirical constants  $A$  and  $B$  are chosen so as to account for the contributions of other rows of molecules without the necessity of considering them explicitly.

The picture of the compression of part of the target (and, similarly, the projectile) is the following. Choosing any row of molecules of the lattice normal to the face of the target, it is assumed that the energy absorbed by this row in the process of being compressed at any time  $t_1$  is utilized by changing the equilibrium distance  $R_0$  between nearest neighbors in the row to some value  $R_1 < R_0$  for the first  $N = N(t_1)$  of these molecule-pairs in the row; all other distances between succeeding molecule-pairs remaining unchanged.

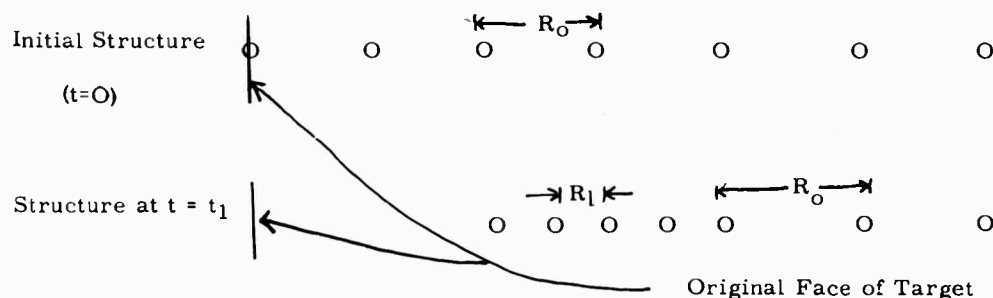


Figure 2

It may be objected here that, in reality no such homogeneous compression can occur and the change in the succeeding-neighbor distance  $\Delta R = R_0 - R_1$  may be expected to be spread out or dispersed over a range, rather than being uniformly distributed over this range. Perusal of the metallurgical photos of impacted material in Reference 2, pages 9 and 15, appears to vindicate the above assumption: These photos show a very close packing in the region immediately adjacent to the craters produced, which packing falls off very rapidly to normal packing on moving into the target material and away from the crater. The assumption of homogeneity is essentially equivalent to the assumption of a retarded potential action; that is, the assumption that the potential function between nearest neighbors does not change until the distance between them has changed by some amount  $\Delta R$  greater than a threshold value. In a sense, this is an assumption of the quantization of potential energy in a lattice (this might be an interesting conjecture to investigate in its own right, but the time and place is not here).

<sup>2</sup> Maiden, Charest and Tardif, An investigation of spalling and crater formation by hypervelocity projectiles: 4th Hypervelocity Impact Symposium, April 1960, Eglin Air Force Base, Florida.

## A MODEL OF NON-EXPLOSIVE IMPACT

In anticipation of a second objection, that of the resistance of motion of one row which is offered by adjacent rows; it should be observed that all rows will be being moved in a similar manner; so that the resulting resistance offered by this mechanism will be but a fraction of its value in the case where only one row undergoes any motion. To be sure, this resistance does not vanish completely except, perhaps, in the special case where the projectile also presents a flat face to the target -- e. g., a right cylindrical projectile. Only in this case can the rows be expected to move in unison.

The cumulative energy of impact available for transfer to the two crystal lattices at any time  $t$  from the "bar" of projectile material as in Figure 1 is taken to be the kinetic energy of the whole bar less that of the uncompressed region of this bar. If  $\rho_1, \rho_2$  denote the density/unit length (measured parallel to the  $s$ -axis) of the projectile and target materials, respectively, then this energy is

$$E = \frac{1}{2} \rho_1 (s_2 - s_1 + s'_4) v_o^2 \quad (2)$$

Only a fraction of this energy,  $\eta E$ , is actually consumed in compressing the two materials, the remainder going into heating the respective areas of the crystal lattices adjacent to the interface.

At this same time  $t$ , then, the respective crystal lattices have each absorbed an amount of energy  $1/2 \eta E$  (cumulatively) due to compression. Then according to Figure 1,

$$\begin{aligned} \frac{1}{2} \eta E &= \Delta V_p = \sum_i (V_i^{(p)} - V_{i_o}^{(p)}) \\ &= \Delta V_T = \sum_i (V_i^{(T)} - V_{i_o}^{(T)}) \end{aligned} \quad (3)$$

where

$\Delta V_p$  = change in compression potential function of projectile lattice  
 $\Delta V_T$  = change in compression potential function of target lattice

The change in potential energy associated with any row of either lattice may be found quite simply. Let

$N_1$  = initial lineal density of molecules in projectile lattice  
 $N_2$  = initial lineal density of molecules in target lattice  
 $R'_{10}$  = equilibrium distance between nearest-neighbors in projectile lattice  
 $R''_{10}$  = equilibrium distance between nearest-neighbors in target lattice  
 $R'_1$  = distance between near-neighbors in part of lattice under homogeneous compression in projectile  
 $R''_1$  = distance between near-neighbors in part of lattice under homogeneous compression in target

# A MODEL OF NON-EXPLOSIVE IMPACT

$$r' = \frac{R_1'}{R_0'} = \frac{s'_4}{s_2 - s_1 + s'_4} = \text{const.} \quad (4)$$

$$r'' = \frac{R_1''}{R_0''} = \frac{s_3 - s_1}{s_3} = \text{const.} \quad (5)$$

The numbers  $1 - r'$  and  $1 - r''$  represent the percentage of (homogeneous) compression suffered by parts of the respective lattices. The numbers  $\bar{N}_1 = N_1 / r'$  and  $\bar{N}_2 = N_2 / r''$  will represent the (new) lineal density in the parts of the respective lattices under compression. The numbers  $\bar{N}_1 \times (s_2 - s_1 + s'_4) = M_1(t)$  and  $\bar{N}_2(s_3 - s_1) = M_2(t)$  may then be expected to be integral (or very nearly so), and will represent the number of molecules in a given row of the respective lattices which are within the compressed area at any time  $t$ .

At any time  $t$ , the change in potential associated with the first molecule in some row of the lattice of the projectile material (the molecule at the interface) is

$$\Delta V_{p_1}(t) = \sum_{n=1}^{M_1(t)-1} V(nR_1) + \sum_{n=1}^{N_p-M_1} V((M_1-1)R_1 + nR_0) - \sum_{n=1}^{N_p} V(nR_0) \quad ; \quad (6)$$

that associated with the second molecule in the row exclusive of that contributed by the first molecule is

$$\Delta V_{p_2}(t) = \sum_{n=1}^{M_1(t)-2} V(nR_1) + \sum_{n=1}^{N_p-M_1-1} V((M_1-1)R_1 + nR_0) - \sum_{n=1}^{N_p-1} V(nR_0) \quad ; \quad (7)$$

and so on. Then the total change in potential associated with the row here is

$$\begin{aligned} \Delta V_p(t) &= \sum_{n=1}^{N_p} \Delta V_{p_m}(t) = \sum_{m=1}^{M_1-1} mV((M_1-m)R_1) \\ &+ \sum_{m=1}^{M_1-1} \sum_{n=1}^{N_p-M_1-m+1} V((M_1-m)R_1 + nR_0) - \sum_{m=1}^{N_p} (N_p-m+1)V(mR_0) \end{aligned} \quad (8)$$

The individual  $\Delta V_{p_i}(t)$  are monotone-increasing, and they also may be expected to satisfy

---

\*  $N_p + 1$  is taken to be the total number of particles in the row considered. For the target material,  $N_T = \infty$ .

# A MODEL OF NON-EXPLOSIVE IMPACT

$$\Delta V_{p_i}(t+2\tau) - \Delta V_{p_i}(t+\tau) \geq \Delta V_{p_i}(t+\tau) - \Delta V_{p_i}(t) \quad (i=1,2,\dots)$$

for any  $t$ ,  $\tau \geq 0$ ; since it is to be expected that the change in potential will increase at an increasing rate, due in part to the ever larger coulomb repulsion between any two molecules as the distance between their centers decreases. Thus  $\Delta V(t)$  may be expected to satisfy the relations

P

$$\Delta V_p(t+\tau) \geq \Delta V_p(t)$$

$$\Delta V_p(t+2\tau) - \Delta V_p(t+\tau) \geq \Delta V_p(t+\tau) - \Delta V_p(t) \quad (t; \tau \geq 0).$$

Translated into physical concepts, this indicates that the work done per unit time against the lattice forces in extending the compressed area of the lattice is an increasing function of time. Then, since energy is being supplied to the process at a very nearly constant rate, it may be expected that the rate-of-growth of the compressed area within the lattice of projectile material will be monotone-decreasing in time. Analogous remarks apply to the target material.

Thus, although the rate-of-growth of the compressed area within the projectile is supersonic at first -- initially, it is  $v_0$ , the velocity of impact -- this rate may be expected to decrease to a subsonic level at some later time, allowing the compression shock to move out away from the interface between the compressed and uncompressed areas within the projectile material.

To continue the discussion, attention must be directed toward particular forms of deformation potentials. The forms of the deformation potentials to be studied are

$$V_p(R) = \frac{A_p}{R} + \frac{B_p}{(R)^p} \quad \text{(projectile)} \quad (9)$$

$$V_\tau(R) = \frac{A_\tau}{R} + \frac{B_\tau}{(R)^\tau} \quad \text{(target)} \quad (10)$$

where it is assumed that  $p, \tau > 2$  . \*

The various sums in the relation (8) must be approximated by reasonably tractable expressions, if the analysis is to proceed. The approximation

$$\sum_{n=1}^N \frac{1}{n} \sim \ln(N+8) + \gamma \quad (11)$$

with

# A MODEL OF NON-EXPLOSIVE IMPACT

$$\delta = e^{1-\gamma} - 1 = .478.... ,$$

$$\gamma = \lim_{N \rightarrow \infty} \sum_{n=1}^N \frac{1}{n} - \ln N = .577.... ,$$

(Euler-Mascheroni constant),

is particularly useful, as it has the following properties: The sum is matched precisely for  $N = 1$  and in the limit of large  $N$ . Thus, this approximation may be expected to introduce only a small error at most (for  $N = 10$ , the error in (11) is already zero to three decimals). The approximation

$$\sum_{n=1}^N \frac{1}{n^p} \sim \zeta(p) - \frac{1}{p-1} (N + \epsilon_p)^{-(p-1)} \quad (p > 1), \quad (12)$$

with

$$\zeta(p) = \sum_{n=1}^{\infty} \frac{1}{n^p}$$

and

$$\epsilon_p = \left\{ (p-1) [\zeta(p) - 1] \right\}^{-\frac{1}{p-1}} - 1$$

will also be utilized. This approximation also has the desirable property of matching the corresponding sum precisely for  $N = 1$  and in the limit of large  $N$ . As an example, for  $p = 10$  (a reasonably representative choice),  $\epsilon_p = .688$ . The following approximations will also be used:

$$\sum_{n=1}^N \frac{1}{(n+a)} \sim \ln(N + \delta) + \gamma \quad (\langle a \rangle = 0) \quad (13)$$

$$\sim \ln\left(\frac{N+a+\delta}{a+\delta}\right) \quad (\langle a \rangle \geq 1), \quad (13)$$

$$\sum_{n=1}^N \frac{1}{(n+a)^p} \sim \zeta(p) - \frac{1}{p-1} (N + \epsilon_p)^{-(p-1)} \quad (\langle a \rangle = 0) \quad (14)$$

$$\sim \frac{1}{p-1} \left\{ (a + \epsilon_p)^{-(p-1)} - (N + a + \epsilon_p)^{-(p-1)} \right\} \quad (\langle a \rangle \geq 1), \quad (14)$$

with

$\langle a \rangle$  = integer closest to  $a$ .

# A MODEL OF NON-EXPLOSIVE IMPACT

The (approximate) validity of the approximations (13) and (13') is established in the following way. For  $a = M = \text{an integer} \geq 1$ , the quantity

$$\sum_{n=1}^N \frac{1}{n+a}$$

in (13) may be rewritten as

$$\sum_{n=M+1}^{N+M} \frac{1}{n} \approx \ln \left( \frac{N+M+\delta}{M+\delta} \right)$$

by the approximation adopted in (11). For  $1 \leq M < a < M+1$  ( $M$  integral), the approximation in (13) is then "extended" to non-integral values of  $a$  in the manner indicated in (13'). Analogous remarks hold for the approximations (14) and (14').

These approximations will now be applied to the individual sums in (8). These sums become, for the projectile material,

$$\begin{aligned} \sum_{m=1}^{M_1-1} m V((M_1-m)R_1) &= \sum_{m=1}^{M_1-1} (M_1-m) V(mR_1) \\ &\sim \frac{M_1 A_p}{R_1} \left\{ \ln(M_1 + \delta - 1) + \gamma - \frac{M_1-1}{M_1} \right\} \\ &\quad + \frac{B_p}{(R_1)^p} \left\{ M_1 \left[ \zeta(p) - \frac{(M_1-1+\epsilon_p)^{-(p-1)}}{p-1} \right] \right. \\ &\quad \left. - \left[ \zeta(p-1) - \frac{(M_1-1+\epsilon_{p-1})^{-(p-2)}}{p-2} \right] \right\}, \\ \sum_{m=1}^{M_1-1} \sum_{n=1}^{N_p-M_1-m+1} V((M_1-m)R_1 + nR_0) &= \sum_{m=1}^{M_1-1} \sum_{n=1}^{N_p-m+1} V(mR_1 + nR_0) \\ &= \sum_{m=1}^{M_1-1} \sum_{n=1}^{N_p-m+1} \left\{ \frac{A_p}{R_0(mr+n)} + \frac{B_p}{(R_0)^p (mr+n)^p} \right\} \\ &\sim \sum_{m=1}^{M_1-1} \frac{A_p}{R_0} \ln \left( \frac{N_p + 1 - m + (mr) + \delta}{\delta + mr} \right) \\ &\quad + \sum_{m=1}^{M_1-1} \frac{B_p}{(R_0)^p} \frac{1}{p-1} \left\{ (mr + \epsilon_p)^{-(p-1)} - (N_p + 1 - m + mr + \epsilon_p)^{-(p-1)} \right\} \end{aligned} \tag{15}$$

$$\begin{aligned}
& \sim \frac{A_p}{R_o} \left\{ (M_1 - 1) \ln \left( \frac{1-r}{r} \right) + \frac{N_p + \delta + r}{1-r} \ln \left( \frac{N_p + \delta + r}{1-r} \right) \right. \\
& \quad - \left( \frac{N_p + \delta + 2-r}{1-r} - M_1 \right) \ln \left( \frac{N_p + \delta + 2-r}{1-r} - M_1 \right) - (M_1 - 2) \left. \right\} \\
& \quad + \frac{B_p}{(R_o)^p} \frac{1}{(p-1)(p-2)} \left\{ \frac{1}{r^{p-1}} \left[ \left( \frac{\epsilon_p}{r} + \epsilon_{(p-1)} \right)^{-(p-2)} \right. \right. \\
& \quad - \left( M_1 - 1 + \frac{\epsilon_p}{r} + \epsilon_{(p-1)} \right)^{-(p-2)} \left. \right] - \frac{1}{(1-r)^{p-1}} \left[ \left( \frac{N_p + 1 + \epsilon_p}{1-r} + \epsilon_{(p-1)} \right)^{-(p-2)} \right. \\
& \quad \left. \left. - \left( M_1 - 1 + \epsilon_{(p-1)} + \frac{N_p + 1 + \epsilon_p}{1-r} \right)^{-(p-2)} \right] \right\}, \quad (16)
\end{aligned}$$

$$\begin{aligned}
& - \sum_{m=1}^{N_p} (N_p - m + 1) V(m R_o) = - \sum_{m=1}^{N_p} (N_p + 1) V(m R_o) + \sum_{m=1}^{N_p} m V(m R_o) \\
& \sim \frac{A_p}{R_o} \left\{ -(N_p + 1) \left[ \ln(N_p + \delta) + \gamma - \frac{N_p}{N_p + 1} \right] \right\} \\
& \quad + \frac{B_p}{(R_o)^p} \left\{ -(N_p + 1) \left[ \zeta(p) - \frac{1}{p-1} (N_p + \epsilon_p)^{-(p-1)} \right. \right. \\
& \quad \left. \left. + \zeta_{(p-1)} - \frac{1}{p-2} (N_p + \epsilon_{p-1})^{-(p-2)} \right] \right\}. \quad (17)
\end{aligned}$$

Addition of (15), (16), and (17) yields the quantity  $\Delta V_p(t)$ , which is the (quantized) change in potential energy of one row.

This is to be utilized in the following manner. Assume the previous (quantized) change, in potential has occurred -- so that there are  $M_1 - 1$  molecules from this row within the compressed area. Now the energy/second being supplied by this row due to its impacting upon the target is  $\frac{\eta}{2} \dot{E}_o = \frac{1}{4} \eta m_1 v_o^2 \left( \frac{V_o}{l_o} \right)$  with

$m_1 = \rho_1 \cdot l_o$ . Then the (quantized) change in potential which will bring

another molecule within the compressed area (bringing the total to  $M_1$ ) will occur at a time  $\Delta t = \Delta V / \frac{\eta}{2} \dot{E}_o$  later than the previous event. Theoretically, then,

this allows a determination of  $M_1(t)$ , the number of molecules in the projectile material which are within the compressed area at any time  $t$ . However, as can be seen from (15), (16), (17), an analytic determination of  $M_1(t)$  is quite impossible; and one can only infer the existence of such a function from the classical implicit function theorem. To continue,  $M_1(t)$  is a monotone increasing function of time which assumes only positive integral values; thus the quantity  $\frac{dM_1}{dt}$  has no meaning.

However, if  $t_1, t_2, t_3, \dots$  denote the time values at which the successive (quantized) changes in potential energy occur, with the projectile material row then the quantity

# A MODEL OF NON-EXPLOSIVE IMPACT

$$\dot{M}_1(t_i) = \frac{M(t_i) - M(t_{i-1})}{t_i - t_{i-1}} \quad (18)$$

will serve quite well as the rate-of-change of  $M_1$  at the point  $t_i$ . Then the rate-of-growth of the compressed area within the projectile material row may be taken as

$$\dot{M}_1 R_1 = -V_4' \quad (19)$$

with  $V_4'$  as in Figure 1.

Clearly, analogous remarks apply to the target material, but with one important difference: the target material is assumed semi-infinite in extent, so that  $N_T = \infty$ . This necessitates a restatement of Equations (6), (7), (8), in order to remove the logarithmic singularities encountered there due to the form (10) assumed. The restatement of (6), (7), (8) for the target material is

$$\begin{aligned} \Delta V_{T_1} &= \sum_{n=1}^{M_2-1} \{V(nR'_1) - V(nR'_0)\} \\ &+ \sum_{n=1}^{\infty} \{V((M_2-1)R'_1 + nR'_0) - V((M_2-1+n)R'_0)\}, \end{aligned} \quad (6)$$

$$\begin{aligned} \Delta V_{T_2} &= \sum_{n=1}^{M_2-2} \{V(nR'_1) - V(nR'_0)\} \\ &+ \sum_{n=1}^{\infty} \{V((M_2-2)R'_1 + nR'_0) - V((M_2-2+n)R'_0)\}, \end{aligned} \quad (7)$$

$$\begin{aligned} \Delta V_T &= \sum_{m=1}^{\infty} \Delta V_{T_m} = \sum_{n=1}^{M_2-1} (M_2-n) \{V(nR'_1) - V(nR'_0)\} \\ &+ \sum_{m=1}^{M_2-1} \sum_{n=1}^{\infty} \{V((M_2-m)R'_1 + nR'_0) - V((M_2-m+n)R'_0)\}. \end{aligned} \quad (8)$$

Utilizing the approximations developed above, the two right-hand quantities in (8') can be written, respectively, as

# A MODEL OF NON-EXPLOSIVE IMPACT

$$\sum_{n=1}^{M_2-1} (M_2-n) \{V(nR'_1) - V(nR'_0)\} \sim A_\gamma M_2 \left(\frac{1}{R'_1} - \frac{1}{R'_0}\right) \left\{ \ln(M_2-1+\delta) + \gamma - \frac{M_2-1}{M_2} \right. \\ \left. + B_\gamma \left(\frac{1}{(R'_1)^\gamma} - \frac{1}{(R'_0)^\gamma}\right) \left\{ M_2 \left[ \zeta(\gamma) - \frac{1}{\gamma-1} (M_2-1 + \epsilon_\gamma)^{-(\gamma-1)} \right. \right. \right. \\ \left. \left. - \left[ \zeta(\gamma-1) - \frac{1}{\gamma-2} (M_2-1 + \epsilon_{\gamma-1})^{-(\gamma-2)} \right] \right\} \right\}, \quad (20)$$

$$\sum_{m=1}^{M_2-1} \sum_{n=1}^{\infty} \{V((M_2-m)R'_1 + nR'_0) - V((M_2-m+n)R'_0)\} \\ \sim A_\gamma \left\{ (M_2 + \delta - 1) \left[ \ln(M_2 + \delta - 1) - 1 \right] - (1 + \delta) \left[ \ln(1 + \delta) - 1 \right] \right. \\ \left. - \left( M_2 + \frac{\delta}{r'} - 1 \right) \left[ \ln(M_2 + \frac{\delta}{r'} - 1) \right] + \left( 1 + \frac{\delta}{r'} \right) \left[ \ln\left(1 + \frac{\delta}{r'}\right) - 1 \right] \right. \\ \left. + (M_2-1) \ln\left(\frac{1}{r'}\right) \right\} + \frac{B_\gamma}{(R'_0)^\gamma} \frac{1}{(\gamma-1)(\gamma-2)} \left\{ \frac{1}{(r')}^{\gamma-1} \left[ \left(\frac{\epsilon_\gamma}{r'} + \epsilon_{\gamma-1}\right)^{-(\gamma-2)} \right. \right. \\ \left. \left. - \left( (M_2-1) + \frac{\epsilon_\gamma}{r'} + \epsilon_{\gamma-1} \right)^{-(\gamma-2)} \right] - \left[ (\epsilon_\gamma + \epsilon_{\gamma-1})^{-(\gamma-2)} \right. \right. \\ \left. \left. - \left( (M_2-1) + \epsilon_\gamma + \epsilon_{\gamma-1} \right)^{-(\gamma-2)} \right] \right\} \quad (21)$$

The treatment accorded the target material above has tacitly assumed that there are precisely as many "rows" of molecules in the projectile material as there are "rows" in the target material with which it makes contact. This assumption requires a high degree of similarity between the two lattice structures, and is

## A MODEL OF NON-EXPLOSIVE IMPACT

seldom attainable, except where the target and projectile materials are the same. \* Perhaps the most reasonable and simple method of extending the procedure to situations where  $M$  rows of molecules of the projectile material lattice "coincide" with  $N$  rows of molecules of the target material lattice is to multiply the effective deformation potential of the target material by the factor  $M/N$ .

Attention has thus far been confined to a single "row" of molecules within either lattice. There remains to be considered the effect of the shape of the (frontal part of the) projectile shape. Consider the shape configuration exhibited in Figure 3:

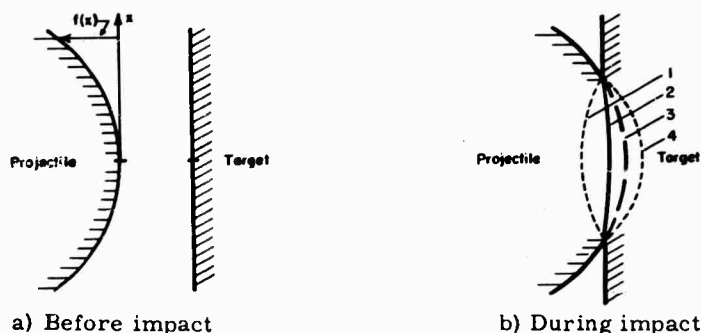


Figure 3

In Figure 3b, curves 1 and 4 represent the lines of demarcation between the normal and compressed areas in the projectile and target materials, respectively; curve 2 the (new) interface between the two materials; and curve 3 the location of the interface if the projectile were to suffer no deformation (i.e., the original projectile "face").

Assume, now that the functions  $M_1(t)$  and  $M_2(t)$  are known for each row of both the material lattices. \*\* Assume a consecutive indexing of the rows of the respective lattices -- denoted by  $(i)$  and  $(j)$  respectively -- with  $i = 0$  ( $j = 0$ ) corresponding to the central row of the projectile lattice (target lattice);  $i > 0$  ( $j > 0$ ) corresponding to the rows lying above this row in Figure 3a; and  $i < 0$  ( $j < 0$ ) corresponding to those rows lying below this row in the figure. Thus  $x_1$  denotes the  $x$ -coordinate of the row in the projectile lattice lying immediately above the "central row", with  $x$ -coordinate  $x_0 = 0$ , and so on. Considering the  $i^{\text{th}}$  row of the projectile lattice, there is a time lag of

$$(\Delta t)_i = f(x_i) v_0. \quad (22)$$

in the impact of this row with some row or rows of the target lattice, relative to the time of impact of the "central row" in each lattice. Suppose, now, that all the row functions  $(M_1(t))_i$  and  $(M_2(t))_j$  have their time origins changed so that they coincide with the time origin of the central row function  $(M_1(t))_0$ . Then, letting

\* Lattice defect effects are ignored here, since the problem is complicated enough without their introduction, and since it appears to be a debatable matter as to their quantitative significance here.

\*\* It is assumed here that the origin of time ( $t = 0$ ) for each row function is taken at the point in time at which that row makes "contact" with a corresponding one in the other lattice.

# A MODEL OF NON-EXPLOSIVE IMPACT

$g(x, t)$ ,  $g_p(x, t)$ , and  $g_r(x, t)$  denote the "amplitudes" (measured parallel to the  $s$ -axis and relative to  $s = 0$  in Fig. 1) of the curves (2), (1), and (4), respectively, in Figure 3b. Then it is easily verified that

$$\begin{aligned} g(x_i, t) &= (R'_0 - R'_1)(M_2(t - \Delta_1 t))_i, \\ g_p(x_i, t) &= g(x_i, t) - R_1(M_1(t - \Delta_1 t))_i, \\ g_r(x_j, t) &= g(x_j, t) + R'_1(M_2(t - \Delta_1 t))_j. \end{aligned} \quad (23)$$

For ease of visualization of these relations, Figure 4 is provided (see Figure 3).

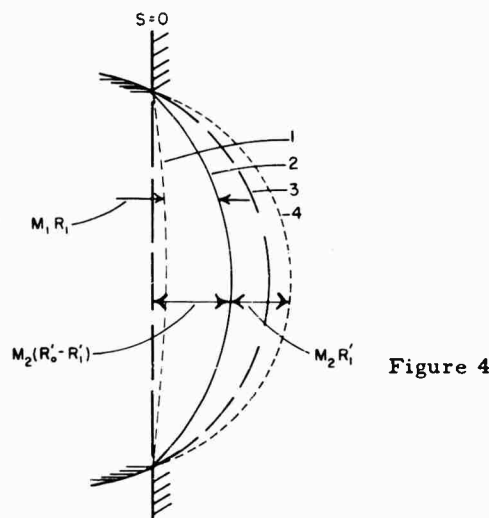


Figure 4

These relations enable one to determine the physical extent of the various regions of interest at any time  $t$ . This brings to a close the treatment of the first regime.

## Second Time Regime

In order to continue the discussion, a specific shape must be chosen for the projectile, in order that the interaction of the advancing and reflected waves may be studied. For purposes of illustration, a right cylinder, of height  $h$  and radius  $a$  with axis parallel to the initial projectile velocity vector  $\underline{V}_0$  will be chosen; though the extension to a more complicated structure (such as a sphere or a cone) will presumably be clear.

The following (Cartesian) coordinate system will be used. The  $x$ -axis will be assumed to coincide with the axis of the cylinder, with positive orientation in the opposite direction to that of the vector  $\underline{V}_0$ . The  $y$ - and  $z$ -coordinate axes are chosen perpendicular to the  $x$ -axis (and to each other) in any consistent manner. The plane  $\{x=0\}$  is assumed to coincide with the undisturbed-homogeneously compressed interface within the projectile at the moment at which the speed of

# A MODEL OF NON-EXPLOSIVE IMPACT

this advancing front becomes subsonic. The time coordinate  $t'$  is measured from this time point as origin (i. e., for  $t' = 0$ ). Only the dilatational or longitudinal disturbance waves will be of interest here; the effect of the transverse or distortional waves are not believed to contribute significantly to the "fracturing."

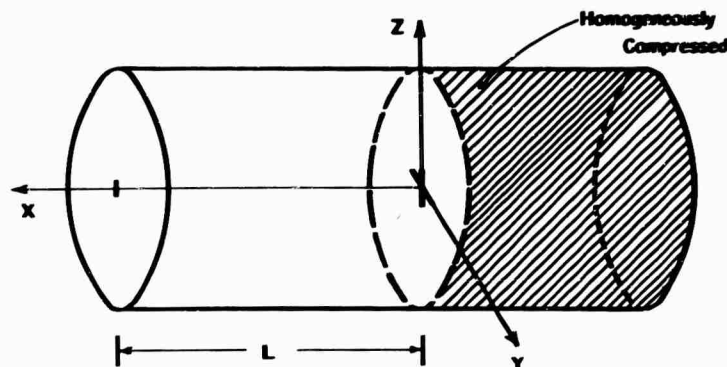


Figure 5

Now, it has been tacitly assumed in the preceding that both materials are at  $0^\circ\text{K}$  initially. The more general situation of non-zero temperature "bath" may be expected to introduce certain changes in the deformation potentials (9) and (10). The most obvious one -- and the one which will be treated here in some detail -- is that of the change of mean inverse distance between two particles due to their vibrations around the respective equilibrium positions.

Let the distance between the equilibrium positions of two particles be  $\bar{R}$ , and suppose the time behavior of each in the direction parallel to their line-of-centers is

$$x_1 = \bar{R} + (\Delta R) \cos \omega t \quad \left( \frac{\Delta R}{\bar{R}} < \frac{1}{2} \right),$$

$$x_2 = (\Delta R) \cos(\omega t + \delta) \quad (\delta \text{ some phase shift})$$

The mean value of the quantity  $(x_1 - x_2)^{-1}$  will then be taken to be

$$\frac{1}{4\pi^2} \int_0^{2\pi} d(\delta) \int_0^{2\pi} \frac{d(\omega t)}{x_1 - x_2} \cdot \equiv \cdot \frac{a}{\bar{R}}. \quad (24)$$

Evaluation of the inner integral yields

$$\begin{aligned} & \int_0^{2\pi} \frac{d(\omega t)}{x_1 - x_2} \\ &= \frac{2}{\bar{R}} \frac{1}{\sqrt{1-b^2}} \left\{ \tan^{-1} \left[ \sqrt{\frac{1+b}{1-b}} \tan\left(\frac{\theta}{2}\right) \right] \right\} \Big|_{\theta=0}^{\theta=\pi} \\ &= \frac{2\pi}{\bar{R}} \frac{1}{\sqrt{1-b^2}}, \end{aligned}$$

# A MODEL OF NON-EXPLOSIVE IMPACT

where

$$b = \frac{2(\Delta R)}{R} \left| \sin\left(\frac{\theta}{2}\right) \right| \quad (0 < \theta < 2\pi)$$

Continuing, there obtains from (24)

$$\frac{a}{R} = \frac{2}{\pi R} F\left(\frac{2(\Delta R)}{R}\right) > \frac{1}{R}, \quad (25)$$

where

$$F(k) = \int_0^{\pi/2} \frac{d\psi}{\sqrt{1-k^2 \sin^2 \psi}} \quad (26)$$

is the complete elliptic integral function of the first kind. The mean inverse distance between two particles which are undergoing vibration is thus greater than the equilibrium inverse distance by a factor

$$\frac{2}{\pi} F\left(\frac{2(\Delta R)}{R}\right) \doteq 1 + \left(\frac{\Delta R}{R}\right)^2 \quad (27)$$

for  $\left(\frac{\Delta R}{R}\right)^2 \ll 1$ . In the situations generally encountered, a reasonable guess would be  $\Delta R/R < 1/5$  so that the approximation in (27) should be good to within two parts in a thousand.

A similar analysis may be made upon the quantity  $(x_1 - x_2)^{-n}$  ( $n > 1$ ), though things are considerably more complicated. However, if it is assumed that, say,  $\Delta R/R < .10$ , then the approximation

$$\frac{\beta}{(\bar{R})^n} \doteq \frac{1}{(x_1 - x_2)^n} \Big|_{\text{Avg.}} \doteq \frac{1}{(\bar{R})^n} \left( \frac{2}{\pi} F\left(\frac{2(\Delta R)}{R}\right) \right)^n \quad (28)$$

may be used within an error of at most about 1 percent. This approximation also has the desirable property that the quantity

$$\tilde{R} = \bar{R} \frac{2}{\pi} F\left(\frac{2(\Delta R)}{R}\right) \quad (29)$$

then becomes the new equilibrium distance. \*

Now the quantity  $F(k)$  defined in (26) is a strictly increasing function of  $k$ , and this will affect the quantities  $R_0$  and  $R_1$  (and, similarly,  $R'_0$  and  $R'_1$ ) introduced in Figure 2 in the following manner. The quantity  $R_0$  will be increased by the factor  $\frac{2}{\pi} F\left(2\frac{\Delta R_0}{R_0}\right)$ , while the quantity  $R_1$  will be increased by the factor  $\frac{2}{\pi} F\left(2\frac{\Delta R_1}{R_1}\right) > \frac{2}{\pi} F\left(2\frac{\Delta R_0}{R_0}\right)$ .

The percentage increase in "packing" distance within the compressed region of the projectile (and also target) material will thus be considerably greater than the corresponding percentage increase in the "undisturbed" region of the material.

Now in the concept of melting of a material (third regime) adopted here,

## A MODEL OF NON-EXPLOSIVE IMPACT

an increase of the equilibrium distance may be taken to be equivalent to lowering the melting temperature of the substance. It is assumed, inter alia, that as the so-called melting temperature of a substance is approached, the corresponding lattice deformation potential becomes "softer" -- less resistant to further deformation. Thus, if the initial temperature of the target material is raised, the projectile material temperature remaining the same, the target material deforms more easily than before and is also closer to the melting temperature of the substance. Both effects may be expected to increase the penetration of the target by the projectile. If, however, the situation is reversed and the initial temperature of the projectile is raised, the effect is not quite what would be expected (at least at first glance). The kinetic energy being converted to deform both objects is still the same; so that although the projectile will deform more easily than before, the deformation of the target will apparently remain unchanged (assuming the empirical factor in (3) is unaffected). However, the local temperature of the lattice of the projectile material is now closer to that required for melting than before, so that the "flow" of projectile material described in regime 4 will begin sooner and take place more readily. However, this will have only a small effect on the cratering of the target produced outside the "shadow" of the projectile on the target -- due to the "boundary layer" assumption in regime 4. The effect will be to increase the cratering slightly. Thus raising the initial temperature of the projectile material may be expected to have at best only a second-order effect on penetration, as compared to the first-order effect produced by increasing the initial temperature of the target material. The increase of initial projectile temperature can be expected to have no effect on the depth of penetration within the target at the center portion of the crater.

Now let  $u, v, w$  be the displacements from equilibrium of any element of the projectile in the region  $x \geq 0$ , measured along the  $x$ -,  $y$ -, and  $z$ -axes respectively. The displacement "waves" may be expected to move with radial symmetry in a plane, parallel to the plane  $\{x=0\}$ , so that the only variation of  $u, v, w$  with position to be expected is that of the  $x$ -dependency: i. e.,

$$u = u(x, t'),$$

$$v = v(x, t') = w = w(x, t')$$

Thus, in the so-called dilation factor <sup>3</sup>

$$\Delta = \frac{\partial u}{\partial x} + \frac{\partial v}{\partial y} + \frac{\partial w}{\partial z}$$

the last two of the three terms are zero; and the defining relation for  $u(x, t)$  in the absence of viscous forces becomes

$$\rho \frac{\partial^2 u}{\partial t'^2} = (\lambda + 2\mu) \frac{\partial^2 u}{\partial x^2}, \quad (30)$$

---

\* That is, the distance for which the static potential of the lattice remains unchanged (preceding page).

<sup>3</sup> The notation and defining equations here are taken from H. Kolsky; Stress Waves in Solids; Oxford Press (1953); pp. 4-15.

# A MODEL OF NON-EXPLOSIVE IMPACT

where  $\rho$  is the density of the medium and  $\lambda$  and  $\mu$  are the well-known Lamé constants (both positive). In the situation here, viscous dissipation will be admitted, so that the defining equation for  $u$  in the model adopted becomes

$$\rho \frac{\partial^2 u}{\partial t'^2} + \nu' \frac{\partial v}{\partial t'} = (\lambda + 2\mu) \frac{\partial^2 u}{\partial x^2}, \quad (30')$$

where  $\nu' > 0$  is an empirical parameter representing the magnitude of viscous dissipation forces.

A velocity  $c = \left[ (\lambda + 2\mu)/\rho \right]^{1/2}$  is associated with the disturbance wave(s) represented by the variation of  $u$ , and it is required that the solution  $u(x, t')$  of (30') satisfy

- 1)  $u(x, t') = 0$  for  $x - ct' > 0$
- 2)  $u$  is continuous everywhere and differentiable a sufficient number of times everywhere except perhaps on the cone  $x - ct' = 0$ .
- 3)  $u$  has a finite discontinuity on this cone.

In Appendix A, it is shown that one such solution

$$u(x, t') = u_0 U(ct' - x) e^{(k + \frac{\nu}{c})(x - ct')} e^{-(k \pm \sqrt{k^2 + (\frac{\nu}{c})^2} + \frac{\nu}{c})x}, \quad (31)$$

$$\text{where } U(s) = 0 \quad s < 0 \\ = 1 \quad s > 0$$

$$\nu = \frac{\nu'}{\rho},$$

$u_0$  is the maximum displacement associated with this wave, and  $k$  is (another) empirical parameter introduced in the solution of (30').

Along the cone  $x - ct' = 0$  (which coincides with the advancing "front" of the disturbance), the envelope of the variation of  $u$  decays as

$$\exp \left[ -\left(k \pm \sqrt{k^2 + \left(\frac{\nu}{c}\right)^2} + \frac{\nu}{c}\right)x \right] \equiv \exp \left[ -dx \right].$$

Referring to Figures 1 and 5, let

$$L = \int_0 - (s_2 - s_1) + s'_4. \quad (32)$$

$L$  then represents the distance from the interface of the compressed and "undisturbed" regions within the projectile to the rear end of the projectile at any time. Let  $L_s$  denote the distance  $L$  at that time at which the magnitude of the velocity of this interface (relative to the rear of the projectile) has just become subsonic. It may then be expected that the first disturbance wave will have decayed in amplitude by a factor  $\exp \left[ -\alpha L_s \right]$  when it has reached the rear of the projectile. Since

# A MODEL OF NON-EXPLOSIVE IMPACT

the normal of the advancing front of the first and all succeeding disturbance waves will be normal to the rear end of the projectile, it may be shown that <sup>4</sup> these waves will be reflected there with no change in direction, speed, or amplitude, but with a phase change of  $\pi$  (radians), so that the compression waves reflect as tension waves.

Just as the (first) disturbance wave produced here is regarded as having been initiated by the growth of the compressed area within the projectile (at the moment that the relative velocity of the interface becomes subsonic), so each succeeding "growth" of this compressed region \* may be expected to produce further disturbance waves. It is now necessary to stipulate what effect the relative rate of advance of the interface,  $\dot{M}_1 R_0$  (see(18)) has upon the maximum displacement  $u_0$  (see (31)) associated with the disturbance wave in question. Since the equation of motion (30') is linear in  $u$ , in the absence of boundary conditions other than those imposed at  $x = 0$  and at  $x = \infty$ , the principle of superposition of solutions applies. If it is assumed that the quantity  $u_0$  is proportional to some power of the quantity  $\dot{M}_1 R_0$ , say

$$u_0 = A(\dot{M}_1 R_0)^n, \quad (33)$$

then apparently the remarks above require that  $n = 1$ , so that  $u_0 \propto \dot{M}_1 R_0$ .

Let  $t = t_S$  denote the time, measured from first impact, at which the rate of advance of the interface within the projectile,  $\dot{M}_1 R_0$ , becomes subsonic (corresponding to  $t' = 0$ ). Thus the two measures of time elapsed are connected by the relation

$$t = t' + t_S \quad (34)$$

Let  $t_S = t_0 < t_1 < t_2 < \dots$  denote the elapsed time at which consecutive particles in any row in the projectile lattice are transferred from the "undisturbed" region to the compressed region. It was observed before that the chain of relations

$$\dot{M}_1(t_0) > \dot{M}_1(t_1) > \dot{M}_1(t_2) > \dots$$

is to be expected from the ever-increasing incremental deformation potential to be overcome within the projectile lattice. It is therefore to be expected that •

$$u_0(t_0) > u_0(t_1) > u_0(t_2) > \dots, \quad (35)$$

so that the maximum displacements associated with the disturbance waves following the first, decrease steadily.

<sup>4</sup> See Kolsky, *ibid.*, pp. 24-31.

\* With reference to Figure 1, these "growths" involve merely the transfer of consecutive molecules with the infinitesimal bar of material from the "undisturbed" to the compressed region.

# A MODEL OF NON-EXPLOSIVE IMPACT

Now the second disturbance wave and the reflection of the first disturbance wave will "meet" at a distance  $1/2 c(t_1 - t_0)$  from the rear of the projectile (and within it). Assuming (albeit naively) that these two waves "meet" at a location where one of the particles which makes up this row of particles within the lattice, the total displacement arising from this coalescence is

$$\begin{aligned} u_0(t_0) \left\{ \exp \left[ - \left( k + \frac{\nu}{c} \right) c(t_1 - t_0) - \alpha \left( L_s - \frac{1}{2} c(t_1 - t_0) \right) \right] \right. \\ \left. + \exp \left[ - \alpha \left( L_s + \frac{1}{2} c(t_1 - t_0) \right) \right] \right\} \\ + u_0(t_1) \exp \left[ - \alpha \left( L_s - \frac{1}{2} c(t_1 - t_0) - R_0 \right) \right] \end{aligned}$$

It will be assumed here that the quantity  $\exp \left[ - \left( k + \frac{\nu}{c} \right) c(t_1 - t_0) \right]$  is  $\ll 1$ , so that only the second and third terms in (36) need be considered. This amounts to ignoring the (residual) effect of the first passage by the wave through the projectile, in comparison with the effect of the "first" and "second" waves due to their current passage past the point. From the remarks above, since  $t_1 - t_0 < t_2 - t_1 < t_3 - t_2 < \dots$ , it must be true that

$$\exp \left[ - \left( k + \frac{\nu}{c} \right) c(t_i - t_j) \right] \ll 1 \quad (i \geq 0, j \geq i+1).$$

Thus the (resultant) total displacement above becomes

$$\begin{aligned} u_0(t_0) \exp \left[ - \alpha \left( L_s + \frac{1}{2} c(t_1 - t_0) \right) \right] \\ + u_0(t_1) \exp \left[ - \alpha \left( L_s - \frac{1}{2} c(t_1 - t_0) - R_0 \right) \right] \\ \equiv \sum_i (u) \end{aligned} \tag{36}$$

More generally, it then becomes apparent that only the quantities

$$\begin{aligned} \sum_n (u) = u_0(t_{n-1}) \exp \left[ - \alpha \left( L_s + \frac{1}{2} c(t_n - t_{n-1}) - (n-1)R_0 \right) \right] \\ + u_0(t_n) \exp \left[ - \alpha \left( L_s - \frac{1}{2} c(t_n - t_{n-1}) - nR_0 \right) \right] \end{aligned} \tag{36'}$$

will figure in the interaction of reflections from the rear which might result in rupture. If this first quantity is greater than some threshold value, say

$$\sum_i (u) > u_r \tag{37}$$

then it is assumed that a rupture will take place within the projectile at this point (in the cylindrical model adopted here, this rupture must occur in an entire plane parallel to the rear surface of the projectile). If rupture occurs at this point, it is assumed here that the net effect is to decrease the total energy available from the impacting projectile by an amount

# A MODEL OF NON-EXPLOSIVE IMPACT

$$\frac{1}{2} m_1 v_0^2 \left\{ 1 - \frac{1}{2n} c(t_1 - t_0) \right\} \xi \quad (0 < \xi < 1); \quad (38)$$

that is, by an amount of energy proportional to that contained in the section of the projectile which is "split off" by the rupture. The quantity  $\xi$  here is another empirical constant, to be determined experimentally.

By assumption, only the quantities  $\sum_n(u)$  in (36') may (possibly) figure in any rupture at the rear of the projectile. But since it is true that

$$\sum_1(u) > \sum_2(u) > \dots,$$

clearly if the rupture does not occur by the interaction of the first and second waves it will not occur by the interaction of the  $n^{\text{th}}$  and  $(n+1)^{\text{th}}$  waves. The analysis is thus considerably simplified.

Assume this (rupture) does occur. First, the rupture will have a certain time lag  $\tau_L$  associated with it, so that the event will not occur simultaneously with the meeting of the wave fronts of the two waves discussed above. This will have the following effect. If

$$\tau_L > t_2 - t_1,$$

then the wave front of the third longitudinal wave (generated at  $t = t_2$ ) will arrive before the rupture occurs and will pass into the material constituting the rear piece of the resulting bisected projectile. In this event, the possible effect of the reflection of this wave is assumed to be lost, though the residual displacement resulting from its passage through the projectile once, remains. This will also be true of the fourth wave, if

$$\tau_L > t_3 - t_1$$

and so on. At some point, however, it must be true that

$$\tau_L < t_n - t_1$$

(this could be true, for example, for  $n = 2$ ). It is then assumed that the  $(n+1)^{\text{th}}$  wave now "sees" the plane in which rupture occurs as the new "rear of projectile" and that subsequent reflections take place in this plane. Thus the quantity  $L_s - \frac{1}{2} c(t_1 - t_0)$  replaces the quantity  $L_s$  in the above, and the analysis proceeds as before.

## Conclusions (II)

A number of conclusions and/or predictions follow from the preceding analysis. The first concerns the effect of initial impact velocity,  $v_0$ . As  $v_0$  is increased without limit, a saturation point must be approached (and exceeded) where a further increase in  $v_0$  actually results in a smaller effect on the resulting crater than did the lower velocity -- e. g., the volume of the resulting crater may decrease. This arises, inter alia, because of the (assumed) linear dependence on penetration velocity of the maximum displacements associated with the dilation waves. The higher  $v_0$  is, the larger the penetration of the compressed region at the time the velocity of the interface becomes subsonic; the larger this

## A MODEL OF NON-EXPLOSIVE IMPACT

penetration, the smaller the distance  $L_S$  from the interface to the rear of the projectile (given that the original projectile length remains unchanged); the smaller  $L_S$ , the greater the resulting interaction between outgoing and reflected waves, and the greater the likelihood of rupture or even multiple rupture. Indeed, if the quantity  $L_S$  defined above may be written as  $L_S(v_0)$  for constant  $h$  -- where  $\frac{dL_S}{dv_0} < 0$

--, then one measure of the likelihood of rupture may be taken to be  $\exp[-\alpha L_S(v_0)]$ : if this quantity is greater than, say, some quantity  $x_n$  (where  $x_1 < x_2 < \dots < x_n < \dots$ ) then  $n$  separate ruptures may be expected to occur, with a corresponding reduction in penetration.

From the remarks above, it is also clear that the effect of increasing the length of the original cylinder (and, presumably other shapes as well) is to "postpone" the attainment of the saturation point defined above. This should result in an increase of cratering over and above that to be expected from the naive extrapolation of cratering due to the extra energy available.

A third prediction concerns the sonic velocity of the projectile material,  $c$ . Starting from  $c$  very small, as  $c$  is increased the deceleration of velocity of the interface to  $c$  will be accomplished in less and less time, with a resulting increase in the distance  $L_S = L_S(c)$ . \* Thus an increase in  $c$  may be expected to increase the likelihood of rupture, all other things remaining the same.

### Third Regime

The treatment of the third regime necessarily begins with the determination of the temperature distribution within the two media. Since the interval over which the action takes place is so small, apparently radiation from the boundaries of the bodies to the surrounding atmosphere may be neglected. Before melting, the configuration of Figure 1 is envisaged. In that figure, let  $x$  replace the coordinate  $s'$  there (with origin at the projectile-target interface) and let  $r$  be the usual radial coordinate, measured from the cylinder axis outward. Let the homogeneously compressed regions within the projectile and target materials be denoted by I and II, respectively. Let the undisturbed regions of the respective materials be denoted by III and IV.

It will also be assumed that the transfer of heat from I and II to III and IV is also negligible, as well as that between III and IV (this last assumption accounts for situations where the initial temperatures of projectile and target,  $T_{P_0}$  and  $T_{T_0}$ , are not equal). It will be recalled that one assumption made in the treatment of time regime I was that, of the total (kinetic) energy made available per unit time by the impacting projectile

$$\frac{1}{2} m v_0^2 \left( \frac{v_0}{\gamma_0} \right) = \dot{E}_0, \quad (39)$$

---

\* It is (albeit, naively) assumed that an increase in  $c$  is not accompanied by any change in the physical characteristics of the projectile material which determine the deformation potential in (9).

# A MODEL OF NON-EXPLOSIVE IMPACT

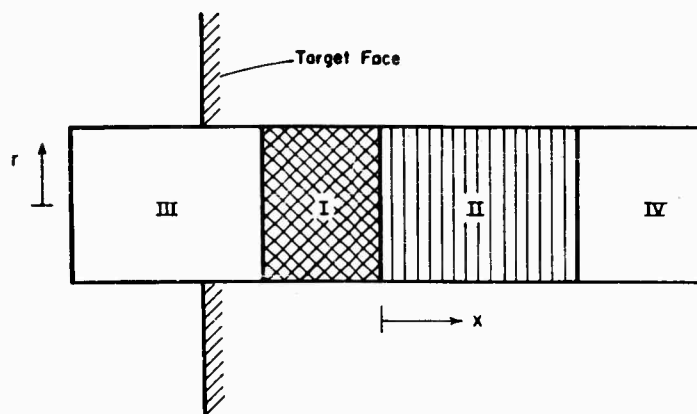


Figure 6

a certain fraction  $1 - \eta$  is consumed in heating the two lattices (locally). It will now be assumed that this (equivalent heat delivered per unit time makes its initial appearance at the I-II interface of Figure 6, and then diffuses into the regions I and II according to the relations

$$\lim_{x \rightarrow 0^-} T_p = \lim_{x \rightarrow 0^+} T_\tau \quad (40)$$

$$\lim_{x \rightarrow 0^-} K_p \frac{\partial T_p}{\partial (-x)} = \lim_{x \rightarrow 0^+} K_\tau \frac{\partial T_\tau}{\partial x}, \quad (41)$$

where  $K_p$  and  $K_\tau$  are the respective thermal conductivity parameters. It is thus to be expected that the heat flux into (the interior of) each of the regions I and II from their common interface will be the same.

Now the regions I and II are of length  $M_1(t)R_1$  and  $M_2(t)R_1'$  in the x-direction, respectively, and so are growing (in x-extent) in time monotonically. From the usual dimensional analysis of the heat equation, it may be inferred that the heat put into the system at the interface ( $z = 0$ ) may be expected to diffuse through either region I or II (roughly) according to the relation

$$\frac{x^2}{Kt} = \text{const. or } x \propto \pm \sqrt{Kt}. \quad (42)$$

Now the magnitude of  $K$  for the metals of interest (in calory - sec<sup>-1</sup> - cm<sup>-1</sup> - deg C) is of the order of one (1) or less, while the (longitudinal) velocity of sound --  $c$  in Equation (31) -- is between 12,000 and 50,000 cm-sec<sup>-1</sup> for the same group of materials.\* The quantities  $M_1(t)R_1$  and  $M_2(t)R_1'$  may be expected to be of the order of magnitude of  $c$  (or better) during impact. Now the average velocity of diffusion, as given by (42), over some interval of time  $\Delta t$  is

\* Chem. -Phys. Handbook, pp. 2247-2249 and pp. 2311-2312, resp.

# A MODEL OF NON-EXPLOSIVE IMPACT

$$\dot{V}_D \equiv \frac{1}{2\Delta t} \int_0^{\Delta t} \sqrt{\frac{K}{t}} dt = \sqrt{\frac{K}{\Delta t}} \sim \frac{1}{\sqrt{\Delta t}}. \quad (43)$$

The time  $\Delta t$  required for a sound wave to traverse a length  $\Delta l$  within the material is

$$\Delta t = \frac{\Delta l}{c}, \quad (44)$$

and the average velocity of diffusion of heat during this interval is

$$V_D = \sqrt{\frac{Kc}{\Delta l}} \sim \sqrt{c}$$

for lengths  $\Delta l$  of reasonable size (1mm to a few meters). Thus the velocities of growth of the compressed regions I and II are roughly the square of the velocities of diffusion of heat in the respective materials, so that the amount of heat reaching the I-III and II-IV interfaces, as well as regions III and IV is a negligible fraction of the total heat being generated. Thus the lattice heating may be expected to have almost no effect upon the deformation processes; and, in addition, the heat generated may be assumed confined to the regions I and II.

The temperature distribution in regions I and II are assumed to be given by

$$T_p - T_{p_0} = \frac{\frac{\dot{E}_0 t}{\frac{1}{2}nk} \sqrt{\frac{2}{\pi t}} e^{-(x^2/4 K_p t)}}{\sqrt{\frac{2}{\pi t}} \left\{ \int_{-M_1 R_1}^0 e^{-(x^2/4 K_p t)} dx + \int_0^{M_2 R_1} e^{-(x^2/4 K_p t)} dx \right\}}, \quad (45)$$

$$T_r - T_{r_0} = \frac{\frac{\dot{E}_0 t}{\frac{1}{2}nk} \sqrt{\frac{2}{\pi t}} e^{-(x^2/4 K_r t)}}{\sqrt{\frac{2}{\pi t}} \left\{ \int_{-M_1 R_1}^0 e^{-(x^2/4 K_p t)} dx + \int_0^{M_2 R_1} e^{-(x^2/4 K_r t)} dx \right\}}. \quad (46)$$

Here,  $k$  is the Boltzmann constant, and the parameter  $n$  (possibly empirical) accounts for the number of degrees of freedom of the molecules in the two lattices which are affected significantly by the rise in temperature -- for molecules in which only the translational degrees partake of the excitation, of course,  $n = 3$ .

These two distributions have two desirable characteristics which should serve to recommend them. First, the "static" components

$$\sqrt{\frac{2}{\pi t}} e^{-x^2/4 K_p t}$$

# A MODEL OF NON-EXPLOSIVE IMPACT

and

$$\sqrt{\frac{2}{\pi t}} e^{-x^2/4K_T t}$$

satisfy the respective homogeneous heat equations. Second, the total heat produced in regions I and II at any time  $t$  is proportional to

$$\int_{-M_1 R_1}^0 (T_p - T_{p_0}) dx + \int_0^{M_2 R_1'} (T_T - T_{T_0}) dx = \frac{E_0 t}{\frac{1}{2} n k},$$

in agreement with what would be expected.

Two qualitative remarks can be made concerning the distributions (45) and (46). If the quantity  $M_1 R_1$  increases faster than the quantity  $M_2 R_1'$  (given that  $K_p$  and  $K_T$  are about equal), then more heat (produced at the interface) must flow into region II than region I, and inversely. Also, if the quantities  $M_1 R_1$  and  $M_2 R_1'$  are about equal, then if  $K_p$  is greater than  $K_T$  more heat must flow into region I than region II, and inversely. Thus, all other things being roughly equal, between any materials comprising the two lattices, the one which deforms most easily and has the higher thermal conductivity parameter may be expected to tend to its melting temperature more quickly. The resistance to deformation may be expected to increase with increasing lineal (number) density, while the thermal conductivity parameter is more or less independent of this quantity (at least in an elementary treatment). Thus the approach to melting temperature (on a relative, not an absolute, basis) must be more rapid, the smaller the lineal density of the host material.

Some of the remarks in the preceding paragraph may be given a more satisfying (quantitative) foundation. Let  $T_{p_{m_1}}$  and  $T_{T_{m_1}}$  denote the temperatures at which melting begins in the respective materials. Observe first that (45) and (46) may be written as

$$T_p - T_{p_0} = A(t) e^{-x^2/4K_p t}, \quad (45')$$

$$T_T - T_{T_0} = A(t) e^{-x^2/4K_T t}, \quad (46')$$

or

$$\ln(T_p - T_{p_0}) - \ln A(t) = \frac{-x^2}{4K_p t} \quad (45'')$$

$$\ln(T_T - T_{T_0}) - \ln A(t) = \frac{-x^2}{4K_T t} \quad (46'')$$

# A MODEL OF NON-EXPLOSIVE IMPACT

If  $x_p$  and  $x$  denote points in the respective materials at which melting has just begun at some time  $t = 0$ , then

$$4t \ln \left[ \frac{T_{p_{m_1}} - T_{p_0}}{T_{p_{m_1}} - T_{p_0}} \right] = \frac{x_p^2}{K_p} - \frac{x_p^2}{K_p}, \quad (47)$$

so that the ratio

$$\Phi = \frac{T_{p_{m_1}} - T_{p_0}}{T_{p_{m_1}} - T_{p_0}} \quad (48)$$

is seen to be the crucial parameter in determining whether the target or the projectile begins to melt first, and in determining the relative rates at which melting "proceeds" through the respective materials. If, for example,  $\Phi < 1$ , so that the projectile begins to melt first, write (48) as

$$\left( \frac{x_p}{\sqrt{K_p}} \right)^2 = \left( \frac{x_p}{\sqrt{K_p}} \right)^2 + 4t \ln \Phi \quad (49)$$

If in addition  $K_p > K_p$ , then at some time

$$t \propto \frac{1 - \frac{K_p}{K_p}}{4K_p \ln \Phi}, \quad (50)$$

$x_p$  must equal  $x_p$ , and from there on the thickness of the melted target material must exceed and grow faster than the thickness of the melted projectile material; while if  $K_p \leq K_p$ , then  $x_p$  must always exceed  $x_p$  (except at  $t = 0$ , at which point both are zero). This may be seen by setting  $x_p = x_p$  in (49) and rewriting it as

$$x_p^2 \left( 1 - \frac{K_p}{K_p} \right) = 4K_p t \ln \Phi \leq 0 \quad (t > 0)$$

Clearly, analogous remarks hold for the situation  $\Phi > 1$ ; but for  $\Phi = 1$ , then the thicknesses of the respective melted materials are similar for all time and correspond to the relation

$$\frac{x_p}{\sqrt{K_p}} = (-) \frac{x_p}{\sqrt{K_p}} \quad (51)$$

## A MODEL OF NON-EXPLOSIVE IMPACT

The process of melting of either material is assumed to be accomplished in the usual manner. After the local temperature of the material is raised to the lower melting temperature  $T_{m1}$ , -- at which point the usual concept of order in the material still prevails -- the material spontaneously "absorbs" (locally) an additional amount of heat  $\Delta T_m$  and also passes to a state of predominant disorder (completely melted) at some upper temperature  $T_{m2} > T_{m1}$ . The difference between  $\Delta T_m$  and  $T_{m2} - T_{m1}$  is interpreted as the heat of fusion  $h_f$  of the

material. At this point, the specific volume  $\bar{V}$  of the material has also increased by a factor  $\beta > 1$  (i. e.,  $\bar{V} \rightarrow \beta \bar{V}$ ). It is then assumed that the material in the melted state ( $T = T_{m2}$ ) is incompressible, so that  $\beta \bar{V}$  is essentially constant. After melting, it is assumed that the temperature is relatively unchanging except for heat transfer effects; these effects will be small until the expulsion of the melted material from the front of the material begins, at which point the heat transfer to the unmelted target and projectile material encountered may be quite large.

After the initial melting of the target and projectile material adjacent to the interface, it is assumed that the respective materials do not intermingle, and that neither do the adjacent layers within either material.

### Conclusions (III)

The conclusions to be drawn from the treatment of the third regime are the following. If any change is made in the factor

$$\Phi = \frac{T_{pm1} - T_{p0}}{T_{rm1} - T_{r0}}$$

say  $\Phi \rightarrow q\Phi$  with  $q < 1$  ( $q > 1$ ), then the projectile (target) material must begin to melt earlier than before by an amount given by the relation

$$4t \{ \ln \Phi + \ln q \} = \frac{X_r^2}{K_r} - \frac{X_p^2}{K_p}$$

where  $X$  and  $X$  denote the  $x$ -coordinates of the planes of material in the respective bodies which have just reached the melting temperature. Second, if the ration  $K_p/K_r = \chi$  is changed, say  $\chi \rightarrow q'\chi$ , then the asymptotic (and, perhaps, also the initial) behavior of the quantity  $\frac{X_p}{X_r}$  is changed by

$$\frac{X_p}{X_r} \rightarrow \sqrt{q'} \frac{X_p}{X_r}$$

### Fourth Regime

This regime overlaps the third regime, since clearly the melting and expulsion processes will be proceeding simultaneously. The following mechanism will be assumed. The intense pressures generated at the projectile-target interface will support only a certain small thickness (normal to the interface)  $\Delta p_n$  of melted projectile material and a certain small thickness  $\Delta r_n$  of melted target material. All thicknesses of the respective materials in excess of these threshold

# A MODEL OF NON-EXPLOSIVE IMPACT

values must be expelled radially outward. It is assumed that the material at the interface (being the hottest) will always be expelled, new (adjacent) material moving in instantaneously to take its place. Letting  $\dot{\Delta}_p$  and  $\dot{\Delta}_\tau$  denote the rates-of-growth (neglecting expulsion) of the respective thicknesses of melted materials. Both quantities are positive. For  $\Delta_p \geq \Delta_{p_0}$  (neglecting expulsion here), the rate-of-production of melted projectile material over and above that which can be supported at the interface is given by

$$\begin{aligned} \pi a^2 \dot{\Delta}_p & \quad (\Delta_p \geq \Delta_{p_0}) \\ \pi a^2 \dot{\Delta}_\tau & \quad (\Delta_\tau \geq \Delta_{\tau_0}) \end{aligned}$$

represents the analogous rate for the target material. Thus the flux unit length (and per unit time) of melted projectile and target materials across the outer boundary of the cylinder and/or its projected "shadow" on the target are, respectively,

$$1/2 a \dot{\Delta}_p \quad (\Delta_p \geq \Delta_{p_0})$$

and

$$1/2 a \dot{\Delta}_\tau \quad (\Delta_\tau \geq \Delta_{\tau_0})$$

The situation envisioned is exhibited in Figures 7 and 8.

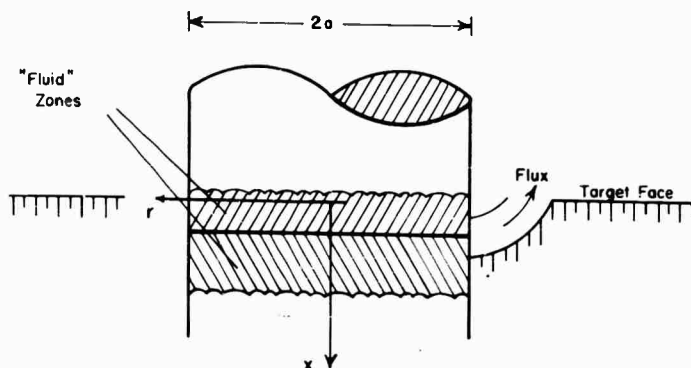


Figure 7

It is assumed that the thickness  $\delta_o$  (normal to the vector velocity of flow of the melted material) in Figure 8 for a given element of "fluid" is constant. This is supported by the following reasoning. The melted material is not free to expand at constant temperature -- in the way a gas might, by diffusion; and so, if kept at roughly constant temperature during the flow, an initial thickness would not change by this mechanism. It is not assumed, however, that this thickness is invariant from one element of fluid to another. In fact, it is assumed that the thickness  $\delta_o(t)$  of some element which is crossing the boundary defined by the circle  $r = a$  in Figure 7 at some time  $t$  is just proportional to the total rate of production of melted material at that time.

$$\delta_o(t) = A'(\dot{\Delta}_p + \dot{\Delta}_\tau). \quad (52)$$

## A MODEL OF NON-EXPLOSIVE IMPACT

Now the element of fluid of thickness  $\delta_o(t)$  is composed of two layers: the upper one (in Figs. 7 and 8) of projectile material, and the lower one of target material. Letting  $\delta_p(t)$  and  $\delta_r(t)$  denote the respective thicknesses of these two components -- subject to the requirement  $\delta_p(t) + \delta_r(t) = \delta_o(t)$  -- a natural assumption here is that the quantities  $\delta_p$  and  $\delta_r$  behave just as  $\delta_o$  does; i. e., that the thicknesses of the respective sublayers of a given element does not change as the fluid flows along. This assumption will also be adopted here.

Now the total flux/unit length of material across the boundary  $r = a$  was shown to be

$$F(t) = \frac{a}{2} (\dot{\Delta}_p + \dot{\Delta}_r)$$

But then the velocity  $V$ , at which flow across said boundary must proceed -- related to the two quantities above by the relation  $F(t) = V \delta_o(t)$  -- is seen to be constant; and is determined as soon as the quantities  $F(t)$  and  $\delta_o(t)$  are known at, say, the first time point at which  $\Delta_p \geq \Delta_{p_0}$  and  $\Delta_r \geq \Delta_{r_0}$ . Let

$v = \dot{V}_1 = \text{const.}$  here. The quantities  $A$  (in (52)) and  $V_1$  must be regarded as empirical parameters here; but knowing one, the other is immediately determined. This result, that the velocity  $v$  above is constant for all elements of fluid, may be expected to make the problem of the determination of the shape of the crater for  $r \geq a$  in Figure 8 (given by the quantity  $f(r)$  there) considerably more tractable.

The cratering for  $r > a$  in Figures 7 and 8 is assumed to be due to a friction-like process taking place between the melted material in motion and the static, solid target material surrounding the cylinder and its "shadow" on the target in Figure 7. It is assumed at the start that this "tearing away" of part of the static target material is accomplished by (only) a layer of fluid of very small thickness adjacent to the static material. This thin layer is pictured as being rather analogous to the boundary layer developed in flow of a gas around a solid; the essential difference being that the fluid here, being of roughly the same density as the solid material and of very high temperature, is capable of melting and wearing away the solid (whereas the corresponding effect of a gas on a solid is relatively infinitesimal). It follows that the process of wearing away the solid material is independent of the thickness  $\delta_o(t)$  of material flowing over the solid, given that  $\delta_o(t)$  is greater than some small threshold value.

Consider, now, the action of a given element of fluid on the solid material. This element appears at the boundary  $\{r = a\}$  with a velocity  $V = V_1$ , just as the preceding elements have. Thus its effect on the first element of solid material which it encounters (assumedly at a distance infinitesimally greater than  $a$  from the radial origin) must be the same as the preceding ones, given that the "angle of impact" (here assumed zero as in Fig. 8) is the same. It may then be inferred that the effect of this element of fluid (or, more correctly, fluid and semi-melted solid) on succeeding elements of solid must also follow that of the preceding elements of fluid; so that the (partially-formed) crater shape at any time must be similar (in the mathematical sense) to that at any other time. This rather surprising result will allow a determination of the crater shape.

The quantity  $f(r)$  exhibited graphically in Figure 8 might better be  $f(r; x_I)$ , with  $x_I$  as in Figure 8, since the initial value of the function (at  $r = a$ ) is given by

$$f|_{r=a} = x_I(t)$$

# A MODEL OF NON-EXPLOSIVE IMPACT

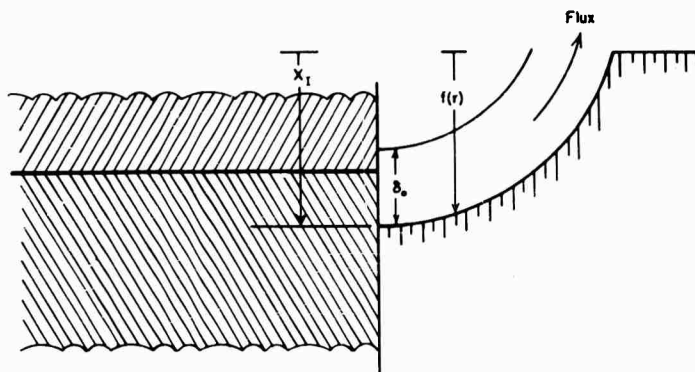


Figure 8

The requirement of mathematical similarity on the quantity  $(r; x_I)$  inferred above may be written as

$$f(r; x_{I_1}) = f(r; x_{I_2}) + (x_{I_1} - x_{I_2})$$

over the  $r$ -range for which both are defined (in each case, this range will depend strongly on the associated  $x_I$  value). Thus, letting  $a \leq r \leq \bar{r}(x_I)$  \* denote strongly the  $r$ -range over which  $f(r; x_I)$  is defined,  $f(r; x_I)$  may evidently be written as

$$f(r; x_I) = f(r) + x_I \quad (a \leq r \leq \bar{r}(x_I)) \quad (53)$$

for some suitable function  $f(r)$ . Thus the particular value of  $x_I$  need play no role in the determination of crater shape, and only the quantity  $f(r)$  need be analyzed.

Now the important quantities in determining the effect of the fluid flow upon the solid material are evidently  $f'(r)$  and  $f''(r)$ : the fluid immediately adjacent to some solid element at a distance  $r = R$  from the radial origin is assumed to be flowing in a direction parallel to the tangent of the fluid-solid interface curve (Fig. 8) at  $r = R$ . The magnitude of this slope is  $(-)' f'(R)$ , and the rate-of-change of this slope is  $f''(R)$ ; and it is this change of slope which is assumed to be responsible for the predominant part friction-like process alluded to above.

Now it must be clear at once that the solid material at the interface defined by the quantity  $f(r)$  in Figure 8 is much more resistant to deformation than is the fluid flowing over it. Thus if the quantity  $f''(r)$  is taken as a measure of the force with which the "wearing away" process is being continued, then since the fluid flow will try to accommodate itself to the shape of the crater already in existence at its

\* For  $\bar{r}(x_I)$  is the smallest value of  $r$  for which  $f(r) = 0$ ; that is, it is the value of  $r$  for which the crater depth goes to zero.

# A MODEL OF NON-EXPLOSIVE IMPACT

passage, it is reasonable to expect the force alluded to above to be constant (or nearly so), so that

$$f''(r) = -2c_1 = \text{const.} \quad (a \leq r \leq \bar{r}(x_1)) \quad (54)$$

But from (53) this then requires that

$$f(r; x_1) = x_1 - c_1(r-a)^2 \quad (a \leq r \leq \bar{r}(x_1)), \quad (55)$$

and it follows that

$$\bar{r}(x_1) = a + \sqrt{\frac{x_1}{c_1}} \quad (56)$$

Thus the shape of the crater outside the region  $\{r \leq a\}$  must be parabolic. The quantity  $c_1$  may be taken as an empirical parameter, or it may be inferred from other empirical parameters by matching the initial flux energy ( $\propto v_0^2$ ) with the

energy required to begin wearing away the solid target material adjacent to the point where expulsion begins.

After the extruded material has flowed up the sides of the crater, it will apparently separate from the target completely, spewing off into the surrounding atmosphere. However, the last portion of the projectile to undergo melting will not be extruded (there being no material behind it to force it radially outward), and so will solidify (on cooling) at the center of the crater. A certain amount of previously melted material may be expected to solidify over the remainder of the crater as well, this amount being proportional to the thickness  $\delta_0(t)$  of that (total) element of material when extruded from the region between the (non-melted) projectile and target. Now  $\delta_0(t)$  is proportional to  $\Delta_p + \Delta_r$  (see (52)) and this may be expected to be very nearly constant (but decreasing slightly in time) over the last stages of melting. Thus it would be expected that a thin and nearly constant layer of previously melted material would be deposited over the sides of the crater, away from the center. A more careful measurement of this thickness would be expected to show that it increases slightly as one proceeds away from the center toward the edge of the crater. With this remark the treatment of the fourth regime is brought to a close.

## A Summing Up

A few weaknesses appear in the preceding analysis, and deserve to be pointed out. In the first place, the plethora of empirical parameters appearing here may be somewhat discouraging:  $\eta$  in (3);  $R_0, R_1, R_0',$  and  $R_1'$  in (4) and (5);  $A_p, B_p, A_r, B_r, p$  and  $\tau$  in (9) and (10);  $k, \nu$  and  $c$  in (31);  $A$  in (33);  $\xi$  in (38);  $n, K_p$  and  $K_r$  in (45) and (46);  $\beta$  in the discussion of the melting process in the third regime,  $A'$  and the components  $\delta_{p,0}$  and  $\delta_{r,0}$  of  $\delta_0$  in (52); the velocity of extrusion  $v_1$  in the fourth regime; and finally the coefficient  $c_1$  in (55). A total of twenty-five. About half of these could be obtained directly experimentally.

# A MODEL OF NON-EXPLOSIVE IMPACT

$(R'_0, R'_1, R''_0, R''_1, A_p, B_p, A_\gamma, B_\gamma, p, \tau, \beta, k, \nu, c, A, K_p, K_\gamma).$

If it were desired to obtain them all precisely, a rather large number of carefully defined trials would have to be made. Thus the use of this model, if any, is in the qualitative and semi-quantitative predictions which may be made with it. A few of the assumptions are somewhat questionable. Two will be dealt with here.

First is the assumption in (38) of a linear relation between energy dissipated or "split off" by rupture and the distance from the rear end at which rupture occurs. This is supported by the following reasoning. The rupture piece (rear end) possessed a certain amount of energy before rupture, equal to the (initial) kinetic energy per unit length times the length of the piece. In rupturing, the kinetic energy of this piece, considered as a unit, will be reduced by a certain amount; but the absolute and reduction in energy must apparently be dependent linearly upon the amount available initially.

The second is the neglecting of the effect of the melting and extrusion of material on the deformation potential "seen" by the remainder of the projectile and target. The particles extruded in the process can no longer effect the incremental change in lattice potential energy, and it might be expected that this would lower the incremental deformation potentials of the lattices at any time by a substantial amount. The author believes, though, that this change would be quite small, rather than substantial.

# APPLICATION OF "HYDRODYNAMIC" THEORY TO THE LOW STRESS RANGE OF HYPERVELOCITY IMPACT PROBLEMS

Ian M. Fyfe

The Boeing Company  
Seattle, Washington

An essential feature of a mathematical model for a physical phenomenon is that it be tractable to known methods of solution. In stress wave propagation this is often achieved by making certain simplifying assumptions, as for example, when the material behaves elastically, or for higher stresses when it follows a particular elasto-plastic rule of behavior. It is the purpose of this paper to show that by limiting the physical configuration of the phenomenon it is possible to reduce the mathematical complexity of a mathematical model without imposing any undue restriction on the physical properties of the material under consideration.

Though the particular theory developed is not restricted to any stress level, it is regarded as being mainly applicable to low stress levels where the assumption that the medium is a fluid may possibly not be valid. In hypervelocity impact, low stresses will occur near the rear surface of a plate when a wave reflects from that surface, or in the tail of a stress pulse.

Starting from the general statements of conservation of mass, momentum and energy (after having made the basic assumption that the process may be described by a continuum and is influenced only by surface, body and inertia forces), we obtain the following equations for a three-dimensional curvilinear system:

$$\frac{\partial \rho}{\partial t} + (\rho v^i)_{,i} = 0 \quad (1)$$

$$\tau^{ij}_{,j} + F^i - \rho a^i = 0 \quad (2)$$

$$\tau^{ij} = \tau^{ji} \quad (3)$$

$$\rho \frac{de}{dt} - (\tau^{ij} v_i)_{,j} - F^i v_i + \rho v^i \frac{\partial v_i}{\partial t} = 0 \quad (4)$$

## HYDRODYNAMIC THEORY TO LOW STRESS RANGE

where  $\tau_{ij}$  is the stress tensor,  $F^i$  the components of the body forces,  $a^i$  the components of acceleration,  $v^i$  the components of velocity,  $\rho$  the density, and  $e$  the internal energy. The notation used is that of Sokolnikoff (1) so that a comma denotes the covariant derivative with respect to the space variables and  $\frac{\partial}{\partial t}$  is the intrinsic derivative. The above equations apply equally well to a solid or fluid, and it is only by the introduction of the constitutive equations (or equations of state) that the medium is defined.

A restriction will be made to the problem under consideration, namely that the wave propagation be one-dimensional. It will be shown that this restriction is quite realistic when considering hypervelocity impact problems. By one-dimensional, we mean the deformation is a function of only one space variable. Thus, if we consider an element enclosed in a body, we see the particles comprising the element are allowed to move in one direction only. We can now let the displacement in the propagation direction be such that  $u_1 = f(x_1, t)$  and  $u_2 = u_3 = 0$ . The closest physical realization to this idealization is shown in Figure 1 where for simplicity the coordinate system is shown to be rectangular. The undeformed element  $a$  is shown deformed to  $b$  after the passage of the wave front  $c$ .

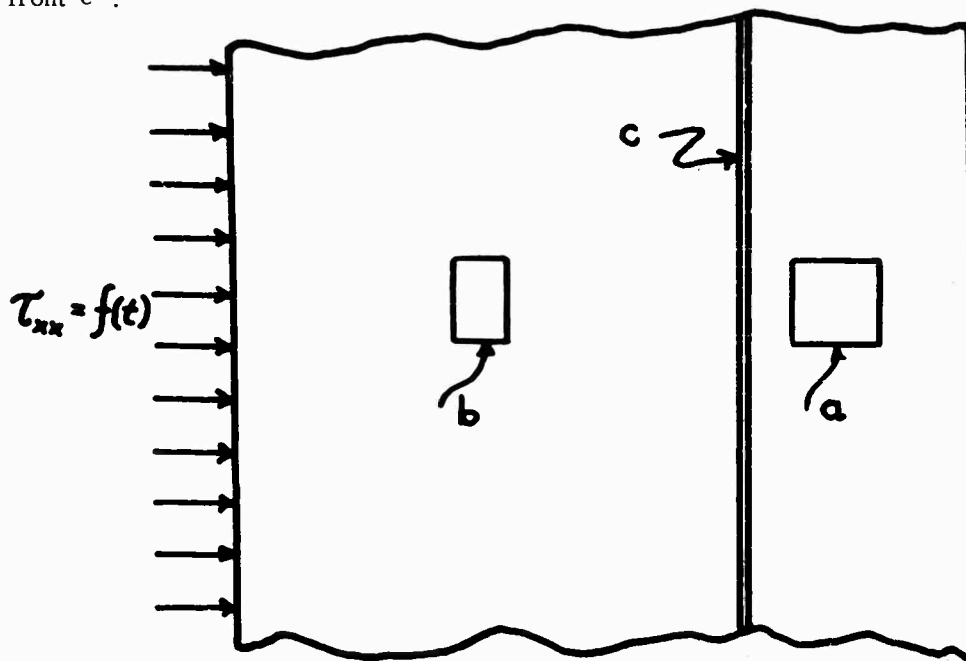


Figure 1. One-Dimensional Wave Propagation

As the head of the stress wave passes over the typical element it will undergo an axial contraction in the  $x_1$  direction. The amount of contraction or elongation in the  $x_2$  direction is controlled by the surrounding elements. As all elements are identically loaded in a plane normal to  $x_1$ , they cannot all expand (or contract) until the wave from the boundary lying in the  $x_2$  direction allows each element to move. Due to the rapidity of the distortion process,

## HYDRODYNAMIC THEORY TO LOW STRESS RANGE

this boundary need not be too far removed to be essentially at  $\infty$ . Those stringent requirements of one-dimensionality are; that the load be uniform in space, and that the wave-length of the disturbance be small as compared to the distance to be travelled by the rarefaction wave from the boundary. Physically such problems can be encountered in the impact of thin plates, high explosive loading, and exploding foil loading.

In most cases, one-dimensional wave propagation can take place in either a sphere, a cylinder, or a flat plate, and for this reason, and also simplicity, we will only consider the classic coordinate systems of rectangular, cylindrical and spherical.

If equations (1) through (4) are expanded for the following coordinate systems, we have:

### (a) Rectangular

coordinates  $x, y, z$

$$\begin{aligned} \frac{d\rho}{dt} + \rho \frac{\partial v_x}{\partial x} &= 0 \\ \rho \frac{dv_x}{dt} - F_x - \frac{\partial \tau_{xx}}{\partial x} &= 0 \\ \rho \frac{de}{dt} - \frac{\partial}{\partial x} (\tau_{xx} v_x) - F_x v_x + \rho v_x \frac{dv_x}{dt} &= 0 \end{aligned} \quad (5)$$

### (b) Cylindrical

coordinates  $r, \theta, z$

$$\begin{aligned} \frac{d\rho}{dt} + \rho \left( \frac{\partial v_r}{\partial r} + \frac{1}{r} v_r \right) &= 0 \\ -\rho \frac{dv_r}{dt} - F_r - \frac{\partial \tau_{rr}}{\partial r} + \frac{1}{r} \tau_{\theta\theta} - \frac{1}{r} \tau_{rr} &= 0 \\ \rho \frac{de}{dt} - \frac{\partial}{\partial r} (\tau_{rr} v_r) - \frac{v_r}{r} \tau_{rr} - F_r v_r + \rho v_r \frac{dv_r}{dt} &= 0 \end{aligned} \quad (6)$$

### (c) Spherical

coordinates  $r, \theta, \phi$

$$\begin{aligned} \frac{d\rho}{dt} + \rho \left( \frac{\partial v_r}{\partial r} + \frac{1}{r} v_r \right) &= 0 \\ \rho \frac{dv_r}{dt} - F_r - \frac{\partial \tau_{rr}}{\partial r} + \frac{1}{r} \tau_{\theta\theta} + \frac{1}{r} \tau_{\phi\phi} - \frac{2}{r} \tau_{rr} &= 0 \\ \rho \frac{de}{dt} - \frac{\partial}{\partial r} (\tau_{rr} v_r) - \frac{2}{r} \tau_{rr} v_r - F_r v_r + \rho v_r \frac{dv_r}{dt} &= 0 \end{aligned} \quad (7)$$

# HYDRODYNAMIC THEORY TO LOW STRESS RANGE

Let us at this point introduce the pressure using the usual definitions of

$$p = -\frac{1}{3} \tau_i^i \equiv -\frac{1}{3} (\tau_1^1 + \tau_2^2 + \tau_3^3)$$

if the material is a fluid this would reduce to

$$p = -\tau_1^1 = -\tau_2^2 = -\tau_3^3$$

and when introduced into equations (5), (6), and (7), we have the following corresponding set of hydrodynamic equations:

(aa) Rectangular

$$\begin{aligned} \frac{d\rho}{dt} + \rho \frac{\partial v_x}{\partial x} &= 0 \\ \rho \frac{dv_x}{dt} - F_x + \frac{\partial p}{\partial x} &= 0 \\ \rho \frac{de}{dt} + \frac{\partial}{\partial x} (p v_x) - F_x v_x + \rho v_x \frac{dv_x}{dt} &= 0 \end{aligned} \quad (8)$$

(bb) Cylindrical

$$\begin{aligned} \frac{d\rho}{dt} + \rho \left( \frac{\partial v_r}{\partial r} + \frac{1}{r} v_r \right) &= 0 \\ \rho \frac{dv_r}{dt} - F_r + \frac{\partial p}{\partial r} &= 0 \\ \rho \frac{de}{dt} + \frac{\partial}{\partial r} (p v_r) + \frac{v_r}{r} p - F_r v_r + \rho v_r \frac{dv_r}{dt} &= 0 \end{aligned} \quad (9)$$

(cc) Spherical

$$\begin{aligned} \frac{d\rho}{dt} + \rho \left( \frac{\partial v_r}{\partial r} + \frac{2}{r} v_r \right) &= 0 \\ \rho \frac{dv_r}{dt} - F_r + \frac{\partial p}{\partial r} &= 0 \\ \rho \frac{de}{dt} + \frac{\partial}{\partial r} (p v_r) + 2 \frac{v_r}{r} p - F_r v_r + \rho v_r \frac{dv_r}{dt} &= 0 \end{aligned} \quad (10)$$

An examination of equations (5) through (10) indicates that these equations can be grouped by considering the number of constitutive equations required to match the number of equations to unknown dependent variables. In equations (5), (8), (9), and (10), assuming body forces are defined, we need only one additional equation. This equation will represent a relationship containing the surface forces, i. e.,  $p = f_1(\rho, e)$  or  $\tau_{xx} = f_2(\rho, e \dots)$

## HYDRODYNAMIC THEORY TO LOW STRESS RANGE

In equations (6) and (7), however, we need at least two constitutive equations, e. g.,  $\tau_{rr} = f_3(\rho, e \dots)$  and  $\tau_{\theta\theta} = f_4(\rho, e \dots)$

Let us consider equations (5) of the first group which is the only set which is not representative of fluid flow. It can be noticed that the only requirement to make equations (5) identical to equations (8) would be to replace  $\tau_{xx}$  by  $p$ . If this is done without requiring  $\tau_{xx} = \tau_{yy} = \tau_{zz}$  we have a set of equations

which are mathematically identical to (8), but not the conservation equations of fluid flow. For want of a better means of identification these equations will be called the "hydrodynamic" equations. This definition of hydrodynamic is purely a mathematical one. If equations (5) can, at least mathematically, be grouped with the hydrodynamic equations we can use some of the well-known techniques to solve such equations as those indicated in (2) and (3); the technique being somewhat controlled by the form of the constitutive equation. In this way, many existing machine codes can be used at all stress levels as long as a rectangular coordinate system is used along with the appropriate constitutive equation depending on the stress level reached in the process, e. g., elastic, plastic, or fluid.

The simplicity obtained by such a configuration is somewhat offset by the information that can be obtained from such a set of equations (5). If these equations are used to obtain the constitutive equations only  $\tau_{xx}$  can be found and no means are directly available to find  $\tau_{yy}$  or  $\tau_{zz}$  as the functional relationships of density, etc. Generally, however, the need to know  $\tau_{yy}$  or  $\tau_{zz}$  is not a requirement and this lack of knowledge presents no problem. An exception to the above does exist, however, where one wishes to use, for example, some yield or failure criterion to predict the change from one constitutive equation to another. This can occur when the stress level rises above the elastic range to the plastic, and it is required to use, for example, either the Tresca or Von Mises yield criterion to indicate when the change occurs. The following outlines how this can be overcome by introducing additional experimental data.

In the elastic range of stresses the following stress-strain or constitutive equations hold for a homogeneous isentropic medium

$$\tau_j^i = \lambda \delta_j^i \nu + 2\mu e_j^i$$

where  $\lambda$  and  $\mu$  are the Lamé constants,  $\nu = e_{ii}$  and  $e_j^i$  is the strain tensor.

If we introduce the requirements that the strain be one-dimensional, we have, for a rectangular coordinate system,

$$\tau_{xx} = (\lambda + 2\mu)e_{xx} \quad (11)$$

$$\tau_{yy} = \tau_{zz} = \lambda e_{xx} \quad (12)$$

## HYDRODYNAMIC THEORY TO LOW STRESS RANGE

where it can be observed that if we require only equation (11) to solve (5) there is no need to distinguish  $\lambda$  from  $\mu$ . However, if we wish to use the Von Mises yield criterion which is, in general

$$f = \frac{2}{3}(\tau_{xx}^2 + \tau_{yy}^2 + \tau_{zz}^2 - \tau_{yy}\tau_{zz} - \tau_{zz}\tau_{xx} - \tau_{xx}\tau_{yy})$$

reducing in particular, on the introduction of (12), to

$$k = |\tau_{xx} - \tau_{yy}|$$

where  $k$  differs by a numerical factor from the yield parameter  $f$ , we require a distinction between  $\lambda$  and  $\mu$  in order to obtain  $\tau_{yy}$ . A number of experimental techniques to do this are outlined in (4). For stresses beyond the yield stress this problem is not so simple and is still a matter for research. Because

$$\tau_{xx} \neq \tau_{yy}$$

we can expect shear stresses of considerable magnitude in some plane not perpendicular to the wave propagation. Using a technique similar to that given in (5), it can be shown for an elastic solid that

$$\tau_{\max} = -\tau_{xx} \left(1 - \frac{\lambda}{\lambda + 2\mu}\right) l \sqrt{1 - l^2}$$

in a plane where  $l$  is the direction cosine of its normal and has a value of  $1/4$ .

The conclusions that can be extracted from these simple observations are important in the analysis of stress wave propagation; in particular when the equations are for a rectangular cartesian coordinate system and the stresses vary from very high compressive stresses to high tensile ones.

When such equations as (5) and (8), or the equivalent Rankine-Hugoniot equations, are used to obtain the constitutive equations, the requirement that the material be considered a fluid is not necessary. If the material were not fluid like, the symbol  $p$  could only represent the principal stress  $\tau_{xx}$ , and further information is required to describe the state of the material. Thus,

$p$  obtained for very high stresses may be considered as pressure with applicability in all coordinate systems while  $p$  at low stresses applies only to a rectangular system.

As many computational schemes for solving stress wave propagation problems are in a machine code, the fact that the same equations, except for the constitutive ones, can be used at all stress ranges is a considerable reduction in complexity.

In systems where the geometry is not rectangular, and the stresses range from extremely high to quite low, for example, an internally loaded cylinder, it is important to determine when the rigidity becomes significant in order that the computations can switch from equations (9) to (6). The difficulties inherent in using equations (6) to obtain constitutive equations for  $\tau_{\theta\theta}$  and  $\tau_{rr}$  as functions of density and energy, etc., as compared to using (9) to obtain one constitutive equation for  $p$ , are obvious.

This work forms part of a research program undertaken by The Boeing Company. I am indebted to the Applied Physics Section for permission to present this work.

## HYDRODYNAMIC THEORY TO LOW STRESS RANGE

### REFERENCES

1. Sokolnikoff, I. S. , Mathematical Theory of Elasticity, New York and London, McGraw-Hill Book Co. , Inc. , 1956.
2. Courant, R. , and Friedrichs, K. O. , Supersonic Flow and Shock Waves, New York, Interscience Publishers, Inc. , 1948.
3. Von Neumann, J. , and Richtmeyer, R. D. , A Method for the Calculation of Hydrodynamic Shocks, Journal of Applied Physics, Vol. 21, p. 232-238, 1950.
4. Huntington, H. B. , Solid State Physics, Vol. 7, New York, Academic Press, Inc. , 1958.
5. Streeter, V. L. , Fluid Dynamics, New York and London, McGraw-Hill Book Co. , Inc. , 1948.

## VISCO-PLASTIC FLOW THEORY IN HYPERVELOCITY

### PERFORATION OF PLATES

Pei Chi Chou

Drexel Institute of Technology  
Philadelphia, Pennsylvania

#### INTRODUCTION

In the analysis of the hypervelocity impact problem, only two theories have been used: the incompressible hydrodynamic theory and the compressible shock wave theory. (Refs. 1 and 2.) Both of these theories consider the solid materials under impact as fluids, and the analyses are similar to that for standard perfect fluid theory in fluid mechanics, where the viscosity of the fluid is neglected. For certain special cases of impact, the omission of the viscosity may be justified, but the fact is, an exact understanding of the effect of the viscosity is still unknown.

In fluid mechanics the importance of viscosity depends on the type of flow motion. For conventional fluid flow, the viscous stress is high inside the boundary layer but may be neglected altogether outside the boundary layer. For a fluid with linear viscosity, that is, a Newtonian fluid, the viscous shear stress is

$$\tau = \mu \frac{\partial v}{\partial x}$$

For ordinary fluids the coefficient of viscosity  $\mu$  is a small number. Nevertheless, inside the boundary layer the velocity gradient  $\partial v / \partial x$  is very large and as a result, the product  $\mu \partial v / \partial x$  is comparable in magnitude to the pressure and inertia stresses. Under hypervelocity impact, the magnitude of the coefficient of viscosity of different materials is still unknown. Regardless of the value of this coefficient (as long as it is not zero), the viscous stress will be high and may become predominant if  $\frac{\partial v}{\partial x}$  is extremely high.

In order to gain some insight into the effect of viscosity, the case of the perforation of a thin plate by a circular cylinder is considered. Based on available test results, it is felt that viscosity plays a more important role in perforation problems than it does in cratering problems. Visco-plastic properties of the material are assumed and the governing equations derived. The solution of these equations are plotted in the form of velocity displacement, strain and strain-rate vs. radial distance curves. The perforation diameter, loss of momentum and residual velocity of the projectile are also obtained.

## VISCO-PLASTIC FLOW THEORY

The results of a preliminary study using viscous theory were first reported in Reference 3. Some additional results and explanations are given here. The mathematical derivations are summarized in Appendix I.

Recently it has come to the author's attention that articles using a similar visco-plastic approach have appeared in the Russian Journal of Applied Mathematics and Mechanics. These purely theoretical treatments by the Russians are discussed and compared with the author's theoretical analysis in Appendix II.

### II. ASSUMPTIONS

Spherical or cylindrical projectiles are considered and thus the problem is axially symmetrical. The mechanism of perforation is assumed to be "plugging" by shear rather than "petaling", "radial flow" or "fragmentation" as depicted in Figure 1. The plugging mode of perforation considered here is different from the low speed plugging of brittle material. Rather it is the type of perforation which usually occurs at high velocity impact (above 3,000 ft/sec) on thin plate. Under hypervelocity impact, fragmentation or shattering is usually observed. It is assumed here that fragmentation occurs after the plug has been sheared out of the plate and that shear strain is the only dominant strain component during the period of perforation. The rigid projectile with radius "a" travels at an initial velocity  $V_0$ . Upon impact with the plate, the projectile with the portion of the plate with radius "a", are assumed to travel as a rigid body with an initial velocity  $v_0$ . The velocity  $v_0$  is calculated from  $V_0$  using momentum relations. We are interested in the motion and stress in the region of the plate with radius  $r > a$  after impact. (See Fig. 2)

The strain is assumed constant across the thickness of the plate; all variables are, therefore, functions of radial distance  $r$  and time  $t$  and are independent of the axial location  $Z$ . This assumption is believed to be valid if the diameter of the projectile is much larger than the thickness of the plate and if the impact velocity is high. Since on the free surfaces of the plate, the shear stress  $\tau r Z$  must vanish, the assumption of constant strain across the thickness is in error near the surfaces of the plate. For this reason, this theory is not accurate for very thin plates. These assumptions will be further discussed at the end of this paper when the solutions of the equations are obtained.

### III. EQUATIONS AND SOLUTIONS

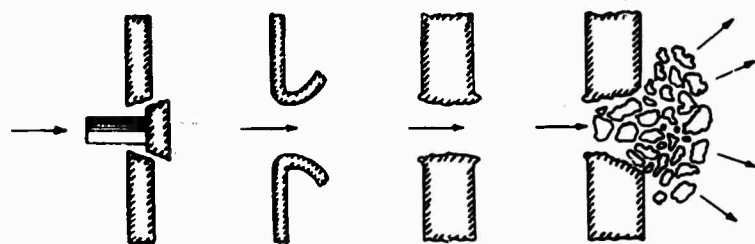
For the assumptions stated, the only equation of motion is

$$\frac{\partial \tau}{\partial r} + \frac{\tau}{r} = \rho \frac{\partial^2 w}{\partial t^2} \quad (1)$$

where  $\tau$  is the shear stress,  $\rho$  the mass density of the plate and  $w$  the displacement in  $Z$ -direction. The left-hand side of this equation represents the resultant shear force and the right-hand member is the inertia force on the circular ring element as depicted in Figure 3.

The visco-plastic property of the material for this special case is assumed

# VISCO-PLASTIC FLOW THEORY



PLUGGING PETALING RADIAL FLOW FRAGMENTATION

Figure 1. Different Types of Plate Perforation

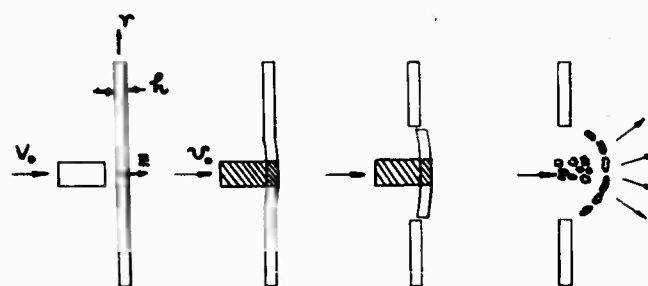


Figure 2. Assumed Mode of Perforation

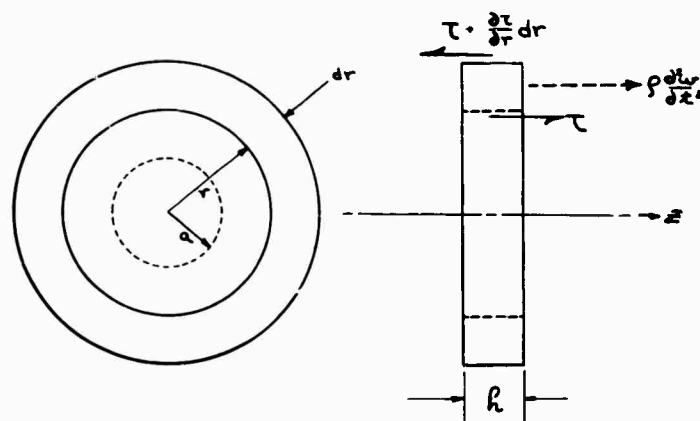


Figure 3. Forces on a Circular Ring Element

## VISCO-PLASTIC FLOW THEORY

to be

$$\tau = \mu \frac{\partial \gamma}{\partial r} - k \quad (2)$$

where  $\gamma$  is the shear strain,  $\mu$  the coefficient of viscosity and  $k$  the yield stress in shear. The relations between  $\gamma$ ,  $\omega$ , and  $v$  are

$$\begin{aligned} \gamma &= \frac{\partial \omega}{\partial r} \\ v &= \frac{\partial \omega}{\partial t} \end{aligned} \quad (3)$$

$$\frac{\partial \gamma}{\partial t} = \frac{\partial v}{\partial r}$$

In Equation 2 the stress  $\tau$  is considered to consist of a constant part, equal to the yield stress, and a viscous part with constant coefficient of viscosity. The elastic stress of the material is neglected, because its value is much smaller than the viscous or inertial stresses under hypervelocity impact. Equation 2 can also be derived from the general three-dimensional visco-plastic equations. (Ref. 2.) Other types of equations relating stress and strain-rate in place of Equation 2 have been used by other investigators and are discussed in Appendix II.

Combining Equations 1, 2 and 3 yields the following governing differential equation,

$$\frac{\partial^2 v}{\partial r^2} + \frac{1}{r} \frac{\partial v}{\partial r} - \frac{1}{r} \frac{k}{\mu} = \frac{1}{\nu} \frac{\partial v}{\partial t} \quad (4)$$

where  $\nu$  = kinematic coefficient of viscosity =  $\frac{\mu}{\rho}$

The initial and boundary conditions may be expressed as

$$\begin{aligned} v &= 0 & \text{AT } t=0, & r > a \\ v &= v_0 & \text{AT } t=0, & r = a \\ -h'k + \mu h' \left( \frac{\partial v}{\partial r} \right) - \frac{\partial v}{\partial t} &= 0 & \text{AT } t > 0, & r = a \\ v &= 0 & \text{AT } r &= \infty \end{aligned} \quad (5)$$

where,

$$h' = \frac{2\pi a h}{M}$$

$$M = M_1 + \pi a^2 h \rho$$

The third equation of Equations 5 is derived from the equation of motion of the projectile (together with a portion of the plate of radius "a") after impact.

Equation 4 is a parabolic partial differential equation of the heat transfer or diffusion type. As summarized in Appendix I, Laplace transforms and asymptotic expansions are used to obtain a solution which satisfies Equations 5.

The solution is expressed in terms of displacement, velocity, shear strain and shear strain-rate, all as functions of the radial space coordinate

## VISCO-PLASTIC FLOW THEORY

$r$  and time  $t$ . Numerical calculations are made for these quantities and the results plotted in Figures 4 through 7. The case  $H = 0$  corresponds to a projectile of infinite mass and constant velocity after impact. The case of  $H = 0.423$  corresponds to the perforation of a plate with the following given values of the parameters:

$$\begin{aligned} a &= \text{radius of projectile} &= 3/64'' \\ M_i &= \text{mass of projectile} &= 3.56 \times 10^{-6} \text{ slug} \\ \rho &= \text{density of plate} &= 5.2 \text{ slug/ft}^3 \\ M &= M_i + \pi a^2 h \rho &= 4.5 \times 10^{-6} \text{ slug} \\ h &= \text{thickness of plate} &= 3/64'' \\ \mu &= \text{coefficient of viscosity} &= 100^{16}\text{-sec/ft}^2 \\ H &= \frac{2\pi a^2 h \rho}{M} &= 0.423 \\ t' &= \text{dimensionless time} &= \frac{\mu}{\rho a^2} t \end{aligned}$$

The displacement  $z$  is shown in Figure 4, velocity  $v$  in Figure 5, strain  $\frac{\partial z}{\partial r}$  in Figure 6 and strain-rate  $\frac{\partial v}{\partial r}$  in Figure 7.

The value for the coefficient of viscosity is estimated, because the exact value is unknown at the present. The basis for the estimation is discussed in Reference 3.

Because of the nature of the differential equation, the calculations indicate that the viscous wave due to impact is felt immediately at infinity, although with infinitesimal intensity. For a disturbance of finite strength, the speed of propagation is finite, although not constant in value. This is in contrast with the case of an elastic wave or a shock wave which propagates with a constant velocity.

### IV. SEPARATION CRITERION

In order to facilitate the discussion of the failure behavior of the material under dynamic loading, the term "failure" is used here to denote the occurrence of an irreversible change, as defined by Dr. Rinehart (Ref. 2). In this sense, failures may be either fractures or plastic flows. It is known that when the impact velocity  $v_0$  is above a few thousand feet per second, the stress at the shear surface is much larger than the ultimate strength of the material. (See Fig. 8.) If the material is not viscous, the plate material will separate at this surface and no stress can be transmitted through it (except the shear yield stress, which is small as compared to other stresses). However, if the material is viscous, even though failure has occurred, it can still transmit shear stress and can be considered as a continuum. In other words, under hypervelocity impact, solid materials behave like fluids. They may behave like non-viscous fluids, which cannot transmit shear, or viscous fluids, which transmit shear. When shear stress (and axial particle velocity) cannot be transmitted, the material ceases

# VISCO-PLASTIC FLOW THEORY

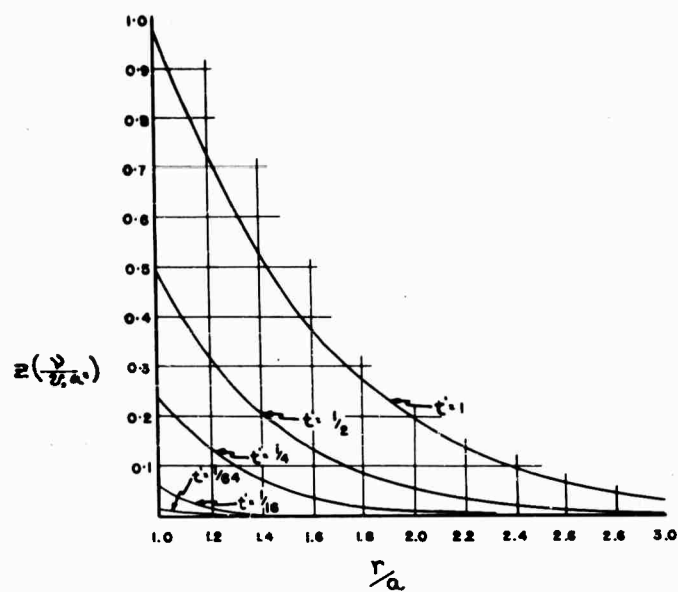


Figure 4a. Displacement vs. Radial Distance Curves ( $H = 0$ )

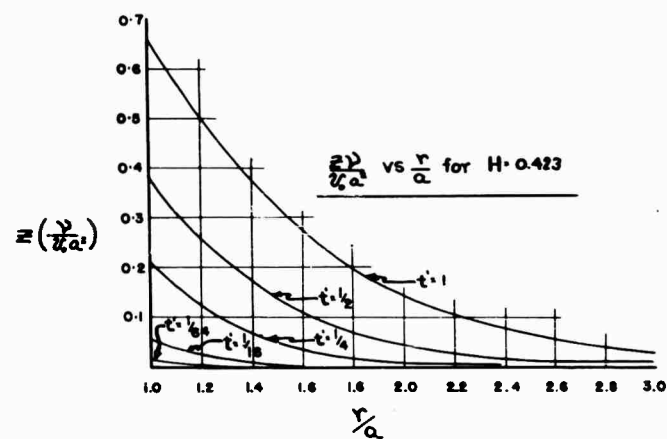


Figure 4b. Displacement vs. Radial Curves ( $H = 0.423$ )

# VISCO-PLASTIC FLOW THEORY

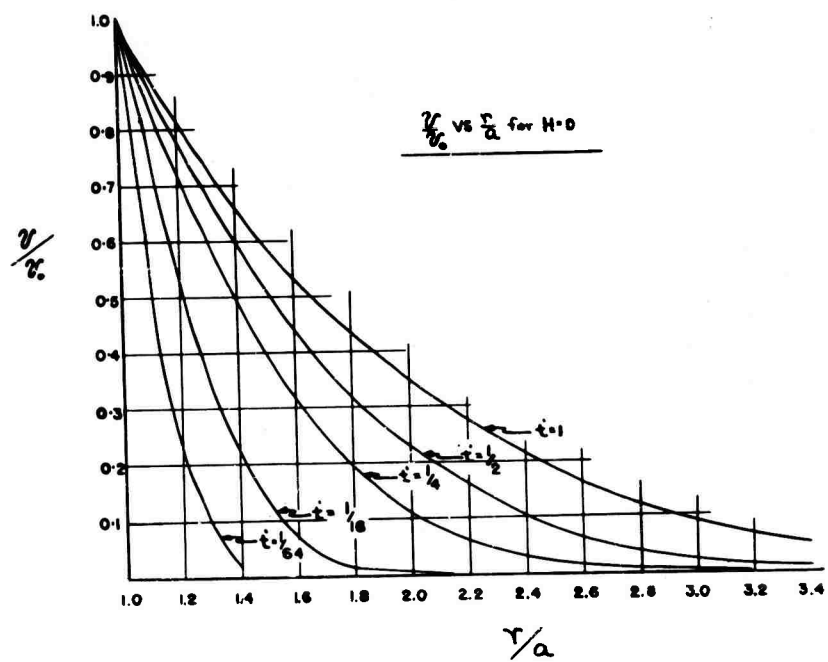


Figure 5a. Velocity vs. Radial Distance Curves ( $H = 0$ )

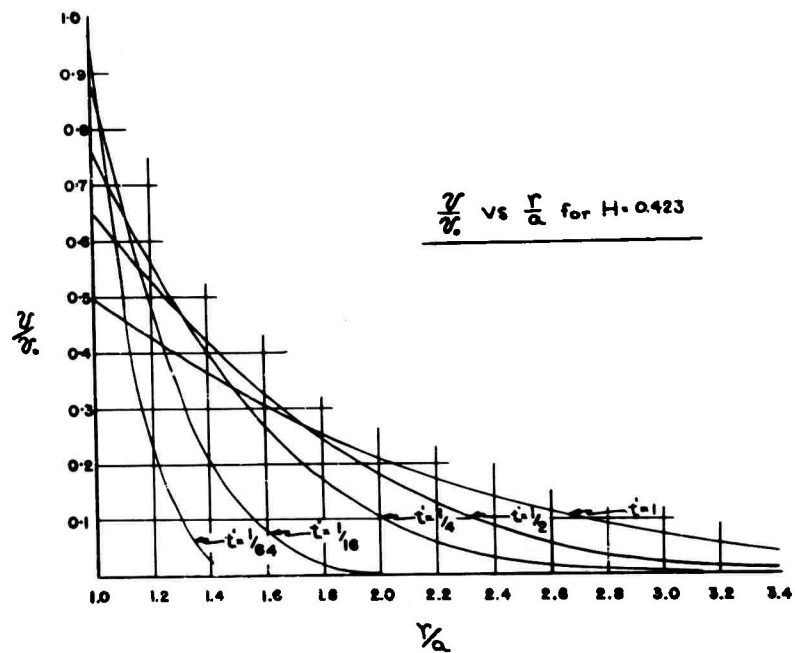


Figure 5b. Velocity vs. Radial Distance Curves ( $H = 0.423$ )

# VISCO-PLASTIC FLOW THEORY

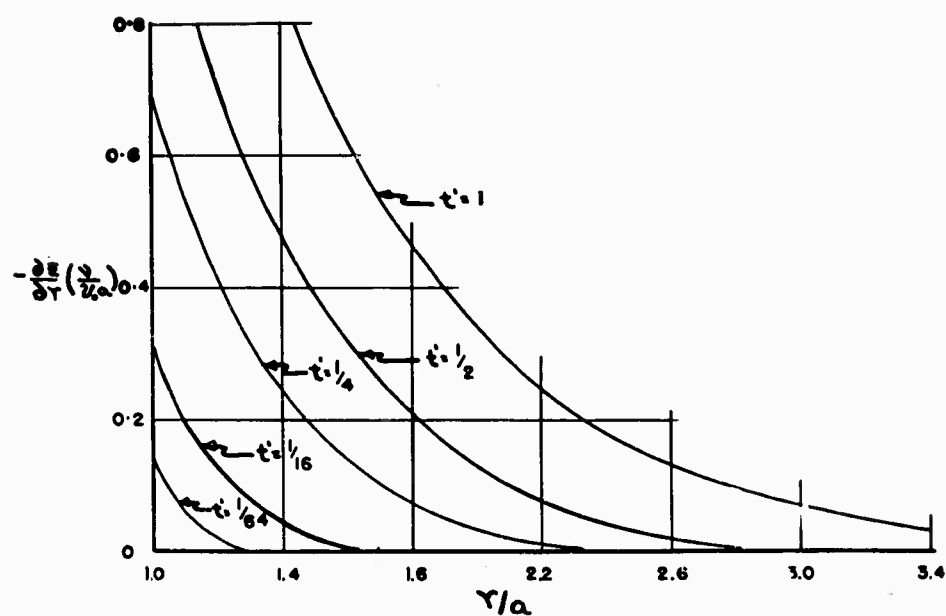


Figure 6a. Strain vs. Radial Distance Curves ( $H = 0$ )

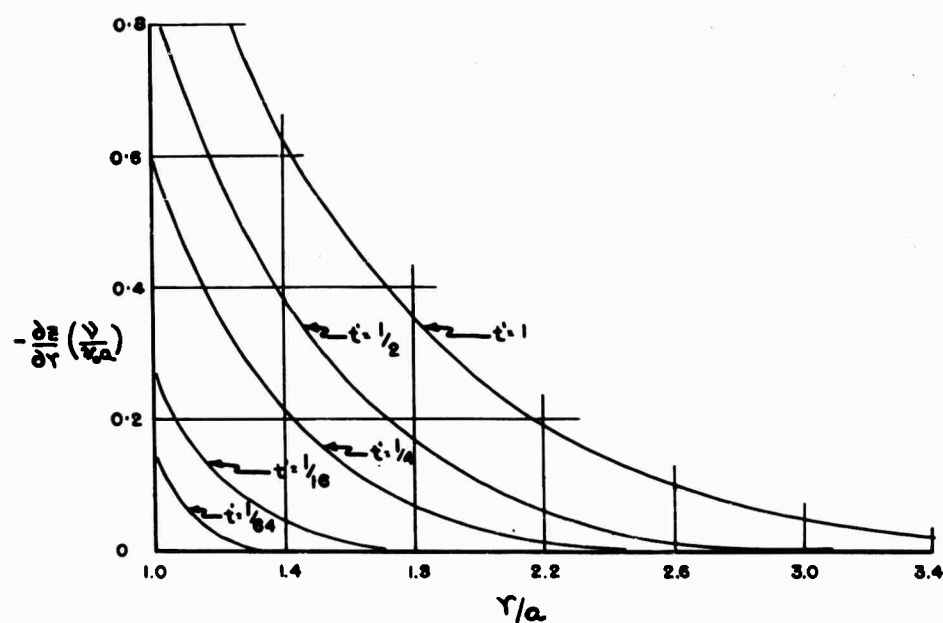


Figure 6b. Strain vs. Radial Distance Curves ( $H = 0.423$ )

# VISCO-PLASTIC FLOW THEORY

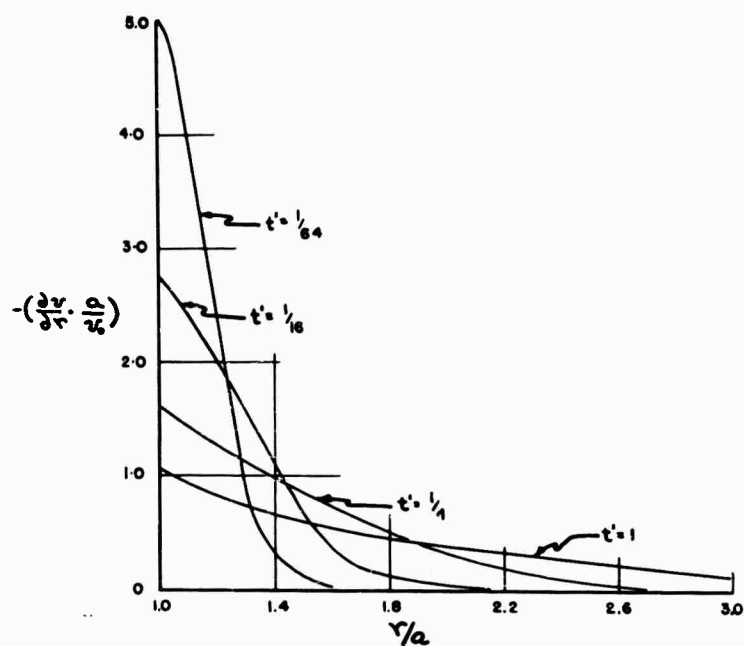


Figure 7a. Strain-Rate vs. Radial Distance Curves ( $H = 0$ )

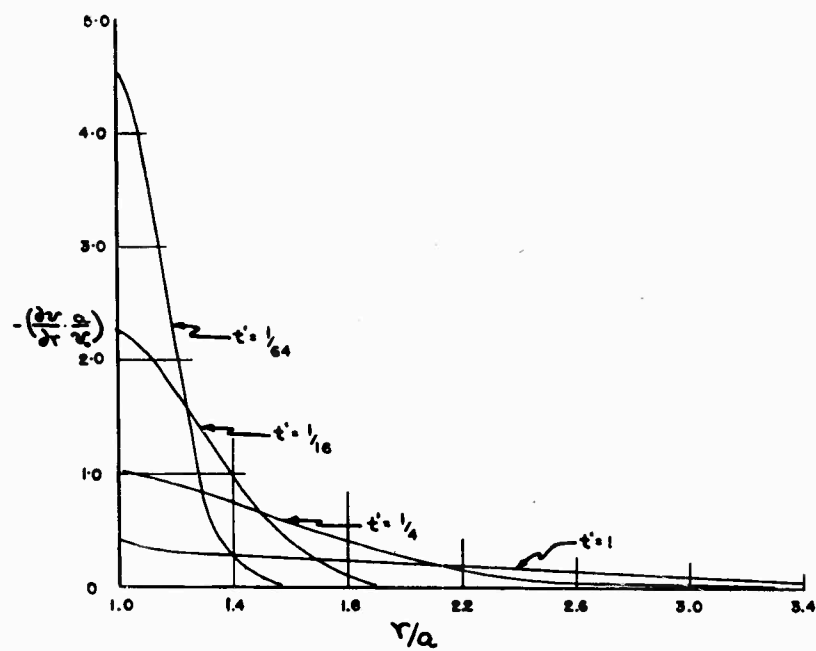


Figure 7b. Strain-Rate vs. Radial Distance Curves ( $H = 0.423$ )

## VISCO-PLASTIC FLOW THEORY

to be a continuum and separation occurs.

It is hypothesized therefore, that the actual separation occurs when the material changes from a "viscous fluid" into a "non-viscous" fluid. In equation form this separation criterion is expressed as

$$\mu \frac{\partial v}{\partial r} < c_1 k \quad \text{and} \quad \frac{\partial z}{\partial r} > c_2$$

or

(6)

$$\left( \frac{\partial v}{\partial r} \right)_{CR} = \frac{c_1 k}{\mu} ; \quad \left( \frac{\partial z}{\partial r} \right)_{CR} = c_2$$

where  $c_1$  and  $c_2$  are two constants. For the numerical calculation in this paper,  $c_1 = 1$  and  $c_2 = 0.02$  are assumed.

### V. RESULTS AND DISCUSSION

The impacts on a 3/64"-thick plate by a 3/32"-diameter sphere ( $H = 0.423$ ), with four different velocities are considered and the results are tabulated in Table I. The values for critical strain  $(\partial z / \partial r)_{CR}$  and critical strain-rate  $(\partial v / \partial r)_{CR}$  are calculated from Equation 6, with the estimated value of  $k = 10^5$  psi. On the expanded strain vs.  $r/a$  curves (Fig. 9), a horizontal dotted line is drawn for each value of  $(\partial z / \partial r)_{CR}$ . From the intersection points between the dotted lines and the solid curves, the critical strain-rate propagation curves are obtained and plotted in Figure 11, with  $t'$  as ordinate and  $r/a$  as abscissa. Similarly the critical strain-rate propagation curves are obtained from Figure 10 and plotted in Figure 11.

In Figure 11 the region above the critical strain  $(\partial z / \partial r)_{CR}$  curve has very large strain and the material may be considered as fluid. The region below  $(\partial z / \partial r)_{CR}$  indicates low shear strain and the material is solid. The critical strain-rate curve also divides the  $t' - x$  plane into two regions; above the curve the material is viscous and below non-viscous. The intersection point P of these two curves gives the time and location of the material separation or perforation, since beyond this point the material would behave like a non-viscous fluid according to the theory.

The radius of perforation  $r_p$  vs. initial impact velocity curve is shown in Figure 12. It may be seen that the radius of perforation increases with increasing impact velocity, which agrees with most experimental results. (Ref. 4)

For all the four initial velocities considered, the perforations occur within one microsecond after the initial contact between the projectile and the plate, as shown in Table I. At the moment of perforation, the displacement and velocity distribution along the radius are shown in Figures 13 and 14 respectively. At the separation surface the displacement is very small, which indicates that the plate remains essentially flat with no "lips" after the impact. The residual velocity of the projectile is denoted by  $v_p$  and may be read from Figure 14.

# VISCO-PLASTIC FLOW THEORY

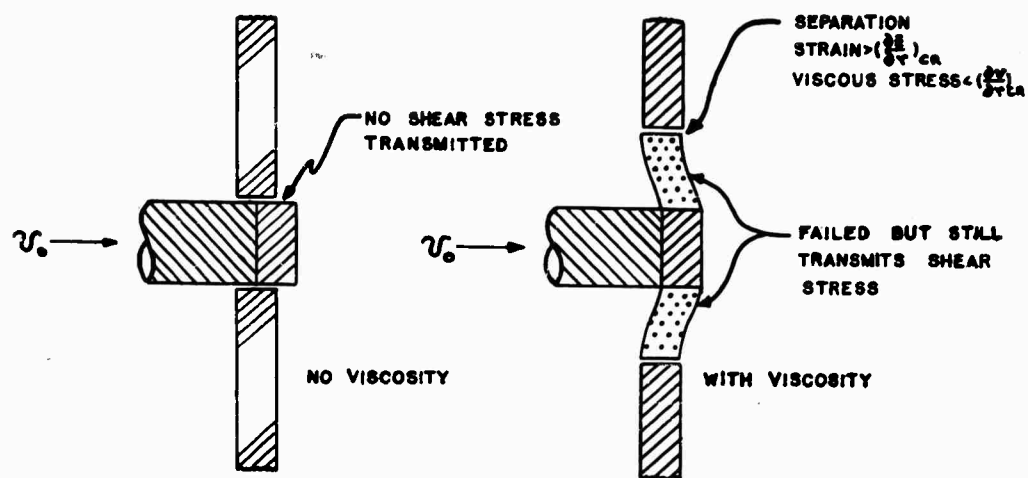


Figure 8. Separation Criterion

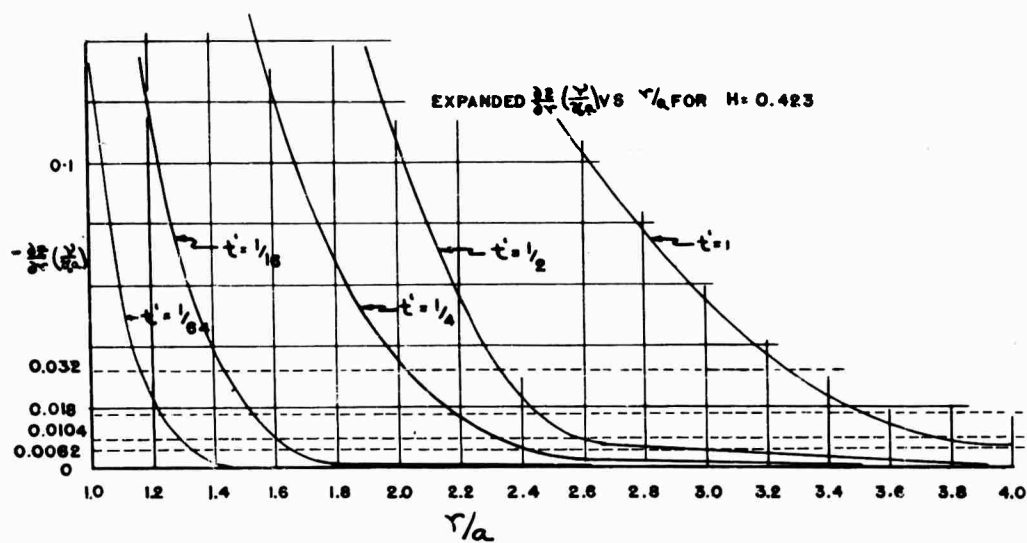


Figure 9. Expanded Strain  $(\frac{3}{8})$  Curves

# VISCO-PLASTIC FLOW THEORY

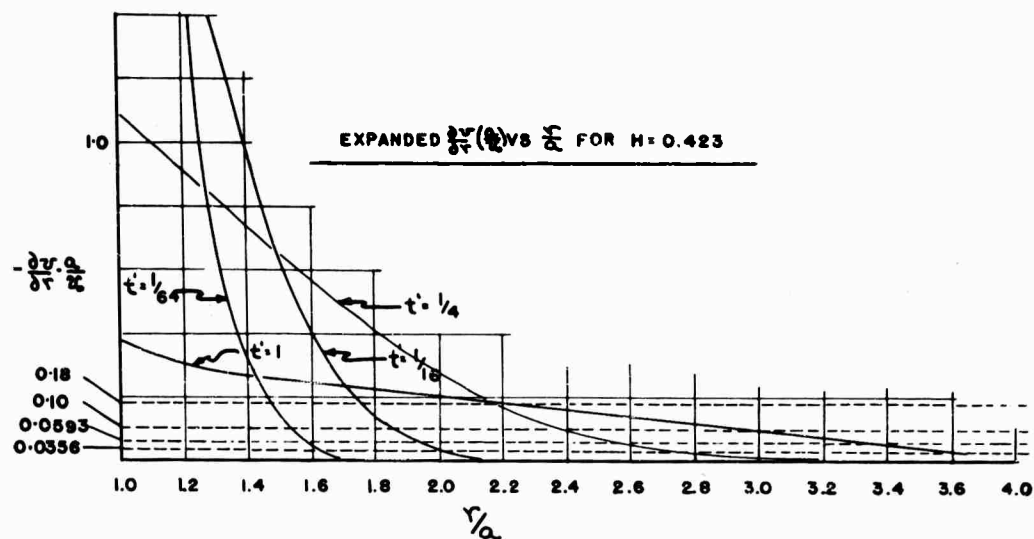


Figure 10. Expanded Strain-Rate  $\left(\frac{dv}{dt}\right)$  Curves

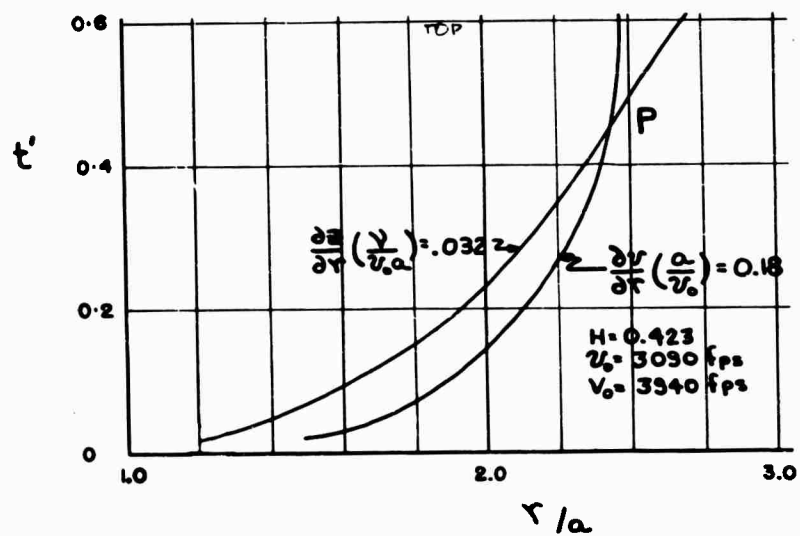


Figure 11a. Critical Strain and Strain-Rate Curves ( $V_o = 3940\text{fps}$ )

# VISCO-PLASTIC FLOW THEORY

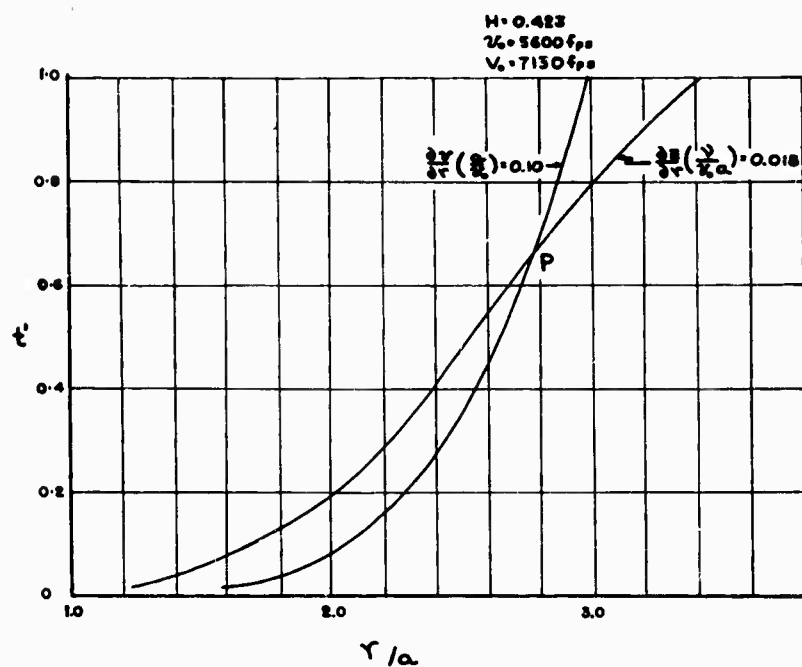


Figure 11b. Critical Strain and Strain-Rate Curves ( $V_0 = 7130 \text{ fps}$ )

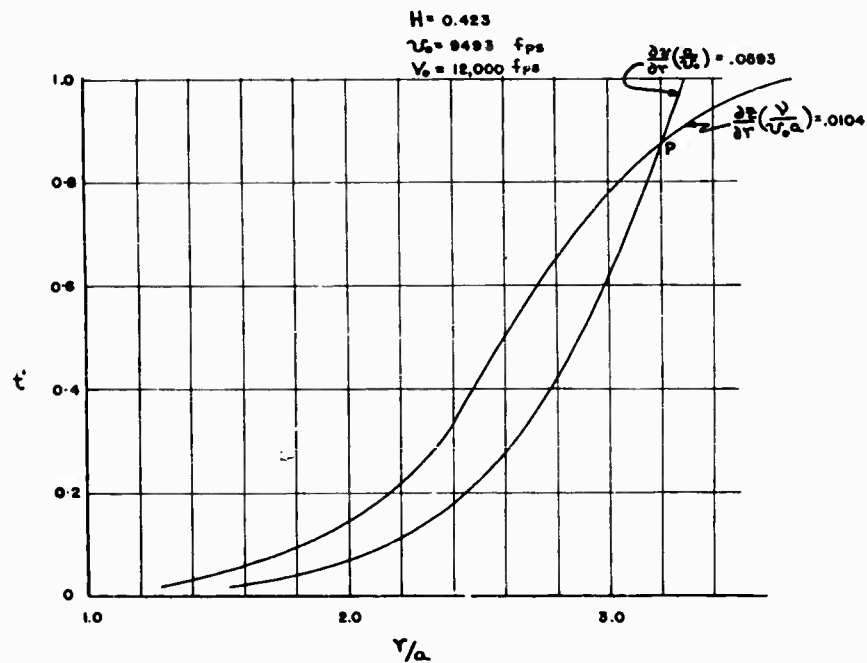


Figure 11c. Critical Strain and Strain-Rate Curves ( $V_0 = 12,000 \text{ fps}$ )

# VISCO-PLASTIC FLOW THEORY

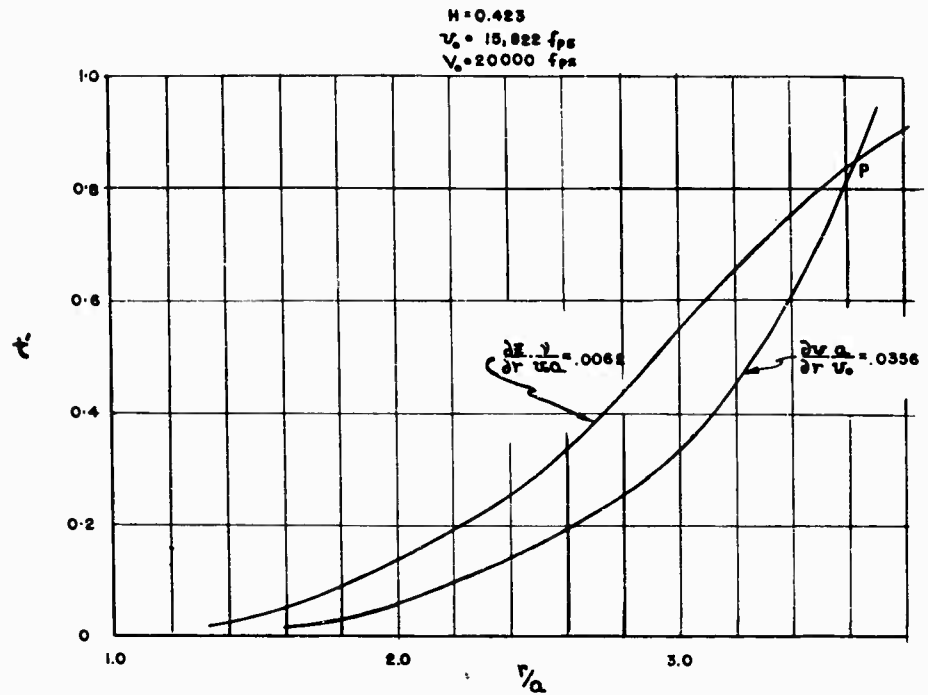


Figure 11d. Critical Strain and Strain-Rate Curves ( $V_0 = 20,000 \text{ fps}$ )

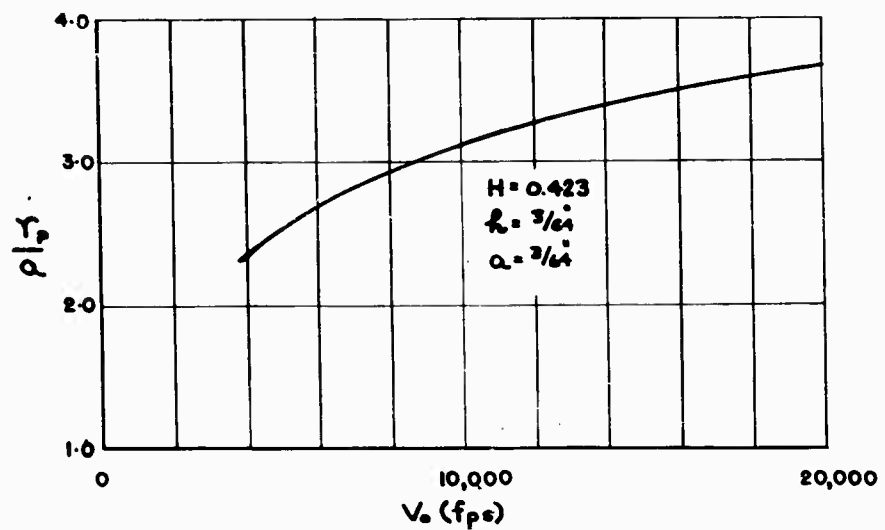


Figure 12. Radius of Perforation ( $r_p$ ) vs. Initial Velocity ( $V_0$ ) Curves

# VISCO-PLASTIC FLOW THEORY

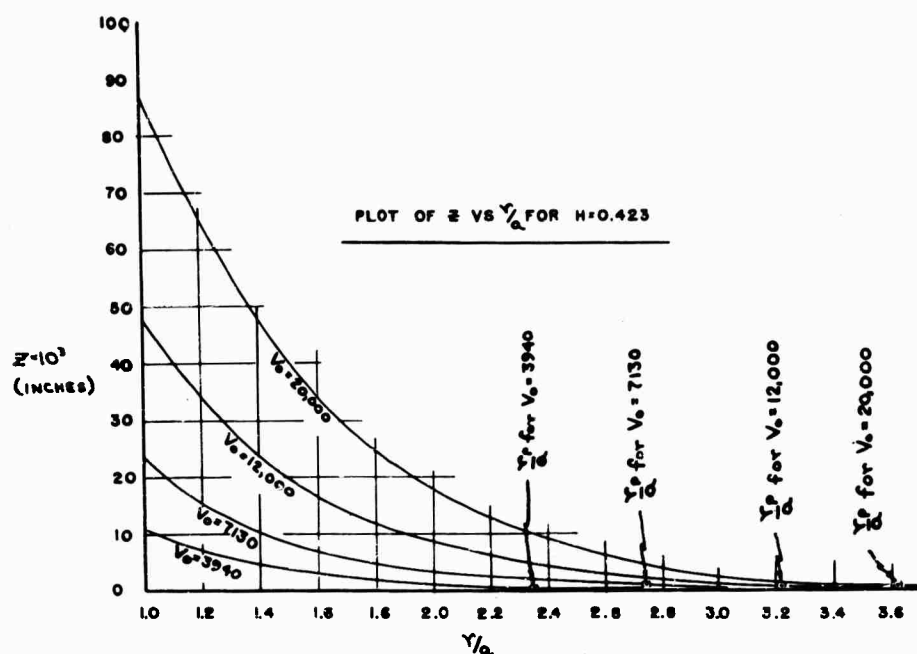


Figure 13. The Displacement Distribution at the Moment of Perforation

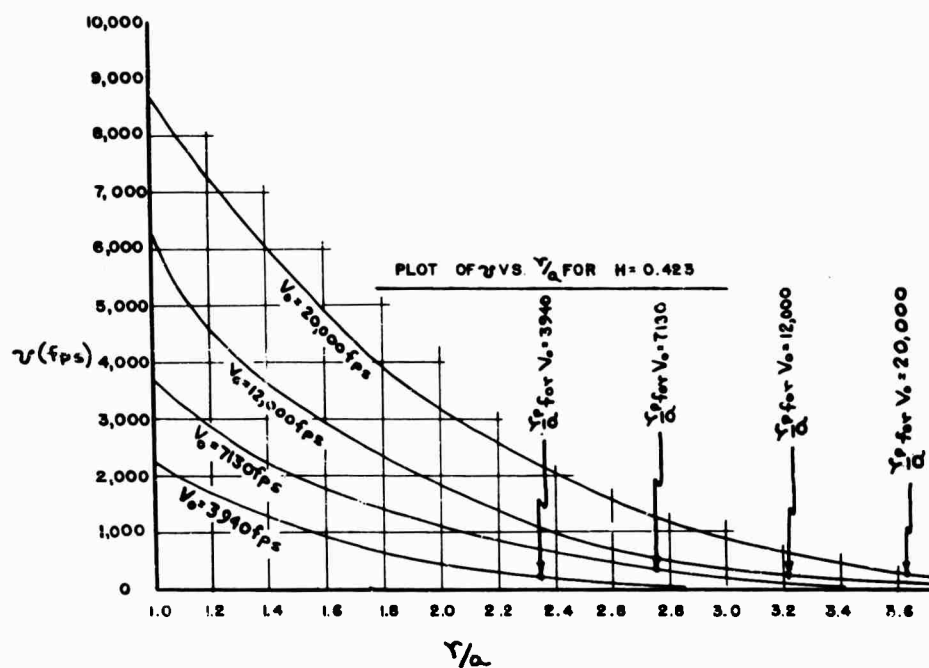


Figure 14. The Velocity Distribution at the Moment of Perforation

## VISCO-PLASTIC FLOW THEORY

The loss of kinetic energy by the projectile is calculated by two formulas

$$\Delta E_1 = \frac{1}{2} M_1 (V_0^2 - v_0^2) = \frac{1}{2} M_1 \left[ 1 - \left( \frac{M_1}{M} \right)^2 \right] V_0^2 \quad (7)$$

$$\Delta E_2 = \frac{1}{2} M_1 (V_0^2 - v_p^2) \quad (8)$$

Equation 7 gives the initial loss of energy by the projectile immediately after impact. Equation 8 gives the total loss of kinetic energy by the projectile. These two energy losses are plotted in Figure 15. The loss  $\Delta E_1$  is a quadratic function of  $V_0$  while  $\Delta E_2$  is proportional to  $V_0^{2.06}$ .

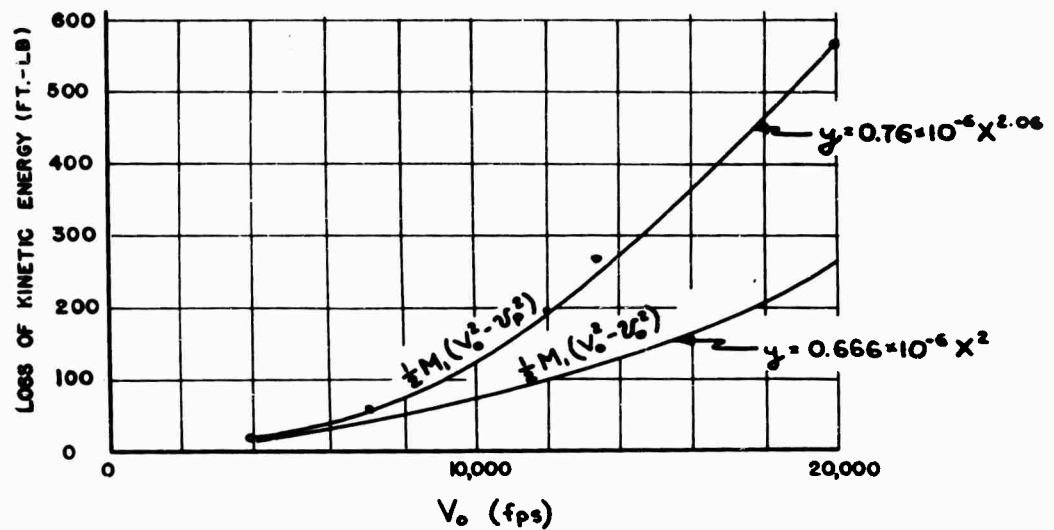


Figure 15. Loss of Kinetic Energy Curves

During the impact, the projectile and the plate material directly in contact with it are under high pressure. They are compressible rather than rigid as assumed in the present theory. However, it can be shown that in certain cases the rigid material assumptions are justified. As discussed in Reference 1, compression shock waves are generated immediately after the impact. If the thickness of the plate is small as compared to the radius of the projectile and if the shock velocity is high, the shock wave pattern is essentially one-dimensional within the first few microseconds, except in the region near the edge of the contact area. Since, according to the present theory, the total perforation process takes place within one microsecond, it seems reasonable to assume that the projectile and the portion of plate directly in contact with it move as a rigid body, and the radial component of the plate particle motion may be neglected. A more detailed analysis is required to establish the accuracy of the present assumptions as influenced by

## VISCO-PLASTIC FLOW THEORY

the initial velocity, projectile radius, plate thickness and coefficient of viscosity.

In conclusion it may be mentioned that although certain of the results of the present analysis agree with known test data, they can only be considered as qualitative indications of the viscosity effect in hypervelocity impact. For a quantitative analysis, the exact values of the coefficient of viscosity must be known; the compressibility effect and the radial component of the particle motion will probably also have to be included.

### REFERENCES

1. Bjork, R. L. , Effects of a Meteoroid Impact on Steel and Aluminum in Space: The 10th International Astronautical Congress, London, England, August 1959.
2. Rinehart, John S. , and Pearson, John, Behavior of Metals Under Impulsive Loads: The American Society of Metals, Cleveland, Ohio, 1954.
3. Chou, Pei Chi, Perforation of Plates by High Speed Projectiles: Presented at the 5th Midwestern Conference on Solid Mechanics, Michigan State University, East Lansing, Michigan, September 1961.
4. Partridge, William S. , Morris, C. Richard and Fullmer, Merlin D. , Perforation and Penetration Effects of Thin Targets: Proceedings of Third Symposium on Hypervelocity Impact, Armour Research Foundation, Chicago, February 1959.
5. Bachshian, F. A. , Visco-plastic Flow by Impact of a Cylinder upon a Plate (in Russian), Priklad. Mat. Mekh. , 12, 1948, 47.
6. Kochetkov, A. M. , On the Propagation of Elastic-Viscous-Plastic Shear Waves in a Plate (in Russian), Priklad. Mat. Mekh. , 14, 1950, 203.
7. Goldsmith, Werner, Impact -- The Theory and Physical Behavior of Colliding Solids: Edward Arnold Ltd. , London, 1960.

# VISCO-PLASTIC FLOW THEORY

TABLE I

## PÉRFORATION OF 3/64"-PLATE

$a = .0469 \text{ in.}$   
 $\rho = 5.2 \text{ slug/ft}^3$   
 $h = .0469 \text{ in.}$   
 $M = 4.5 \times 10^{-6} \text{ slug}$   
 $M_1 = 3.56 \times 10^{-6} \text{ slug}$   
 $H = 0.423$

$V_o \text{ fps}$	3940	7130	12,000	20,000
$v_o \text{ fps}$	3090	5600	9490	15,800
$-(\frac{\partial v}{\partial r})_{CR} \frac{a}{v_o}$	0.18	0.10	.0593	.0356
$-(\frac{\partial z}{\partial r})_{CR} \frac{v}{av_o}$	0.032	0.018	.0104	.0062
$\frac{r_p}{a}$	2.34	2.77	3.25	3.63
$t_p \text{ (SEC)}$	$0.378 \times 10^{-6}$	$0.493 \times 10^{-6}$	$0.572 \times 10^{-6}$	$0.684 \times 10^{-6}$
$v_p \text{ at } (\frac{r}{a} = 1) \text{ fps}$	2200	3800	6200	8700

## APPENDIX I: SOLUTION OF THE GOVERNING EQUATIONS

Applying the Laplace transform to Equation 4 results in

$$\frac{\partial^2 \bar{v}}{\partial r^2} + \frac{1}{r} \frac{\partial \bar{v}}{\partial r} - \frac{1}{r} \frac{k}{\mu p} = q^2 \bar{v} \quad (I-1)$$

where  $\bar{v}$  is the transform of  $v$ ;  $q^2 = \frac{p}{\nu}$  and  $p$  is the parameter of the transform. Introducing

$$r' = qr, \quad a' = qa \quad \text{AND} \quad c = \frac{k}{\mu p q}, \quad \text{Equation I-1 becomes}$$

$$\frac{\partial^2 \bar{v}}{\partial r'^2} + \frac{1}{r'} \frac{\partial \bar{v}}{\partial r'} - \bar{v}' = \frac{c}{r'} \quad (I-2)$$

The boundary conditions, Equations 5, transform into

# VISCO-PLASTIC FLOW THEORY

$$h' \mu q \frac{\partial \bar{v}}{\partial r'} - \frac{h' k}{p} - p \bar{v} + v_0 = 0 \quad \text{AT } r' = a' \quad (I-3)$$

$$\text{AS } r' \rightarrow \infty, \bar{v} = 0 \quad (I-4)$$

The initial conditions are satisfied by the transforms I-2 and I-3. The general solution of the homogeneous equation associated with Equation I-2 is

$$\bar{v} = AK_0(r') + BI_0(r') \quad (I-5)$$

where  $I_0$  and  $K_0$  are the modified Bessel functions of the zero order, and of the first and second kind respectively; A and B are constants. The particular solution for Equation I-2 is obtained by the method of variation of parameters. The Wronskian of the general solution of the homogeneous equation is

$$W = (K_0 I_0' - I_0 K_0') = \frac{1}{r'} \quad (I-6)$$

where prime represents differentiation. It can be shown that the particular solution of Equation I-2 is

$$\bar{v} = C \left[ I_0 \int K_0 \partial r' - K_0 \int I_0 \partial r' \right] \quad (I-7)$$

The general solution of Equation I-2 is thus

$$\bar{v} = AK_0(r') + BI_0(r') + C \left[ I_0 \int K_0 \partial r' - K_0 \int I_0 \partial r' \right] \quad (I-8)$$

At  $r' = \infty$ , the functions  $K_0$ ,  $I_0 \int K_0 \partial r'$  and  $K_0 \int I_0 \partial r'$  all vanish. Therefore, to satisfy Equation I-4, it is only necessary to set  $B = 0$ . Substituting Equation I-8 into Equation I-3 yields the constant A,

$$A = \frac{\bar{v}_0 - \frac{h' k}{p} + \int_{K_0 \partial r'}^a C [h' \mu q I_0'(a') - p I_0(a')] + \int_{I_0 \partial r'}^a C [-h' \mu q K_0'(a') + p K_0(a')]}{p K_0(a') - h' \mu q K_0'(a')} \quad (I-9)$$

and the solution of Equation I-2 which satisfies Equations I-3 and I-4 is

$$\bar{v} = AK_0(r') + C \left[ I_0 \int K_0 \partial r' - K_0 \int I_0 \partial r' \right] \quad (I-10)$$

Using the inversion theorem,  $v$  could be obtained from Equation I-10, although it would be too cumbersome for numerical evaluation. For simplicity, the yield stress  $k$  is dropped, because it is much smaller than the viscous or inertia stresses. Because only a small time interval is of interest, the following asymptotic expansions of  $K_0$  and  $K_1$  are used:

$$K_0(r') = \left(\frac{\pi}{2r'}\right)^{1/2} e^{-r'} \left\{ 1 - \frac{1}{8r'} + \frac{9}{128r'^2} + \dots \right\} \quad (I-11)$$

$$K_1(r') = \left(\frac{\pi}{2r'}\right)^{1/2} e^{-r'} \left\{ 1 + \frac{3}{8r'} - \frac{15}{128r'^2} + \dots \right\} \quad (I-12)$$

The resulting equation, after algebraic simplification, is

$$\begin{aligned} \bar{v} = v_0 \left(\frac{a}{r}\right)^{1/2} \frac{e^{-q(r-a)}}{p} \left\{ 1 - \left[ \frac{h'}{v} + \frac{q-r}{8ra} \right] \frac{1}{q} \right. \\ \left. + \left[ \frac{9a^2 - 2ar - 7r^2}{128a^2r^2} + \frac{h'}{v} \left( \frac{a-5r}{8ar} \right) + \frac{h'^2}{v^2} \right] \frac{1}{q^2} + \dots \right\} \end{aligned} \quad (I-13)$$

Using standard transform tables gives

$$\begin{aligned} v = v_0 \left\{ \sqrt{\frac{1}{r}} \operatorname{erfc} \frac{\bar{r}-1}{2\sqrt{1}} + R_4 2\sqrt{1} i \operatorname{erfc} \frac{\bar{r}-1}{2\sqrt{1}} \right. \\ \left. + R_5 4i^2 \operatorname{erfc} \frac{\bar{r}-1}{2\sqrt{1}} + \dots \right\} \end{aligned} \quad (I-14)$$

where  $\bar{r} = \frac{r}{a}$

The corresponding displacement, strain and strain-rate are

$$\begin{aligned} z = (4v_0 t) \left\{ \sqrt{\frac{1}{r}} i^2 \operatorname{erfc} \frac{\bar{r}-1}{2\sqrt{1}} + R_4 2\sqrt{1} i^3 \operatorname{erfc} \frac{\bar{r}-1}{2\sqrt{1}} \right. \\ \left. + R_5 4i^4 \operatorname{erfc} \frac{\bar{r}-1}{2\sqrt{1}} + \dots \right\} \end{aligned} \quad (I-15)$$

$$\begin{aligned} \frac{\partial z}{\partial r} = \frac{4v_0}{a} 4t \left\{ -\frac{1}{2\sqrt{1}} \sqrt{\frac{1}{r}} i \operatorname{erfc} \frac{\bar{r}-1}{2\sqrt{1}} + R_1 i^2 \operatorname{erfc} \frac{\bar{r}-1}{2\sqrt{1}} \right. \\ \left. + 2\sqrt{1} R_2 i^3 \operatorname{erfc} \frac{\bar{r}-1}{2\sqrt{1}} + 4t R_3 i^4 \operatorname{erfc} \frac{\bar{r}-1}{2\sqrt{1}} + \dots \right\} \end{aligned} \quad (I-16)$$

$$\begin{aligned} \frac{\partial v}{\partial r} = \frac{v_0}{a} \left\{ -\frac{2}{\sqrt{\pi}} \frac{1}{2\sqrt{1}} e^{-\frac{(\bar{r}-1)^2}{4t}} \sqrt{\frac{1}{r}} + R_1 \operatorname{erfc} \frac{\bar{r}-1}{2\sqrt{1}} \right. \\ \left. + 2\sqrt{1} R_2 i \operatorname{erfc} \frac{\bar{r}-1}{2\sqrt{1}} + 4t R_3 i^2 \operatorname{erfc} \frac{\bar{r}-1}{2\sqrt{1}} + \dots \right\} \end{aligned} \quad (I-17)$$

where

$$\begin{aligned} R_1 &= \sqrt{\frac{1}{r}} \left[ -\frac{3}{8} \frac{1}{r} - \frac{1}{8} + H \right] \\ R_2 &= \sqrt{\frac{1}{r}} \left[ \frac{15}{128} \frac{1}{r^2} - \frac{3}{64} \frac{1}{r} + \frac{7}{128} + \frac{H}{8} \left( 5 + \frac{3}{r} \right) - H^2 \right] \\ R_3 &= \sqrt{\frac{1}{r}} \left[ -\frac{45}{256} \frac{1}{r^3} + \frac{3}{128} \frac{1}{r^2} + \frac{7}{256} \frac{1}{r} + \frac{H}{16} \left( \frac{5}{r} - \frac{3}{r^2} \right) - \frac{1}{2} H^2 \frac{1}{r} \right] \\ R_4 &= \sqrt{\frac{1}{r}} \left[ \frac{1}{8} - \frac{1}{8r} - H \right] \\ R_5 &= \sqrt{\frac{1}{r}} \left[ \frac{9}{128} \frac{1}{r^2} - \frac{1}{64} \frac{1}{r} - \frac{7}{128} + H \left( \frac{1}{8r} - \frac{5}{8} \right) + H^2 \right] \end{aligned}$$

## VISCO-PLASTIC FLOW THEORY

### APPENDIX II: OTHER VISCO-PLASTIC SOLUTIONS

The visco-plastic shear wave propagation following an impact on a plate has also been studied by Bachshian (Ref. 5) and Kochetkov (Ref. 6). The basic assumptions made by these authors are similar to those discussed in the present paper. The main difference is that in References 5 and 6, the wave propagations due to low speed impacts (below 100 m/sec) are studied, as in contrast to the high speed perforation analyzed in the present paper.

The basic differential equation derived in Reference 5 is identical to Equation 4 of the present paper. The initial conditions are also identical, but the boundary conditions are different. In Reference 5 the velocity of the projectile is assumed constant after the impact (equivalent to  $H = 0$  case), and thus the solution is limited to very large mass projectiles. To avoid the difficulty at  $r = \infty$ , a plate with finite radius  $r = b$  is considered and the boundary condition at the edge of the plate is

$$v = 0 \quad \text{AT} \quad r = b \quad (\text{II-1})$$

Since low speed impact is of interest, the yield shear stress  $k$  is retained in the equation. By introducing non-dimensional variables

$$\begin{aligned} x &= r/a \\ \tau &= kt/\mu \\ u &= v/v_0 \end{aligned} \quad (\text{II-2})$$

the differential equation is changed into the form

$$RS \frac{\partial u}{\partial \tau} = \frac{\partial^2 u}{\partial x^2} + \frac{1}{x} \frac{\partial u}{\partial x} - \frac{S}{x} \quad (\text{II-3})$$

where

$$S = \frac{\sigma k}{\mu v_0} \quad = \text{Saint Venant Number (or Bingham Number)} \quad (\text{II-4})$$

$$R = \frac{\rho v_0}{\mu} \quad = \text{Reynold Number} \quad (\text{II-5})$$

The solution involves a combination of Bessel functions. For numerical example, the following values are used

$$k = 4000 \text{ kg/cm}^2 \quad (\cong 62000 \text{ psi})$$

$$\mu = 0.4 \text{ kg-sec/cm}^2 \quad (\cong 820 \text{ lb-sec/ft}^2)$$

$$a = 10 \text{ cm}$$

$$\rho = 8 \times 10^{-6} \text{ kg-sec}^2/\text{cm}^4$$

## VISCO-PLASTIC FLOW THEORY

Dimensionless deflection and shear stress during the impact are plotted.

In Reference 6, the material of the plate is assumed to be elastic-visco-plastic. When the shear stress is below the yield limit, an elastic stress-strain relation is used. Above the yield limit, the following relation is assumed:

$$\frac{\partial \gamma}{\partial t} = \frac{1}{G} \frac{\partial}{\partial t} [\tau - F(\gamma)] + \frac{1}{\mu} [\tau - F(\gamma)] \quad (\text{II-6})$$

where  $G$  is the shear modulus of elasticity and  $F(\gamma)$  is an empirical function. For the ideally plastic case,  $F(\gamma) = k$ , where  $k$  is the yield limit. For a linear strain hardening material,  $F(\gamma) = k \left[ 1 + (m^2 - 1) \left( \frac{\gamma G}{k} - 1 \right) \right]$

is assumed. The resulting equations are of the hyperbolic type and the method of characteristics is used for their solutions. Graphs are plotted for the ideally plastic case giving the stress and velocity histories in the plate and the distribution of the residual strain.

## SUMMARY FOR THE THEORY SESSIONS

Floyd E. Allison

Ballistic Research Laboratories  
Aberdeen Proving Ground, Maryland

The papers presented during the last two sessions have considered some of the problems encountered in describing the mechanics of hypervelocity impact. Due to time limitations, there are also a number of papers published in the proceedings that have not been presented for open discussion. However, there has been sufficient discussion to indicate the magnitude of the problem. For obvious reasons it is not possible to evaluate at this time the progress that has been made in developing the theory. However, a few comments of a more general nature do seem appropriate.

There does not appear to be sufficient evidence to assume a priori that mechanical resistance to shear is going to be completely negligible in the 10 to 20 km/sec velocity range. At the same time it is not possible to extrapolate the purely empirical relations between crater dimensions and velocity, which have been obtained in the 0 to 10 km/sec velocity range. Therefore, empirical relations determined at higher velocities or a theory that is valid in the lower velocity range and can be used to extrapolate to the higher velocities is urgently needed.

In order to obtain a solution to the hypervelocity impact problem based on fundamental principles of mechanics, one must eventually come to grips with the problem of non-linear time-dependent differential equations in two space dimensions. It is obvious that a satisfactory solution of the problem based on this approach will require the use of high-speed digital computers. During the early phase of the crater formation process, the problem can be described by non-steady compressible fluid flow, and most of the tools for solving this part of the problem are available. The subsequent motion of the material, during which some fraction of the projectile energy may be dissipated in doing work against internal forces of the target, poses a more difficult problem. The resistance of the material to shear in the flow behind the shock may be considerably important. Unfortunately, one-dimensional treatments that include the effects of strength and viscosity on the shock structure do not provide any real information concerning the effects of these parameters under conditions of shear. As Dr. Hopkins has pointed out, basic data on the behavior of solids, particularly data relevant to the constitutive equations, are potentially useful provided the rate of deformation approaches that encountered during hypervelocity impact.

There is also an alternative approach to the problem which would use some form of simplified theoretical model. However, if the theoretical model is to be

## SUMMARY

useful as a guide for planning the research program, it must be chosen to represent physical reality, and not merely because it is mathematically tractable. Also, the mathematical difficulties are a property of the differential equations governing the process, and they cannot be removed solely by means of simplifying assumptions. If a satisfactory theoretical model is found, it will almost surely require the empirical determination of additional quantities or functions, which will then enable one to circumvent the difficulties inherent in the rigorous treatment of the problem. Unfortunately it appears that calculations involving hypervelocity impact effects are relatively insensitive to the assumptions used in setting up the theoretical model. Experimental observations over a limited range of any one of the commonly measured parameters can apparently be explained by several different theoretical models.

Another way of phrasing the difficulty is that critical parameters are not being measured experimentally. Additional data of the final crater dimensions in the lower velocity range are not going to assist the development of a rigorous theory or a physically acceptable theoretical model. Additional data of the usual type in the higher velocity range for a few selected materials would be useful in clarifying one or two difficult questions. Detailed and accurate data concerning the flow pattern during the formation of a crater as a function of time for a few selected target materials are potentially very useful, even if the impact velocities are in the lower velocity range. It is interesting to speculate about the possibility that hypervelocity impact experiments, together with a sound theoretical analysis of the problem, may provide the means for obtaining basic information concerning the appropriate constitutive equations.